PIPELINE HEALTH MONITORING

by

Andrea Galvagni

A thesis submitted to Imperial College London for the degree of

Doctor of Engineering

Department of Mechanical Engineering
Imperial College London
London SW7 2AZ

September 2013

This page has been intentionally left blank.

Declaration of Originality

The material presented in the thesis **“Pipeline Health Monitoring”** is entirely the result of my own independent research under the supervision of Professor Peter Cawley. All published or unpublished material utilised in this thesis has been given full acknowledgement.

Andrea Galvagni

London, the 6th of September 2013

This page has been intentionally left blank.

Copyright Declaration

“Se non potete parlare bene di una persona, non parlatene.”

Rosa Falasca

This page has been intentionally left blank.

Abstract

Worldwide, BP operates many thousand kilometres of pipelines carrying valuable yet toxic and corrosive fluids. The structural integrity of these pipelines is crucial, as any failure may result in environmental damage, economic losses and injuries to personnel. Conventionally, pipeline integrity is assessed on a time basis. This inherently limits the amount of information available about its structural health, as any damage which develops in unexpected circumstances or while the pipeline is not being inspected may remain undetected. Such lack of information hinders the reliability of any prognosis and of Risk-Based Inspection and Maintenance strategies, increases the risk of unexpected critical damage development and pipeline failure, and forces the use of costly time-based maintenance, following the safe-life design approach. Conversely, if sufficient information about pipeline integrity were available to produce reliable prognoses, then it would become possible to dramatically reduce the risk of unexpected failures and to utilise cost-efficient condition-based maintenance, which prescribes the replacement of a pipeline only when it is about to suffer critical damage and has therefore reached the actual end of its operational life. In this way, pipeline networks would become safer and more reliable while at the same time more productive and less costly. This thesis introduces and demonstrates a Structural Health Monitoring approach that has the potential to fill the integrity information gap and ultimately enable the use of condition-based pipeline maintenance. This approach, embodied by a practical automated pipeline damage detection procedure, complements permanently installed guided wave sensors to create a complete pipeline health monitoring solution. Utilising experimental data from a permanently installed guided wave sensor installed on a purpose-built NPS 8 Schedule 40 pipe loop facility at BP's Naperville Campus, it is shown that the procedure is very effective at detecting and quantifying actual damage, thereby achieving the intended aim of this thesis.

This page has been intentionally left blank.

Acknowledgements

I am deeply grateful to my supervisor, Professor Peter Cawley, for making me discover that what I enjoy most in life is to challenge myself, and without whose guidance, support and encouragement this thesis might have never been written, perhaps more so in the present case than ever before.

I am also very grateful to Professor Chris Scruby for introducing me to and giving me the opportunity to join the Engineering Doctorate in Non-Destructive Evaluation programme, an invaluable experience that I will fondly remember for the rest of my career.

At Imperial College, I would like to thank Professor Mike Lowe, Dr Francesco Simonetti, Dr Fredric Cegla and all the past and present members of the Non-Destructive Evaluation group for creating a vibrant, stimulating and fruitful research environment. I take this occasion to extend my heartfelt gratitude to Rosalba and Remo for their deep friendship, to Tim for being one of the most intelligent and ingenious persons I have ever met, to Andrew for being a Yorkshireman, to Vatche for being himself, and also to Jake, Greg, David, Robin, Kit, Sam and Keith, of the Engineering Doctorate cohorts of 2007 and 2008, for making my Engineering Doctorate experience not just constructive but also entertaining.

At BP, I would like to thank Simon Webster, Ian Bradley and Tom Knox for their insights, suggestions and for their technical, logistical and financial support during the whole course of this project. I would also like to extend my gratitude to Steve Orwig, Tom Eason and Mark Lozev for kindly lending their facilities at BP's Naperville Campus, and to Aaron Nyholt for his dedication and excellent contribution during the experimental stages of this project.

Furthermore, I would like to thank Professor Paul Wilcox at the University of Bristol and Professor Mike Todd at the University of California, San Diego, for the fruitful discussions about the field of Structural Health Monitoring.

I would also like take this occasion to thank Guided-Ultrasonics Ltd and all its past and

present directors and employees for their help and support, and for giving me very precious insights. In particular, I would like to thank, in alphabetical order: David Alleyne, Alex Demma, Nick Kemp, Brian Pavlakovic, Malcolm Russell, Martina Skripova, Keith Vine and Tom Vogt.

Finally, I would like to acknowledge the financial support of the Engineering and Physical Sciences Research Council through the Research Centre in Non-Destructive Evaluation and in particular the Centre for Doctoral Training in Non-Destructive Evaluation.

Contents

1 Introduction **27**

1.1 Structural Health Monitoring 27

1.2 Permanently Installed Guided Wave Sensors 29

1.3 Thesis Aim & Outline 30

2 Guided Wave Pipeline Inspection **33**

2.1 Guided Wave Propagation 33

2.2 Guided Wave Inspection 37

2.2.1 Mode Choice 39

2.2.2 Early Development 40

2.2.3 Modern Commercial Implementation 40

2.2.4 Recent Advances 47

2.3 Conclusions 48

3 The Interaction of Guided Waves with Simple Supports in Pipes **49**

3.1 Contact Interface 50

3.2 Guided Wave Propagation in Supported Pipes 53

3.2.1 Guided Wave Propagation Model 53

3.2.2 Guided Wave Propagation Analysis 58
3.3 Finite-Element Analysis of Echoes from Simple Supports 64
3.4 Experimental Validation 74
3.5 Conclusions 76

4 Pipeline Health Monitoring **79**

4.1 Permanently Installed Guided Wave Sensors 82
4.2 Damage Detection 85
4.3 Environmental and Operating Conditions Effects 89
4.4 Baseline Subtraction Compensation 92
4.4.1 Localised Baseline Signal Stretch 93
4.4.2 Optimal Baseline Selection 102
4.4.3 Practical Baseline Subtraction Compensation 103
4.4.4 Effect of Compensation on Damage Growth Echoes 116
4.4.5 Summary 129
4.5 Uncompensated EOC Effects 130
4.6 Conclusions 132

5 Change Detection **133**

5.1 Change Detection Algorithms 134
5.1.1 Sequential Probability Ratio Test 135
5.1.2 Cumulative Sum Algorithm 139
5.1.3 Generalised Likelihood Ratio Algorithm 140
5.2 Step Change Detection 141

5.2.1 General Detectability Charts 145
5.3 Gradual Change Detection 148
5.3.1 General Detectability Charts 151
5.4 Conclusions 156

6 Damage Detection in Pipelines 157

6.1 Linear Regression for Damage Detection 162
6.2 Change Detection with Linear Regression 167
6.2.1 Sequential Probability Ratio Test 170
6.2.2 Generalised Likelihood Ratio Algorithm 171
6.3 Practical Pipeline Damage Detection 172
6.3.1 Damage Detection Procedure 182
6.3.2 Practical Damage Detection 187
6.4 Conclusions 221

7 Conclusion 223

7.1 Thesis Review 224
7.2 Main Contributions 226
7.2.1 The Interaction of Guided Waves with Simple Supports in Pipes 226
7.2.2 Baseline Subtraction Compensation 226
7.2.3 Damage Detection in Pipelines 227
7.3 Future Work 229
7.3.1 The Interaction of Guided Waves with Simple Supports in Pipes 229
7.3.2 Damage Detection in Pipelines 229

A Nominal Pipe Size 235

B Sequential Analysis 237

B.1 Neyman-Pearson Lemma 238

B.2 Sequential Probability Ratio Test 238

B.3 Test Boundaries 239

B.4 Average Sample Number 241

B.4.1 General Density 241

B.4.2 Parameterised Density 242

B.4.3 Normal Density 245

C Linear Regression 247

C.1 Samples Joint Distribution 248

C.2 Parameter Estimation 250

C.3 Parameter and Covariance Estimation 250

References 257

List of Publications 269

List of Tables

3.1 Material properties utilised to determine the properties of the contact interfaces for the SAFE guided wave propagation analysis 60

3.2 Contact stiffnesses utilised in the SAFE guided wave propagation analysis 60

4.1 Baseline subtraction compensation performance (operative pipeline) 105

4.2 Baseline subtraction compensation performance (inoperative pipeline) 111

6.1 Details of the damage introduced in the BP Naperville gPIMS® pipe loop damage 176

6.2 List of the gPIMS® P1 sensor readings gathered between July and August 2011 177

A.1 Summary of common Nominal Pipe Size (NPS) dimensions 235

List of Figures

2.1 Phase velocity dispersion curves for a NPS 3 Schedule 40 pipe 38

2.2 Group velocity dispersion curves for a NPS 3 Schedule 40 pipe 38

2.3 Example of commercial guided wave inspection equipment 43

2.4 Example of a commercial guided wave sensor installed on a pipeline 43

2.5 gPIMS® sensor before and after its installation on a pipe 44

2.6 Example torsional and flexural signals recorded by a gPIMS® sensor 45

2.7 Example envelope of the torsional signal recorded by a gPIMS® sensor 45

2.8 Example RC envelope of the torsional signal recorded by a gPIMS® sensor . . . 46

3.1 Diagram of the contact interface between a pipe and a simple support 51

3.2 Diagram of the SAFE model representing a pipe in contact with a simple support 56

3.3 Phase velocity dispersion curves for a free NPS 3 Schedule 40 pipe 59

3.4 Phase velocity dispersion curves for a hardwood-supported NPS 3 Schedule 40 pipe 59

3.5 Phase velocity dispersion curves for a steel-supported NPS 3 Schedule 40 pipe 60

3.6 Greyscale-coded phase velocity dispersion curves for a steel-supported NPS 3 Schedule 40 pipe 63

3.7 Phase velocity dispersion curves exemplifying mode repulsion in a steel-supported NPS 3 Schedule 40 pipe 65

3.8 Diagram of the FEA model representing an infinitely long pipe supported at one location 66

3.9 Example torsional signal from a FEA simulation of a NPS 3 Schedule 40 carbon steel pipe 68

3.10 Example modulus of the torsional FFT spectra from a FEA simulation of a NPS 3 Schedule 40 carbon steel pipe 68

3.11 Torsional RC spectrum from a FEA simulation of a NPS 3 Schedule 40 carbon steel pipe together with the total MAC spectrum 69

3.12 Example of two repelling modes summing to form a third mode 69

3.13 Torsional RC spectra from FEA simulations of a NPS 3 Schedule 40 carbon steel pipe resting on supports of various axial extents with 1kN loading 71

3.14 Torsional RC spectra from FEA simulations of a NPS 3 Schedule 40 carbon steel pipe resting on a 0.2m support with various loadings 71

3.15 Torsional RC spectra from FEA simulations of various Schedule 40 carbon steel pipes with different NPS resting on a 0.2m support with 1kN loading 72

3.16 Torsional RC spectra from FEA simulations of various NPS 3 carbon steel pipes with different Schedules resting on a 0.2m support with 1kN loading 72

3.17 Diagram of the experimental setup 75

3.18 Torsional RC spectrum from experiments and FEA simulations of a NPS 3 Schedule 40 carbon steel pipe resting on a 0.1m support with various loadings 77

3.19 Torsional RC spectrum from experiments and FEA simulations of a NPS 3 Schedule 40 carbon steel pipe resting on a 0.2m support with various loadings 77

4.1 Example of a gPIMS® sensor installed on a pipeline 83

4.2 Diagram of the baseline subtraction technique 90

4.3 Current and baseline torsional signals recorded by sensor gPIMS®-138 (operative pipeline). 104

4.4 LBSS gate functions for the torsional signals recorded by sensor gPIMS®-138. . 104

4.5 RC envelope of residual signals obtained from sensor gPIMS®-138 (operative pipeline) with different compensation approaches 108

4.6 RC envelope of residual signals obtained from sensor gPIMS®-138 (operative pipeline) with different baselines 108

4.7 Current and baseline torsional signals recorded by sensor gPIMS®-138 (inoperative pipeline). 110

4.8 LBSS gate functions for the torsional signals recorded by sensor gPIMS®-138. . 110

4.9 RC envelope of residual signals obtained from sensor gPIMS®-138 (inoperative pipeline) with different compensation approaches 114

4.10 RC envelope of residual signals obtained from sensor gPIMS®-138 (inoperative pipeline) with different baselines 114

4.11 Diagram of damage growth at and away from pipeline features 122

4.12 Amplitude of the damage growth echo with BSS compensation with damage growing at and away from pipeline features 122

4.13 Peak amplitude of the artefact echoes with BSS compensation with damage growing at and away from pipeline features 123

4.14 Relative amplitude of the peak artefact to the damage growth echo with damage growing at pipeline features after BSS compensation 123

4.15 Diagram of damage growth with dense and sparse pipeline features 126

4.16 Amplitude of the damage growth echo with BSS compensation with dense and sparse features 126

4.17 Peak amplitude of the artefact echoes with BSS compensation with dense and sparse features 127

4.18 Relative amplitude of the peak artefact to the damage growth echo with dense and sparse features after BSS compensation 127

5.1 Random variable y undergoing a step change in its mean. 142

5.2 Generalised Likelihood Ratio detection of a step change in mean. 144

5.3 Generalised Likelihood Ratio estimation of the step change in mean. 144

5.4 Generalised Likelihood Ratio estimation of the time of the step change in mean. 144

5.5 Average Sample Number as a function of the step change detectability ratio. . . 146

5.6 Detectability chart for step changes in mean. 147

5.7 Random variable y undergoing a change in the slope of its mean. 148

5.8 Generalised Likelihood Ratio detection of a change in the slope of the mean. . 152

5.9 Generalised Likelihood Ratio estimation of the change in the slope of the mean. 152

5.10 Generalised Likelihood Ratio estimation of the time of the change in the slope of the mean. 152

5.11 Average Sample Number as a function of the slope change detectability ratio. . 154

5.12 Detectability chart for slope changes. 155

6.1 Diagram of BP Naperville gPIMS® pipe loop 173

6.2 gPIMS® P1 sensor before and after its installation on the pipe loop 174

6.3 Example torsional signal from the gPIMS® P1 sensor 178

6.4 Example torsional RC signal from the gPIMS® P1 sensor 178

6.5 Torsional RC signals from the gPIMS® P1 sensor 179

6.6 Torsional residual RC signals from the gPIMS® P1 sensor 179

6.7 Baseline torsional residual RC signals with and without baseline subtraction compensation 181

6.8 Details of the baseline torsional residual RC signals with and without baseline subtraction compensation 181

6.9 Section of torsional residual RC signals from the gPIMS® P1 sensor 182

6.10 Torsional residual RC signals with 0.25% cross-sectional area loss damage 188

6.11 Details of the torsional residual RC signals with 0.25% cross-sectional area loss damage . . . 188

6.12 GLR false-call probability with 0.25% cross-sectional area loss damage . . . 190

6.13 GLR damage echo amplitude with 0.25% cross-sectional area loss damage . . . 191

6.14 Torsional residual RC signals with 0.50% cross-sectional area loss damage . . . 193

6.15 Details of the torsional residual RC signals with 0.50% cross-sectional area loss damage . . . 193

6.16 GLR false-call probability with 0.50% cross-sectional area loss damage . . . 194

6.17 GLR damage echo amplitude with 0.50% cross-sectional area loss damage . . . 195

6.18 Torsional residual RC signals with 0.75% cross-sectional area loss damage ($\Delta T =$ 0°F (0°C)) . . . 198

6.19 Details of the torsional residual RC signals with 0.75% cross-sectional area loss damage ($\Delta T =$ 0°F (0°C)) . . . 198

6.20 Torsional residual RC signals with 0.75% cross-sectional area loss damage ($\Delta T =$ 10°F (5.56°C)) . . . 199

6.21 Details of the torsional residual RC signals with 0.75% cross-sectional area loss damage ($\Delta T =$ 10°F (5.56°C)) . . . 199

6.22 Torsional residual RC signals with 0.75% cross-sectional area loss damage ($\Delta T =$ 20°F (11.11°C)) . . . 200

6.23 Details of the torsional residual RC signals with 0.75% cross-sectional area loss damage ($\Delta T =$ 20°F (11.11°C)) . . . 200

6.24 Torsional residual RC signals with 0.75% cross-sectional area loss damage ($\Delta T =$ 30°F (16.67°C)) . . . 201

6.25 Details of the torsional residual RC signals with 0.75% cross-sectional area loss damage ($\Delta T =$ 30°F (16.67°C)) . . . 201

6.26 Torsional residual RC signals with 0.75% cross-sectional area loss damage ($\Delta T =$ 40°F (22.22°C)) . . . 202

6.27 Details of the torsional residual RC signals with 0.75% cross-sectional area loss damage ($\Delta T = 40$°F (22.22°C)) . . . 202

6.28 Torsional residual RC signals with 0.75% cross-sectional area loss damage ($\Delta T =$ 50°F (27.78°C)) . . . 203

6.29 Details of the torsional residual RC signals with 0.75% cross-sectional area loss damage ($\Delta T = 50$°F (27.78°C)) . . . 203

6.30 GLR false-call probability with 0.75% cross-sectional area loss damage ($\Delta T =$ 0°F (0°C)) . . . 208

6.31 GLR damage echo amplitude with 0.75% cross-sectional area loss damage ($\Delta T =$ 0°F (0°C)) . . . 209

6.32 GLR false-call probability with 0.75% cross-sectional area loss damage ($\Delta T =$ 10°F (5.56°C)) . . . 210

6.33 GLR damage echo amplitude with 0.75% cross-sectional area loss damage ($\Delta T =$ 10°F (5.56°C)) . . . 211

6.34 GLR false-call probability with 0.75% cross-sectional area loss damage ($\Delta T =$ 20°F (11.11°C)) . . . 212

6.35 GLR damage echo amplitude with 0.75% cross-sectional area loss damage ($\Delta T =$ 20°F (11.11°C)) . . . 213

6.36 GLR false-call probability with 0.75% cross-sectional area loss damage ($\Delta T =$ 30°F (16.67°C)) . . . 214

6.37 GLR damage echo amplitude with 0.75% cross-sectional area loss damage ($\Delta T =$ 30°F (16.67°C)) . . . 215

6.38 GLR false-call probability with 0.75% cross-sectional area loss damage ($\Delta T =$ 40°F (22.22°C)) . . . 216

6.39 GLR damage echo amplitude with 0.75% cross-sectional area loss damage ($\Delta T =$ 40°F (22.22°C)) . . . 217

6.40 GLR false-call probability with 0.75% cross-sectional area loss damage ($\Delta T =$ 50°F (27.78°C)) . . . 218

6.41 GLR damage echo amplitude with 0.75% cross-sectional area loss damage ($\Delta T =$ 50°F (27.78°C)) 219

Chapter 1

Introduction

BP is one of the world's leading international oil and gas companies, providing its customers with fuel for transportation, energy for heating and lighting, retail services and petrochemical products for everyday items. It is vertically integrated and is active in every area of the oil and gas industry, including exploration and production, refining, distribution and marketing, power generation, and energy trading. It also has interests in renewable energy sources such as biofuels and wind power.

Worldwide, BP operates many thousand kilometres of pipelines carrying valuable yet toxic and corrosive fluids. The structural integrity of these pipelines is of paramount importance, as any failure may result in environmental damage, economic losses and injuries to personnel. Furthermore, there is an ever stronger economic drive towards pipeline networks that are safer and more reliable while at the same time more productive and less costly. Novel Structural Health Monitoring (SHM) approaches that enable the use of condition-based maintenance are needed to achieve these seemingly contrasting targets.

1.1 Structural Health Monitoring

SHM consists in the implementation of a strategy to detect and diagnose damage [1, 2]. Damage is a change in the properties of a system, whether geometrical, physical or other, that adversely affects its current and future performance and safety. Conversely, defects or flaws are imperfections that all manufactured materials contain at micro-structural level. Therefore, a system will operate at its optimum even if its constituent materials contain defects, but its performance will deteriorate and it will become less safe to operate if it suffers damage [1, 2]. Although most engineering systems are damage tolerant and can withstand a certain amount of damage while maintaining a safe and satisfactory performance, it is of fundamental importance to detect, diagnose and monitor damage growth as early as possible to predict the remaining operational life of a system and to minimise the risk of unexpected failures, which in the case of petrochemical pipelines can have severe consequences and may result in environmental damage, economic losses and personnel injuries. The process of predicting the remaining operational life of a system given some assessment of its current structural health and some prediction of its anticipated future operational conditions is referred to as prognosis [1, 2].

Conventionally, the integrity of petrochemical pipelines is assessed periodically at regular intervals. For example, a pipeline is inspected at certain locations and with a certain frequency depending on various considerations, which are often formalised in a Risk-Based Inspection and Maintenance (RBIM) strategy [3] and which may include known or assumed structural integrity conditions, typical damage mode and growth rate, severity of consequences in case of failure, cost of inspection, personnel availability, as well as many others. This approach inherently limits the amount of information available about the structural health of a pipeline, as any damage which develops in unexpected circumstances or while the pipeline is not being inspected may remain undetected. Furthermore, any change in the petrochemical production process, perhaps following opportunity oil, as well as variabilities in the quality of the manufactured components and of the welding and assembly processes can increase the likelihood of unexpected damage occurrences. Such lack of information hinders the reliability of any prognosis and of RBIM strategies, increases the risk of unexpected critical damage development and pipeline failure, and forces the use of the costly time-based maintenance, which prescribes the partial or complete replacement of pipework at set points in time irrespective of their actual remaining operational life, following the safe-life design approach.

In contrast, if one were to have sufficient information about the structural health of a pipeline to produce a reliable prognosis, then one could in principle utilise the cost-efficient condition-based maintenance, which prescribes the partial or complete replacement of pipework only when it is about to suffer critical damage and has therefore reached the actual end of its operational life. Through early detection, diagnosis and monitoring of damage growth, SHM can lead to the formulation of reliable prognoses and to the reduction of the risk of unexpected failures, ultimately enabling the shift from the costly time-based maintenance to the more cost-efficient condition-based maintenance [1].

To detect, locate, diagnose and monitor damage SHM relies on a network of permanently installed sensors that monitor one or more damage-sensitive properties of a system over time without impairing system functionality. The principal advantages of SHM and condition-based maintenance from the petrochemical industry standpoint are:

- **Operational.** No components will be taken out of service unless absolutely necessary, and since it becomes very unlikely for critical damage to grow undetected the overall safety and reliability of the pipeline network is increased. Furthermore, reliable prognoses imply that maintenance interventions can be appropriately planned in advance and synchronised to minimise pipeline down-time.
- **Economic.** Minimised pipeline down-time boots production, revenue and profit. Furthermore, time-based integrity assessment and maintenance become superfluous, resulting in significant savings especially because it becomes no longer necessary to routinely service pipelines that may be buried, underwater, in deserts, or in other harsh environments, and that can prove extremely costly and problematic to access.

SHM and condition-based maintenance therefore promise to make pipeline networks safer and more reliable while at the same time more productive and less costly. Importantly though, the effective SHM of petrochemical pipelines requires the development of:

- **Sensor Systems.** SHM requires sensors that are reliable and predictable, sensitive enough to detect small changes in structural properties yet rugged enough to operate in harsh environments. Importantly, it is desirable to have sensor systems capable of monitoring the full volume of a pipeline.
- **Software.** SHM requires data analysis algorithms capable of discerning between harmless and harmful changes in structural properties, and of providing sufficient warning and information so that appropriate action can be taken well before failures occur.

1.2 Permanently Installed Guided Wave Sensors

Guided wave inspection is a pipeline Non-Destructive Evaluation (NDE) method routinely utilised in the petrochemical sector worldwide [4–19]. Conventional NDE methods such as Ultrasonic Testing (UT) and Eddy Currents (EC) perform localised measurements of pipe wall thickness, thereby requiring a large number of sensors to monitor even short lengths of pipeline. By contrast, guided wave inspection enables the fully-volumetric inspection of several metres of pipe from a single sensor location, and consequently represents a very advantageous option for SHM applications since the entire volume of a pipeline can be monitored with a practical quantity of sensors.

Permanently installed guided wave sensors, such as the Guided Wave Permanently-Installed Monitoring System (gPIMS®) sensors produced and commercialised by Guided Ultrasonics Ltd. [20], are guided wave sensors specifically designed for SHM applications. Contrary to standard guided wave sensors, permanently installed guided wave sensors are remotely operated, and once installed are typically left in place for the whole of the operating life of the pipeline. Consequently, access to the pipeline that needs to be inspected is required only once at installation, and the cost of routine guided wave inspection is dramatically reduced. Moreover, because the inspections performed with permanently installed sensors are highly repeatable, the damage sensitivity compared to standard guided wave sensors can be enhanced through baseline subtraction.

Permanently installed guided wave sensors transmit guided wave packets along a pipe and listen for echoes. Echoes originate from pipe features, such as welds and supports, as well as from damage. Because echoes from pipe features should remain constant between repeat inspections, by detecting and monitoring changes over time in the recorded echo sequence from permanently installed guided wave sensors it should in principle become possible to detect and monitor damage growth in pipelines.

1.3 Thesis Aim & Outline

The aim of this thesis is to introduce a practical automated pipeline damage detection procedure that utilises data gathered from permanently installed guided wave sensors over time to detect and monitor damage growth in pipelines. The framework provides the software complement to permanently installed guided wave sensors, thereby providing the petrochemical industry with a complete pipeline SHM solution.

This thesis can be conceptually divided in two major parts.

In the first part of this thesis a lot of emphasis is put on the study of the fundamental mechanics of guided wave propagation.

Firstly, **chapter 2** introduces the principles of guided wave propagation in free pipes, discussed how these principles can be utilised to inspect pipelines, and reviews the state-of-the-art of guided wave pipeline inspection.

Successively, **chapter 3** thoroughly investigates how guided waves propagating along a free pipe interact with simple pipe supports, a subject of particular relevance to petrochemical pipeline SHM since effective detection and characterisation of damage at pipe support locations relies on the ability to distinguish between the echoes produced by the simple supports on which an undamaged pipe is lying and the echoes produced by damage. Very little work has previously been reported on this subject.

The second part of this thesis focuses entirely on the practical challenges of implementing an effective pipeline SHM solution based on permanently installed guided wave sensors.

Chapter 4 at first introduces the concept of SHM, and then thoroughly reviews its advantages, challenges and recent advances particularly in light of its utilisation for petrochemical pipelines. Successively, it introduces permanently installed guided wave sensors, highlighting the differences and advantages compared to deployable guided wave sensors, and presents the concept of baseline subtraction, through which the sensitivity to damage growth of permanently installed guided wave sensors can be greatly enhanced. Then, it discusses the fundamental problem of damage detection, showing how it is effectively a problem of change detection. In particular, it explains the challenge that variations in the Environmental and Operational Conditions (EOC) of a pipeline represent to effective baseline subtraction, to effective damage detection, and ultimately to effective SHM, thereby motivating the need to utilise advanced techniques to synthetically compensate for EOC variations. Importantly, in this chapter the formal mathematical foundations for the analysis of the effects that pipeline operating temperature variations have on the signals recorded by permanently installed guided wave sensors are laid and successively utilised firstly to introduce two techniques to synthetically compensate for EOC variations in baseline subtraction, namely the Baseline Signal Stretch (BSS) technique and the novel Localised Baseline Signal Stretch (LBSS) technique, and secondly to thoroughly analyse the side-effects that baseline subtraction compensation techniques, and in particular BSS and LBSS, might have in practical situations. Finally, this chapter illustrates the challenge of dealing with the remaining uncompensated EOC effects that will invariably feature in the measurements from any SHM sensor, hence motivating the need for advanced damage detection, and consequently change detection, strategies.

Chapter 5 thoroughly discusses the general change detection problem, introduces the concept of sequential analysis, and presents the mathematical principles behind the Cumulative

Sum (CUSUM) algorithm for the solution of simple change detection problems and the Generalised Likelihood Ratio (GLR) algorithm for the solution of composite change detection problems. It also discusses how the CUSUM and GLR algorithms have been mathematically proven to be capable of optimally solving change detection problems so that the probability of detecting a change is maximised, the probability of false-calling a change is minimised, and the required number of samples, and therefore the delay between change time and detection time, is minimised. Finally, it exemplifies step change detection and gradual change detection in the case of a normally distributed random variable utilising the GLR algorithm.

Finally, **chapter 6** discusses and demonstrates how the concepts of baseline subtraction and baseline subtraction compensation can be combined together with the GLR change detection algorithm to introduce a practical automated pipeline damage detection procedure. Specifically, utilising experimental data from a gPIMS® sensor, which is a permanently installed guided wave sensor produced and commercialised by Guided Ultrasonics Ltd. [20], installed on a purpose-built NPS 8 Schedule 40 pipe loop facility at BP's Naperville Campus, it illustrates how the procedure is able to consistently ignore uncompensated EOC effects which will invariably feature in the measurement from any permanently installed guided wave sensors, while being very effective at detecting and quantifying actual damage growth, thereby achieving the intended aim of this thesis.

For convenience, table A.1 in appendix A presents a summary of common Nominal Pipe Size (NPS) dimensions utilised throughout this thesis.

Chapter 2

Guided Wave Pipeline Inspection

The use of guided waves to detect and locate damage in pipelines is a topic that has received considerable interest [4–19]. The potential of this method, proven and documented as early as the Seventies [16, 21, 22], remained unfulfilled until the Nineties, when most of the practical problems hindering its successful development and application were addressed. These problems were caused primarily by poorly controlled transduction, resulting in the uncontrolled excitation and reception of multiple dispersive guided wave modes propagating in both directions along a pipe, and consequently in very high levels of coherent noise that could not be removed by averaging [23]. The development of improved transduction methods [24] and effective dispersion compensation techniques [25] enabled guided waves to become a prominent Non-Destructive Evaluation (NDE) method that can inspect the full volume of several metres of pipeline from a single sensor location.

In this chapter the physics of guided wave propagation along pipes are introduced in section 2.1, while the use of guided waves for the detection of damage in pipelines is described and reviewed in section 2.2.

2.1 Guided Wave Propagation

For an elastic and isotropic solid with density ρ and Lamé's constants λ and μ the equations of motion can be derived directly from Newton's second law and from Hooke's law, and can be shown [26] to be given by

$$\mu\nabla^2\mathbf{u}+(\lambda+\mu)\nabla\nabla\cdot\mathbf{u}=\rho\left(\partial^2\mathbf{u}/\partial t^2\right) \tag{2.1}$$

where **u** is the displacement vector and t is the time. By the Helmoltz decomposition **u** can be expressed as a sum of irrotational and rotational components $\nabla\phi$ and $\nabla\times\mathbf{H}$ so that

$$\mathbf{u}=\nabla\phi+\nabla\times\mathbf{H},\quad \nabla\cdot\mathbf{H}=f(\mathbf{r},t) \tag{2.2}$$

where ϕ is a compressional scalar potential, **H** is a equivoluminal vector potential, and **r** is the coordinate vector. The function f can be chosen arbitrarily because of the gauge invariance of the Helmoltz decomposition [27, 28]. Since by definition

$$\begin{aligned}&\nabla\cdot\nabla\phi=\nabla^2\phi\\&\nabla^2\left(\nabla\phi\right)=\nabla\left(\nabla^2\phi\right)\\&\nabla\cdot\nabla\times\mathbf{H}=0\end{aligned}$$

substituting equation 2.2 into 2.1 yields

$$\nabla\left(\left(\lambda+2\mu\right)\nabla^2\phi-\rho\left(\partial^2\phi/\partial t^2\right)\right)=\nabla\times\left(\rho\left(\partial^2\mathbf{H}/\partial t^2\right)-\mu\nabla^2\mathbf{H}\right) \tag{2.3}$$

The left and right sides of equation 2.3 govern respectively irrotational (compressional) and rotational (shear) displacement. Because irrotational and rotational displacement are normal to each other, equation 2.3 is satisfied if and only if both sides vanish. Therefore, equation 2.1 can be decomposed in two simplified wave equations

$$v_c^2\nabla^2\phi=\partial^2\phi/\partial t^2,\quad v_c^2=\left(\lambda+2\mu\right)/\rho \tag{2.4}$$

$$v_s^2\nabla^2\mathbf{H}=\partial^2\mathbf{H}/\partial t^2,\quad v_s^2=\mu/\rho \tag{2.5}$$

Equations 2.4 and 2.5 govern respectively irrotational and rotational displacement. The terms v_c and v_s are respectively the compressional and shear bulk wave velocity.

If no boundary conditions are specified, and thus it is assumed that wave propagation occurs in the bulk of an unbounded medium, then equations 2.4 and 2.5 are independent, and their only possible solutions are straightforward to find and are given by

$$\phi=a_c e^{i(\mathbf{N}_c k_c\cdot\mathbf{r}-\omega t)},\quad k_c=\omega/v_c \tag{2.6}$$

$$\mathbf{H}=\mathbf{a}_s e^{i(\mathbf{N}_s k_s\cdot\mathbf{r}-\omega t)},\quad k_s=\omega/v_s \tag{2.7}$$

Equations 2.6 and 2.7 describe respectively compressional and shear bulk waves of amplitudes a_c and $\mathbf{a}_s$ and wavenumbers k_c and k_s propagating along the direction of the unit vectors $\mathbf{N}_c$ and $\mathbf{N}_s$.

Conversely, if a set of boundary conditions representing a structure's geometry are specified, and thus it is assumed that wave propagation occurs along that structure's boundaries, then equations 2.4 and 2.5 may or may not be independent and solutions can be difficult to find. The analytical foundation for the study of solutions when boundary conditions represent an infinitely long hollow cylinder, *i.e.* a pipe, is largely due to Gazis [27], whose analytical predictions were later confirmed by Fitch [29] who carried out experiments utilising both axisymmetric and non-axisymmetric guided wave modes. Specifically, because the Helmoltz decomposition of equation 2.2 is separable, any solution to both equations 2.4 and 2.5 can be expressed as a product of functions of each of the spatial dimensions [28], and a general harmonic solution will therefore be of the form

$$\phi, \mathbf{H} = \Xi_1(r)\Xi_2(\theta)\Xi_3(z)\, e^{i(\mathbf{k}\cdot\mathbf{r}-\omega t)} \tag{2.8}$$

where $\mathbf{r} = (r, \theta, z)$ is the cylindrical coordinate vector, $\mathbf{k} = (k_r, k_\theta, k_z)$ is the wavenumber vector, and $\Xi_1(r)$, $\Xi_2(\theta)$ and $\Xi_3(z)$ describe field variation in each of the spatial dimensions. Assuming that the wave does not propagate along the radial direction r, and that the displacement field varies harmonically in the circumferential and axial directions θ and z, then equation 2.8 reduces to

$$\phi, \mathbf{H} = \Xi_1(r)\, e^{i(k_\theta \theta + k_z z - \omega t)} \tag{2.9}$$

where the wavenumber k_θ along the circumferential dimension, known as the circumferential order, can only take integer values n as otherwise the solution would be different at θ and at $\theta + 2\pi$ and would not be unique. Gazis proposed that the compressional scalar potential ϕ and the equivoluminal vector potential $\mathbf{H}$ should take the form

$$\phi = f(\mathbf{r})\, e^{i(n\theta + k_z z - \omega t)} = f(\mathbf{r})\cos(n\theta)\, e^{i(k_z z - \omega t)} \tag{2.10}$$

and

$$\begin{aligned} H_r &= -g_r(\mathbf{r})\, e^{i(n\theta + k_z z - \omega t)} = -i g_r(\mathbf{r})\sin(n\theta)\, e^{i(k_z z - \omega t)} \\ H_\theta &= -i g_\theta(\mathbf{r})\, e^{i(n\theta + k_z z - \omega t)} = -i g_\theta(\mathbf{r})\cos(n\theta)\, e^{i(k_z z - \omega t)} \\ H_z &= -i g_z(\mathbf{r})\, e^{i(n\theta + k_z z - \omega t)} = g_z(\mathbf{r})\sin(n\theta)\, e^{i(k_z z - \omega t)} \end{aligned} \tag{2.11}$$

Substituting equations 2.10 and 2.11 into respectively equations 2.4 and 2.5 yields a set of Bessel's differential equations

$$\mathscr{B}_{n,\alpha\mathbf{r}}(f) = 0 \tag{2.12}$$

with $\alpha^2 = \omega^2/v_l^2 - k_z^2$, and

$$\begin{aligned} &\mathscr{B}_{n,\beta\mathbf{r}}(g_z) = 0 \\ &\mathscr{B}_{n+1,\beta\mathbf{r}}(g_r - g_\theta) = 0 \\ &\mathscr{B}_{n+1,\beta\mathbf{r}}(g_r + g_\theta) = 0 \end{aligned} \tag{2.13}$$

with $\beta^2 = \omega^2/v_s^2 - k_z^2$, where $\mathscr{B}_{n,x}$ is the differential operator defined as

$$\mathscr{B}_{n,x} = \frac{\partial^2}{\partial x^2} + \frac{1}{x}\frac{\partial}{\partial x} - \left(\frac{n^2}{x^2} - 1\right) \tag{2.14}$$

with x equal to either $\alpha\mathbf{r}$ or $\beta\mathbf{r}$. The functions f, g_r, g_θ and g_z that describe compressional and equivoluminal field variation in each of the spatial coordinates must therefore be the linear combination of either a pair of Bessel functions $J_n(x)$ and $Y_n(x)$, or of a pair of modified Bessel functions $I_n(x)$ and $K_n(x)$, or of a pair of Hankel functions $H_n^{(1)}(x)$ and $H_n^{(2)}(x)$. The choice of which combination of functions to utilise depends on whether the modelled system is attenuative, leaky, neither, or both, and is discussed extensively by Pavlakovic [30]. Once an appropriate choice is made and the functions f, g_r, g_θ and g_z are obtained, the displacement field $\mathbf{u} = (u_r, u_\theta, u_z)$ can be calculated and consequently so can the strain and stress fields $\boldsymbol{\eta}$ and $\boldsymbol{\sigma}$. Imposing the boundary conditions

$$\sigma_{rr} = \sigma_{rz} = \sigma_{r\theta} = 0 \tag{2.15}$$

for free motion at the inner and outer radii of an infinitely long hollow cylinder yields a characteristic frequency equation whose solutions describe all propagating and non-propagating guided waves [27, 31]. For any given pipe, *i.e.* for given values of the inner and outer radii, there exists an infinite number of modes of guided wave propagation, each corresponding to a solution of the characteristic frequency equation. The modes can be subdivided into:

- **Longitudinal.** Longitudinal $\mathrm{L}(0,m)$ modes are axisymmetric with a displacement field $u_r \neq 0$, $u_\theta = 0$ and $u_z \neq 0$. They are similar to the Lamb modes in plates.
- **Torsional.** Torsional $\mathrm{T}(0,m)$ modes are axisymmetric with a displacement field $u_r = 0$, $u_\theta \neq 0$ and $u_z = 0$. They are similar to the SH modes in plates.
- **Flexural.** Flexural $\mathrm{F}(n,m)$ modes are non-axisymmetric with a displacement field $u_r \neq 0$, $u_\theta \neq 0$ and $u_z \neq 0$.

The dual index (n,m) labelling system reflects the one first created by Silk & Bainton [16]. The circumferential order n is the wavenumber k_θ along the circumferential dimension and represents the number of harmonic variations of the mode along the circumference of the hollow cylinder. The counter variable m reflects the type of the harmonic motion through the cylinder wall. Modes that can propagate at zero frequency, known as the fundamental modes, are given $m = 1$ and further modes are numbered consecutively. For example, all $\mathrm{F}(n,2)$ modes will display a similar harmonic motion through the cylinder wall but will have different circumferential orders n.

Figures 2.1 and 2.2 present respectively the phase velocity v_{ph} and group velocity v_{gr} dispersion curves for the modes that can propagate along a NPS 3 Schedule 40 steel pipe in the range $0-100$kHz. The phase velocity

$$v_{ph} = \omega / \Re(k_z) \tag{2.16}$$

describes the velocity at which individual wave crests move, while the group velocity

$$v_{gr} = \partial\omega / \partial\Re(k_z) \tag{2.17}$$

describes the velocity at which wave packets propagate. The dispersion curves in figures 2.1 and 2.2 were generated utilising the Semi-Analytical Finite Element (SAFE) method [32–47] implemented through COMSOL® Multiphysics® [48] and MATLAB® [49]. The SAFE method will be discussed in detail in chapter 3, and in particular in section 3.2.

2.2 Guided Wave Inspection

The capability of detecting, locating and potentially sizing damage in pipelines utilising guided waves has been demonstrated by several authors [4–19]. Over the past two decades guided waves have seen an increasingly successful commercial exploitation, and are now a pipeline NDE method routinely utilised in the petrochemical industry worldwide.

Conventional petrochemical pipeline NDE practices involve the measurement of pipe wall thickness at a number of locations utilising methods such as Ultrasonic Testing (UT) and Eddy Currents (EC). These methods require direct access to the area to be inspected and only test the region of pipeline directly below the probe. Consequently, the inspection of long lengths of pipeline tends to be very time-consuming, particularly if coverage of the entire volume of a section of pipeline is required. Furthermore, because petrochemical pipelines are often thermally insulated or situated in hazardous and problematic locations, it may prove difficult, costly, or even impossible to obtain the necessary direct access.

Guided wave inspection represent a very advantageous option as it enables the inspection of the entire volume of a length of pipeline from a single axial location, thereby mitigating accessibility issues and avoiding the time-consuming scanning required by conventional NDE methods. Guided wave inspection relies on the principle that any pipeline discontinuity, from features such as welds and supports to damage such as cracks and corrosion, will reflect part of an incident guided wave packet propagating along the pipeline. Echoes can be detected and utilised to locate and characterise the discontinuities.

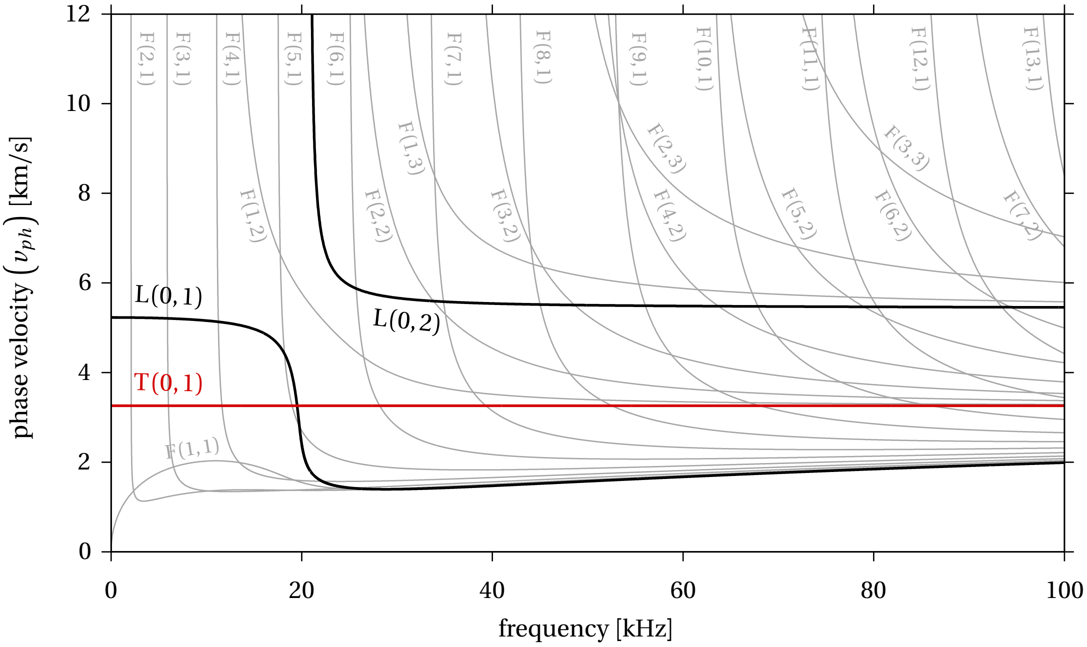

Figure 2.1: Phase velocity dispersion curves for a NPS 3 Schedule 40 carbon steel pipe; the fundamental torsional mode T(0, 1) is shown in red; the dispersion curves were generated utilising the SAFE method [32–47] implemented through COMSOL® Multiphysics® [48] and MATLAB® [49].

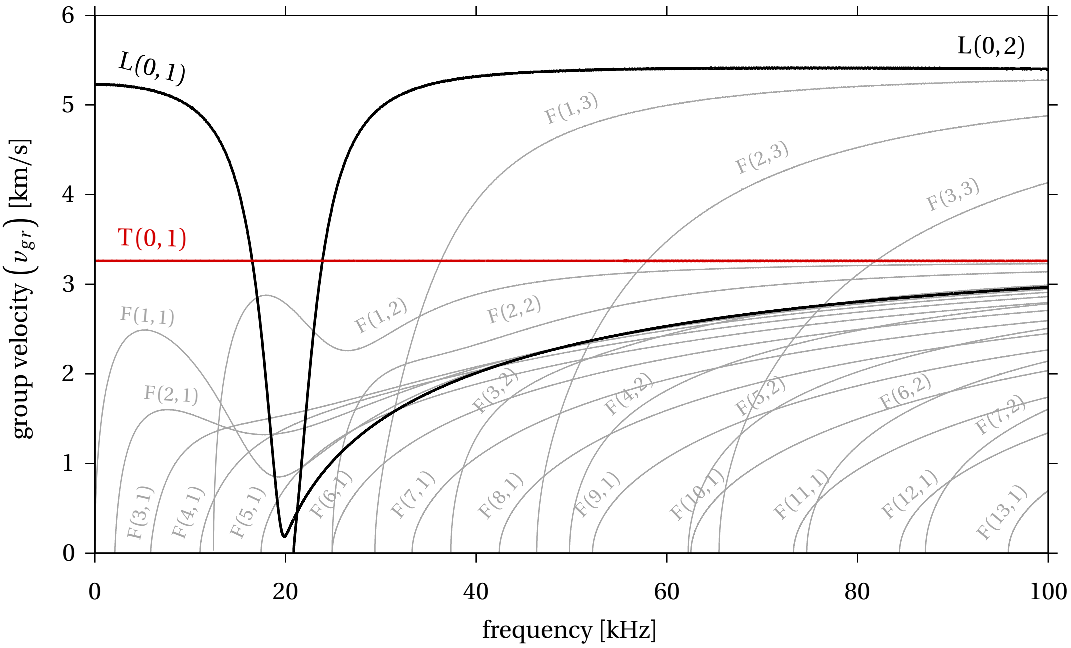

Figure 2.2: Group velocity dispersion curves for a NPS 3 Schedule 40 carbon steel pipe; the fundamental torsional mode T(0, 1) is shown in red; the dispersion curves were generated utilising the SAFE method [32–47] implemented through COMSOL® Multiphysics® [48] and MATLAB® [49].

2.2.1 Mode Choice

The choice of which guided wave mode to excite in a pipe can *a priori* determine the effectiveness of guided wave inspection [50]. The ideal incident mode is one that is:

- **Easy to selectively excite.** Guided wave transduction is complex. Because many modes with similar displacement fields can propagate along the same pipe at similar velocities and frequencies, *e.g.* the $\mathrm{T}(0,1)$ and $\mathrm{F}(n,2)$ modes shown in figures 2.1 and 2.2, it is difficult to excite exclusively one mode in one direction and therefore limit coherent noise [23]. By choosing a mode whose displacement field is easy to replicate and has the least commonality with other modes it becomes inherently possible to design simpler and more reliable transduction systems and limit coherent noise.
- **Non-dispersive.** Figures 2.1 and 2.2 indicate that, with the exception of $\mathrm{T}(0,1)$, all modes are dispersive, *i.e.* their phase and group velocities are functions of frequency. Dispersion causes an excited guided wave packet to stretch as it propagates since its different frequency components have different velocities. Consequently, its peak amplitude will quickly dip below noise, limiting the practical propagation range. Although to an extent it is possible to compensate for dispersion [25], by choosing a mode that is entirely non-dispersive, or a dispersive mode but within a frequency range over which it is virtually non-dispersive, propagation ranges are maximised and the length of the wave packets in the recorded signal is minimised, making it easier to distinguish closely spaced features and damage.
- **Axisymmetric.** Even though either axisymmetric or non-axisymmetric modes could be utilised for guided wave inspection, axisymmetric modes are the preferred option because they are easier to excite and have a simpler acoustic field [9].

The choice of which incident mode to utilise also depends substantially on the type of damage one intends to detect. When no prior knowledge exists about the damage type, or when a variety of damage types are to be detected, one should utilise a general purpose mode that has the most uniform displacement field throughout the pipe wall thickness and that is therefore equally sensitive to damage irrespectively of where it is located.

Furthermore, the type of damage one seeks to detect determines the choice of which frequencies to utilise. Ideally, to maximise the propagation range one would choose a frequency range over which the incident mode suffers from the least attenuation. Long-range propagation in the order of dozens of metres can be achieved by utilising low frequencies at which guided waves typically suffer from limited attenuation. However, by utilising too low a frequency sharp damage could be missed, and conversely shallow damage could be missed by utilising too high a frequency [9, 51–53].

In summary, to ensure the detection of multiple damage types it is desirable to excite a general purpose axisymmetric guided wave mode that can propagate over a wide range of frequencies and that remains easy to excite and non-dispersive over the entire frequency range.

2.2.2 Early Development

Early development efforts sought to utilise $\mathrm{L}(0,2)$ as the incident mode to detect damage with small axial extent, such as cracks and notches [4, 13, 19]. $\mathrm{L}(0,2)$ offers the advantage of being virtually non-dispersive in the frequency range utilised at the time for guided wave inspection, of suffering from very limited attenuation, and, importantly, of being substantially faster than any other mode, thereby rendering echo separation by time-domain gating straightforward. Furthermore, its displacement field consists almost exclusively of axial motion and is virtually uniform throughout the pipe wall, thus implying that $\mathrm{L}(0,2)$ is equally sensitive to internal and external damage. However, $\mathrm{L}(0,2)$ suffers from the disadvantage of requiring a rather complex transduction system that must be carefully designed to suppress the fundamental longitudinal mode $\mathrm{L}(0,1)$, which also exists in the same frequency range, has a displacement field that also consists of radial and axial components, and whose accidental excitation would increase coherent noise.

Studies have shown that the amplitude of the $\mathrm{L}(0,2)$ echo from notches in pipes is correlated to their circumferential and axial extent [4], and that it is possible to distinguish between echoes from axisymmetric and from non-axisymmetric discontinuities [13], such as between welds and corrosion, because non-axisymmetric discontinuities mode-convert part of the incident axisymmetric mode into non-axisymmetric mode echoes as a function of their circumferential extent. In particular, it has been shown that non-axisymmetric discontinuities mode-convert part of the incident $\mathrm{L}(0,2)$ mode into $\mathrm{F}(n,3)$ mode echoes.

2.2.3 Modern Commercial Implementation

Modern commercial implementations of guided wave inspection utilise the fundamental torsional mode $\mathrm{T}(0,1)$ as the incident mode. $\mathrm{T}(0,1)$ has many advantages over $\mathrm{L}(0,2)$. Firstly, because it consists of a superposition of shear bulk waves, it exists at all frequencies and is non-dispersive. Secondly, because fluids do not support rotational displacement, its propagation is not influenced by the presence of low-viscosity fluids on either side of the pipe wall and energy leakage into high-viscosity fluids carried by or surrounding the pipe remains limited, ultimately resulting in extended propagation ranges especially in under-water inspection scenarios. Thirdly, no other torsional mode can exist in standard industrial pipes in the frequency range typically utilised for guided wave inspection, and as a result a perfectly axisymmetric torsional transduction will excite just $\mathrm{T}(0,1)$, thereby inherently reducing coherent noise and simplifying transduction system design. Finally, because the amplitude of its displacement field varies linearly with radial position, it follows that $\mathrm{T}(0,1)$ is in practice equally sensitive to damage located on the inside or on the outside of a pipe since in standard industrial pipes its displacement field remains virtually uniform throughout the pipe wall.

Modern commercial implementations typically utilise either deployable ring sensors, such as the ones shown in figures 2.3 and 2.4 produced and commercialised by Guided Ultrasonics Ltd. [54], or permanently installed ring sensors, such as the Guided Wave Permanently-Installed Monitoring System (gPIMS®) sensor shown in figure 2.5 also produced and commercialised by Guided Ultrasonics Ltd. [20], to excite incident $\mathrm{T}(0,1)$ guided wave packets in both directions along a pipe and to detect and record the echoes from pipe discontinuities. Deployable sensors are clamped on the pipe prior to the inspection, as shown in figure 2.4, and removed once the inspection is complete. Conversely, permanently installed sensors are clamped and adhesively bonded to the pipe, as shown in figure 2.5, and can be left in place and re-utilised to inspect the pipe indefinitely. A permanently installed sensor is operated through a convenient umbilical cable, and after it has been installed the pipe can be buried or thermally insulated without compromising the performance of the sensor. Permanently installed sensors can further mitigate accessibility issues for pipes that are thermally insulated or situated in hazardous and problematic locations, such as at height or underground, and that may prove complex and costly to routinely access even at a single axial location. Moreover, permanently installed sensors can perform highly accurate repeat inspections and therefore offer enhanced damage sensitivity through baseline subtraction, as will be discussed in chapters 4 and 6.

Both deployable and permanently installed sensors are composed of two circular rows of shear piezoelectric transducers that contact the outside of the pipe wall. The transducers are circumferentially oriented and usually dry-coupled, since the low frequencies of operation imply no significant loss of transduction performance is incurred [24]. To enable direction control, the two rows are separated along the axial dimension by a distance roughly equivalent to a quarter of the wavelength of the central frequency of the excited wave packet. The introduction of a phase delay in transmission and reception between the two rows results in constructive interference in one axial direction and destructive interference in the other, thereby transmitting and receiving $\mathrm{T}(0,1)$ in only one axial direction. It is also possible to transmit and receive from each single transducer separately and synthetically combine the recorded signals to achieve directionally controlled $\mathrm{T}(0,1)$ transduction as well as $\mathrm{F}(n,2)$ reception. Finally, an upper bound to the spacing between the transducers along the circumferential dimension is imposed by the Nyquist-Shannon sampling theorem, whose implications dictate that to excite a pure axisymmetric mode of wavelength λ the circumferential transducer spacing Δ must be smaller than $\lambda/2$, or, equivalently, that the number of transducers in each row must be greater than n, where $\mathrm{F}(n,m)$ is the highest circumferential order flexural mode that can propagate along the pipe under consideration within the frequency bandwidth of the excited guided wave packet.

Deployable sensors consist essentially of a rigid or a flexible collar that can be clamped on a pipe. The collar holds the two circular rows of shear piezoelectric transducers in place, and is designed to push each transducer against the pipe wall with even force to enable a quasi-uniform transduction along the pipe circumference. To push the transducers, rigid collars typically utilise springs, while flexible collars, such as the ones shown in figures 2.3 and 2.4, are typically pneumatically inflated.

Permanently installed sensors, such as the gPIMS® sensor shown in figure 2.5, utilise a slightly different packaging solution that consists in essence of a spring-tensioned flexible metal collar to which the two circular rows of shear piezoelectric transducers are directly bonded. Prior to installation the collar is encapsulated in a synthetic rubber, such as the green polyurethane rubber that can be observed in figure 2.5, which provides environmental protection. Before the sensor is finally clamped on a pipe, a further layer of polymer adhesive is laid on its inside surface to seal the area between the sensor and the pipe and to fix the position of the transducers on the outside of the pipe wall.

Note that different collar sizes are utilised for different sizes of pipes.

Both deployable and permanently installed sensors are usually driven by an integrated signal generator and receiver, such as the Guided Ultrasonics Ltd. Wavemaker® G4 [54] shown in figure 2.3. A laptop computer connected to the integrated signal generator and receiver is generally utilised to set the inspection parameters, such as the inspection frequency, and to visualise and analyse the inspection results.

Figure 2.3: Example of commercial guided wave inspection equipment, consisting of a Guided Ultrasonics Ltd. flexible deployable ring sensor [54] (left), a Guided Ultrasonics Ltd. Wavemaker® G4 [54] integrated signal generator and receiver (right), and a laptop computer (centre) to set the inspection parameters and to visualise and analyse the inspection results.

Figure 2.4: Typical example of a Guided Ultrasonics Ltd. flexible deployable ring sensor [54] installed on a pipeline and inflated during a guided wave inspection.

Figure 2.5: Guided Ultrasonics Ltd. gPIMS® sensor [20] before and after its installation on a pipe; note the green polyurethane rubber encapsulant and the spring-loaded closure mechanism.

The first thorough study documenting the damage detection capabilities of $\mathrm{T}(0,1)$ was completed by Demma [9]. In particular, it was proposed and partially demonstrated that the ratios of the amplitudes of the mode converted $\mathrm{F}(n,2)$ echoes to the amplitude of the $\mathrm{T}(0,1)$ echo could be utilised to estimate the circumferential extent of damage. However, such ratios are not very sensitive to differences in circumferential extent when the circumferential extent of the damage is already small, making it difficult to size damage extending over less than a tenth of the pipe circumference.

During an inspection, sensors are utilised to transmit incident $\mathrm{T}(0,1)$ guided wave packets in both directions along a pipe and to listen for echoes. Echoes originate from features, such as welds and supports, as well as from damage, and are utilised to locate and potentially characterise both features and damage. Figure 2.6 presents example torsional $\mathrm{T}(0,1)$ and mode converted flexural $\mathrm{F}(1,2)$ signals recorded by a gPIMS® sensor, while figure 2.7 presents the envelope of the torsional $\mathrm{T}(0,1)$ signal. The sensor lies at the origin, and each peak corresponds to an echo of the transmitted guided wave packet. Because the velocities of propagation of the $\mathrm{T}(0,1)$ and $\mathrm{F}(1,2)$ modes are known, and because $\mathrm{F}(1,2)$ dispersion is low over the typical inspection frequency ranges and can be compensated for [25], the time of arrival of each echo can be correlated to the position along the pipe from where it originates and thus to the pipe feature that produced it. For example, the echo at 11m originates from the weld at the beginning of a bend. Note the false echo at 1m, a mirror artefact of the weld echo at -1m caused by inaccuracies in direction control.

For a given amplitude of the incident $\mathrm{T}(0,1)$ guided wave packet, the typical amplitude of the $\mathrm{T}(0,1)$ echo from features such as welds or flanges is known. Therefore, from the amplitude of the recorded $\mathrm{T}(0,1)$ echoes it is possible to infer the amplitude of the incident

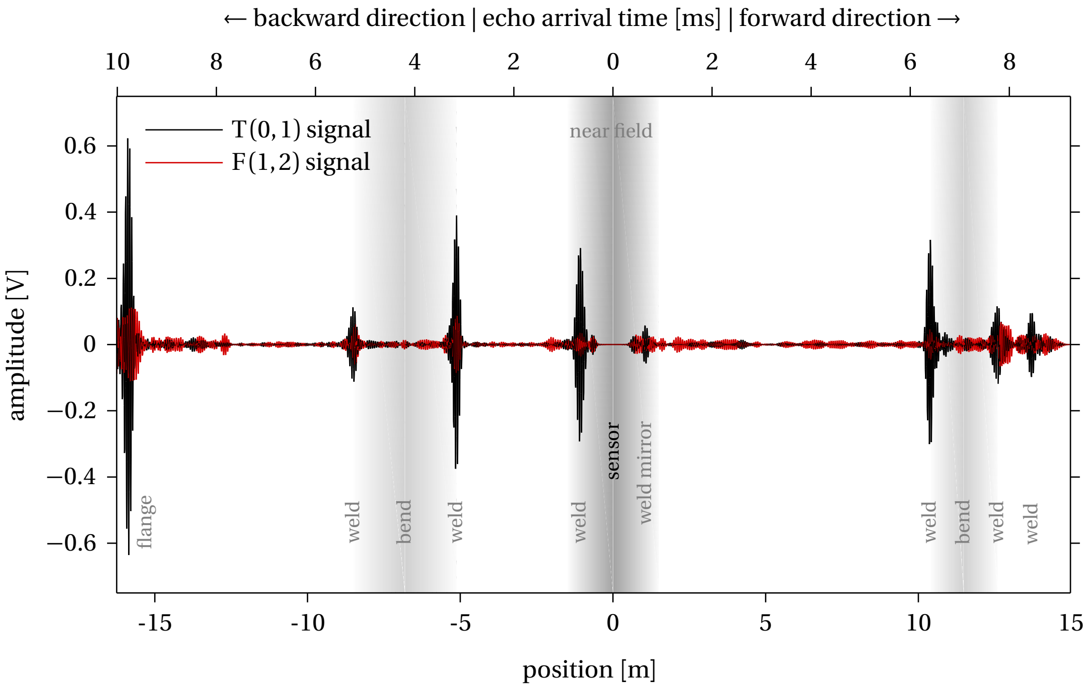

Figure 2.6: Torsional T(0,1) and flexural F(1,2) signals recorded by a Guided Ultrasonics Ltd. gPIMS® sensor [20].

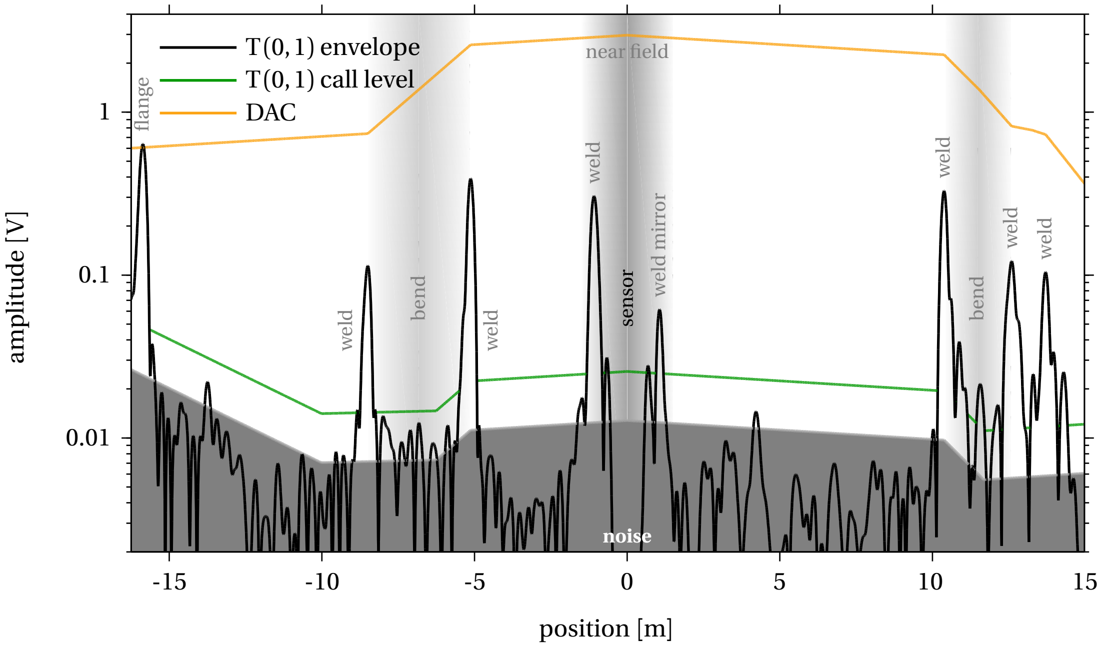

Figure 2.7: Envelope of the torsional T(0,1) signal recorded by a Guided Ultrasonics Ltd. gPIMS® sensor [20] on a logarithmic scale, together with noise and the damage call level.

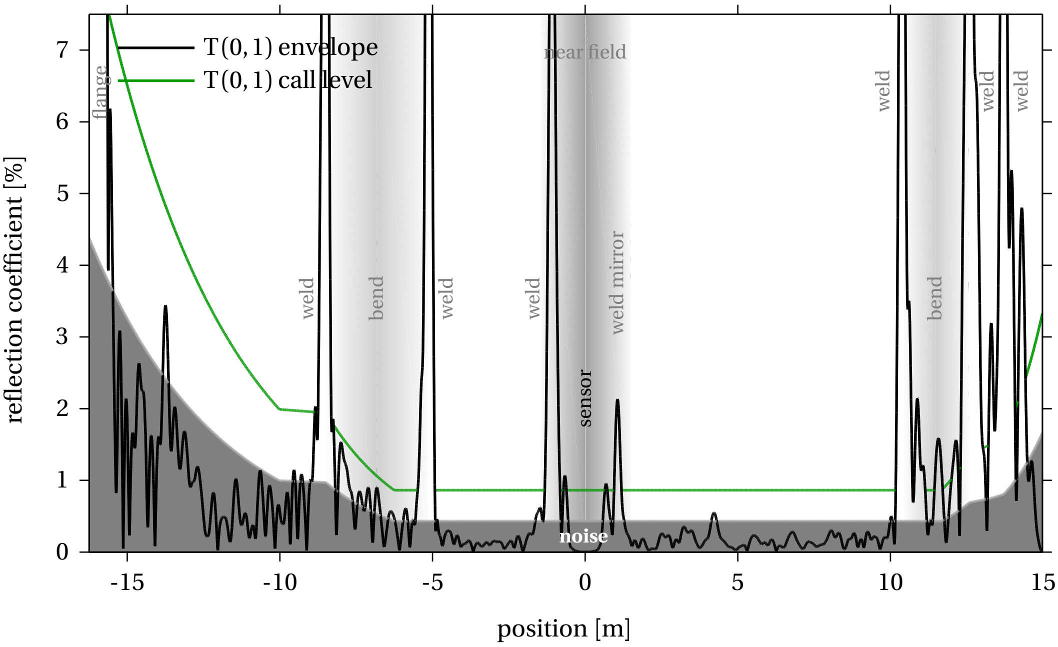

Figure 2.8: Reflection Coefficient (RC) envelope of the torsional T(0,1) signal recorded by a Guided Ultrasonics Ltd. gPIMS® sensor [20], together with noise and the damage call level

T(0,1) guided wave packet at those features. Furthermore, the typical T(0,1) Transmission Coefficient (TC) and attenuation for features such as welds and bends is also known. Consequently, assuming that the attenuation due to material damping and contents viscosity remains constant along the pipe or is known *a priori*, it follows that a Distance Amplitude Correction (DAC) curve representing the amplitude of the incident T(0,1) guided wave packet can be reconstructed at all positions along the pipe, as shown in figure 2.7. Dividing the envelope of the torsional T(0,1) signal by the DAC curve results in a Reflection Coefficient (RC) envelope, shown in figure 2.8, that expresses the amplitude of each observed T(0,1) echo as a percentage of the amplitude of the incident T(0,1) guided wave packet at that position.

Damage detection in guided wave inspection consists primarily in detecting echoes in the recorded T(0,1) signal that do not originate from known features and that rise significantly above noise. Similarly to conventional ultrasonic NDE methods, any echo that does not originate from a known feature and whose peak amplitude is 6dB above noise is regarded as a reliable indication of damage. Therefore a damage call level can be defined as the curve that lies 6dB above noise, as shown in figures 2.7 and 2.8. Importantly, virtually all noise in recorded guided wave signals is coherent [23]. Because coherent noise amplitude is not constant along a pipe and typically increases past bends, it follows that the damage call level is also not constant along a pipe. For example, figure 2.8 shows that the minimum damage that could be called at 5m is one that would produce an echo with an amplitude of roughly 1% of the transmitted wave packet, while the minimum damage that could be called at 10m is one that would produce an echo with an amplitude of roughly 2% of the transmitted wave packet. Once a reliable damage indication has been found, the amplitudes of the $T(0,1)$ and $F(1,2)$ echoes at the damage position can be utilised to roughly size and characterise the damage [9], although this approach has limitations and therefore should not be relied upon if precise damage information is required. Note that for an incident $T(0,1)$ guided wave packet the $F(1,2)$ echo from a feature or damage must have a lower amplitude than the $T(0,1)$ echo from the same feature or damage [9]. Therefore, the $F(1,2)$ signal can have a higher amplitude than the $T(0,1)$ signal at a given position along a pipe only as a result of coherent noise. Finally, the damage call level cannot be defined at features because their large $T(0,1)$ echoes can mask both $T(0,1)$ echoes from damage and local noise. The damage detection capabilities of guided wave inspection at or near features are therefore very limited and consist primarily in detecting anomalous $F(1,2)$ echoes from nominally axisymmetric features, the presence of which can represent indication that the nominally axisymmetric features have become damaged and therefore have actually ceased to be axisymmetric.

2.2.4 Recent Advances

Guided wave inspection is receiving continuing research attention. The interaction of $T(0,1)$ with complex pipe features such as bends has been explored [8], and the possibility of utilising it to detect axial cracks has been evaluated [55].

A major limitation of guided wave inspection lies in its poor damage sizing and characterisation capabilities. As a result, it is primarily utilised as a fast screening tool to identify areas of concern along a pipeline. If precise damage information is required, then the identified areas are further inspected with complementary methods such as Ultrasonic Testing (UT), Eddy Currents (EC), and radiography. In the recent past, significant efforts have been directed towards addressing this major limitation. A synthetic focusing method has been developed for imaging damage in pipelines [56], and considerable work has been done towards improving the understanding of the interaction of $T(0,1)$ with complex, corrosion-like damage profiles [51–53, 57, 58] and specifically with pit clusters [59, 60].

Guided wave inspection of coated pipelines is also a topic that is being investigated [61, 62], as is the transduction of non-axisymmetric guided wave modes [63, 64].

Notably, the interaction between $T(0,1)$ and simple supports that may be present along a pipeline is a topic that has never been systematically explored before, as the echoes from simple supports are below the typical reporting thresholds for standard guided wave pipeline inspection. However, the increase in resolution, sensitivity and signal-to-noise ratio associated with the introduction of permanently installed sensors and enhanced guided wave inspection equipment creates a growing need to better understand the characteristics of simple support echoes so that they can be distinguished from damage echoes. Chapter 3 discusses this topic.

2.3 Conclusions

In this chapter the physics of guided wave propagation along pipes have been discussed in section 2.1, while the use of guided waves for the detection of damage in pipelines has been described and reviewed in section 2.2.

Chapter 3

The Interaction of Guided Waves with Simple Supports in Pipes

Pipeline corrosion is a major problem for the petrochemical industry. Wall thinning as well as localised pitting corrosion can occur on both the inside and the outside pipe walls. Locations where pipelines rest on simple supports such as round bars and I-beams are particularly problematic since it is common for moisture and dirt to accumulate near the contact interfaces, thereby creating favourable conditions for corrosion initiation. Formally, a simple support is defined as a hard and non-conformable surface, such as the top surface of the I-beam exemplified in figure 3.1, on which a pipeline rests but to which it is not bonded, clamped or secured in any way.

Inspection at simple support locations presents a number of challenges. Common methods utilised to measure wall thickness, such as Ultrasonic Testing (UT) and Eddy Currents (EC), require direct access to the area to be inspected. At simple support locations this is difficult, impractical and often prohibitively expensive to obtain, and consequently such inspection methods do not represent a viable option. Furthermore, even visual inspection may be difficult to perform at a simple support location since the geometrical layout tends to hide the presence of severe corrosion. Guided wave inspection represents a potential solution to this problem as it enables the remote inspection of pipelines at simple support locations without requiring direct access, thus dramatically reducing inspection costs.

The interaction of guided waves with damage in pipelines is a thoroughly studied topic [4–19]. However, the successful detection of damage at simple support locations relies on the ability to distinguish between the echoes produced by the support itself and the echoes produced by damage. Depending on loading conditions, pipe size and support geometry, it is possible for a simple support to produce a significant echo that might mask or be mistaken for damage, especially since echoes from damage are likely to present the same degree of asymmetry as echoes from simple supports. Consequently, it is essential to understand how the echoes produced by simple supports behave. Very little work has so far been reported on this subject, primarily because the echoes from simple supports are below the typical reporting thresholds for standard guided wave pipeline inspection. Cheng et al. [65] performed an experimental study of the effect of clamped supports on the propagation of the fundamental torsional mode $T(0,1)$, focussing on the attenuation caused by the presence of rubber gaskets and the implications this has on the detectability of damage located past the supports. Utilising experimentally gathered data as well as finite elements simulations, Yang et al. [66] studied the interaction between an incident $T(0,1)$ guided wave packet and axially welded supports with an emphasis on the detection of damage located past the support.

The increase in resolution, sensitivity and signal-to-noise ratio associated with the introduction of permanently installed sensors and enhanced guided wave inspection equipment creates a growing need to better understand the characteristics of simple support echoes so that they can be distinguished from damage echoes. This chapter presents an attempt to develop a systematic understanding of how guided waves propagating along a pipe, and in particular the fundamental torsional mode $T(0,1)$, interact with simple supports. First of all, in section 3.1 the general mechanical properties of a contact interface between a pipe and a simple support are derived from Hertzian theory. Guided wave propagation along a supported section of pipe is then analysed in section 3.2 utilising the Semi-Analytical Finite Element (SAFE) method in order to establish which modes can propagate and how they differ from those that can propagate in a free pipe. In section 3.3, Finite Element Analysis (FEA) is utilised to study the echoes from simple supports, and the defining characteristics of these echoes are interpreted in light of the results from the guided wave propagation analysis performed utilising the SAFE method. Finally, in section 3.4 simple support echoes recorded experimentally are compared to those obtained from FEA simulations and utilised to validate them.

3.1 Contact Interface

Consider a length of pipe resting on a simple support, as exemplified in figure 3.1. A contact interface exists between the two bodies with an extent e along the axial direction of the pipe,

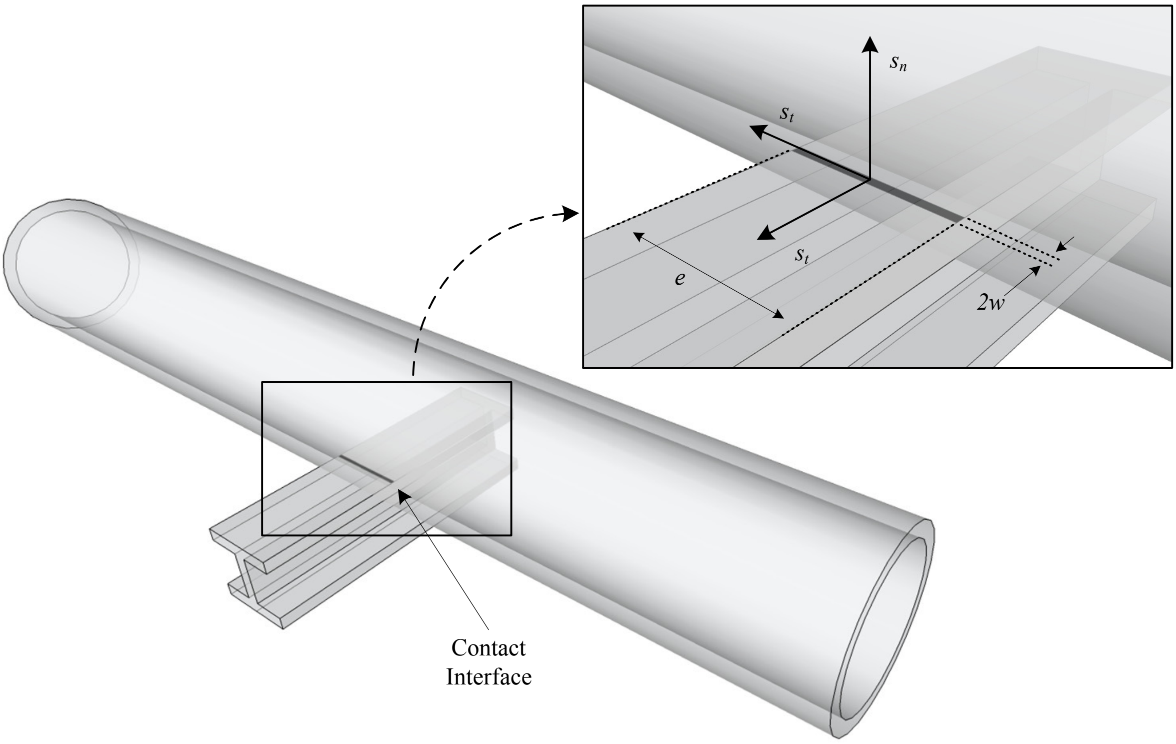

Figure 3.1: Diagram of the contact interface between a pipe and a simple support.

a width $2w$ along the circumferential direction, a normal stiffness s_n that acts in the radial direction and a tangential stiffness s_t that acts in the circumferential and axial directions. The two contacting bodies can be assumed to reasonable accuracy to have smooth surfaces, to be loaded within the elastic limits of their material and to be non-conformable. The contact stiffness can therefore be calculated utilising Hertzian contact theory [67].

Note that in practice there may be occasions where the previously discussed assumptions are not valid. For example, under loading a simple support may bend around the pipe, or the pipe wall may flatten around the contact zone. In such cases, the problem involves conformable bodies and presents an increased degree of complexity since contact stiffness can vary significantly along the interface as a function of the actual contact area, the physical condition of the surfaces in contact, etc. The use of dedicated FEA models, which is beyond the scope of this study, would then be required to represent the contact interface [67]. Johnson [67] thoroughly discusses the assumptions behind Hertzian contact theory.

Two variants of Hertzian contact theory describe two different types of non-conformable contact [67]: three-dimensional Hertzian theory describes point contact, *i.e.* elliptical contact, while two-dimensional Hertzian theory describes line contact. Elliptical contact occurs when two non-conforming bodies come into contact, as in the case of a pipe resting on a round bar. Conversely, line contact occurs when infinitely long cylinders with parallel axes come into contact. Away from end effects, the line contact model adequately describes the interaction between contacting solids in commonly occurring circumstances such as a pipe resting on a I-beam, as shown in figure 3.1. In the present study the analysis is restricted to the case of line contact only because initial experiments as well as FEA simulations revealed that point contact supports typically produce negligible echoes due to their extremely short axial section.

According to Hertzian theory [67–69], in the case of line contact the contact interface is assumed to have constant width

$$2w = 2\sqrt{\frac{2PR^\star}{\pi E^\star}} \tag{3.1}$$

over the contact length e, where $P = F/e$ is the force per unit length normal to the contact interface, *i.e.* the force per unit length with which the two bodies are pressed together, and F, also referred to as contact loading, is the total force normal to the contact interface, *i.e.* the total force with which the two bodies are pressed together. The contact modulus $E^\star$ is given by

$$\frac{1}{E^\star} = \frac{1-{\nu_1}^2}{E_1} + \frac{1-{\nu_2}^2}{E_2} \tag{3.2}$$

where ν_1, E_1, ν_2 and E_2 are respectively Poisson's ratio and Young's modulus for the material of the first and second body, while the relative radius $R^\star$ equivalent to a cylinder on a plane is given by

$$\frac{1}{R^\star} = \frac{1}{R_1} + \frac{1}{R_2} \tag{3.3}$$

where R_1 and R_2 are respectively the radius of the first and second cylinder. Note that in the case of contact between a cylinder of radius R_1, *i.e.* the pipe, and a planar surface, *e.g.* an I-beam, $R^\star$ is equal to R_1 since R_2 tends to infinity. On the basis of the approach of distant points, it can be shown that normal interface stiffness s_n is given by [67–69]

$$\begin{aligned} s_n &= \frac{\pi e}{\frac{1-{\nu_1}^2}{E_1} d_1^\star + \frac{1-{\nu_2}^2}{E_2} d_2^\star - \frac{1}{E^\star}} \\ d_1^\star &= 2\ln\left(\frac{4d_1}{w}\right) - 1 \\ d_2^\star &= 2\ln\left(\frac{4d_2}{w}\right) - 1 \end{aligned} \tag{3.4}$$

where $d_1 = 2R_1$ and $d_2 = 2R_2$. In the case of contact between a cylinder of radius R_1 and a planar surface then $d_1 = d_2 = 2R_1$.

Although it is possible to extend Hertzian theory to account for tangential forces that may develop in applications where surfaces slide or carry traction [67–69], one of the most convenient ways to establish a realistic value for the tangential stiffness of a contact interface is to use an empirical model such as the one for steel-to-steel interfaces developed by Sherif and Kossa [70], which prescribes a constant ratio between tangential and normal stiffness. It is acknowledged that such a model is supposed to work for nominally flat and smooth steel surfaces only, but it is reasonable to assume that in the region of contact the surfaces of the two contacting bodies have very limited curvature. According to the model, the ratio between tangential stiffness s_t and normal stiffness s_n for a steel-to-steel contact interface is given by [70]

$$\frac{s_t}{s_n} = \frac{\pi(1-\nu)}{2(2-\nu)} \tag{3.5}$$

where ν is Poisson's ratio for steel.

3.2 Guided Wave Propagation in Supported Pipes

Guided wave propagation along free sections of pipe has long been studied and understood [27, 29]. On the contrary, guided wave propagation along supported sections of pipe has never been formally investigated before and is considerably more complicated. The increased level of complexity arises as a consequence of the contact between the pipe and the simple support that significantly alters the properties of the waveguide, *i.e.* the pipe, and, importantly, renders it non-axisymmetric. Section 3.2.1 presents an extension of the Semi-Analytical Finite Element (SAFE) method to model wave propagation in constrained waveguides, such as along a pipe resting on a simple support, while section 3.2.2 presents a detailed analysis of how the modes that can propagate along a supported section of pipe differ from those that can propagate in a free pipe.

3.2.1 Guided Wave Propagation Model

In the present study it is assumed that the only effect of simple supports is to impose a constraint on the movement of the region of pipe wall that lies in direct contact with a support. The properties of the constraint are assumed to be the same as those of the contact interface. From a guided wave propagation standpoint, the introduction of such a constraint is equivalent to a change in boundary conditions of the waveguide under consideration, *i.e.* the pipe.

There exist several methods to model guided wave propagation in a given waveguide. In the case of waveguides with simple, regular cross-sectional geometries, such as flat plates and cylindrical structures, possibly embedded in infinite media and composed of multiple layers of anisotropic materials, dispersion curves and mode shapes can be determined using analytical dispersion equations [71, 72] or matrix methods [31, 73–75]. These methods however fail to model wave propagation in waveguides with complex, irregular cross-sectional geometries, such as for example railway lines or T-shaped beams. In such cases the use of the Semi-Analytical Finite Element (SAFE) method [32–47], which utilises a finite element representation of the cross-section of the waveguide and thereby enables arbitrary definitions of waveguide shape, represents a convenient option.

There have been several significant extensions of the SAFE method that enable the modelling of evanescent as well as propagating elastic waves [76], the modelling of waveguides made of viscoelastic materials [77], the definition of waveguides with periodic boundary conditions [78], the excitation and reception of modes by realistic representations of transducers [79], and the modelling of waveguides embedded in infinite media [80]. In this section, the SAFE method is extended to model wave propagation in constrained waveguides, such as along a pipe resting on a simple support. The proposed model can be readily extended further to model other types of constrained waveguides such as, for example, a pipe resting on a clamped support.

Principles of the SAFE Method

The Semi-Analytical Finite Element (SAFE) method utilised in this study is based on the three-dimensional elasticity approach, and therefore no simplifications are made to the elastic tensor or to the displacement field of the waveguide [78, 80]. With reference to figure 3.2, only harmonic guided waves propagating along the x_3 axis are considered. Consequently, the waveguide displacement vector u_m along the x_m axis can be written as

$$u_m(x_1, x_2, x_3, t) = U_m(x_1, x_2)\, e^{i(kx_3 - \omega t)} \tag{3.6}$$

where k is the wavenumber along the axial direction x_3, ω is the angular frequency, and t is time [78, 80]. It follows from equation 3.6 that the displacement gradients are

$$\begin{aligned}
&\frac{\partial u_m}{\partial x_1} = \frac{\partial U_m}{\partial x_1} e^{i(kx_3-\omega t)}\\
&\frac{\partial u_m}{\partial x_2} = \frac{\partial U_m}{\partial x_2} e^{i(kx_3-\omega t)}\\
&\frac{\partial u_m}{\partial x_3} = ikU_m e^{i(kx_3-\omega t)}
\end{aligned} \tag{3.7}$$

The differential equations of motion in a general anisotropic domain D of mass density ρ and elastic constants C_{mjnl} are given by

$$\sum_{n,j,l=1}^{3} \left(C_{mjnl} \frac{\partial^2 U_n}{\partial x_j x_l} \right) + \rho \omega^2 U_n = 0 \tag{3.8}$$

with $m = 1,2,3$. Utilising equations 3.7 and 3.8, the equation of dynamic equilibrium can be written in the form of the eigenvalue problem [78]

$$C_{mjnl} \frac{\partial^2 U_n}{\partial x_j x_l} + i \left(C_{m3nl} + C_{mjn3} \right) \frac{\partial (kU_n)}{\partial x_j} - kC_{m3n3}(kU_n) + \rho \omega^2 \delta_{mn} U_n = 0 \tag{3.9}$$

with summation over the indices $n = 1,2,3$ and $j,l = 1,2$. The components of the stress vector **T** on the boundaries δD of domain D are given by [78]

$$T_m = \sum_{n,j,l=1}^{3} C_{mjnl} \frac{\partial U_n}{\partial x_l} \hat{n}_j \tag{3.10}$$

with $m = 1,2,3$ and where $\hat{\mathbf{n}}$ is the outward unit vector normal to δD. Similarly, utilising equations 3.7 and 3.10, components of the stress vector **T** can be written as

$$T_m = C_{mjnl} \frac{\partial U_n}{\partial x_l} \hat{n}_j + iC_{mjn3}(kU_n)\hat{n}_j \tag{3.11}$$

with summation over the indices $n = 1,2,3$ and $j,l = 1,2$. The coefficients C_{mjnl}, which can be expressed utilising the standard contracted notation C_{mn} with $m,n = 1,\dots,6$, represent the stiffness moduli which can have real or complex values depending on whether the material is respectively elastic or viscoelastic. For this study, viscoelasticity effects are assumed to be negligible, and thus the coefficients C_{mn} will only take real values.

Phase velocity v_{ph} and group velocity v_{gr} dispersion curves over the desired frequency range can then be traced by finding the eigenvalues of the wavenumber k for each of the chosen values of the angular frequency ω. Each solution at any single frequency will reveal all of the modes that can possibly exist in the waveguide at that frequency [78, 80]. Predoi et al. [78] present an extensive discussion of how the SAFE method can be implemented utilising commercially available Finite Element Analysis (FEA) software.

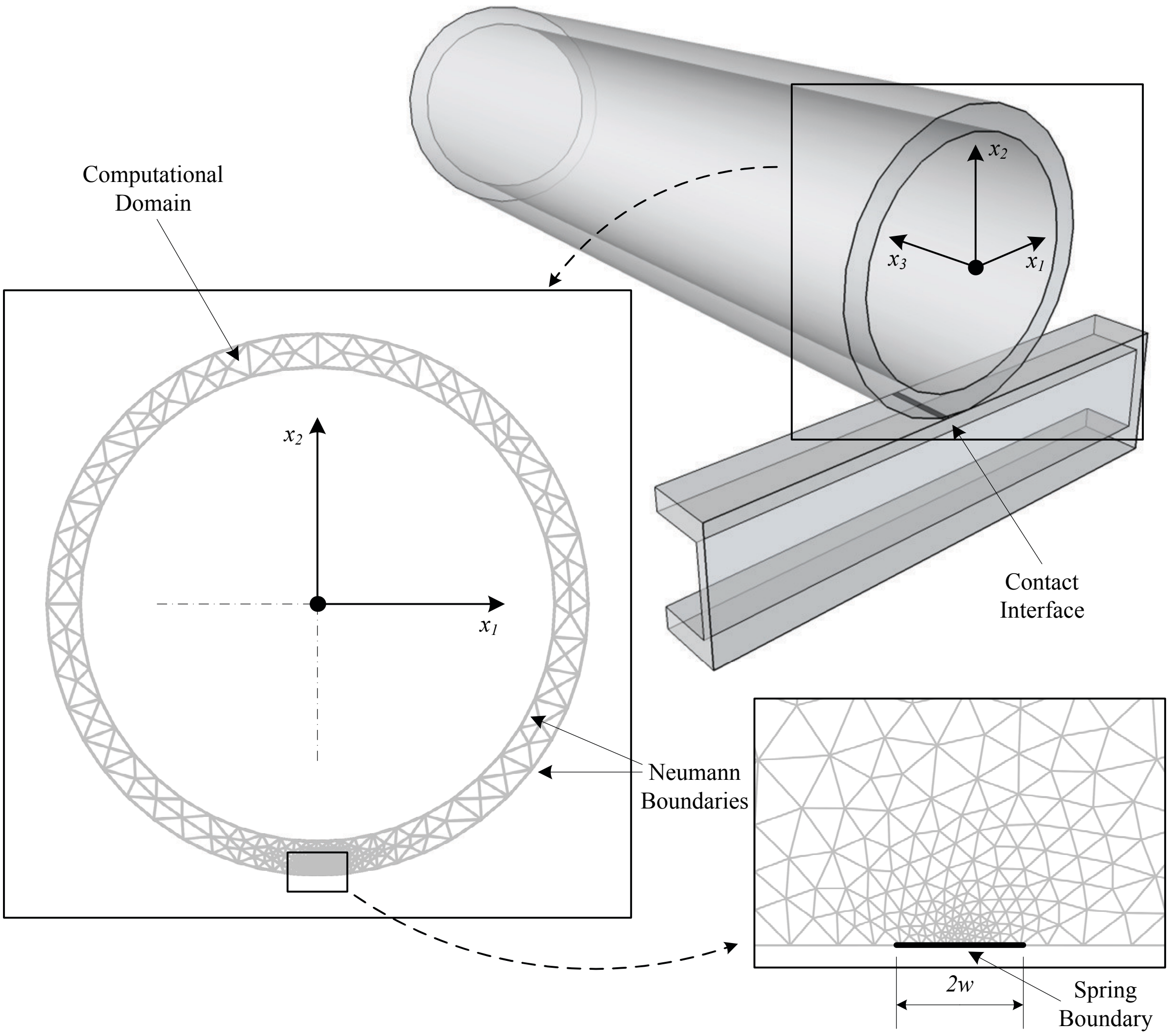

Figure 3.2: Diagram of the Semi-Analytical Finite Element (SAFE) model representing a pipe in contact with a simple support; the model is comprised only of the cross-sections of the pipe and of the contact interface.

SAFE Method for Constrained Waveguides

In this study, the Semi-Analytical Finite Element (SAFE) method is extended to model wave propagation in constrained waveguides, such as along a pipe resting on a simple support.

One of the simplest methods to model a contact interface between two solid bodies is by utilising linear springs in parallel with viscous dampers that link the two bodies at the location of the interface. In the absence of lubricant at the interface it is generally acknowledged that contact damping is very low [81], and consequently viscous dampers can be eliminated from the model without significantly compromising its validity. As a result, the behaviour of the contact interface remains dependent only on its geometrical dimensions and on the stiffness of the linear springs.

Because in the present study it is assumed that the only effect of simple supports is to constrain the movement of the region of pipe that lies in direct contact with the support, rather than modelling two separate bodies linked by springs, *i.e.* the pipe and the support, it was chosen to model solely the pipe and to simulate the presence of the contact interface, and therefore of the support, by elastically constraining the movement of a portion of the outside surface of the pipe to “ground”, *i.e.* to a spatially fixed position.

Figure 3.2 presents a diagram of the proposed SAFE model. The model represents the cross-section of a supported pipe that extends to infinity, and consists of a finite-element domain with the material properties of carbon steel and obeying the PDE expressed in the previous section. All the boundaries of the finite-element domain satisfy Neumann conditions, *i.e.* $T_m = 0$ for $m = 1,2,3$, except for a small region in which a spring boundary is implemented to reproduce the contact interface. The spring boundary covers a circumferential extent of $2w$, corresponding to the width of a Hertzian line contact interface. At the spring boundary, the components of the stress vector **T** are defined as

$$T_1 = \frac{-s_n u_n \hat{n}_1 + s_t u_t \hat{t}_1}{S} \tag{3.12}$$

$$T_2 = \frac{-s_n u_n \hat{n}_2 - s_t u_t \hat{t}_2}{S} \tag{3.13}$$

$$T_3 = \frac{s_t u_3}{S} \tag{3.14}$$

where $\hat{\mathbf{n}}$ is the outward unit vector normal to δD, $\hat{\mathbf{t}}$ is the anti-clockwise unit vector tangential to δD, u_n is outward normal waveguide displacement at δD, u_t is anti-clockwise tangential waveguide displacement at δD, $S = 2we$ is the contact interface area, and s_n and s_t are respectively the normal and tangential contact stiffness. Equivalently, the stresses at the spring boundary can be incorporated in the conventional Cauchy stress tensor

$$\boldsymbol{\sigma} = \begin{bmatrix} \sigma_{11} & \sigma_{12} & \sigma_{13} \\ \sigma_{21} & \sigma_{22} & \sigma_{23} \\ \sigma_{31} & \sigma_{32} & \sigma_{33} \end{bmatrix} = \begin{bmatrix} \frac{s_t u_t \hat{t}_1}{S} & \frac{-s_n u_n \hat{n}_1}{S} & 0 \\ \frac{-s_n u_n \hat{n}_2}{S} & \frac{-s_t u_t \hat{t}_2}{S} & 0 \\ 0 & 0 & \frac{s_t u_3}{S} \end{bmatrix} \tag{3.15}$$

from which the stress vector **T** can also be obtained.

For given contact loading and material properties, equation 3.4 indicates that the normal contact stiffness s_n can be approximated as being linearly proportional to the axial extent of contact e, and consequently from equation 3.5 so can the tangential contact stiffness s_t.

It follows that the stresses at the spring boundary, and thus the behaviour of the proposed SAFE model, are virtually independent of the contact length e, but only depend on contact stiffness per unit length of axial contact.

The proposed SAFE model can be readily extended further to model other types of constrained waveguides, such as, for example, a pipe resting on a clamped support, by appropriately varying the circumferential extent of the spring boundary and by utilising appropriate values for the normal and tangential contact stiffness.

3.2.2 Guided Wave Propagation Analysis

Figures 3.3, 3.4 and 3.5 present the phase velocity dispersion curves for a NPS 3 Schedule 40 steel pipe under various conditions. The dispersion curves in figures 3.3, 3.4 and 3.5 were generated utilising the SAFE method described in section 3.2.1, implemented through COMSOL® Multiphysics® [48] and MATLAB® [49]. In figure 3.3 the pipe is free and in vacuum. The fundamental torsional mode $\mathrm{T}(0,1)$, shown in red in figure 3.3, is the mode of choice for pipeline inspection applications, as previously discussed in chapter 2 and in particular in section 2.2.3. In figures 3.4 and 3.5 the pipe in vacuum is supported by, respectively, a hardwood plank and a steel plate, both extending 0.1m in the axial direction and being pushed against the pipe with a force of 1kN. Table 3.1 presents the material properties utilised to determine the properties of the contact interfaces. Note that it has been assumed that hardwood-steel contact is similar in behaviour to steel-steel contact, and that therefore the ratio of tangential stiffness to normal stiffness for hardwood-steel contact is also expressed by equation 3.5 but with $\nu = (\nu_{\text{steel}} + \nu_{\text{hardwood}})/2$. Note also that the axial extent of the support has been defined for the sole purpose of calculating the force per unit length P. All contact stiffness values utilised in this study are summarised in table 3.2.

Figures 3.3, 3.4 and 3.5 show that there are substantial differences between the dispersion curves and consequently between the modes that can propagate in a free pipe and in a supported pipe.

First of all, in a supported pipe all modes have a non-zero cut-off frequency. This behaviour can be explained by considering that a pipe resting on a simple support cannot be rotated or translated in any direction as long as the force utilised is not sufficient to break traction or lift the pipe, in which case the pipe cannot be considered to be in contact with the support anymore. In other words, no modes can exist in a supported pipe at zero-frequency, and consequently all modes will present a non-zero cut-off frequency.

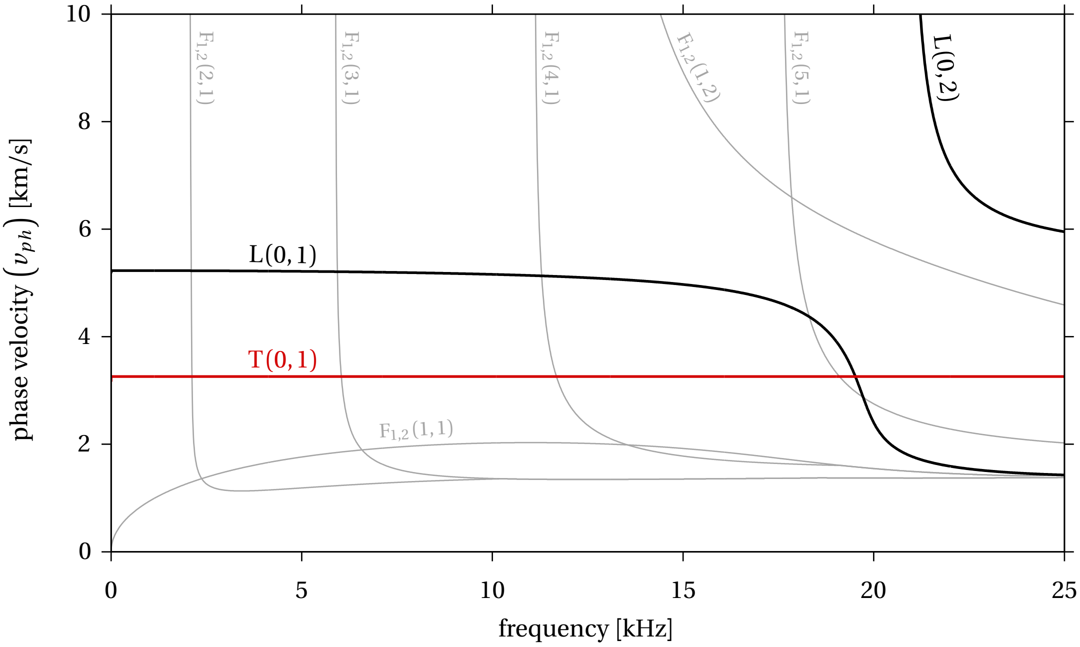

Figure 3.3: Phase velocity dispersion curves for a free NPS 3 Schedule 40 carbon steel pipe in vacuum; the fundamental torsional mode T(0,1) is shown in red.

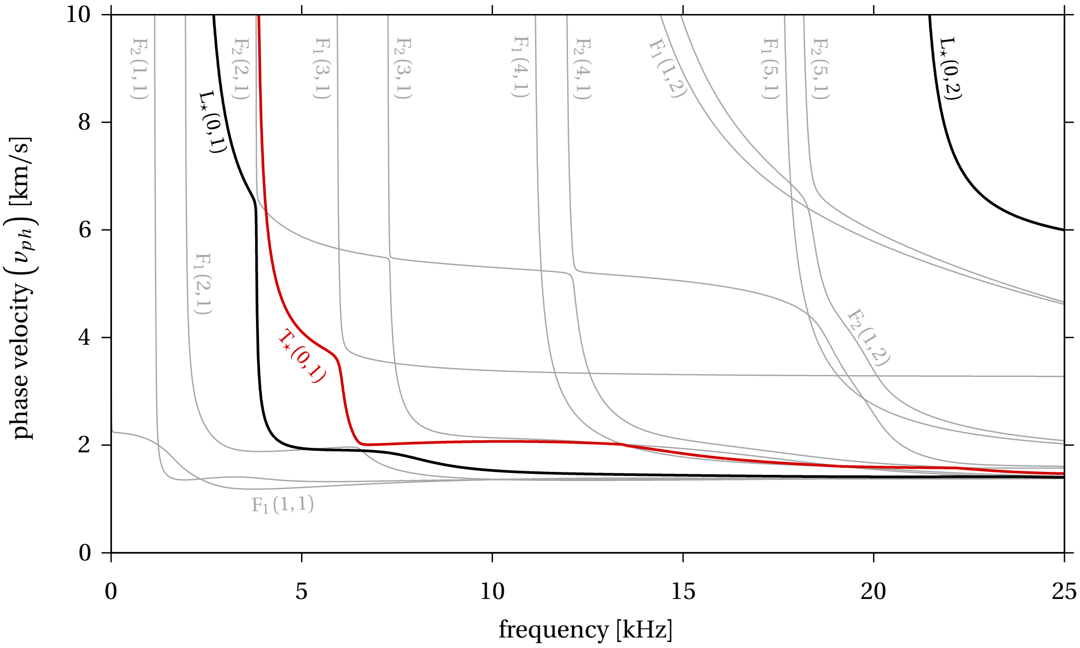

Figure 3.4: Phase velocity dispersion curves for a NPS 3 Schedule 40 carbon steel pipe in vacuum and resting on a hardwood support of 0.1m axial extent with a constant loading of 1kN.

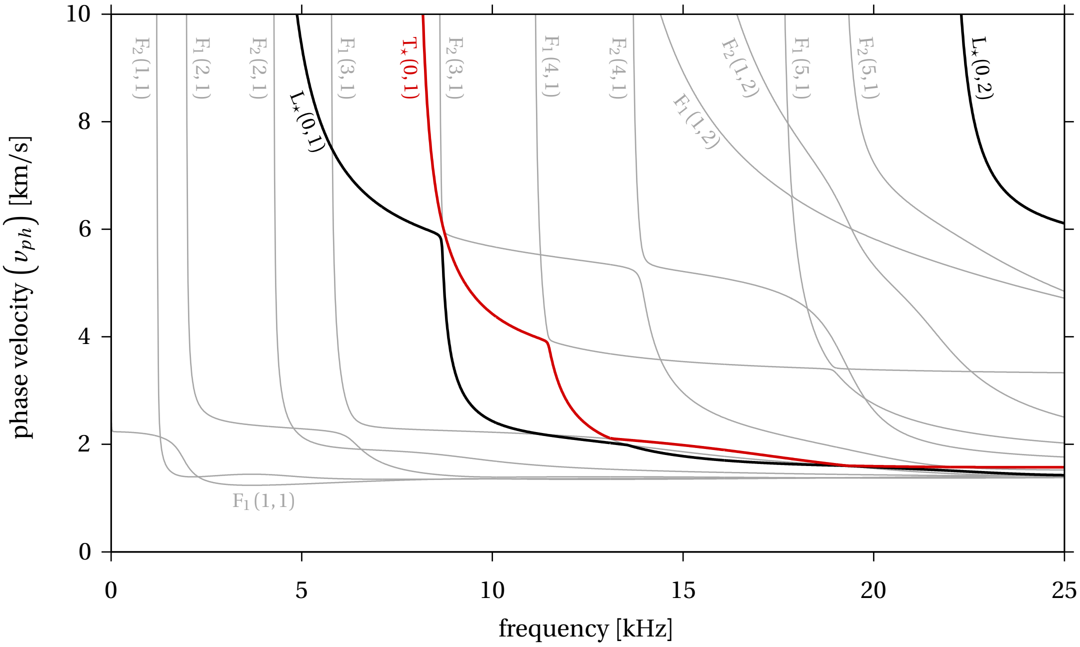

Figure 3.5: Phase velocity dispersion curves for a NPS 3 Schedule 40 carbon steel pipe in vacuum and resting on a steel support of 0.1m axial extent with a constant loading of 1kN.

Table 3.1: Material properties utilised to determine the properties of the contact interfaces for the Semi-Analytical Finite Element (SAFE) guided wave propagation analysis.

material	density [kg/m^3]	Young's modulus [GPa]	Poisson's ratio
hardwood	720	15.78	0.40
steel	7932	216.9	0.2865

Table 3.2: Contact stiffnesses utilised in the Semi-Analytical Finite Element (SAFE) guided wave propagation analysis.

support type	F [kN]	e [m]	s_n/e [GN/m^2]	s_t/e [GN/m^2]
free pipe	N/A	N/A	0	0
hardwood	1	0.1	3.94	2.46
steel	1	0.1	23.5	15.4

Secondly, it can be seen that flexural modes which are described by a single dispersion curve in a free pipe appear to be described by two distinct dispersion curves in a supported pipe. In reality the two distinct dispersion curves and their associated modes, for instance $\mathrm{F}_1(4,1)$ and $\mathrm{F}_2(4,1)$, already exist in a free pipe but because of the axisymmetry of the waveguide they coincide. Moreover, the shapes of the two modes are identical up to a rotation of the coordinate system about the pipe axis. However, as had previously been observed for wave propagation along pipe bends [8], the loss of axisymmetry in a supported pipe implies flexural modes behave differently according to their orientation. In particular, if the orientation of a mode is such that pipe wall movement is minimal near the contact interface, then the presence of the support will have a limited influence on the behaviour of the mode; this is the case for modes $\mathrm{F}_1(n,m)$. Conversely, if the orientation of a mode is such that significant pipe wall movement occurs near the contact interface, then the presence of the support will have a considerable influence on the behaviour of the mode; this is the case for modes $\mathrm{F}_2(n,m)$. As a result, while the cut-off frequency of $\mathrm{F}_2(n,m)$ modes increases significantly with contact stiffness per unit length, as can be seen by comparing figures 3.4 and 3.5, the cut-off frequency of $\mathrm{F}_1(n,m)$ modes remains virtually unaltered. Intuitively, this behaviour can be explained by considering that as contact stiffness per unit length decreases to infinitesimally small values, the supported pipe becomes more and more akin to a free one, implying that the presence of the support has less and less influence, while the opposite is true when contact stiffness per unit length increases. Note in particular that $\mathrm{F}_1(1,1)$ in figures 3.4 and 3.5 has a cut-off extremely close to zero.

Finally, in a supported pipe the longitudinal and torsional modes are also significantly influenced by the presence of the support, resulting in the loss of their axisymmetric shape and in the appearance of non-zero cut-off frequencies. $\mathrm{L}(0,1)$, $\mathrm{L}(0,2)$ and $\mathrm{T}(0,1)$ in a free pipe become respectively $\mathrm{L}_*(0,1)$, $\mathrm{L}_*(0,2)$ and $\mathrm{T}_*(0,1)$ in a supported pipe, and all present a non-zero cut-off frequency that increases with contact stiffness per unit length, as can be seen by comparing figures 3.4 and 3.5.

Figure 3.6 presents the same phase velocity dispersion curves as those in figure 3.5, but in this case the phase velocity lines are greyscale-coded so that the darker they are the more similar the shape of the corresponding mode is to the shape of $\mathrm{T}(0,1)$. The degree of mode shape similarity has been calculated utilising the Modal Assurance Criterium (MAC) [82], which is a scalar quantity comprised in the interval between zero and one that provides a measure of the degree of similarity between two mode shapes. A MAC of one means the two modes are identical, while a MAC of zero means the two modes are orthogonal. The MAC between mode A and mode B is defined in terms of the inner product of their mode shape vectors

$$\mathrm{MAC}(A,B)=\frac{\left|\psi_A^{\top}\psi_B\right|^2}{\left(\psi_A^{\top}\psi_A\right)\left(\psi_B^{\top}\psi_B\right)} \tag{3.16}$$

where ψ_A and ψ_B are the mode shape vectors of respectively mode A and mode B. To obtain the greyscale-coded phase velocity lines of figure 3.6, for each mode and at each frequency in the supported pipe the MAC between the shape of that mode and the shape of $\mathrm{T}(0,1)$ in a free pipe at the same frequency is calculated. The phase velocity dispersion curve corresponding to that mode is then shaded between white and black at each frequency depending on the MAC value obtained at that frequency. In figure 3.6, a MAC of zero corresponds to white, while a MAC of one corresponds to black.

Figure 3.6 reveals that in the considered frequency range there are six modes whose shape bears a significant degree of similarity to that of $\mathrm{T}(0,1)$. Below 8.4kHz, the modes $\mathrm{F}_1(1,1)$, $\mathrm{F}_1(2,1)$ and $\mathrm{F}_1(3,1)$ have shapes that involve the pivoting of the pipe about the support contact position and that bear a limited similarity to $\mathrm{T}(0,1)$ that decreases as the frequency increases. Conversely, above 8.4kHz the modes $\mathrm{T}_*(0,1)$, $\mathrm{F}_1(4,1)$ and $\mathrm{F}_1(5,1)$ appear to have shapes that are very similar to that of $\mathrm{T}(0,1)$, with a degree of similarity that quickly increases with frequency. It can be seen in figure 3.6 that as the frequency increases the mode shapes become increasingly akin to pure torsional motion, to the point where at 24.5kHz the mode shape of $\mathrm{F}_1(5,1)$ is extremely similar to that of $\mathrm{T}(0,1)$. Furthermore, figure 3.6 reveals that as the frequency increases the phase velocity of the mode most similar to $\mathrm{T}(0,1)$ tends asymptotically to the phase velocity of $\mathrm{T}(0,1)$.

In conclusion, this analysis indicates that in a supported pipe there is a frequency corresponding to the cut-off of the $\mathrm{T}_*(0,1)$ mode, which in the discussed case is around 8.4kHz, below which very little torsional motion is allowed and above which there exist modes that are very similar to $\mathrm{T}(0,1)$. From a practical standpoint this implies that when a $\mathrm{T}(0,1)$ guided wave packet propagating in a free pipe encounters a supported section of pipe it cannot propagate through that section as a $\mathrm{T}(0,1)$ guided wave packet but must convert into a guided wave packet composed of a combination of other suitable modes that can propagate along that supported section. The reflection coefficient for the support will then be high at frequencies where there is little mode similarity to $\mathrm{T}(0,1)$ in the supported region, while it will remain low at frequencies where there is high mode similarity to $\mathrm{T}(0,1)$ in the supported region.

Note finally that in figure 3.6 there are small regions of low mode similarity, *i.e.* light spots, around 11.5kHz and 18.95kHz that appear to be caused by a mode repulsion phenomenon

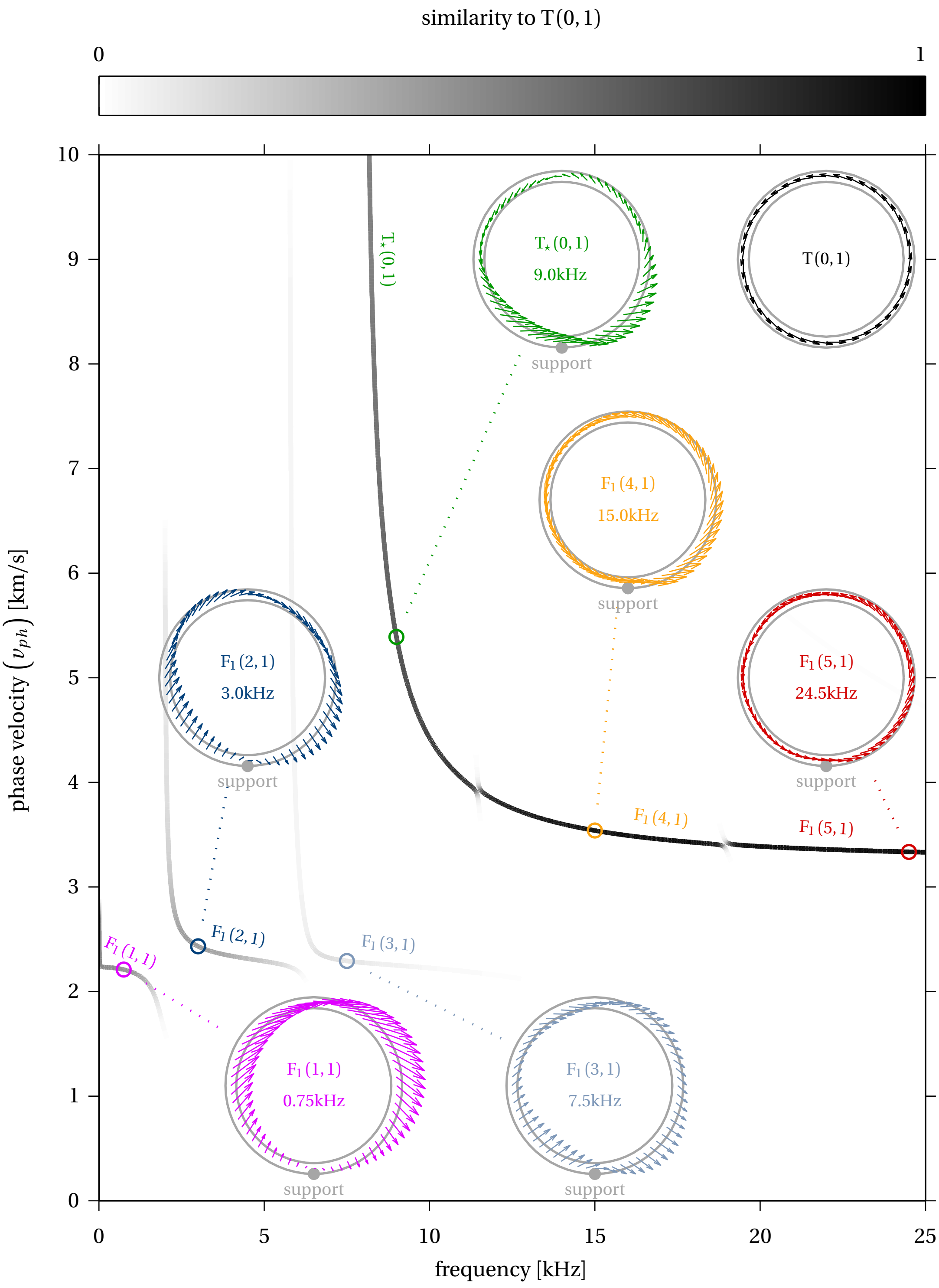

Figure 3.6: Phase velocity dispersion curves for a NPS 3 Schedule 40 carbon steel pipe in vacuum and resting on a steel support of 0.1m axial extent with a constant loading of 1kN; the curves are greyscale-coded so that the darker they are the more similar the corresponding mode is to T(0, 1); displacement mode shapes on the x_1x_2 plane are presented at selected frequencies, with arrows representing pipe wall displacement.

similar to that previously observed by other authors [83–88]. For example, figure 3.7 illustrates mode repulsion between $F_1(4,1)$ and $F_1(5,1)$. Interestingly, it can be seen from figure 3.7 that the modes $F_1(4,1)$ and $F_1(5,1)$ appear to be exchanging shapes in the vicinity of the 18.95kHz repulsion point. In particular, as the frequency increases the shape of $F_1(4,1)$ changes from being very akin to pure torsional motion near 17kHz, to being pure flexural motion near 19.4kHz. Conversely, as the frequency increases the shape of $F_1(5,1)$ changes from being pure flexural motion near 18.7kHz, to being very similar to pure torsional motion near 21.4kHz.

3.3 Finite-Element Analysis of Echoes from Simple Supports

Finite Element Analysis (FEA) is widely utilised to study the interaction between guided waves propagating along a structure and the features of the structure itself [4, 6, 8, 9, 12, 13, 18, 19]. Figure 3.8 presents the FEA model utilised in this study. The model was implemented utilising ABAQUS Unified FEA [89] and MATLAB® [49], and consists of a fully three-dimensional mesh composed of elastic hexahedral elements that represents a carbon steel pipe of a chosen NPS and Schedule. Element spacings of approximately 2mm in each direction and a time step of 0.1μs have been utilised [90]. An Absorbing Layer with Increasing Damping (ALID) [80, 91–94] is situated at each end of the model. In this way the ends produce no echoes and the model effectively behaves as if it were infinitely long.

The fundamental torsional mode $T(0,1)$ is excited at axial position **AA** by applying tangentially oriented concentrated forces of equal direction and amplitude to each of the nodes situated on the outside pipe circumference, as shown in figure 3.8. The amplitude of each concentrated force varies in time following a multi-cycle Hann windowed toneburst, and as a result a guided wave packet comprising exclusively the fundamental torsional mode $T(0,1)$ propagates axially from **AA** in each direction along the pipe. The packet that propagates directly towards one ALID is immediately absorbed by the ALID itself, while the other packet will interact with the contact interface **S'-S"**, *i.e.* with the support, before being also eventually absorbed by the other ALID. Any echo produced as the packet interacts with the contact interface **S'-S"** will propagate back towards **AA**, where it is detected and recorded by monitoring the tangential displacement over time of each of the nodes situated on the outside pipe circumference.

The support contact interface **S'-S"** is located at a distance away from **AA**, and its axial length, which corresponds to e in figure 3.1, varies between simulations. Similarly to the SAFE

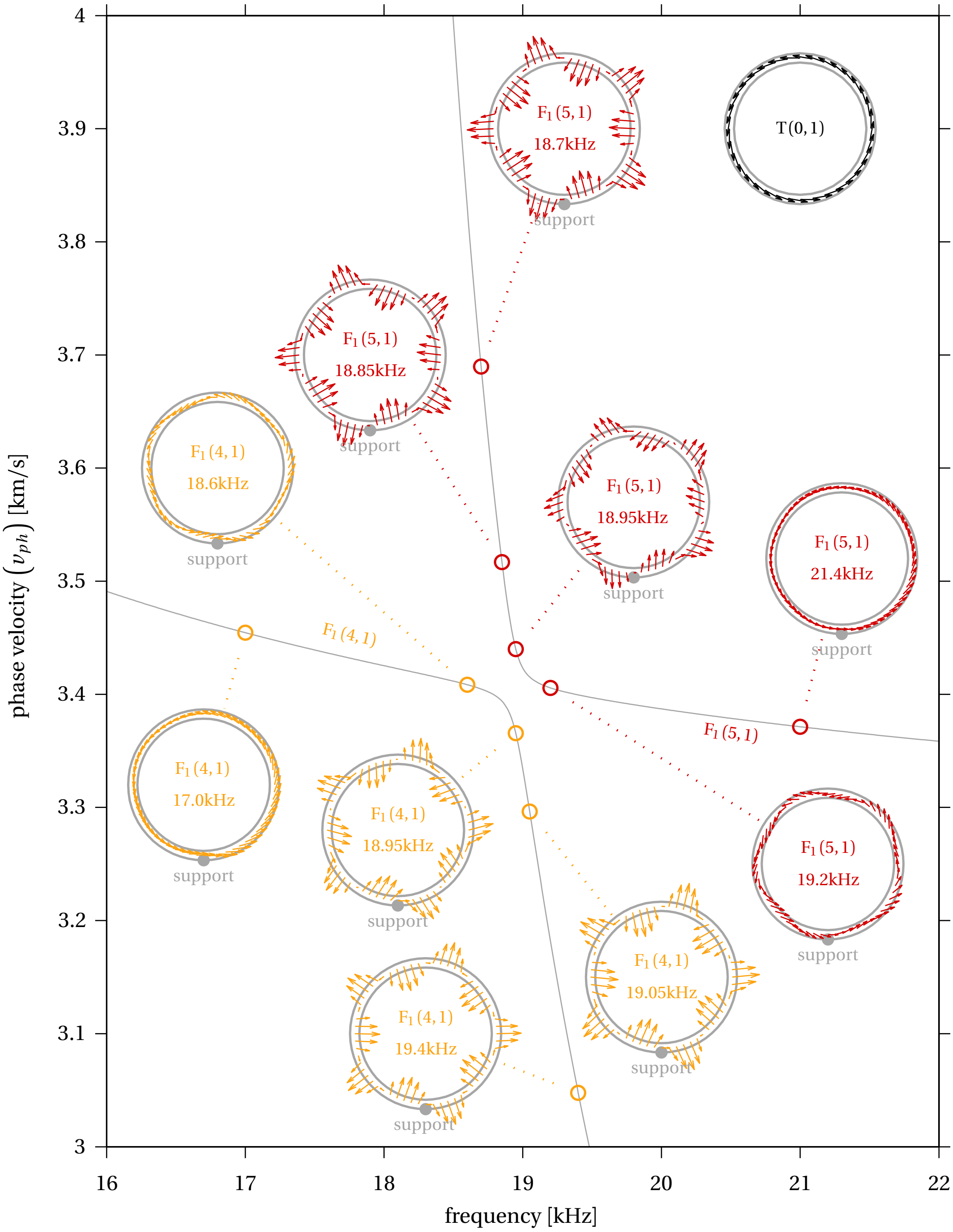

Figure 3.7: Phase velocity dispersion curves exemplifying mode repulsion between $F_1(4,1)$ and $F_1(5,1)$ for a NPS 3 Schedule 40 carbon steel pipe in vacuum and resting on a steel support of 0.1m axial extent with a constant loading of 1kN; displacement mode shapes on the x_1x_2 plane are presented at selected frequencies, with arrows representing pipe wall displacement.

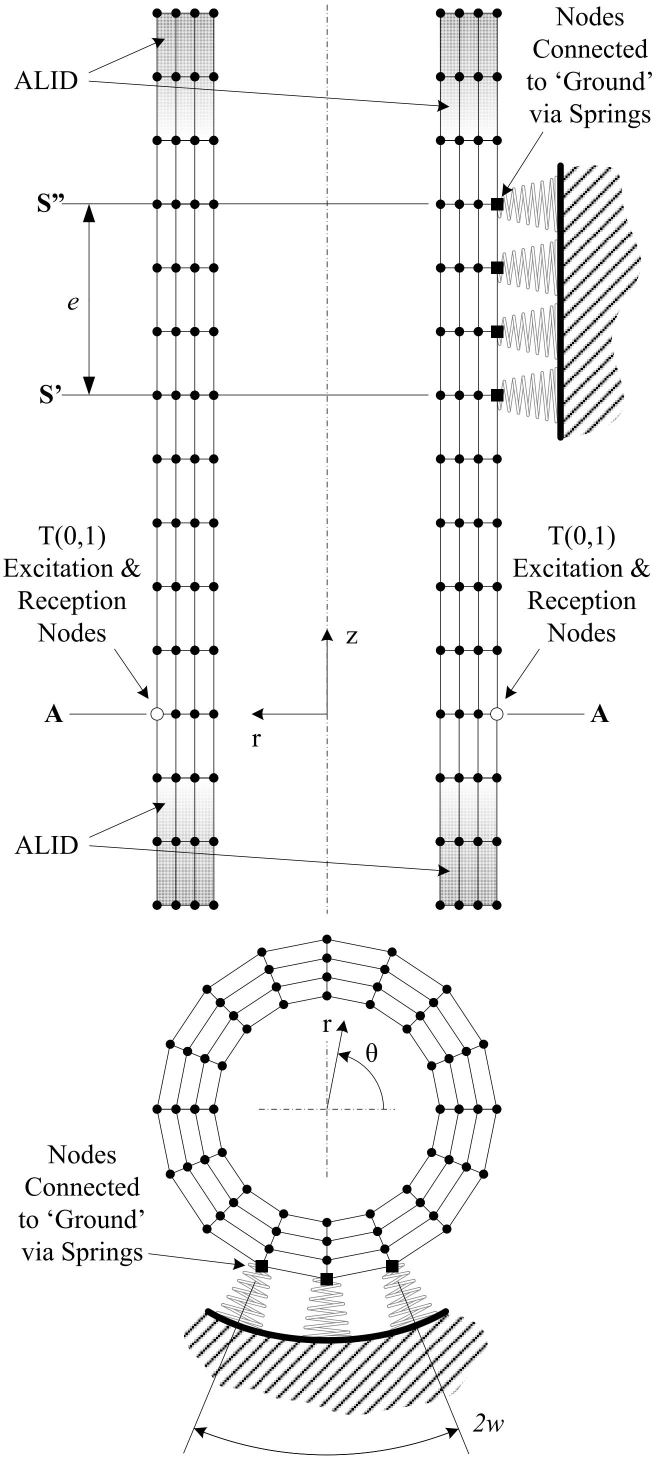

Figure 3.8: Diagram of the Finite Element Analysis (FEA) model representing an infinitely long pipe supported at one location.

model discussed in section 3.2, the contact interface is modelled by constraining the movement of the appropriate outer surface nodes through linear springs that connect these nodes to "ground", *i.e.* to a spatially fixed position, as shown in figure 3.8. The axial extent e and circumferential extent $2w$ of the contact interface are varied by changing the number of nodes connected to ground. The spring constraining each node has a stiffness expressed by a three dimensional vector $\mathbf{s} = (s_r, s_\theta, s_z)$, where s_r, s_θ and s_z are respectively the spring stiffness in the radial, circumferential and axial directions. The stiffness in the radial direction models the normal contact stiffness, so $s_r = s_n/N$, while the stiffnesses in the circumferential and axial directions model the tangential contact stiffness $s_\theta = s_z = s_t/N$, where N is the number of nodes connected to ground.

Figure 3.9 presents a typical torsional $\mathrm{T}(0,1)$ signal from a FEA simulation of a NPS 3 Schedule 40 carbon steel pipe resting on a 0.2m axially long steel support with 1kN loading. The torsional $\mathrm{T}(0,1)$ signal was obtained by summing the tangential displacement signals of each of the nodes situated on the outside pipe circumference at **AA**. Figure 3.10 presents the modulus of the Fast Fourier Transform (FFT) spectra of the incident and echo portions of torsional $\mathrm{T}(0,1)$ signal shown in figure 3.9. A torsional $\mathrm{T}(0,1)$ Reflection Coefficient (RC) spectrum can then be obtained by dividing the echo spectrum by the incident spectrum.

Figure 3.11 shows the torsional $\mathrm{T}(0,1)$ RC spectrum from a FEA simulation of a NPS 3 Schedule 40 carbon steel pipe resting on a steel support of 0.1m axial extent with a loading of 1kN, together with the total MAC spectrum. The total MAC

$$\text{total MAC} = \sum_{j=1}^{J} \frac{\left|\psi_j^{\top} \psi_{T(0,1)}\right|^2}{\left(\psi_j^{\top}\psi_j\right)\left(\psi_{T(0,1)}^{\top}\psi_{T(0,1)}\right)} \tag{3.17}$$

at each frequency has been calculated by adding all MAC calculated between $\mathrm{T}(0,1)$ and each mode $\psi_1, \psi_2, \ldots, \psi_J$ that can exist at that frequency in the supported section of pipe under consideration. The total MAC is a scalar quantity comprised in the interval between zero and one that provides a measure of the amount of torsional motion that can exist in the supported section of pipe at a given frequency. A value of one means $\mathrm{T}(0,1)$ can exist, while a value of zero means no torsional motion is possible.

From figure 3.11 it is possible to see that in the low frequency region below 8.4kHz the total MAC remains under 0.5 and generally decreases as the frequency increases, indicating that limited torsional motion is possible along the supported section of pipe in this frequency range. Consequently, an incident $\mathrm{T}(0,1)$ guided wave packet that encounters the supported section in this frequency range of pipe will mostly reflect, as indicated by the relatively high RC value.

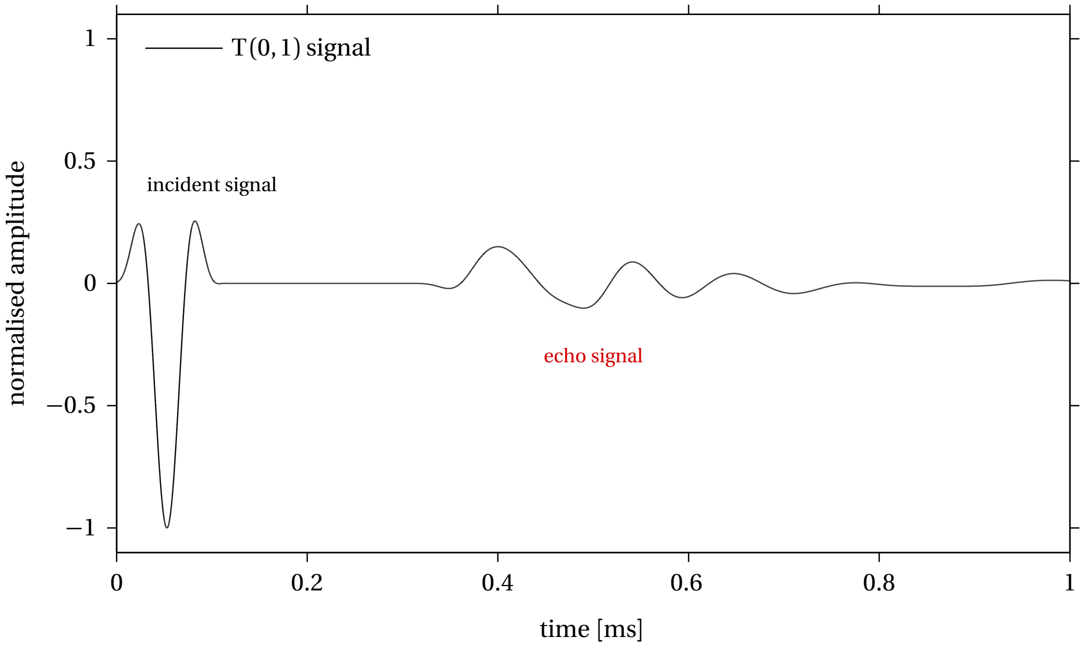

Figure 3.9: Example torsional signal from a Finite-Element Analysis (FEA) simulation of a NPS 3 Schedule 40 carbon steel pipe resting on a 0.2m axially long steel support with 1kN loading.

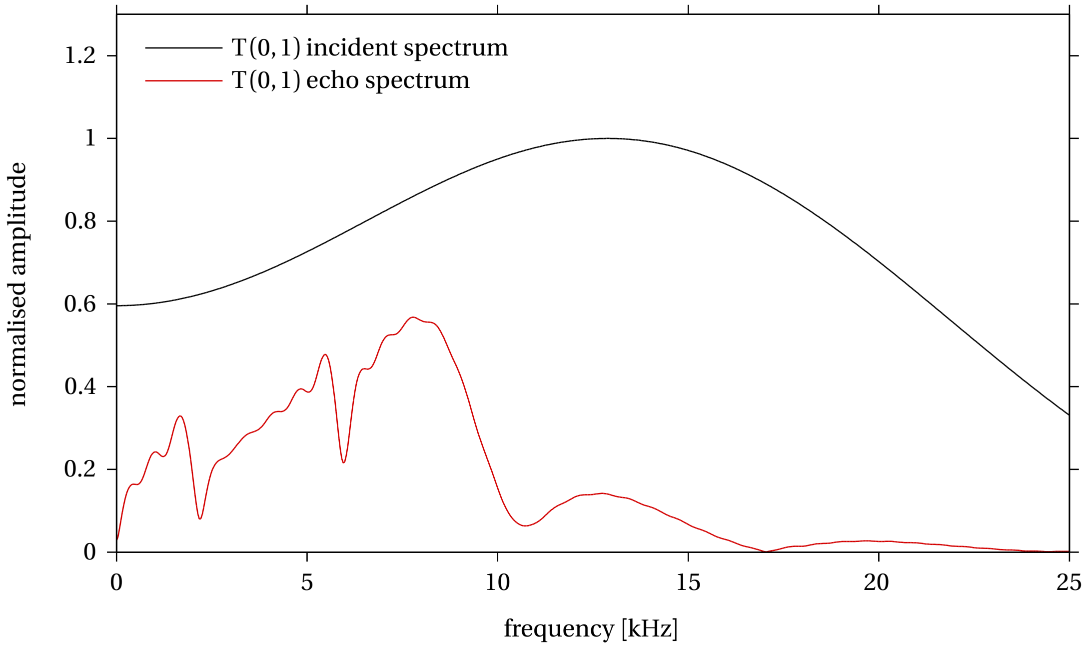

Figure 3.10: Example modulus of the torsional Fast Fourier Transform (FFT) spectra from a Finite-Element Analysis (FEA) simulation of a NPS 3 Schedule 40 carbon steel pipe resting on a 0.2m axially long steel support with 1kN loading.

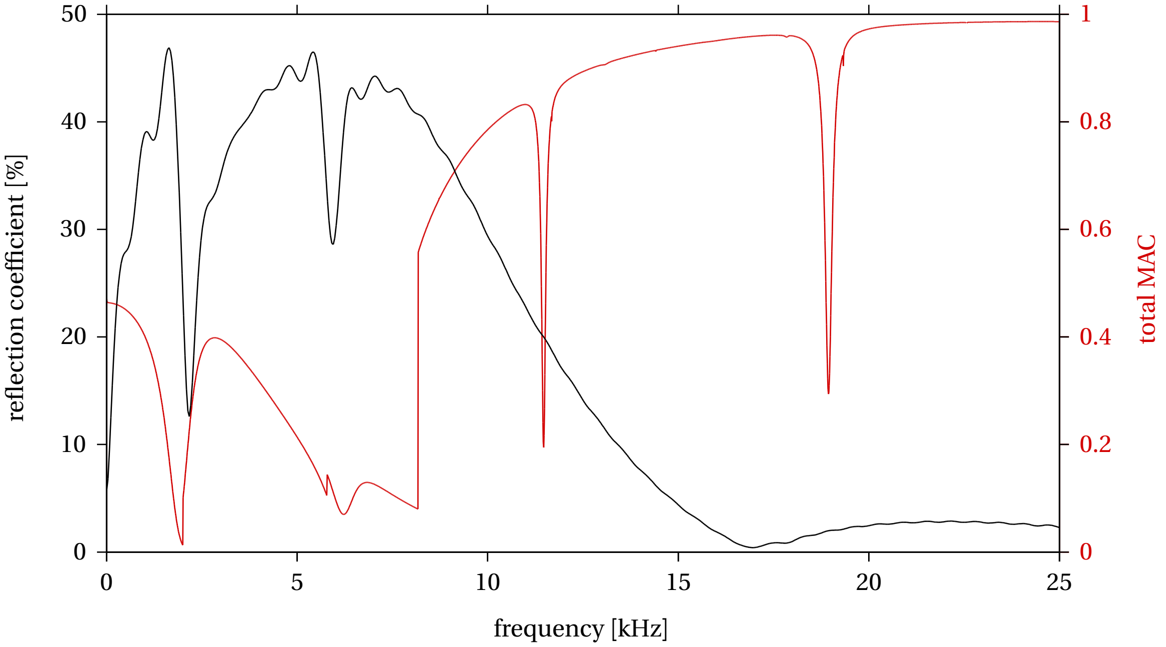

Figure 3.11: Torsional T(0, 1) Reflection Coefficient (RC) spectrum from a Finite-Element Analysis (FEA) simulation of a NPS 3 Schedule 40 carbon steel pipe resting on a steel support of 0.1m axial extent with a constant loading of 1kN, together with the total Modal Assurance Criterion (MAC) spectrum.

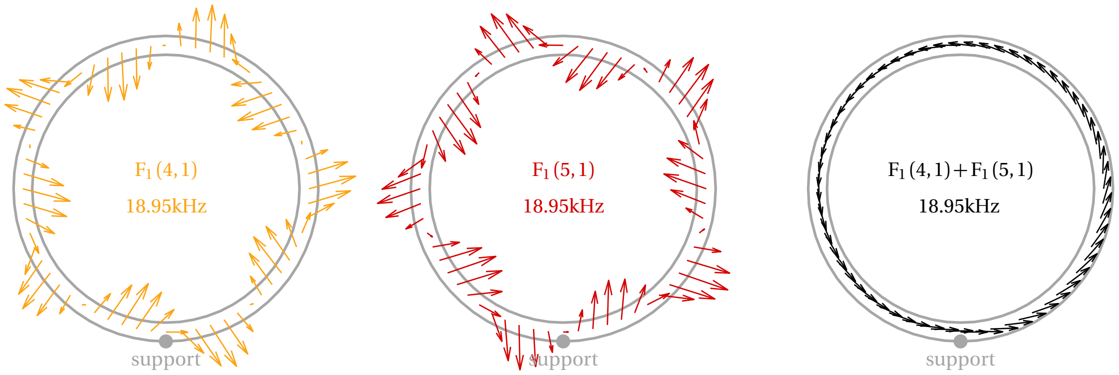

Figure 3.12: Example of the repelling $F_1(4,1)$ and $F_1(5,1)$ modes summing to form a third mode.

Conversely, above 8.4kHz it can be seen that the total MAC increases significantly, coming close to unity as the frequency increases and therefore indicating that considerable torsional motion is possible along the supported section of pipe above 8.4kHz. Therefore, an incident $T(0,1)$ guided wave packet that encounters the supported section of pipe in this frequency range will mostly propagate through the supported section with limited echoes being produced, as indicated by the relatively low RC value.

Importantly, the rapid increase in total MAC and the corresponding drop in RC seen in figure 3.11 occur at a frequency of 8.4kHz that corresponds to the cut-off of the $T_*(0,1)$ mode. Above this frequency, as previously discussed in section 3.2.2, there exist modes with a shape that becomes virtually indistinguishable from that of $T(0,1)$ as the frequency increases.

Guided wave echoes are generated where the impedance of the waveguide changes. In the case of damage, impedance changes arise from reductions in the cross-sectional area of the waveguide as a result of the loss of material caused by the damage. However, in the case of supports, impedance changes along the waveguide arise from differences in boundary conditions brought about by the presence of contact interfaces. Such differences in boundary conditions and associated impedance changes manifest themselves in the form of mode shape mismatches across the impedance change. Therefore, a large mode shape mismatch is indicative of a large impedance change, and conversely a small mode shape mismatch is indicative of a small impedance change. Of particular interest is that, because of the observed wave propagation mechanics, in the case of supports the impedance change presents a very strong frequency dependence, implying that impedance changes are high at low frequency and low at high frequency. Consequently, supports act as a high-pass filter for incident guided waves.

In figure 3.11 the total MAC has deep, sharp troughs at 11.5kHz and 18.95kHz to which there is no corresponding increase in RC. These troughs occur at the frequencies where there is strong modal repulsion between, respectively, $T_*(0,1)$ and $F_1(4,1)$, and $F_1(4,1)$ and $F_1(5,1)$, as can be observed in figures 3.6 and 3.7. Initial studies indicate that at these frequencies the two repelling modes, each with a mode shape quite different from that of $T(0,1)$ but with very similar phase velocities, sum to form a third mode whose shape is virtually identical to the mode shape of $T(0,1)$, as exemplified in figure 3.12 for modes $F_1(4,1)$ and $F_1(5,1)$ at 18.95kHz. As a result, no significant echo is generated. This phenomenon has been observed in the past in the case of Lamb waves in plates [95].

Figures 3.13, 3.14, 3.15 and 3.16 present the torsional $T(0,1)$ RC spectra from FEA simulations as a function of different variables.

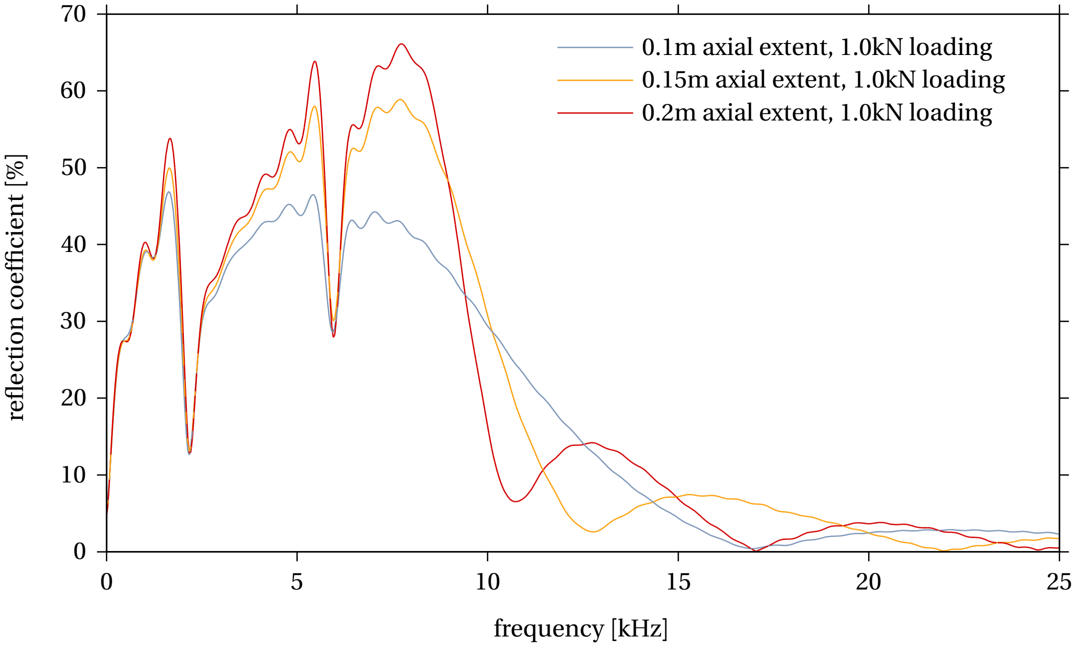

Figure 3.13: Torsional T(0,1) Reflection Coefficient (RC) spectra from Finite-Element Analysis (FEA) simulations of a NPS 3 Schedule 40 carbon steel pipe resting on steel supports of 0.1m, 0.15m and 0.2m axial extent with a constant loading of 1kN.

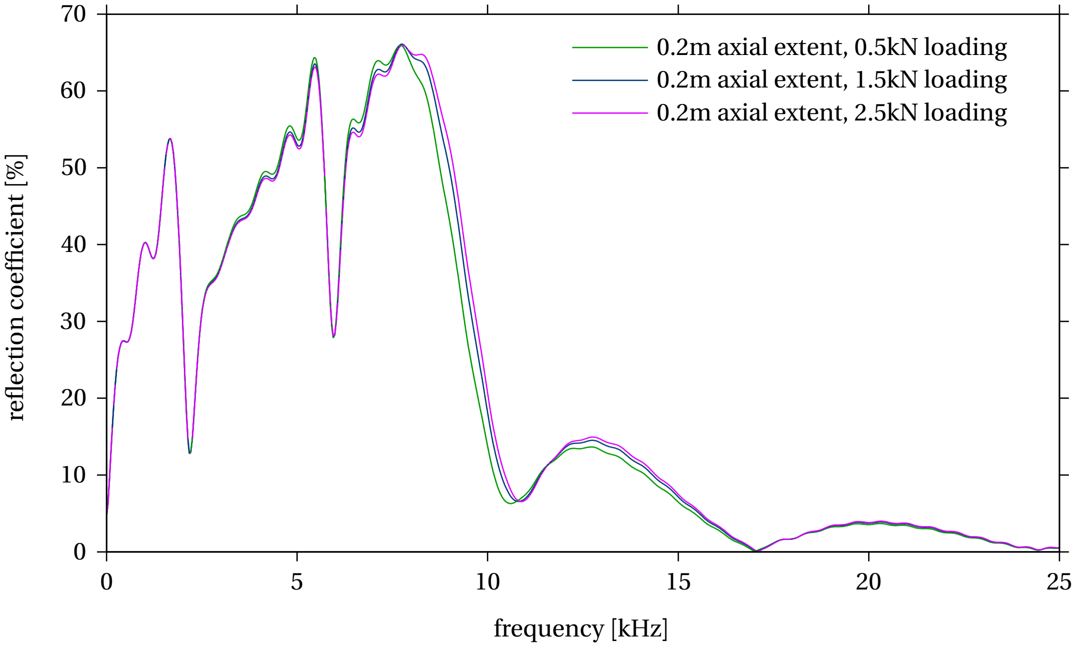

Figure 3.14: Torsional T(0,1) Reflection Coefficient (RC) spectra from Finite-Element Analysis (FEA) simulations of a NPS 3 Schedule 40 carbon steel pipe resting on a steel support of 0.2m axial extent with constant loadings of 0.5kN, 1.5kN and 2.5kN.

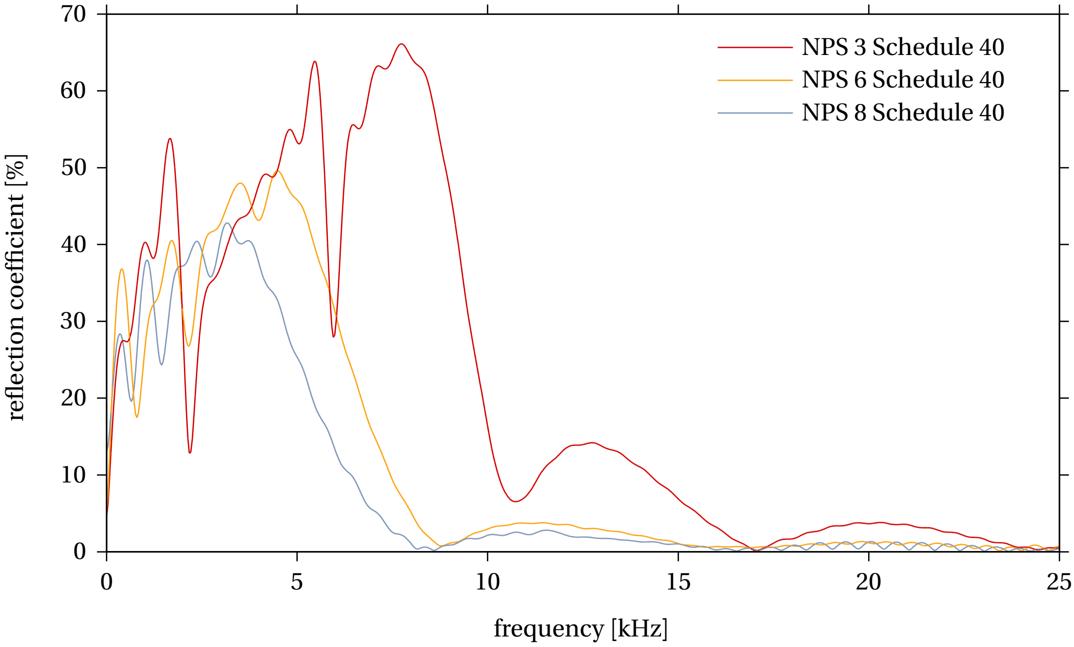

Figure 3.15: Torsional T(0, 1) Reflection Coefficient (RC) spectra from Finite-Element Analysis (FEA) simulations of NPS 3, NPS 6 and NPS 8 Schedule 40 carbon steel pipes resting on a steel support 0.2m axial extent with a constant loading of 1kN.

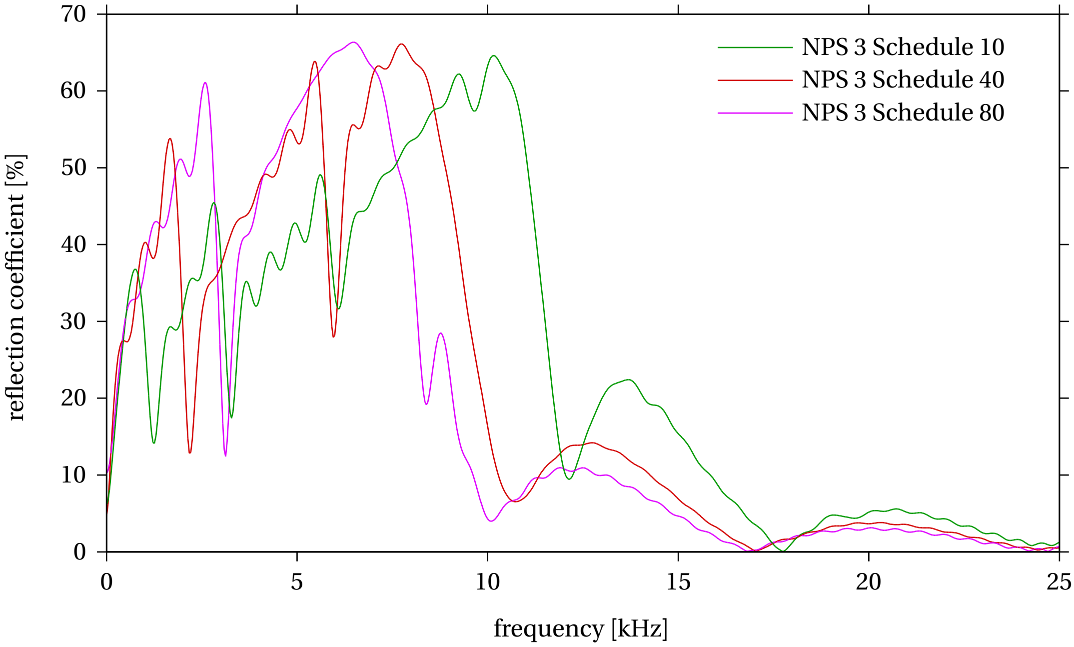

Figure 3.16: Torsional T(0, 1) Reflection Coefficient (RC) spectra from Finite-Element Analysis (FEA) simulations of NPS 3 Schedule 10, Schedule 40 and Schedule 80 carbon steel pipes resting on a steel support 0.2m axial extent with a constant loading of 1kN.

Figure 3.13 shows the torsional $T(0,1)$ RC spectra from FEA simulations of a NPS 3 Schedule 40 carbon steel pipe resting on steel supports of 0.1m, 0.15m and 0.2m axial extent with a constant loading of 1kN. It can be seen that in all cases the RC quickly drops to very low values once the frequency increases past 8.4kHz, *i.e.* the cut-off frequency of $T_*(0,1)$. As was mentioned in section 3.2.2, the $T_*(0,1)$ cut-off frequency increases with contact stiffness per unit length. However, because as was discussed in Section 3.2.1 contact stiffness per unit length is virtually independent of support axial extent, it follows that the $T_*(0,1)$ cut-off occurs at virtually the same frequency in all cases. The effect of different support axial extents is therefore limited to changing the maximum amplitude of the echo produced by the support at frequencies below the $T_*(0,1)$ cut-off, with longer supports resulting in higher peaks in the RC spectrum. Note also that the longer the support the sharper the RC drop once frequency is increased past the $T_*(0,1)$ cut-off frequency. This effect is caused by constructive and destructive interactions between reflections from the beginning and the end of the supported region that, when the support is longer than a quarter of the wavelength of the propagating mode, results in peaks and troughs in the RC spectrum. Such interactions are very evident just past 8.4kHz for the longer supports, but are not so evident for the 0.1m support because this support is shorter than a quarter of the wavelength of the propagating mode up to frequencies in excess of 10kHz.

Figure 3.14 shows the torsional $T(0,1)$ RC spectra from FEA simulations of a NPS 3 Schedule 40 carbon steel pipe resting on a steel support of axial extent of 0.2m with constant loadings of 0.5kN, 1.5kN and 2.5kN. It appears that changes in loading, albeit large, have a very limited effect on the RC spectrum. In particular, figure 3.14 shows that the effect of increasing loading is a small shift of the RC spectrum towards higher frequencies, which can be expected since an increased loading on the support results in an increased contact stiffness per unit length, which in turn causes the $T_*(0,1)$ cut-off to shift to higher frequencies as discussed in section 3.2.2.

Figure 3.15 shows the torsional $T(0,1)$ RC spectra from FEA simulations of NPS 3, NPS 6 and NPS 8 Schedule 40 carbon steel pipes resting on a steel support of axial extent of 0.2m with a loading of 1kN. Figure 3.15 indicates that, for a given pipe Schedule, an increase in pipe diameter leads to a progressive reduction of the frequency at which the $T_*(0,1)$ cut-off occurs, together with a progressive reduction of the maximum amplitude of the echo produced by the support. Figure 3.16 shows the torsional $T(0,1)$ RC spectra from FEA simulations of NPS 3 Schedule 10, Schedule 40 and Schedule 80 carbon steel pipes resting on a steel support 0.2m axial extent with a constant loading of 1kN. It can be seen that a progressive increase in pipe wall thickness results in a progressive reduction of the frequency at which the $T_*(0,1)$ cut-off occurs. However, the maximum amplitude of the echo produced by the support remains virtually unaltered. The decrease in cut-off frequency with increasing cross-sectional area occurs because at the torsional cut-off frequency the whole pipe pivots around the contact interface in a manner akin to an inertia attached to a torsional spring. Since in an inertia-spring system the natural frequency increases with the stiffness of the spring and decreases as the inertia increases, an increase in the inertia of the system, brought about by increase in the cross-sectional area of the pipe, not accompanied by any significant increases in the stiffness of the contact interface results in a reduction in the frequency at which the $T_*(0,1)$ cut-off, or resonance, occurs.

3.4 Experimental Validation

Laboratory experiments have been performed to validate the torsional $T(0,1)$ Reflection Coefficient (RC) spectra from FEA simulations presented in section 3.3. The experimental setup, a diagram of which is shown in figure 3.17, consists of a 6m long NPS 3 Schedule 40 carbon steel pipe resting on wooden supports. A deployable Guided Ultrasonics Ltd. [54] ring sensor capable of operating in the frequency range between 8kHz and 25kHz was positioned at one end of the pipe and utilised both to excite the $T(0,1)$ mode and to detect and record any echo propagating along the pipe. The ring sensor was driven by a Guided Ultrasonics Ltd. WaveMaker® G3 [54] integrated signal generator and receiver.

The steel simple support was simulated utilising a steel plate. An hydraulic cylinder reacting against a wooden support resting on the opposite side of the pipe with respect to the steel plate, as shown in figure 3.17, forces the pipe and the steel plate against each other, thus simulating support loading. A load cell was located between the hydraulic cylinder and the steel plate to precisely measure support loading. With this setup it was therefore possible to vary support loading by varying the hydraulic pressure in the cylinder, and to vary support axial extent by utilising steel plates of different sizes. Note that within the frequency range of the transducer ring the wooden supports produce negligible reflections, as the associated contact stiffness per unit length is very low and thus the $T_*(0,1)$ cut-off occurs at very low frequencies. At 8kHz, $T_*(0,1)$ in a wooden supported NPS 3 Schedule 40 pipe already is virtually identical to $T(0,1)$.

To obtain torsional $T(0,1)$ RC spectra, an initial measurement was taken with no hydraulic pressure in the cylinder and no contact between the steel plate and the pipe. Assuming attenuation to be very limited, the echo from the end of the pipe recorded during this initial

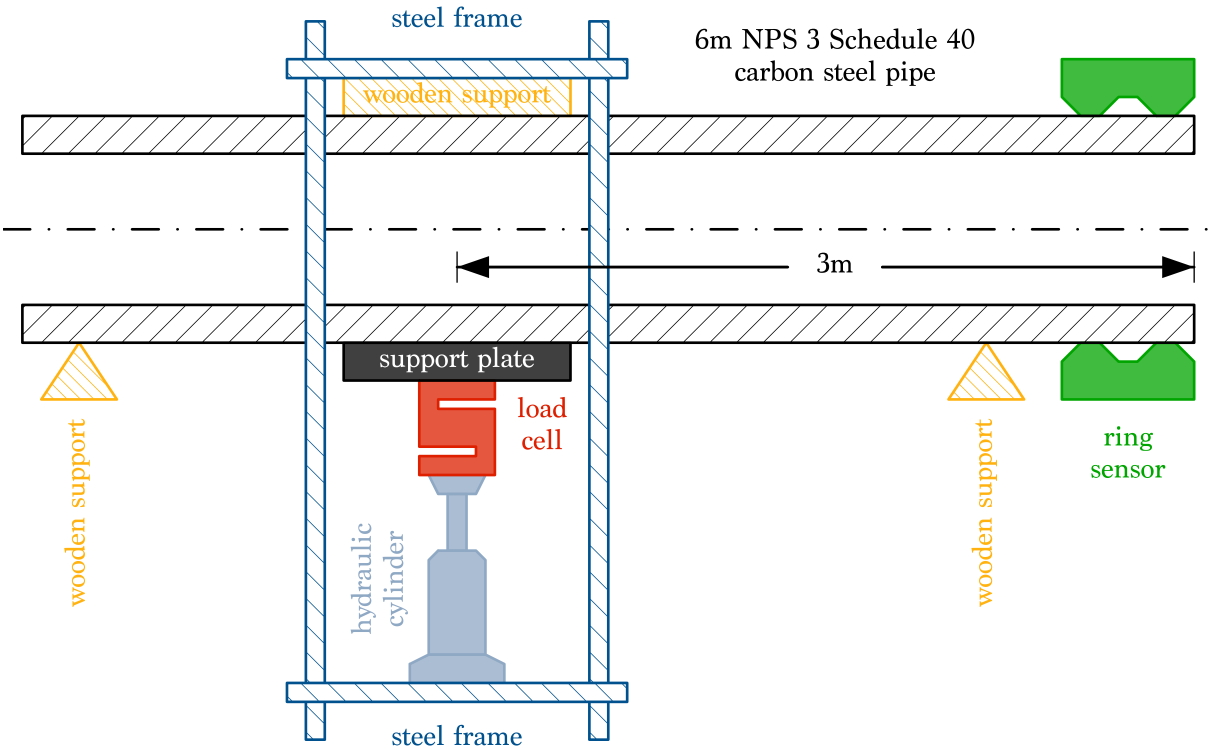

Figure 3.17: Diagram of the experimental setup (not to scale).

measurement was utilised as the reference incident signal to compute the torsional T$(0,1)$ RC spectra for the support. A set of support echo measurements was then taken utilising a given plate and increasing support loading, after which a further measurement with no hydraulic pressure in the cylinder and no contact between the steel plate and the pipe was taken to ensure that the echo from the end of the pipe, and thus the performance of the instrumentation, remained virtually unaltered throughout the experimental run.

Figure 3.18 presents a comparison between the torsional T$(0,1)$ RC spectra from experiments and from FEA simulations for a NPS 3 Schedule 40 carbon steel pipe resting on a steel support of axial extent of 0.1 m with different loadings. It can be seen that both numerical and experimental RC spectra present a clear decreasing trend once frequency is increased past the T$_*(0,1)$ cut-off frequency of 8.4kHz, with large RC values at frequencies below 10kHz and very small RC values once the frequency reaches 25kHz. The experimental results show a minor fluctuating behaviour not present in the numerical predictions, probably caused by minor imbalances in the coupling of the transducers that compose the two circular rows in the ring sensor. It is also clear from figure 3.18 that changes in support loading result in limited changes in the RC spectrum. However, at lower frequencies the RC increases more with load in the experiments than in the FEA simulations, probably as a result of some bedding-in of the pipe on the support since the real contacting surfaces are not perfectly smooth as assumed in the FEA model. Similarly, figure 3.19 presents a comparison between the torsional $T(0,1)$ RC spectra from experiments and from FEA simulations for a NPS 3, Schedule 40 carbon steel pipe resting on a steel support of axial extent of 0.2 m with different loadings. As in figure 3.18, there is good agreement between data from experiments and from FEA simulation, with a clear decreasing trend in the RC spectra once the frequency is increased past 8.4kHz, the $T_*(0,1)$ cut-off frequency. Note that the longer support tends to produce a sharper drop in the value of the RC once frequency is increased past the $T_*(0,1)$ cut-off frequency. As previously discussed in section 3.3, this effect originates from constructive and destructive interactions between reflections from the beginning and the end of the supported region which are only evident once the support length becomes a significant fraction of the wavelength of the propagating mode.

3.5 Conclusions

In this chapter a quantitative study of the interactions between guided waves propagating along a pipe and simple supports has been performed, with selected FEA simulations validated through experiments. The study reveals that, independently of pipe size, all modes that can propagate along a supported section of pipe, including torsional, present a non-zero cut-off frequency. Furthermore, it has been observed that because a supported section of pipe is not an axisymmetric waveguide, all flexural modes that can propagate along it behave differently depending on their orientation.

It has also been shown both experimentally and through FEA simulations that the $T(0,1)$ echo from a simple support quickly reduces to very low values once the frequency is increased past the torsional motion cut-off, independently of pipe size, support configuration and support loading. In particular, it was shown that variations in support loading have a very limited effect on the amplitude of the $T(0,1)$ echo from a simple support.

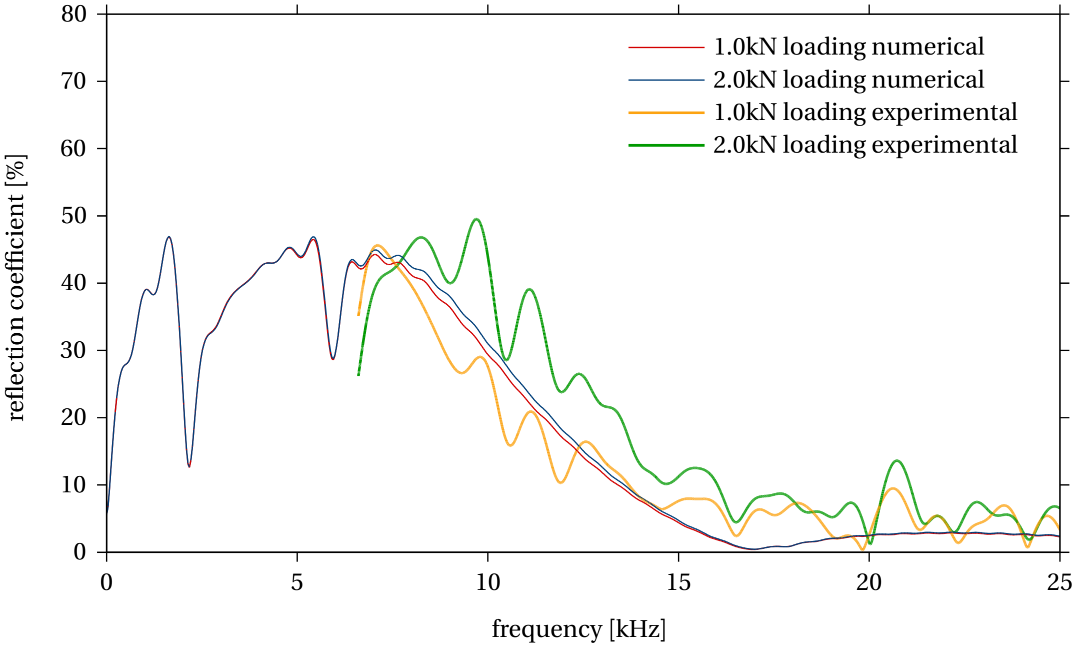

Figure 3.18: Torsional T(0,1) Reflection Coefficient (RC) spectra from experiments and Finite-Element Analysis (FEA) simulations of a NPS 3 Schedule 40 carbon steel pipe resting on a steel support of 0.1m axial extent with constant loadings of 1kN and 2kN.

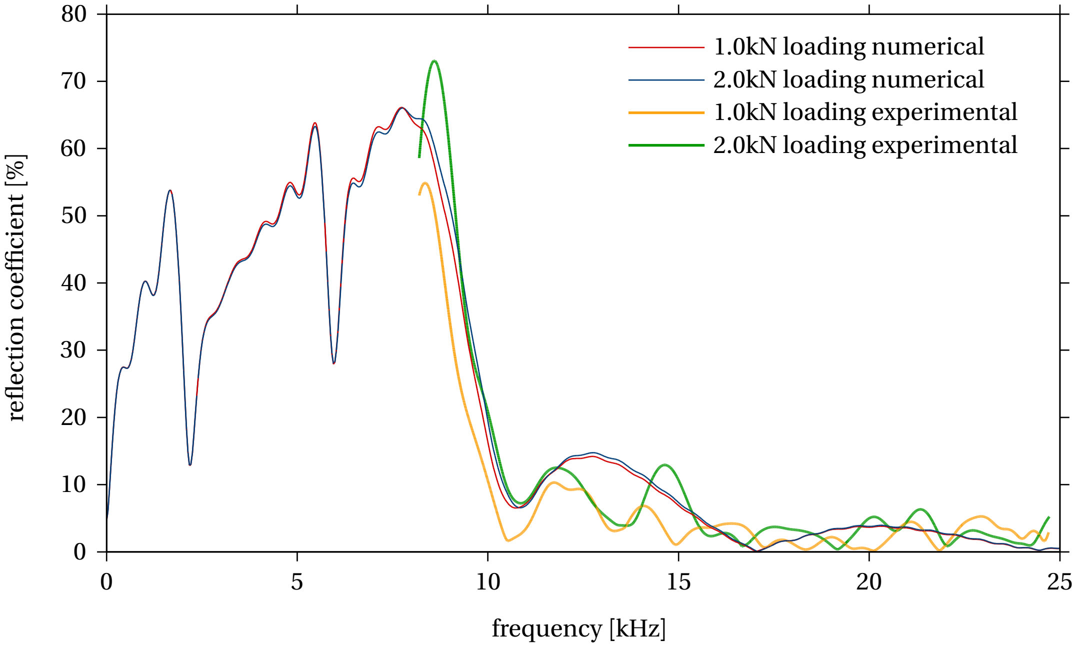

Figure 3.19: Torsional T(0,1) Reflection Coefficient (RC) spectra from experiments and Finite-Element Analysis (FEA) simulations of a NPS 3 Schedule 40 carbon steel pipe resting on a steel support of 0.2m axial extent with constant loadings of 1kN and 2kN.

Chapter 4

Pipeline Health Monitoring

Structural Health Monitoring (SHM) of a petrochemical pipeline consists in implementing a strategy to detect and diagnose any damage that may impair the ability of that pipeline to safely transport pressurised petrochemical products.

In its most general definition, **damage** is a change in the properties of a system, whether geometrical, physical or other, that adversely affects its current and future performance and safety. Conversely, **defects** or **flaws** are imperfections that all manufactured materials contain at micro-structural level. Therefore, a system will operate at its optimum even if its constituent materials contain defects, but its performance will deteriorate and it will become less safe to operate if it suffers damage [1, 2].

Damage can occur with different mechanisms. For example, under suitable loading or shock-loading conditions, defects in the constituent material of a component could grow and coalesce to cause damage to the component and consequently to the whole system. In the case of pipelines the primary form of damage is corrosion, which can be external or internal and consists in a gradual, complex-shaped loss of wall thickness caused by various chemical reactions between the constituent material of the pipe wall and the outside environment or the transported petrochemical products [96–101]. External corrosion essentially consists in rusting induced by the exposure of the pipe wall to water or wet materials, *e.g.* wet insulation cladding, in oxygenated atmospheres. Conversely, internal corrosion can occur in various forms depending on the type of petrochemical product being transported. The most frequent form of internal corrosion is “sweet” CO_2 corrosion of carbon and low-alloy steels, but as oilfields deplete “sour” H_2S corrosion is becoming increasingly common [98]. Most internal corrosion, particularly in the case of “sour” H_2S corrosion, occurs in the form of localised attacks involving pitting, pit clusters, mesa corrosion, crevice corrosion and stress-corrosion cracking [99] concentrated in small areas while the surrounding pipe wall remains essentially corrosion-free [101]. There also exist forms of pipeline damage other than corrosion such as stress-induced cracking following ground movements and internal erosion caused by fast-flowing, particle-rich petrochemical products.

Damage does not necessarily imply a complete loss of system functionality or safety. Most engineering systems are damage tolerant and can withstand a certain amount of damage while maintaining a safe and satisfactory performance. However, as damage keeps growing its increasing effect will at some point render system operation no longer possible or acceptable, and ultimately resulting in **failure** [1, 2]. In this context **critical damage** refers to the most damage a system can withstand before failure occurs. Specifically, petrochemical pipelines can often function at or very near their optimum even after sustaining considerable damage, and there rarely are significant performance deteriorations to signal the presence of critical damage and the consequent possibility of imminent failure. Therefore, as damage grows pipelines can maintain design performance but will become increasingly unsafe to operate. It is therefore of fundamental importance to detect, diagnose and monitor damage growth as early as possible to predict the remaining operational life of a pipeline and to minimise the risk of unexpected failures, which in the case of petrochemical pipelines can have severe consequences and may result in environmental damage, economic losses and personnel injuries. The process of predicting the remaining operational life of a system given some assessment of its current structural health and some prediction of its anticipated future operational conditions is referred to as **prognosis** [1, 2].

Conventionally, the integrity of petrochemical pipelines is assessed periodically at regular intervals. For example, a pipeline is inspected at certain locations and with a certain frequency depending on various considerations, which are often formalised in a Risk-Based Inspection and Maintenance (RBIM) strategy [3] and which may include known or assumed structural integrity conditions, typical damage mode and growth rate, severity of consequences in case of failure, cost of inspection, personnel availability, as well as many others. This approach inherently limits the amount of information available about the structural health of a pipeline, as any damage which develops in unexpected circumstances or while the pipeline is not being inspected may remain undetected. Furthermore, any change in the petrochemical production process, perhaps following opportunity oil, as well as variabilities in the quality of the manufactured components and of the welding and assembly processes can increase the likelihood of unexpected damage occurrences. Such lack of information hinders the reliability of any prognosis and of RBIM strategies, increases the risk of unexpected critical damage development and pipeline failure, and forces the use of the costly time-based maintenance, which prescribes the partial or complete replacement of pipework at set points in time irrespective of their actual remaining operational life, following the safe-life design approach.

In contrast, if one were to have sufficient information about the structural health of a pipeline to produce a reliable prognosis, then one could in principle utilise the cost-efficient condition-based maintenance, which prescribes the partial or complete replacement of pipework only when it is about to suffer critical damage and has therefore reached the actual end of its operational life.

Through early detection, diagnosis and monitoring of damage growth, SHM can lead to the formulation of reliable prognoses and to the reduction of the risk of unexpected failures, ultimately enabling the shift from time-based maintenance to the more cost-efficient condition-based maintenance [1]. Specifically SHM seeks to:

1. **Detect** the development and growth of damage.
2. **Locate** the system region or component where damage has developed.
3. **Diagnose** the type and severity of damage and potentially its growth rate.
4. **Monitor** the damage growth rate.

To detect, locate and diagnose and monitor damage SHM relies on a network of permanently installed sensors that monitor one or more damage-sensitive properties of a system over time without impairing system functionality. The principal advantages of SHM and condition-based maintenance from the petrochemical industry standpoint are:

- **Operational.** No components will be taken out of service unless absolutely necessary, and since it becomes very unlikely for critical damage to grow undetected the overall safety and reliability of the pipeline network is increased. Furthermore, reliable prognoses imply that maintenance interventions can be appropriately planned in advance and synchronised to minimise pipeline down-time.
- **Economic.** Minimised pipeline down-time boots production, revenue and profit. Furthermore, time-based integrity assessment and maintenance become superfluous, resulting in significant savings especially because it becomes no longer necessary to routinely service pipelines that may be buried, underwater, in deserts, or in other harsh environments, and that can prove extremely costly and problematic to access.

SHM and condition-based maintenance therefore promise to make pipeline networks safer and more reliable while at the same time more productive and less costly.

In this chapter, section 4.1 introduces permanently installed guided wave sensors, such as the Guided Wave Permanently-Installed Monitoring System (gPIMS®) sensors produced and commercialised by Guided Ultrasonics Ltd. [20], and explains how they can be utilised to monitor the structural integrity of petrochemical pipelines and how baseline subtraction can be implemented utilising the signals recorded by them. Successively, section 4.2 introduces and explains the fundamental problem of damage detection, while section 4.3 explains the challenge that changes in Environmental and Operational Conditions (EOC) represent to effective damage detection and ultimately effective SHM, thereby motivating the need to utilise advanced techniques to synthetically compensate for EOC variations. Section 4.4 lays the formal mathematical foundations for the analysis of the effects that pipeline operating temperature variations have on the signals recorded by permanently installed guided wave sensors, on the basis of which firstly it introduces a novel technique to synthetically compensate for EOC effects in the residual signals obtained by baseline subtraction, and secondly it thoroughly analyses the side-effects that baseline subtraction compensation techniques, and in particular Baseline Signal Stretch (BSS) and Localised Baseline Signal Stretch (LBSS), might have in practical situations. Finally, section 4.5 summarises why uncompensated EOC effects will invariably feature in the measurements from any SHM sensor, and illustrates what challenge this represents for effective SHM.

4.1 Permanently Installed Guided Wave Sensors

As discussed in chapter 2, and in particular in section 2.2, guided waves enable the fully-volumetric inspection of several metres of pipe from a single sensor location, and consequently represent a very advantageous option for SHM applications since damage growth over the entire volume of a pipeline could be monitored with a practical number of sensors. However, guided wave inspection suffers from several limitations.

From a practical point of view, it may still prove very difficult, expensive or downright unfeasible to routinely access even a small section of a pipeline that needs to be inspected. For example, the cost of obtaining access to sections of a buried or submerged pipeline can be far higher than the cost of the inspection or even of the inspection equipment.

Moreover, from a purely technical standpoint, guided wave inspection suffers from poor

Figure 4.1: Example of a Guided Ultrasonics Ltd. gPIMS® sensor [20] installed on a pipeline.

damage sizing and characterisation capabilities. Specifically, the damage sensitivity of guided wave inspection is in general relatively low because in feature-free pipeline sections damage echoes can be masked by coherent noise, while near features, such as welds and supports, damage echoes can be masked by the often large feature echo. Damage sensitivity can be particularly low for intricate pipe networks, such as those found in petrochemical plants, because the relatively high feature density results in many overlapping feature echoes that can mask even large damage echoes.

Permanently-installed guided wave sensors, such as the Guided Wave Permanently-Installed Monitoring System (gPIMS®) sensor shown in figure 4.1 produced and commercialised by Guided Ultrasonics Ltd. [20], are guided wave sensors specifically designed to overcome accessibility issues and enhance damage sensitivity.

Similarly to deployable guided wave sensors, permanently installed guided wave sensors transmit guided wave packets along a pipe and listen for echoes that originate from pipe features, such as welds and supports, as well as from damage. Therefore the damage-sensitive system property monitored by permanently installed guided wave sensors is the response to a guided wave excitation of each discontinuity in the monitored waveguide, *i.e.* in the pipeline. Were damage to grow then either a response from a new discontinuity will appear or the response from an existing discontinuity will change.

Being remotely operated, permanently installed guided wave sensors require access to the pipeline that needs to be inspected only once at installation, and therefore they dramatically reduce the cost of routine guided wave inspection compared to deployable sensors. Moreover, inspections performed with permanently installed sensors are highly repeatable because the position of the transducers on the outside of the pipe wall is fixed, and therefore the damage sensitivity compared to standard guided wave sensors can be enhances through baseline subtraction.

In principle, in the absence of damage growth the echoes from all features and pre-existing damage should remain constant across repeat inspections, and so should coherent noise since it is deterministic rather than stochastic. Suppose an initial inspection is performed when the pipeline is in a known health condition, whether undamaged or partially damaged, and the signal recorded during the inspection is stored. If the initial signal is then subtracted from a signal recorded during a successive repeat inspection, then the echoes from all features and pre-existing damage should cancel out and so should coherent noise. Therefore, the signal after subtraction should only include echoes from damage that has developed in the pipeline since the initial inspection was performed. This process is known as **baseline subtraction** [2, 102, 103]. The initial signal is known as the **baseline signal** while the signal resulting from subtraction is known as the **residual signal**. By utilising baseline subtraction, it becomes therefore possible to enhance damage sensitivity and detect the presence of damage whose echo would normally be masked by coherent noise or by large feature echoes.

In conclusion, by detecting and monitoring changes over time in the residual signal from permanently installed guided wave sensors it should in principle be possible to detect and monitor damage growth in pipelines with enhanced sensitivity to damage and in a cost-effective manner. However, there remain in practice many challenges associated with damage detection and with baseline subtraction.

4.2 Damage Detection

Damage detection, and thence the core part of SHM, consists in the detection of some change in one or more damage-sensitive properties of a system over time. The **damage detection** problem is therefore a **change detection** problem that requires the comparison between two system states before and after the occurrence of change. The state of the system before the change is commonly referred to as **baseline**, and any property sample collected while the system is in its baseline state is called a **baseline sample**. Note that in its baseline state the system may be undamaged or may present some pre-existing damage. It must be stressed that each gathered property sample y will be corrupted by some random noise ϵ with probability density function $p(\epsilon)$. If μ represents the true underlying value of a damage-sensitive property when its sample y was gathered, then y can be expressed as

$$y = \mu + \epsilon \tag{4.1}$$

Because the noise ϵ is a random variable, and μ is a deterministic if unknown variable, it follows that the damage-sensitive property y will also be a random variable with probability density function $p\left(y\right) = p\left(\mu + \epsilon\right)$. Therefore, changes in a damage-sensitive property of a system will be reflected by changes in the probability density function $p\left(y\right)$ of the gathered property samples y. Assume that before an unknown change time t_c the probability density function of y is given by $p_0\left(y\right)$, and that after t_c the probability density function of y is given by $p_1\left(y\right)$. A change detection algorithm is a procedure to detect the onset of change in the probability density function of y and to estimate t_c. Formally, there are two possible change detection problems:

- **Simple Change Detection.** The first and simplest scenario is based on the principle of **simple hypothesis testing** and assumes that both the baseline probability density function $p_0\left(y\right)$ and the damaged probability density function $p_1\left(y\right)$ are known. The task therefore consists solely in estimating t_c.

- **Composite Change Detection.** The second, more complex scenario is based on the principle of **composite hypothesis testing** and assumes that the baseline probability density function $p_0\left(y\right)$ is known and that the damaged probability density function $p_1\left(y\right) = p\left(y \mid \theta_1\right)$ is a differently parameterised version of the baseline probability density function $p_0\left(y\right) = p\left(y \mid \theta_0\right)$. The task therefore consists in estimating t_c and the parameter change $\nu = \theta_1 - \theta_0$. Note that such assumption is generally trivial since the probability density function of the noise ϵ is almost invariably assumed to be in-

> dependent of the true underlying value μ of the damage-sensitive property and consequently independent of the occurrence of the change. Therefore, before the change one has $p_0\left(y\right) = \mu_0 + p\left(\epsilon\right)$ while after the change one has $p_1\left(y\right) = \mu_1 + p\left(\epsilon\right)$, and it follows that the probability density function of y is identical before and after the change up to the change in the mean $\nu = \mu_1 - \mu_0$ of the true underlying value μ of the damage-sensitive property that one intends to detect.

Chapter 5 will thoroughly discuss change detection and will introduce the Cumulative Sum (CUSUM) algorithm for the solution of simple change detection problems and Generalised Likelihood Ratio (GLR) algorithm for the solution of composite change detection problems. It will be shown that these algorithms can optimally solve change detection problems so that the required number of samples of y is minimised, the probability of detecting a change is maximised and the probability of false-calling a change is minimised.

Besides detecting the occurrence of change, the biggest damage detection challenge consists in establishing the value of the damage-sensitive properties while a system is in its baseline state. There are two main approaches for modelling the baseline state of a system [2].

If a high-fidelity model of the damage-sensitive properties of a system while it remains in its baseline state can be precisely computed in advance, then the damage detection problem is a composite change detection problem that seeks to determine whether a newly gathered property sample is consistent or not with the model. In one case the system is still in its baseline state, while in the other case damage has grown. Collected samples are also typically utilised to actively update the model. After an initial baseline sample is gathered to finely tune the model to a specific system, any further collected sample deemed to be representative of damage growth can be fed to the model to locate the damage, diagnose it and formulate a prognosis, as well as to update the model to a new baseline state. This approach has been utilised extensively and successfully, perhaps most notably in the case of the finite element updating methodology [2, 104–107].

Conversely, if a high-fidelity model of the damage-sensitive properties of a system while it remains in its baseline state cannot be precisely computed in advance, as in the case of the signal from a permanently installed guided wave sensor monitoring a petrochemical pipeline, then damage detection will have to be based on some form of **machine learning** [108, 109]. Machine learning is concerned with constructing, *i.e.* learning, computational relationships between variables given an observed set of noisy samples known as the **learning set**. These computational relationships should model the underlying mechanism that generated the samples, and once constructed they can be utilised to predict the probability density function of samples that may or may not belong to the learning set. Machine learning for damage detection problems can be fundamentally divided into unsupervised and supervised learning.

Supervised learning is applied when there is availability of samples of the damage-sensitive properties of a system in its undamaged and damaged states. In this case, a supervised learning algorithm is utilised to create a statistical model of the system in all its states, and the damage detection problem then becomes a simple change detection problem seeking to determine whether a newly gathered sample of the damage-sensitive properties of a system is consistent with any of the undamaged or damaged states. A typical example of the utilisation of supervised learning is in the detection of damage in rotating machinery [2], in which case algorithms can rely on large databases of vibration data compiled by running nominally identical pieces of machinery to some threshold damage condition or to failure. By utilising a supervised learning algorithm to compare the vibrations of a monitored piece of operational machinery to those contained in a database, it becomes possible to detect damage growth, diagnose it and produce a prognosis.

Conversely, unsupervised learning is applied when there is availability only of samples of the damage-sensitive properties of a system while it is in its baseline state. These baseline samples are utilised to derive a statistical model of the damage-sensitive properties while the system is in its baseline state, and the model is then utilised to predict the likely future evolution of the damage-sensitive properties were the system to remain in its baseline state. The damage detection problem therefore becomes a composite change detection problem which seeks to determine whether a newly gathered properties sample is consistent or not with the obtained statistical model. In one case the system is still in its baseline state, while in the other case damage has grown. Damage detection based on unsupervised learning can typically only detect and locate the growth of damage, but cannot in general formulate a diagnosis or a prognosis. However, if information exists about the changes in the measured damage-sensitive properties that a particular damage mode is typically likely to produce, then in principle it could be possible to diagnose the damage and formulate a prognosis by comparing the difference between the newly gathered properties sample and the statistical model to the change in damage-sensitive properties that a particular damage configuration would have likely produced had it occurred.

It is worth noting that there exists a number of approaches that claim to be baseline-less and not to require baseline samples or a comparison between two system states to ascertain the growth of damage. However, upon close analysis it can be concluded that these claims are based on a terminology misunderstanding [2]. For example, strain energy methods [110] rely on the assumption that the monitored structure in its baseline, undamaged state behaves as an Euler-Bernoulli beam, while time-reversal acoustics [111] assumes that when it is in its baseline, undamaged state the monitored structure is an ideal linear elastic solid exhibiting the time-reversal property, even though this assumption may not be experimentally verifiable [2]. Similarly, other non-linear acoustic approaches [112–114] also assume that the monitored structure behaves like an ideal linear elastic solids unless damage grows. One of the major issues with approaches that rely on very specific assumptions to model a system's undamaged state is that they can only be utilised to detect a change in the system state from undamaged to damaged but cannot be utilised to monitor damage growth, since their underlying assumptions often break down when the system is partly but not yet critically damaged.

In principle, a true **baseline-less** approach would be one capable of distinguishing between different system states without any information about the composition of the sample set under analysis except that the samples have been gathered in a given temporal sequence. Therefore, up to some statistical confidence and subject to a minimum damage size that is of interest to detect, a true baseline-less approach should be capable of partitioning the sample set into two or possibly more subsets representative of the baseline condition and of the various stages of damage growth and development.

Importantly, the effectiveness of damage detection, and therefore of the core part of SHM, can be hindered by changes in Environmental and Operational Conditions (EOC). As discussed, damage detection consists in the detection of some change in the damage-sensitive system properties over time, and is therefore a change detection problem that requires comparison between two system states before and after the occurrence of change, *i.e.* of damage growth. However, if the measured damage-sensitive system properties were to change not just following damage growth but also following EOC variations, then damage growth and changes in EOC could be mistaken for each other. The effects of EOC variations on the measured damage-sensitive system properties represent arguably the major issue hindering practical large-scale SHM deployment [1, 2, 102, 115].

4.3 Environmental and Operating Conditions Effects

The sensors that SHM relies upon do not directly measure damage growth, but rather measure a set of damage-sensitive system properties from which the growth of damage can be inferred, in a similar way to which one measures the strain on a beam to infer its stress level. In the case of pipelines, the damage-sensitive system property that permanently installed guided wave sensors measure is the response to a guided wave excitation of each discontinuity in the waveguide under consideration, *i.e.* in the pipeline. Were damage to grow then either a response from a new discontinuity will appear or the response from an existing discontinuity will change.

More specifically, if one utilises a strain gauge to measure strain, then one is actually measuring the change in resistivity of the strain gauge wire from which, by knowing the strain gauge geometry, strain and ultimately stress can be inferred. Similarly, with a permanently installed guided wave sensor one transmits an incident guided wave packet by applying a voltage difference to several piezo-electric transducers in contact with the outside of the pipeline, and detects echoes from discontinuities by measuring the voltage difference produced by the same piezo-electric transducers when the echoes travel underneath them.

To infer stress from a strain measurement utilising, for example, Hooke's law one must know the material's modulus of elasticity and the performance of the strain gauge at the particular temperature the material is at while the strain measurement is being taken. If the temperature changes, then one must appropriately correct for changes in the modulus of elasticity and in the performance of the strain gauge to infer the true value of stress and therefore be able to detect any actual change in it. In the case of stress measurements it is quite easy to compensate for changes in Environmental and Operational Conditions (EOC) such as temperature variations because it is well known how resistivity and modulus of elasticity change with temperature.

Conversely, in the case of permanently installed guided wave sensors even a simple change in the operating temperature of the monitored pipeline can have profound, complex and often unpredictable effects on the measured discontinuity responses. In general discontinuity responses will change over time as a function of many EOC variations and primarily of changes in the operating temperature of the monitored pipeline. In the context of SHM, EOC refer to the conditions the monitored system is operating at and in when its damage-sensitive properties are measured, while EOC effects refer to the influence EOC variations have on the damage-sensitive properties. In the case of petrochemical pipelines EOC in-

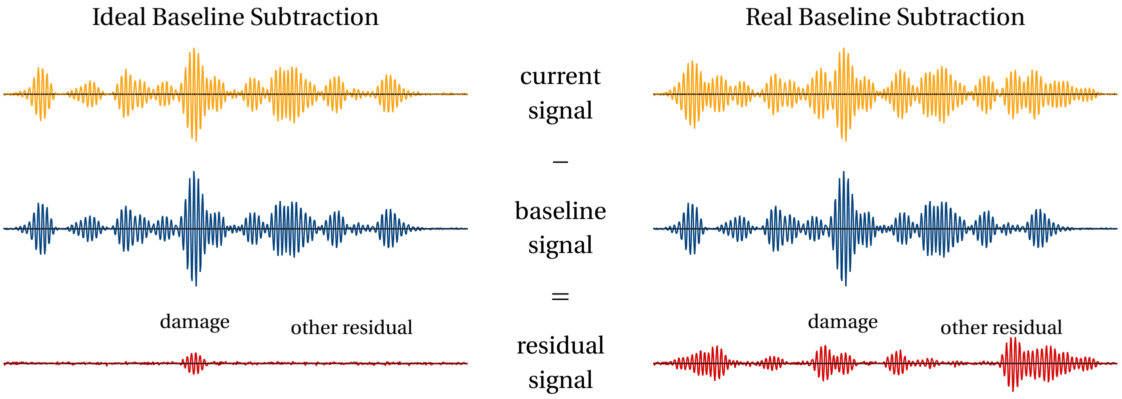

Figure 4.2: Diagram of the baseline subtraction technique: the baseline signal is subtracted from the current signal to obtain the residual signal which ideally only contains information about damage that has developed since the baseline signal was recorded (left); in reality the residual signal also contains information about benign changes (right).

clude parameters such as operating temperature, environmental temperature, type of petrochemical product transported, and many others.

Specifically, in baseline subtraction it is assumed that the baseline component of recorded signals remains stable over time. Equivalently, echoes from features, such as welds and supports, and from pre-existing damage are assumed to remain constant over time unless damage grows, or else the residual signals would contain not just information about damage growth, but also confusing information about benign changes. Unfortunately, as exemplified in figure 4.2 this assumption is false under most circumstances because the baseline component of recorded signals will change over time as a function of many EOC variations and primarily of changes in the operating temperature of the monitored pipeline [2, 102, 103, 115–124].

Variations in operating temperature result primarily in changes to the Lamé constants λ and μ and to the density ρ of the constituent material of the pipeline, leading to thermal expansion and, from equations 2.4 and 2.5, to changes to the velocity of propagation of all stress waves. Operating temperature changes also produce changes in the damping of the constituent material of the pipeline as well as in the viscosity of the contents transported by the pipeline. As a result, guided wave packets will cover different distances at different velocities and will undergo different attenuations between repeat inspections performed at different operating temperatures, and consequently echoes from features and pre-existing damage will not cancel out during subtraction. Furthermore, in the case of coated pipelines, operating temperature variations can significantly modify the mechanical properties of the coating and consequently change the nature of the guided wave modes that can propagate along the pipeline between repeat inspections.

The amplitude and frequency content of feature echoes can also vary as functions of environmental and operating temperatures, as well as of the density of the pipeline contents and therefore of pipeline weight. Typical examples include features such as simple supports and clamps, but also complex features such as vents, drains and welded supports. As discussed in chapter 3, the properties of the contact patch between a simple support or a clamp and the pipeline determine the amplitude and the frequency content of the produced echo. Therefore, changes in contact patch properties following the thermal expansion of both the pipeline, as a result of changes in operating temperature, and the supporting structure, as a result of changes in the temperature of the environment, can lead to significant changes in the echoes from simple supports and clamps. In particular, differential thermal expansion may induce a clamp to tighten or loosen itself around the pipe, thereby changing the shape and stiffness of the contact patch. Importantly, simple supports and clamps act as high-pass filters for incident guided waves with a cut-off frequency dependent on the properties of their contact patch. Consequently, any change in their contact patch properties will induce significant changes in the frequency content of all guided wave packets propagating past them and therefore in the frequency content of all the echoes from features and pre-existing damage located past simple supports and clamps.

Finally, changes in operating temperature can also lead to variations in the behaviour of permanently installed guided wave sensors. Typically, most of the noise in recorded guided wave signals is coherent. Coherent noise is non-random and consistently generated by permanently installed guided wave sensors as a result of minor imbalances in transducer coupling around the pipe circumference and of minor sensor misalignments, and as a result it should cancel out during baseline subtraction assuming the sensor behaviour remains stable over time. However, operating temperature variations can change the behaviour of the piezo-electric transducers as well as the mechanical properties of any of the materials, particularly adhesives, that surround them and act as backing and matching layers, and can induce differential thermal expansion between a sensor and the monitored pipeline, ultimately leading to the operating temperature-dependent behaviour of permanently installed guided wave sensors. Consequently, the generated coherent noise will vary between repeat inspections performed at different temperatures and will no longer cancel out during baseline subtraction. Moreover, transduction efficiency is a function of temperature. Consequently, the amplitude of the transmitted guided wave packet and of the received echoes will change between readings collected at different temperatures, and as a result the echoes from features and pre-existing damage will not cancel out during subtraction.

In summary, permanently installed guided wave sensors just as any other SHM sensor will measure EOC changes, such as operating temperature variations, that can be just as strong a source of change in the damage-sensitive properties of a system, and in the baseline component of recorded signals, as actual damage growth [103]. Consequently, a strategy is required to synthetically compensate for changes in the damage-sensitive properties of a system caused by EOC variations, and in particular to compensate for changes in the baseline component of recorded signals so that the residual signal is solely representative of information on damage growth.

4.4 Baseline Subtraction Compensation

As previously discussed, Environmental and Operational Conditions (EOC) effects, such as those originating from operating temperature variations, can be just as strong a source of change in the baseline component of recorded signals as actual damage growth [103]. It follows that baseline subtraction can only be effective when a strategy exists to synthetically compensate for changes in the baseline component due to EOC variations so that the residual signal only includes information on damage growth.

The primary objective of this section is to lay the formal mathematical foundations for the analysis of the effects that pipeline operating temperature variations have on the signals recorded by permanently installed guided wave sensors, on the basis of which first the novel LBSS technique will be introduced, and secondly the side-effects that baseline subtraction compensation techniques, and in particular BSS and LBSS, might have in practical situations will be thoroughly analysed.

The LBSS technique essentially consists in an extension of the BSS technique previously proposed by many authors [115–117, 119] that enables the synthetic compensation for global and local differences in pipeline operating temperature as well as for variations in the transduction efficiency of permanently installed guided wave sensors. Similarly to BSS, LBSS is utilised as part of a two-stage baseline subtraction compensation procedure [115–117, 119] for which at first the difference in EOC between baseline and current readings, and thus the impact of EOC effects, is minimised utilising Optimal Baseline Selection (OBS), and successively a formulation of the BSS or LBSS technique is utilised to synthetically compensate for any remaining difference in operating temperature. Interestingly, the examples of typical baseline subtraction scenarios presented in this section suggest that the two distinct OBS and BSS or LBSS steps should be integrated to maximise their effect, although a thorough systematic test is still required to obtain definitive proof.

4.4.1 Localised Baseline Signal Stretch

Because the Lamé constants λ and μ and the density ρ of the constituent material of a pipeline are functions of the operating temperature of the pipeline, operating temperature variations lead to thermal expansion and, from equations 2.4 and 2.5, to changes in the velocity of propagation of all waves [125]. Consequently, guided wave packets will cover different distances at different velocities and their arrival time will vary between readings collected at different temperatures. This EOC effect is detrimental for baseline subtraction because the echo from a given feature or pre-existing damage will develop apparent phase differences as the operating temperature of the pipeline varies between readings and therefore will not cancel out during subtraction resulting in large artefact echoes in the residual signal [102].

Localised Baseline Signal Stretch (LBSS) is a novel technique designed to minimise the impact of uniform and non-uniform operating temperature variations on the residual signal. To lay the formal foundations for the LBSS technique, first a mathematical model will be constructed of a general signal recorded by a guided wave sensor and it will be shown how uniform operating temperature variations affect it. Successively, a BSS technique similar to the one already discussed by other authors [115–117, 119] will be introduced to compensate for this EOC variation. The BSS technique will then be generalised for when operating temperature variations are not uniform along a pipeline, obtaining the novel LBSS technique.

Recorded Guided Wave Signals

Consider a signal $u(t)$ recorded by a guided wave sensor. Because $\mathrm{T}(0,1)$ is non-dispersive, and $\mathrm{F}(1,2)$ is virtually non-dispersive within the frequency range typically utilised for guided wave inspection applications, it can be assumed that wave propagation is non-dispersive. Then, without loss of generality $u(t)$ can be expressed as the sum of many filtered echoes of the transmitted wave packet $s(t)$ each with arrival time t_j

$$u(t) = \sum\nolimits_j h_j * s\left(t - t_j\right) \tag{4.2}$$

where convolution between signals $h_j(t)$ and $s(t)$ is defined as

$$h_j * s(t) = \int^{t} s(\tau)\, h(t-\tau)\, \mathrm{d}\tau \tag{4.3}$$

and $h_j(t)$ is the impulse response of the filter of the j^{th} echo which represents the impulse response of the j^{th} pipeline discontinuity as recorded by the guided wave sensor. The function of the filter of the j^{th} echo can be easily understood when transforming the problem to the frequency domain. The spectrum $U(\omega)$ of $u(t)$ is given by

$$U(\omega) = \int_{-\infty}^{\infty} u(t)\, e^{-i\omega t}\, \mathrm{d}t = \int_{-\infty}^{\infty} \left(\sum_j h_j * s\left(t - t_j\right) \right) e^{-i\omega t}\, \mathrm{d}t \tag{4.4}$$

or, because of the sum rule in integration and of the convolution theorem, by

$$U(\omega) = \sum_j e^{-i\omega t_j} \left(\int_{-\infty}^{\infty} s(t)\, e^{-i\omega t}\, \mathrm{d}t \right) \left(\int_{-\infty}^{\infty} h_j(t)\, e^{-i\omega t}\, \mathrm{d}t \right) \tag{4.5}$$

If $S(\omega)$ is the spectrum of the transmitted wave packet $s(t)$, then

$$U(\omega) = \sum_j e^{-i\omega t_j} S(\omega) H_j(\omega) = S(\omega) \sum_j e^{-i\omega t_j} H_j(\omega) \tag{4.6}$$

where the frequency response $H_j(\omega)$ of the filter of the j^{th} echo represents the frequency response of the j^{th} pipeline discontinuity as recorded by the guided wave sensor.

Importantly, the frequency response $H_j(\omega)$ of the j^{th} pipeline discontinuity that the guided wave sensor records is not equal to its Reflection Coefficient (RC). Suppose a guided wave sensor transmits a wave packet $S(\omega)$ along a pipeline, and suppose $R_1(\omega)$ and $T_1(\omega)$ are respectively the Reflection Coefficient (RC) and the Transmission Coefficient (TC) of the first discontinuity encountered by the wave packet $S(\omega)$ as it propagates from the guided wave sensor along the pipe. Ignoring material damping, the discontinuity will reflect back to the guided wave sensor a wave packet $S(\omega) R_1(\omega)$ and will transmit past itself a wave packet $S(\omega)\, T_1(\omega)$. Therefore the frequency response $H_1(\omega)$ of the first discontinuity will be equal to its RC $R_1(\omega)$. However, for the second discontinuity the incident wave packet will no longer be the wave packet $S(\omega)$ transmitted by the guided wave sensor, but will be the wave packet $S(\omega)\, T_1(\omega)$ transmitted by the first discontinuity. The second discontinuity will therefore reflect toward the guided wave sensor a wave packet $S(\omega)\, T_1(\omega) R_2(\omega)$ and will transmit past itself a wave packet $S(\omega)\, T_1(\omega)\, T_2(\omega)$. As it propagates along the pipe from the second discontinuity toward the guided wave sensor, the reflected wave packet $S(\omega)\, T_1(\omega) R_2(\omega)$ will encounter the first discontinuity once again. The first discontinuity will transmit past itself toward the guided wave sensor a wave packet $S(\omega) (T_1(\omega))^2 R_2(\omega)$ and will reflect toward the second discontinuity a wave packet $S(\omega)\,T_1(\omega)\,R_1(\omega)\,R_2(\omega)$ which eventually will also interact with the second discontinuity. Ignoring material damping, it can be easily verified that because of the described reflection pattern the frequency response of the second discontinuity will be given by

$$\begin{aligned} H_2(\omega) = {} & S(\omega)(T_1(\omega))^2 R_2(\omega) + S(\omega)(T_1(\omega))^2 R_1(\omega)(R_2(\omega))^2 \\ & + S(\omega)(T_1(\omega))^2 (R_1(\omega))^2 (R_2(\omega))^3 + \ldots \end{aligned} \tag{4.7}$$

which is clearly different from the RC $R_2(\omega)$ of the second discontinuity. In reality, because of material attenuation the frequency response $H_1(\omega)$ of even the first discontinuity will be different from its RC $R_1(\omega)$, and will in general be equal to $A(\omega, 2d_1)\,R_1(\omega)$. The attenuation $A(\omega, d)$ experienced by a propagating guided wave packet is a function of the guided wave mode it is composed of, the frequency content it has, and the distance d it covers, which in the case of the first discontinuity is equal to twice the distance d_1 between the guided wave sensor and the discontinuity itself. Accounting for material damping, and therefore for guided wave attenuation, the frequency response of the second discontinuity will be given by

$$\begin{aligned} H_2(\omega) = {} & A(\omega, 2d_2)S(\omega)(T_1(\omega))^2 R_2(\omega) \\ & + A(\omega, 2d_2 + 2(d_2 - d_1))S(\omega)(T_1(\omega))^2 R_1(\omega)(R_2(\omega))^2 + \ldots \end{aligned} \tag{4.8}$$

In practice because of material attenuation and since for most realistic pipeline discontinuities $\left|R_j(\omega)\right| \le 0.2$ for any frequency ω, most terms in equation 4.8 have negligible amplitude and can be ignored, and so to a first approximation the frequency response of the second discontinuity will be given by

$$H_2(\omega) \approx A(\omega, 2d_2)S(\omega)(T_1(\omega))^2 R_2(\omega) \tag{4.9}$$

It can then be easily verified that in general the frequency response $H_j(\omega)$ of the j^{th} pipeline discontinuity will to a first approximation be given by

$$H_j(\omega) \approx A\left(\omega, 2d_j\right) S(\omega) \prod_{i=0}^{j-1} (T_i(\omega))^2 R_j(\omega), \quad T_0(\omega) = 1 \tag{4.10}$$

which clearly shows the relationship between the frequency response $H_j(\omega)$ of the j^{th} pipeline discontinuity as recorded by the guided wave sensor and its Reflection Coefficient (RC) $R_j(\omega)$.

Uniform Operating Temperature Variations

To understand the effect of uniform variations in operating temperature, consider a permanently installed guided wave sensor that records the baseline signal

$$u_b(t) = \sum_j h_j^b * s\left(t - t_j\right), \quad U_b(\omega) = S(\omega) \sum_j e^{-i\omega t_j} H_j^b(\omega) \tag{4.11}$$

After a uniform operating temperature variation δT the pipeline will expand or contract by a factor $1 + \alpha\delta T$, where α is the coefficient of thermal expansion of the material, while the wave propagation propagation velocity v will change by δv. Therefore following a uniform operating temperature variation the arrival time of the j^{th} echo will change by a factor γ [102]

$$t_j \to t_j\gamma, \quad \gamma = 1 + \alpha\delta T - \delta v/v \tag{4.12}$$

Furthermore, pipeline discontinuity impulse responses h_j^b are temperature dependent, if only because as previously discussed they are a function of material damping which is notoriously temperature dependent. It follows that after a uniform operating temperature variation impulse responses will change from h_j^b to h_j^c. Therefore the current signal $u_c(t)$ recorded by the permanently installed guided wave sensor after a uniform operating temperature variation will be

$$u_c(t) = \sum_j h_j^c * s\left(t - t_j\gamma\right), \quad U_c(\omega) = S(\omega) \sum_j e^{-i\omega t_j\gamma} H_j^c(\omega) \tag{4.13}$$

Consequently, the residual signal will be

$$r(t) = u_c(t) - u_b(t) = \sum_j \left(h_j^c * s\left(t - t_j\gamma\right) - h_j^b * s\left(t - t_j\right)\right) \tag{4.14}$$

and the residual spectrum will be

$$R(\omega) = U_c(\omega) - U_b(\omega) = S(\omega) \sum_j \left(e^{-i\omega t_j\gamma} H_j^c(\omega) - e^{-i\omega t_j} H_j^b(\omega)\right) \tag{4.15}$$

Clearly, the residual spectrum can nullify if and only if

$$\sum_j \left(e^{-i\omega t_j\gamma} H_j^c(\omega) - e^{-i\omega t_j} H_j^b(\omega)\right) \tag{4.16}$$

nullifies, and therefore if and only if

$$e^{-i\omega t_j\gamma} H_j^c(\omega) = e^{-i\omega t_j} H_j^b(\omega), \quad \forall\, j \tag{4.17}$$

It is trivial to verify that this condition will only be satisfied when no uniform operating temperature variation occurs, in which case $\gamma = 1$ and $H_j^c(\omega) = H_j^b(\omega)$.

Therefore, it can be seen how as a result of a uniform operating temperature variation the residual signal will display artefact echoes because the echoes from pipeline features and pre-existing damage will not cancel out during baseline subtraction.

Baseline Signal Stretch

It is of interest to suppress the artefact echoes in the residual signal. Equivalently, it is of interest to compensate for variations in echo arrival time and therefore for uniform variations in operating temperature between the baseline and current signals.

If the frequency responses $H_j^b(\omega)$ and $H_j^c(\omega)$ of all pipeline features and pre-existing damage before and after a uniform operating temperature variation were known in advance, then by definition it would become possible to exactly compensate for any uniform operating temperature difference between the baseline and current signals by predicting in advance the baseline signal at any uniform operating temperature, thereby completely removing artefact echoes from the residual signal. However, the frequency responses $H_j^b(\omega)$ and $H_j^c(\omega)$ of all pipeline features and pre-existing damage before and after a uniform operating temperature variation are in practice mostly unknown, and consequently exact compensation for uniform variations in operating temperature is practically unachievable.

Alternatively, consider the intuitive approach of compensating for variations in echo arrival time between the current signal $u_c(t)$ recorded at one operating temperature and the baseline signal $u_b(t)$ recorded at a different operating temperature by scaling the time axis of the baseline signal $u_b(t)$ by a factor γ so that $t \to t\gamma$, as commonly done by other authors [115] to implement Baseline Signal Stretch (BSS) techniques. Then the baseline signal will become

$$u_b(t\gamma) = \sum_j h_j * s\left(t\gamma - t_j\gamma\right), \quad U_b(\omega/\gamma) = \gamma^{-1} S(\omega/\gamma) \sum_j e^{-i\omega t_j \gamma} H_j(\omega/\gamma) \tag{4.18}$$

As can be seen, scaling the time axis artificially contracts or dilates the echoes that compose the baseline signal and therefore changes their frequency content. Consequently, the residual spectrum will become

$$R(\omega) = U_c(\omega) - U_b(\omega/\gamma) = \sum_j e^{-i\omega t_j \gamma} \left(S(\omega) H_j^c(\omega) - \gamma^{-1} S(\omega/\gamma) H_j^b(\omega/\gamma)\right) \tag{4.19}$$

and will nullify if and only if

$$S(\omega) H_j^c(\omega) = \gamma^{-1} S(\omega/\gamma) H_j^b(\omega/\gamma), \quad \forall j \tag{4.20}$$

Even under the simplifying assumption that all pipeline features have a frequency and temperature independent response $H_j^c(\omega) = H_j^b(\omega) = H_j^b(\omega/\gamma) = a_j$, with $0 < a_j < 1$, the residual spectrum

$$R(\omega) = U_c(\omega) - U_b(\omega/\gamma) = \sum_j a_j e^{-i\omega t_j \gamma} \left(S(\omega) - \gamma^{-1} S(\omega/\gamma)\right) \tag{4.21}$$

will nullify if and only if

$$S(\omega) = \gamma^{-1} S\left(\omega/\gamma\right) \tag{4.22}$$

It can be easily verified that this condition will only be satisfied when no uniform operating temperature variation occurs, in which case $\gamma = 1$. Therefore, scaling the time axis to compensate for a uniform operating temperature variation will not remove the artefact echoes in the residual signal because it changes the frequency content of the echoes that compose the baseline signal.

To prevent changes in the frequency content of baseline signal echoes following a scaling of the time axis, consider compensating by not only scaling the time axis of the baseline signal by a factor γ, but also by scaling the baseline spectrum by the ratio between the spectrum $S(\omega)$ of the transmitted wave packet $s(t)$ and the spectrum $\gamma^{-1} S\left(\omega/\gamma\right)$ of the transmitted wave packet $s\left(\gamma t\right)$ whose time axis has also been scaled by a factor γ, resulting in the compensated baseline spectrum

$$U_b^{\star}\left(\omega,\gamma\right) = \gamma U_b\left(\omega/\gamma\right) \frac{S(\omega)}{S\left(\omega/\gamma\right)} = S(\omega) \sum\nolimits_j e^{-i\omega t_j \gamma} H_j\left(\omega/\gamma\right) \tag{4.23}$$

which can readily be computed in practice for any value of γ since it relies solely on the knowledge of the transmitted wave packet $s(t)$ and of the baseline signal $u_b(t)$ recorded by the permanently installed guided wave sensor. The residual spectrum

$$R\left(\omega,\gamma\right) = U_c(\omega) - U_b^{\star}\left(\omega,\gamma\right) = S(\omega) \sum\nolimits_j e^{-i\omega t_j \gamma} \left(H_j^c(\omega) - H_j^b\left(\omega/\gamma\right)\right) \tag{4.24}$$

will nullify if and only if

$$\sum\nolimits_j e^{-i\omega t_j \gamma} \left(H_j^c(\omega) - H_j^b\left(\gamma/\omega\right)\right) \tag{4.25}$$

nullifies. Under the simplifying assumption that all pipeline discontinuities have a frequency and temperature independent response $H_j^c(\omega) = H_j^b(\omega) = H_j^b\left(\omega/\gamma\right) = a_j$, with $0 < a_j < 1$, it is trivial to verify that this condition will be satisfied, from which it follows that under this assumption it is possible to compensate exactly for variations in echo arrival time and therefore for uniform variations in operating temperature, thereby completely removing artefact echoes from the residual signal. Unfortunately in reality all pipeline discontinuities, and in particular pre-existing damage and complex features such as supports, branches, drains and vents, have a frequency and temperature dependent response that will generally vary from $H_j^b(\omega)$ to $H_j^c(\omega)$ following a uniform operating temperature variation, thereby negating the assumption and confirming that exact compensation is in practice unachievable.

In conclusion, although exact compensation is unrealistic, by finding the value of γ that minimises the Sum of the Squares (SS) of the residual signal

$$r_{SS}(\gamma) = \int \left(r(t,\gamma)\right)^2 \mathrm{d}t, \quad r(t,\gamma) = \int_{-\infty}^{\infty} R(\omega,\gamma)\, e^{i\omega t}\, \mathrm{d}\omega \tag{4.26}$$

with

$$R(\omega,\gamma) = U_c(\omega) - U_b^{\star}(\omega,\gamma) = S(\omega) \sum\nolimits_j e^{-i\omega t_j \gamma} \left(H_j^c(\omega) - H_j^b(\omega/\gamma)\right) \tag{4.27}$$

it remains nevertheless possible to partially compensate for variations in echo arrival time and therefore for uniform variations in operating temperature, thereby minimising the amplitude of the artefact echoes in the residual signal $r(t,\gamma)$ with what is known as the Baseline Signal Stretch (BSS) technique [115, 119]. Note that because the RMS of the residual signal is given by

$$r_{RMS}(\gamma) = \sqrt{r_{SS}(\gamma)/T_r} \tag{4.28}$$

where T_r is the temporal duration of the residual signal $r(t,\gamma)$, it follows that minimising the SS is equivalent to minimising the RMS, which is the typical minimisation target for the BSS as well as for other baseline subtraction compensation procedures [115, 119, 123].

Importantly, actual sensor systems often suffer from jitter and may not switch from transmit mode to record mode at exactly the same time on all occasions. Consequently, one recorded signal might appear delayed by a time τ relative to another. Furthermore, transduction efficiency is widely known to be a function of temperature, and consequently the amplitude of one recorded signal might appear scaled by a factor κ relative to another.

In situations where the sensor system has a pitch-catch configuration, transduction efficiency variations are typically compensated for by normalising each recorded signal by the amplitude of the first arrival, *i.e.* by the amplitude of the wave packet that travels along a straight line from the emitter to the receiver sensor. Under the assumption that no damage is growing in the region of the structure between the emitter and the receiver sensor, any variation in the amplitude of the first arrival will be caused by variations in transduction efficiency, and therefore by normalising each recorded signal by the amplitude of the first arrival it should in principle be possible to compensate for transduction efficiency variations [115]. However, beside its reliance on the assumption that damage will always grow away from selected locations, first arrival normalisation suffers from the problematic limitation that it can only be utilised with pitch-catch sensor systems but not with pulse-echo sensor systems, such as permanently installed guided wave sensors, for which the first arrival does not exist.

By introducing a scale factor κ and a time delay τ in the compensated baseline spectrum

$$U_b^\star(\omega,\gamma,\tau,\kappa) = e^{-i\omega\tau}\kappa\gamma U_b(\omega/\gamma)\frac{S(\omega)}{S(\omega/\gamma)} = \kappa S(\omega)\sum_j e^{-i\omega(t_j\gamma+\tau)}H_j^b(\omega/\gamma) \tag{4.29}$$

and by finding the values of γ, τ and κ that minimise the SS of the residual signal

$$r_{\mathrm{SS}}(\gamma,\tau,\kappa) = \int\left(r(t,\gamma,\tau,\kappa)\right)^2 \mathrm{d}t, \quad r(t,\gamma,\tau,\kappa) = \int_{-\infty}^{\infty} R(\omega,\gamma,\tau,\kappa)\,e^{i\omega t}\,\mathrm{d}\omega \tag{4.30}$$

with

$$\begin{aligned} R(\omega,\gamma,\tau,\kappa) &= U_c(\omega) - U_b^\star(\omega,\gamma,\tau,\kappa) \\ &= S(\omega)\sum_j e^{-i\omega(t_j\gamma+\tau)}\left(H_j^c(\omega) - \kappa H_j^b(\omega/\gamma)\right) \end{aligned} \tag{4.31}$$

it becomes possible to compensate for changes in transduction efficiency, transmission and reception delays, and partially compensate for variations in echo arrival time. This procedure relies neither on the existence of the first arrival nor on the assumption that damage will always grow away from selected locations, and consequently overcomes the inherent limitations of the first arrival normalisation procedure. Therefore, the final result is an enhanced BSS technique that can partially compensate for uniform variations in operating temperature and that minimises the amplitude of the artefact echoes in the residual signal $r(t,\gamma,\tau,\kappa)$.

Localised Baseline Signal Stretch

Large, environmentally exposed structures such as pipelines often experience operating temperature gradients along their length as a result of the heating or cooling of their contents, of gaps in coatings and insulations, of entrances into ground and walls, and also of the irradiation from the sun which can give rise to operating temperature gradients both along the length of pipelines as well as around their circumference. The temperature difference between two locations along a pipeline can reach several degrees, resulting in non-uniform changes in the arrival time of guided wave packet between readings. It is generally impossible to know the exact temperature profile and therefore to compensate exactly for this EOC variation.

However, a pipeline can be divided into a number of sections along each of which the operating temperature can be assumed to remain constant, *e.g.* before and after entering into ground. Similarly, the residual signal can be subdivided into several gated sections

$$r_n(t,\gamma_n,\tau_n,\kappa) = w_n(t)\,r(t,\gamma_n,\tau_n,\kappa) \tag{4.32}$$

where $w_n(t)$ is a gate function chosen so that the gated residual signal $r_n\left(t, \gamma_n, \tau_n, \kappa\right)$ corresponds to a pipeline section along which the operating temperature can be assumed to stay uniform. By finding the values of γ_n, τ_n and κ that minimise the Sum of the Squares (SS) of the gated residual signal

$$r_{n,SS}\left(\gamma_n, \tau_n, \kappa\right) = \int \left(r_n\left(t, \gamma_n, \tau_n, \kappa\right)\right)^2 \mathrm{d}t \tag{4.33}$$

it becomes possible to compensate for changes in transduction efficiency, transmission and reception delays, and partially compensate for variations in the arrival time of guided wave packets along the n^{th} pipeline section. Note that τ_n accounts for any apparent delay between gated recorded signals that could be caused by both jitter, *i.e.* variations in the time at which the sensor system switches from transmit mode to record mode, as well as by any change in operating temperature, and therefore change in propagation distance and velocity, that affected the pipeline sections preceding the one under consideration. Importantly, because transduction efficiency is independent of the specific pipeline section, the value of κ is unique and does not depend on just a single pipeline section.

More generally, the Localised Baseline Signal Stretch (LBSS) technique consists in finding the values of $\Gamma = \left(\ldots, \gamma_{n-1}, \gamma_n, \gamma_{n+1}, \ldots\right)$, $\mathrm{T} = \left(\ldots, \tau_{n-1}, \tau_n, \tau_{n+1}, \ldots\right)$ and κ that minimise the Sum of the Squares (SS)

$$r_{l,SS}(\Gamma, \mathrm{T}, \kappa) = \int \left(r_l(t, \Gamma, \mathrm{T}, \kappa)\right)^2 \mathrm{d}t \tag{4.34}$$

of the localised residual signal

$$r_l(t, \Gamma, \mathrm{T}, \kappa) = \frac{\sum_n r_n\left(t, \gamma_n, \tau_n, \kappa\right)}{\sum_n w_n(t)} \tag{4.35}$$

In this way, it is possible to compensate for changes in transduction efficiency and for jitter, and partially compensate for non-uniform changes in the arrival time of guided wave packets along a pipeline. Note that because the exact temperature profile along the pipeline as well as the frequency responses of the features are unknown, the values of Γ, T and κ that minimise the SS of the localised residual signal $r_{l,SS}(\Gamma, \mathrm{T}, \kappa)$ cannot be computed analytically but have to be determined iteratively through blind optimisation algorithms such as Genetic Algorithms, Simulated Annealing or Pattern Search [126–128]. The choice of which algorithm to utilise will in general depend on the particular signals, and therefore on the particular permanently installed guided wave sensor and pipeline under consideration. Although there does not exist a formal methodology to guide the choice, as a guideline one would give preference to Genetic Algorithms [127] when the number of pipeline sections, and thus the number of variables, is large, and to Simulated Annealing [126, 128] when the number of pipeline sections, and thus the number of variables, is small. Finally, while the Pattern Search algorithm [126, 128] can work well for high-dimensionality as well as low-dimensionality problems and can offer significant speed advantages as it generally requires a lower number of target function calls, it is nevertheless the most likely to get trapped in local minima when attempting to minimise highly non-linear target functions such as the SS of the localised residual signal $r_{l,SS}(\Gamma, \mathrm{T}, \kappa)$. Therefore, one should give preference to Pattern Search solely when the operating temperature difference between readings is either known or very limited, in which cases initial estimates can be computed for the values of Γ, T and κ that are very close to those that would globally minimise the target function $r_{l,SS}(\Gamma, \mathrm{T}, \kappa)$, and consequently the chance that the algorithm falls into local minima is much reduced.

The choice of how to partition the pipeline into sections, and therefore what gate functions to utilise, must be carefully considered because it can have a significant impact on the effectiveness of the compensation. As will be discussed in section 4.4.4, obtaining estimates for the values of γ_n, τ_n and κ that minimise the SS of the gated residual signal $r_n\left(t, \gamma_n, \tau_n, \kappa\right)$, and therefore partially compensating for changes in the operating temperature of a pipeline over each pipeline section n, is a sensible option if and only if over each pipeline section n the echoes from damage growth are very small compared to the echoes from features and pre-existing damage. If this is the case, then the localised residual signal $r_l(t, \Gamma, \mathrm{T}, \kappa)$ will contain mostly unaltered damage growth echoes. Otherwise the localised residual signal $r_l(t, \Gamma, \mathrm{T}, \kappa)$ will contain an altered version of the damage growth echo together with other artefact echoes.

4.4.2 Optimal Baseline Selection

The Optimal Baseline Selection (OBS) technique seeks to minimise the impact of EOC variations by utilising several baseline readings collected in different Environmental and Operational Conditions (EOC) representative of all the typical ones that the monitored pipeline can be expected to experience. The optimal baseline for a given current reading is then chosen to be the one that minimises the Sum of the Squares (SS), or the RMS, of the residual signal [115, 123] and that therefore should have been gathered in the most similar EOC. Importantly, the OBS technique assumes that all baselines are collected when the pipeline is in a known and stable health condition, whether undamaged or partially damaged.

4.4.3 Practical Baseline Subtraction Compensation

This section presents two examples of a typical baseline subtraction scenario utilising the torsional $T(0,1)$ signals recorded by the permanently installed guided wave sensor gPIMS®-138, which is deployed on a NPS 10 Schedule 40 carbon steel pipeline at the Wytch Farm oil-field. It is known that no appreciable damage has grown in the section of pipeline monitored by sensor gPIMS®-138 in the period of time over which the signals have been recorded. The primary objective of this section is to exemplify the use of Optimal Baseline Selection (OBS) and Localised Baseline Signal Stretch (LBSS) to minimise changes in the baseline component due to EOC variations. Interestingly, the two examples presented in this section suggest that the amplitude of the artefact echoes in the residual signal are minimised when the optimal baseline for a given reading is chosen to be the one that minimises the Sum of the Squares (SS) of the residual signal after the effects of global and local differences in pipeline operating temperature as well as of variations in the transduction efficiency of the sensor gPIMS®-138 have been compensated for utilising BSS or LBSS, or in other words when the OBS and BSS or LBSS techniques are integrated rather than utilised separately.

Operative Pipeline

Figure 4.3 presents three torsional $T(0,1)$ signals recorded by sensor gPIMS®-138. The signals nominally consist of a current signal and of two baseline signals, all of which were recorded when the pipeline was operating at a temperature of roughly 50°C, as indicated in figure 4.3. The two baseline signals have both been selected utilising the OBS methodology, except in one case, which will be referred to as baseline **A** and which corresponds to the left side of table 4.1, the optimal baseline was chosen to be the one that minimises the SS of the residual signal after LBSS compensation, while in the other case, which will be referred to as baseline **B** and which corresponds to the right side of table 4.1, the optimal baseline was chosen to be the one that minimises the SS of the residual signal without any LBSS compensation applied, as indicated in figure 4.3 and in table 4.1.

Table 4.1 compares the performance of different baseline subtraction compensation approaches to that of baseline subtraction without any compensation applied. Since it is known that no appreciable damage growth echo is present, the RMS of the residual signal has been chosen as the performance measure of the effectiveness of the different compensation approaches, since it gives a clear indication of the generalised amplitude of artefact echoes that are present in the residual signal.

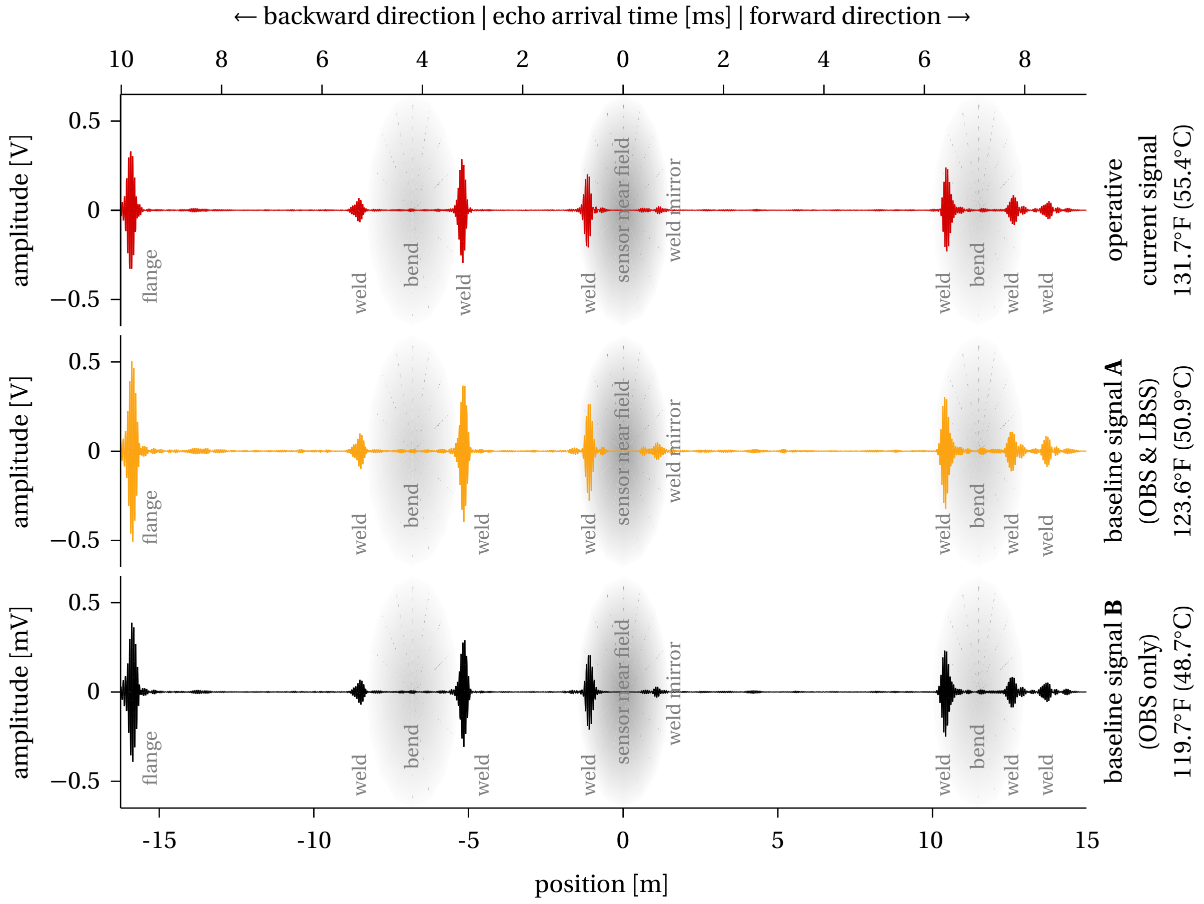

Figure 4.3: Current and baseline T(0,1) signals recorded by sensor gPIMS®-138; all signals were recorded while the pipeline was operative; the transmitted wave packet is an eight-cycle, 27kHz Hann-windowed tone-burst; of the two baseline signals, one has been selected utilising the combined OBS & LBSS methodology, while the other has been selected utilising OBS only.

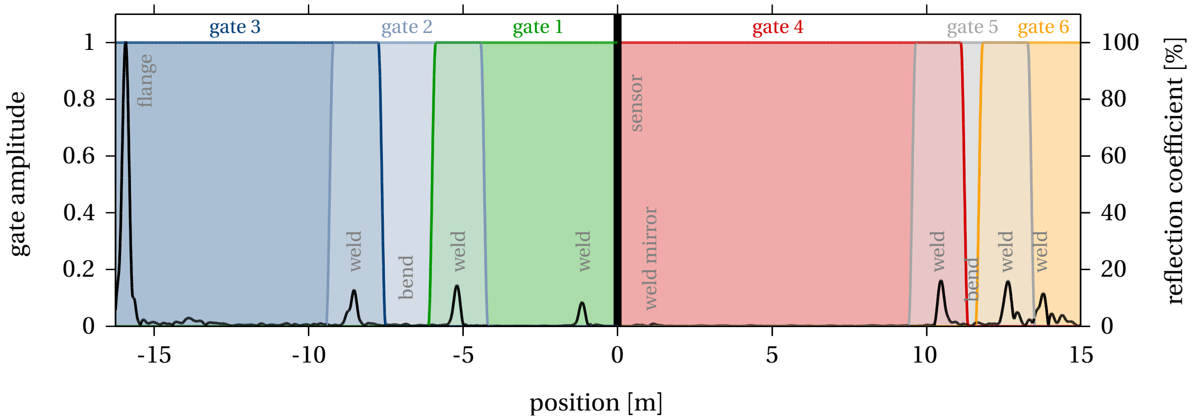

Figure 4.4: LBSS gate functions $w_n(t)$, with $n = 1, 2, \ldots, 6$; each gate satisfies the necessary condition of containing at least one major reflector; each gated residual signal $r_n(t, \gamma_n, \tau_n, \kappa)$ corresponds to a pipeline section along which the operating temperature is assumed to stay uniform.

Table 4.1: Performance comparison of different baseline subtraction compensation approaches on the signals recorded by sensor gPIMS®-138; all current and baseline T(0,1) signals were recorded while the pipeline was operative; the transmitted wave packet is an eight-cycle, 27kHz Hann-windowed tone-burst; the left and right columns illustrate the compensation performance when the baseline signal has been selected utilising respectively the combined OBS & LBSS methodology and OBS only.

	baseline signal A (OBS & LBSS)				**baseline signal B (OBS only)**			
compensation parameters	stretch γ	delay τ [μs]	scale κ	residual RMS [mV]	stretch γ	delay τ [μs]	scale κ	residual RMS [mV]
no compensation	N/A	N/A	N/A	**19.13**	N/A	N/A	N/A	**12.27**
stretch only compensation	1.001	N/A	N/A	**15.04**	1.001	N/A	N/A	**7.850**
stretch & delay compensation	1.001	0.026	N/A	**15.03**	1.001	0.793	N/A	**7.679**
stretch & scale compensation	1.001	N/A	0.700	**6.426**	1.001	N/A	0.906	**6.911**
stretch, delay & scale compensation	1.001	0.073	0.700	**6.413**	1.001	-0.521	0.906	**6.792**
localised stretch, delay & scale compensation	$\gamma_1 = 1.001$ $\gamma_2 = 1.001$ $\gamma_3 = 1.001$ $\gamma_4 = 1.001$ $\gamma_5 = 1.001$ $\gamma_6 = 1.001$	$\tau_1 = -0.261$ $\tau_2 = -0.075$ $\tau_3 = -0.220$ $\tau_4 = -0.485$ $\tau_5 = 0.690$ $\tau_6 = -0.362$	0.701	**6.383**	$\gamma_1 = 1.001$ $\gamma_2 = 1.000$ $\gamma_3 = 1.000$ $\gamma_4 = 1.000$ $\gamma_5 = 1.001$ $\gamma_6 = 1.001$	$\tau_1 = 0.375$ $\tau_2 = 1.107$ $\tau_3 = 0.619$ $\tau_4 = 0.489$ $\tau_5 = -3.999$ $\tau_6 = -2.586$	0.911	**6.675**

Table 4.1 indicates that, when no baseline subtraction compensation is applied, the residual signal RMS varies significantly depending on which baseline is subtracted from the current signal. Specifically, the residual RMS for baseline **A** is 19.13mV, which is significantly higher than the residual RMS of 12.27mV for baseline **B**.

Enabling compensation for variations in echo arrival time caused by uniform variations in operating temperature, *i.e.* finding the value of the stretch parameter γ that minimises the SS of the residual signal of equation 4.30, results in a reduction of the residual RMS from 19.13mV to 15.04mV in the case of baseline **A**, with the optimal value of $\gamma \approx 1.001$, and from 12.27mV to 7.850mV in the case of baseline **B**, with the optimal value of $\gamma \approx 1.001$.

Utilising the Metallic Materials Properties Development and Standardization (MMPDS) handbook [129], it can be shown that at the temperature of 55.4°C at which the current signal was recorded the shear modulus of steel is equal to 83.91GPa, and that at the temperatures of 50.9°C and 48.7°C at which baselines **A** and **B** were respectively recorded the shear modulus of steel is respectively 84.01GPa and 84.06GPa. Assuming the density of steel is 7932kg/m^3 [129] and that it does not change appreciably within the temperature range under consideration, it follows from equation 2.7 that the shear wave velocity, and therefore the $\mathrm{T}(0,1)$ phase and group velocities, at the temperature of 55.4°C at which the current signal was recorded is equal to 3252m/s, and at the temperatures of 50.9°C and 48.7°C at which baselines **A** and **B** were respectively recorded is equal to respectively 3254m/s and 3255m/s. Since the thermal expansion coefficient α for steel is roughly 1.5×10^{-5}/°C, it therefore follows that in the case of baseline **A** the theoretical value for the stretch parameter γ is approximately

$$\gamma = 1 + \alpha\delta T - \delta v/v = 1 + \frac{1.5(55.4°\mathrm{C} - 50.9°\mathrm{C})}{100000°\mathrm{C}} - \frac{3252\mathrm{m/s} - 3254\mathrm{m/s}}{3252\mathrm{m/s}} \approx 1.001$$

which is consistent with the value of 1.001 determined by the compensation algorithm. Similarly in the case of baseline **B** the theoretical value for the stretch parameter γ is approximately

$$\gamma = 1 + \alpha\delta T - \delta v/v = 1 + \frac{1.5(55.4°\mathrm{C} - 48.7°\mathrm{C})}{100000°\mathrm{C}} - \frac{3252\mathrm{m/s} - 3255\mathrm{m/s}}{3252\mathrm{m/s}} \approx 1.001$$

which is also consistent with the value of 1.001 determined by the compensation algorithm.

Enabling compensation for variations in echo arrival time caused by uniform variations in operating temperature and for transmission and reception delays, *i.e.* finding the values of the delay time τ and of the stretch parameter γ that minimise the SS of the residual signal of equation 4.30, results in a minor reduction of the residual RMS from 15.04mV to 15.03mV in the case of baseline **A**, with the optimal values of $\tau \approx 0.026\mu$s and of $\gamma \approx 1.001$, and from 7.850mV to 7.679mV in the case of baseline **A**, with the optimal values of $\tau \approx 0.793\mu$s and of $\gamma \approx 1.001$.

Alternatively, enabling compensation for variations in echo arrival time caused by uniform variations in operating temperature and for changes in transduction efficiency, *i.e.* finding the values of the scale factor κ and of the stretch parameter γ that minimise the SS of the residual signal of equation 4.30, results in a major reduction of the residual RMS from 15.04mV to 6.426mV in the case of baseline **A**, with the optimal values of $\kappa \approx 0.700$ and of $\gamma \approx 1.001$, and in a reduction of the residual RMS from 7.850mV to 6.911mV in the case of baseline **A**, with the optimal values of $\kappa \approx 0.906$ and of $\gamma \approx 1.001$.

Enabling compensation for variations in echo arrival time caused by uniform variations in operating temperature, for transmission and reception delays and for changes in transduction efficiency, *i.e.* finding the values of the delay time τ, of the scale factor κ and of the stretch parameter γ that minimise the SS of the residual signal of equation 4.30, results in a minor further reduction of the residual RMS from 6.426mV to 6.413mV in the case of baseline **A**, with the optimal values of $\tau \approx 0.073\mu$s, of $\kappa \approx 0.700$ and of $\gamma \approx 1.001$, and from 6.911mV to 6.792mV in the case of baseline **B**, with the optimal values of $\tau \approx -0.521\mu$s, of $\kappa \approx 0.906$ and of $\gamma \approx 1.001$.

Finally, enabling compensation for localised variations in echo arrival time caused by uniform variations in operating temperature, for transmission and reception delays and for changes in transduction efficiency, *i.e.* finding the values of $\Gamma = (\gamma_1, \gamma_2, \gamma_3, \gamma_4, \gamma_5, \gamma_6)$, $\mathrm{T} = (\tau_1, \tau_2, \tau_3, \tau_4, \tau_5, \tau_6)$ and κ that minimise the SS of the residual signal of equation 4.34, results in a minor further reduction of the residual RMS from 6.413mV to 6.383mV in the case of baseline **A**, and from 6.792mV to 6.675mV in the case of baseline **B**. Figure 4.4 shows the gate functions $w_n(t)$, with $n = 1, 2, \ldots, 6$, chosen so that the gated residual signal $r_n(t, \gamma_n, \tau_n, \kappa)$ corresponds to a pipeline section along which the operating temperature is assumed to stay uniform. Note that, for reasons that will be discussed in section 4.4.4, the gate functions have also been chosen so that each satisfied the necessary condition of containing at least one major reflector.

As can be seen from table 4.1, enabling compensation, and especially compensation for variations in echo arrival time caused by uniform variations in operating temperature and for changes in transduction efficiency, can significantly reduce the residual RMS. Specifically, the residual RMS, and therefore the amplitude of the artefact echoes in the residual signal, has been reduced by roughly 66% in the case of baseline **A** and by 50% in the case of baseline **B**. Figure 4.5, which shows the RC envelopes of residual signals obtained by subtracting from the current signal baseline **A** with different compensation approaches, illustrates the benefit of enabling compensation. It can be clearly seen that large artefact echoes are present in the residual signal in correspondence of pipeline features such as welds and flanges, which reduce gradually as more comprehensive compensation approaches are utilised.

Importantly, it can be seen from table 4.1 as well as in figure 4.6, which shows the RC envelopes of residual signals obtained by subtracting from the current signal baselines **A** and **B** with different compensation approaches, that although when no baseline subtraction compensation is applied the artefact echoes in the residual signal in correspondence of pipeline features such as welds and flanges are smaller when baseline **B** is subtracted from the cur-

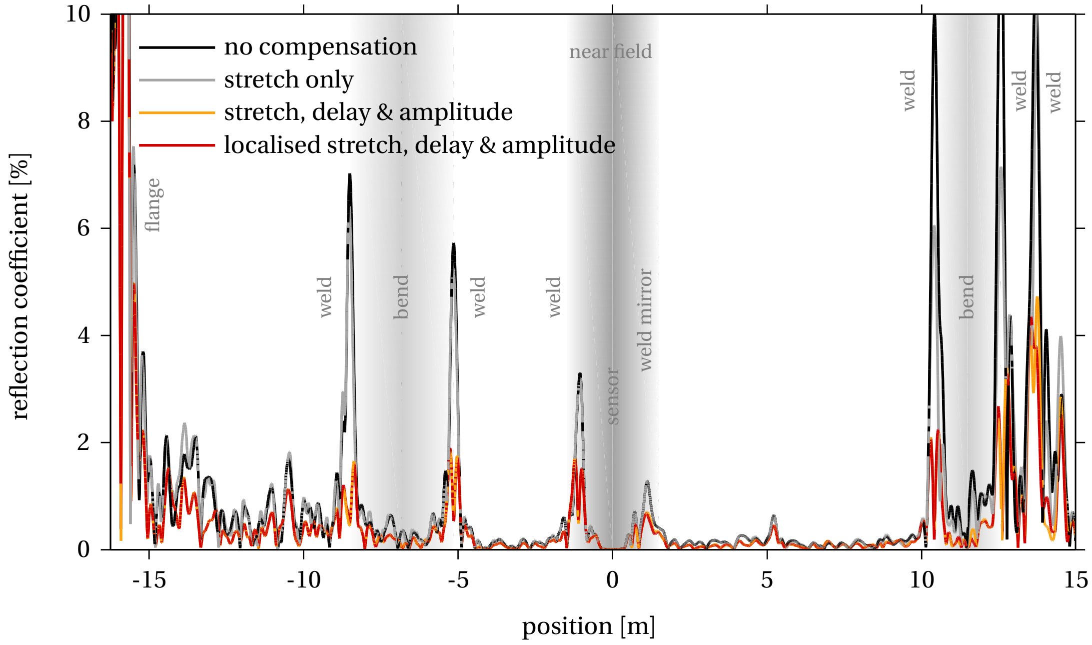

Figure 4.5: Reflection Coefficient (RC) envelopes of residual signals obtained from sensor gPIMS®-138 (operative pipeline) by subtracting baseline **A** from the current signal with different compensation approaches.

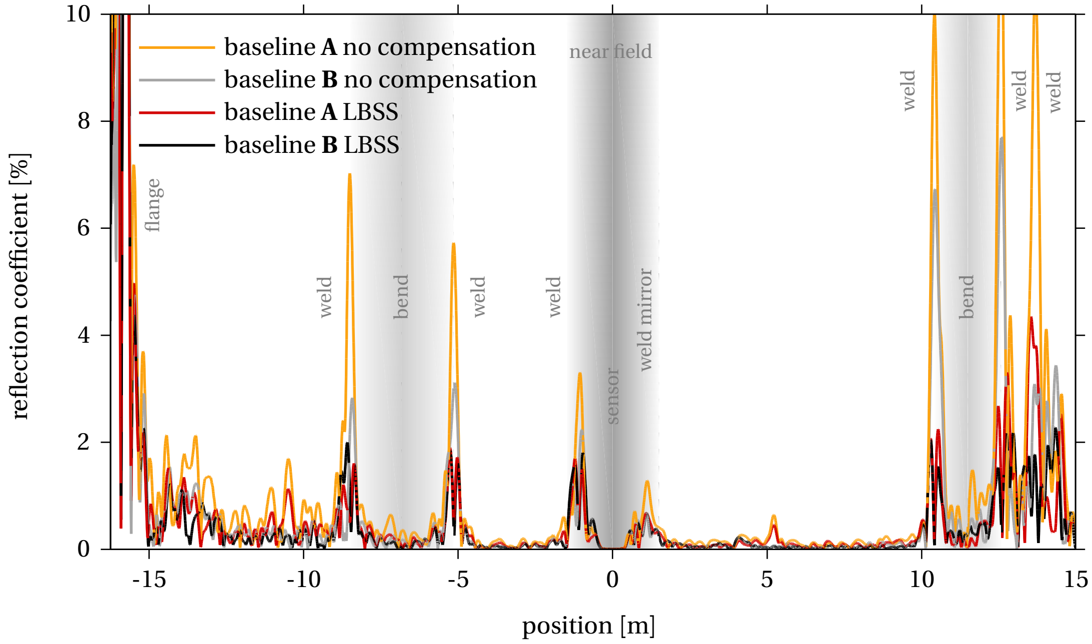

Figure 4.6: Reflection Coefficient (RC) envelopes of residual signals obtained from sensor gPIMS®-138 (operative pipeline) by subtracting baselines **A** and **B** from the current signal with different compensation approaches.

rent signal, once baseline subtraction compensation is enabled the artefact echoes in the residual signal in correspondence of pipeline features such as welds and flanges are smaller when baseline **A** is subtracted from the current signal. This analysis therefore suggests that baseline **A**, which was selected utilising the OBS methodology that minimises the SS of the residual signal after LBSS compensation, rather than baseline **B**, which was selected utilising the OBS methodology that minimises the SS of the residual signal without any LBSS compensation applied, is actually the optimal baseline for the current signal, thereby hinting that it could be advantageous to integrate OBS and LBSS to minimise the amplitude of the artefact echoes in the residual signal.

Inoperative Pipeline

Figure 4.7 presents three torsional $T(0,1)$ signals recorded by sensor gPIMS®-138. The signals nominally consist of a current signal, which was recorded when the pipeline was inoperative and at a temperature of roughly 5°C, and of two baseline signals, which were recorded when the pipeline was operating at a temperature of roughly 50°C, as indicated in figure 4.7. As for the previous example, the two baseline signals have both been selected utilising the OBS methodology, except in one case, which will be referred to as baseline **C** and which corresponds to the left side of table 4.2, the optimal baseline was chosen to be the one that minimises the SS of the residual signal after LBSS compensation, while in the other case, which will be referred to as baseline **D** and which corresponds to the right side of table 4.2, the optimal baseline was chosen to be the one that minimises the SS of the residual signal without any LBSS compensation applied, as indicated in figure 4.7 and in table 4.2.

Table 4.2 compares the performance of different baseline subtraction compensation approaches to that of baseline subtraction without any compensation applied. Since it is known that no appreciable damage growth echo is present, the RMS of the residual signal has been chosen as the performance measure of the effectiveness of the different compensation approaches since it gives a clear indication of the generalised amplitude of artefact echoes that are present in the residual signal.

Table 4.2 indicates that, when no baseline subtraction compensation is applied, the residual signal RMS varies significantly depending on which baseline is subtracted from the current signal. Specifically, the residual RMS for baseline **C** is 62.56mV, which is significantly higher than the residual RMS of 57.63mV for baseline **D**.

As could be envisaged given the large operating temperature difference between the read-

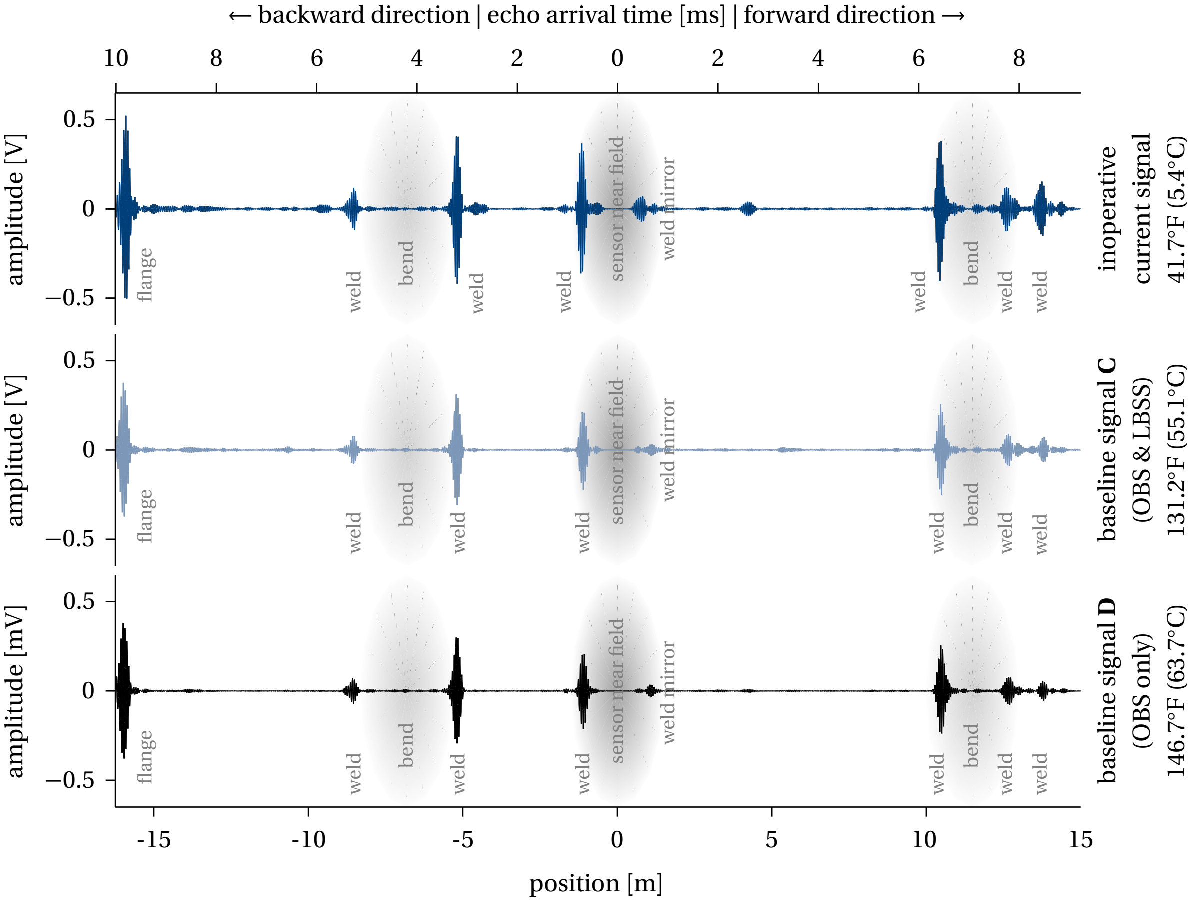

Figure 4.7: Current and baseline T(0,1) signals recorded by sensor gPIMS®-138; the current signal was recorded while the pipeline was inoperative, whereas the two baseline signals were recorded while the pipeline was operative; the transmitted wave packet is an eight-cycle, 27kHz Hann-windowed tone-burst; of the two baseline signals, one has been selected utilising the combined OBS & LBSS methodology, while the other has been selected utilising OBS only.

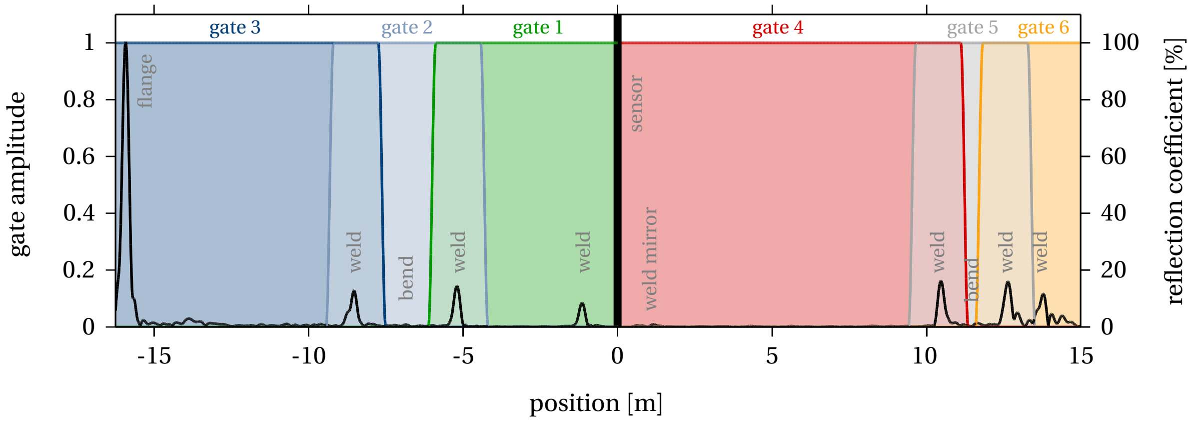

Figure 4.8: LBSS gate functions $w_n(t)$, with $n = 1, 2, \ldots, 6$; each gate satisfies the necessary condition of containing at least one major reflector; each gated residual signal $r_n(t, \gamma_n, \tau_n, \kappa)$ corresponds to a pipeline section along which the operating temperature is assumed to stay uniform.

Table 4.2: Performance comparison of different baseline subtraction compensation approaches on the signals recorded by sensor gPIMS®-138; the current signal was recorded while the pipeline was inoperative, whereas the two baseline signals were recorded while the pipeline was operative; the transmitted wave packet is an eight-cycle, 27kHz Hann-windowed tone-burst; the left and right columns illustrate the compensation performance when the baseline signal has been selected utilising respectively the combined OBS & LBSS methodology and OBS only.

	baseline signal C (OBS & LBSS)				**baseline signal D (OBS only)**			
compensation parameters	stretch γ	delay τ [μs]	scale κ	residual RMS [mV]	stretch γ	delay τ [μs]	scale κ	residual RMS [mV]
no compensation	N/A	N/A	N/A	**62.56**	N/A	N/A	N/A	**57.63**
stretch only compensation	0.992	N/A	N/A	**20.87**	0.992	N/A	N/A	**20.94**
stretch & delay compensation	0.993	−1.130	N/A	**20.16**	0.992	−0.320	N/A	**20.73**
stretch & scale compensation	0.992	N/A	1.437	**15.60**	0.992	N/A	1.463	**15.38**
stretch, delay & scale compensation	0.993	−3.062	1.447	**14.20**	0.992	0.551	1.465	**14.99**
localised stretch, delay & scale compensation	$\gamma_1 = 0.993$ $\gamma_2 = 0.993$ $\gamma_3 = 0.993$ $\gamma_4 = 0.993$ $\gamma_5 = 0.993$ $\gamma_6 = 0.993$	$\tau_1 = -2.208$ $\tau_2 = -0.555$ $\tau_3 = -2.610$ $\tau_4 = -6.811$ $\tau_5 = -3.574$ $\tau_6 = -5.623$	1.460	**13.35**	$\gamma_1 = 0.992$ $\gamma_2 = 0.992$ $\gamma_3 = 0.992$ $\gamma_4 = 0.991$ $\gamma_5 = 0.991$ $\gamma_6 = 0.991$	$\tau_1 = -1.406$ $\tau_2 = 0.472$ $\tau_3 = -0.877$ $\tau_4 = -1.870$ $\tau_5 = 6.049$ $\tau_6 = -0.707$	1.645	**14.18**

ings, enabling compensation for variations in echo arrival time caused by uniform variations in operating temperature, *i.e.* finding the value of the stretch parameter γ that minimises the SS of the residual signal of equation 4.30, results in significant reductions of the residual RMS, which drops from 62.56mV to 20.87mV in the case of baseline **C**, with the optimal value of $\gamma \approx 0.992$, and from 57.63mV to 20.94mV in the case of baseline **D**, with the optimal value of $\gamma \approx 0.992$.

Utilising the MMPDS handbook [129], it can be shown that at the temperature of 5.4°C at which the current signal was recorded the shear modulus of steel is equal to 85.01GPa, and that at the temperatures of 55.1°C and 63.7°C at which baselines **C** and **D** were respectively recorded the shear modulus of steel is respectively 83.92GPa and 83.73GPa. Assuming the density of steel is 7932kg/m^3 [129] and that it does not change significantly within the temperature range under consideration, it follows from equation 2.7 that the shear wave velocity, and therefore the T(0,1) phase and group velocities, at the temperature of 5.4°C at which the current signal was recorded is equal to 3274m/s, and that at the temperatures of 55.1°C and 63.7°C at which baselines **C** and **D** were respectively recorded the shear wave velocity is respectively 3253m/s and 3249m/s. Since the thermal expansion coefficient α for steel is roughly 1.5×10^{-5}/°C, it therefore follows that in the case of baseline **C** the theoretical value for the stretch parameter γ is approximately

$$\gamma = 1+\alpha\delta T-\delta v/v = 1+\frac{1.5(5.4°\text{C}-55.1°\text{C})}{100000°\text{C}}-\frac{3274\text{m/s}-3253\text{m/s}}{3274\text{m/s}}\approx 0.993$$

which is consistent with the value of 0.992 determined by the compensation algorithm. Similarly in the case of baseline **D** the theoretical value for the stretch parameter γ is approximately

$$\gamma = 1+\alpha\delta T-\delta v/v = 1+\frac{1.5(5.4°\text{C}-63.7°\text{C})}{100000°\text{C}}-\frac{3274\text{m/s}-3249\text{m/s}}{3274\text{m/s}}\approx 0.991$$

which is also consistent with the value of 0.992 determined by the compensation algorithm.

Enabling compensation for variations in echo arrival time caused by uniform variations in operating temperature and for transmission and reception delays, *i.e.* finding the values of the delay time τ and of the stretch parameter γ that minimise the SS of the residual signal of equation 4.30, results in a minor reductions of the residual RMS from 20.87mV to 20.16mV in the case of baseline **C**, with the optimal values of $\tau \approx -1.130\mu$s and of $\gamma \approx 0.993$, and from 20.94mV to 20.73mV in the case of baseline **D**, with the optimal values of $\tau \approx -0.320\mu$s and of $\gamma \approx 0.992$.

Alternatively, enabling compensation for variations in echo arrival time caused by uniform variations in operating temperature and for changes in transduction efficiency, *i.e.* finding the values of the scale factor κ and of the stretch parameter γ that minimise the SS of the residual signal of equation 4.30, results in major reductions of the residual RMS from 20.87mV to 15.60mV in the case of baseline **C**, with the optimal values of $\kappa \approx 1.437$ and of $\gamma \approx 0.992$, and from 20.94mV to 15.38mV in the case of baseline **D**, with the optimal values of $\kappa \approx 1.463$ and of $\gamma \approx 0.992$.

Enabling compensation for variations in echo arrival time caused by uniform variations in operating temperature, for transmission and reception delays and for changes in transduction efficiency, *i.e.* finding the values of the delay time τ, of the scale factor κ and of the stretch parameter γ that minimise the SS of the residual signal of equation 4.30, results in minor further reductions of the residual RMS from 15.60mV to 14.20mV in the case of baseline **C**, with the optimal values of $\tau \approx 3.062\mu$s, of $\kappa \approx 1.447$ and of $\gamma \approx 0.993$, and from 15.38mV to 14.99mV in the case of baseline **D**, with the optimal values of $\tau \approx 0.551\mu$s, of $\kappa \approx 1.465$ and of $\gamma \approx 0.992$.

Finally, enabling compensation for localised variations in echo arrival time caused by uniform variations in operating temperature, for transmission and reception delays and for changes in transduction efficiency, *i.e.* finding the values of $\Gamma = (\gamma_1, \gamma_2, \gamma_3, \gamma_4, \gamma_5, \gamma_6)$, $\mathrm{T} = (\tau_1, \tau_2, \tau_3, \tau_4, \tau_5, \tau_6)$ and κ that minimise the SS of the residual signal of equation 4.34, results in further reductions of the residual RMS from 14.20mV to 13.35mV in the case of baseline **C**, and from 14.99mV to 14.18mV in the case of baseline **D**. Figure 4.8 shows the gate functions $w_n(t)$, with $n = 1, 2, \ldots, 6$, chosen so that the gated residual signal $r_n(t, \gamma_n, \tau_n, \kappa)$ corresponds to a pipeline section along which the operating temperature is assumed to stay uniform. Note that, for reasons that will be discussed in section 4.4.4, the gate functions have also been chosen so that each satisfied the necessary condition of containing at least one major reflector.

As can be seen from table 4.2, enabling compensation, and especially compensation for variations in echo arrival time caused by uniform variations in operating temperature and for changes in transduction efficiency, can significantly reduce the residual RMS. Specifically, the residual RMS, and therefore the amplitude of the artefact echoes in the residual signal, has been reduced by roughly 80% in the case of baseline **C** and by 75% in the case of baseline **D**. Figure 4.9, which shows the RC envelopes of residual signals obtained by subtracting from the current signal baseline **C** with different compensation approaches, illustrates the benefit of enabling compensation. It can be clearly seen that large artefact echoes are present in the residual signal in correspondence of pipeline features such as welds and flanges, which reduce gradually as more comprehensive compensation approaches are utilised. Moreover, it can be noticed from table 4.2 that LBSS reduces the residual RMS appreciably when compared to BSS, and it can be observed in figure 4.9 that the artefact echoes in the residual signal in the vicinity of the welds are appreciably lower when LBSS, rather than just BSS, is utilised.

Importantly, it can be seen from table 4.2 as well as in figure 4.10, which shows the RC envelopes of residual signals obtained by subtracting from the current signal baselines **C** and **D** with different compensation approaches, that although when no baseline subtraction compensation is applied the artefact echoes in the residual signal in correspondence of pipeline

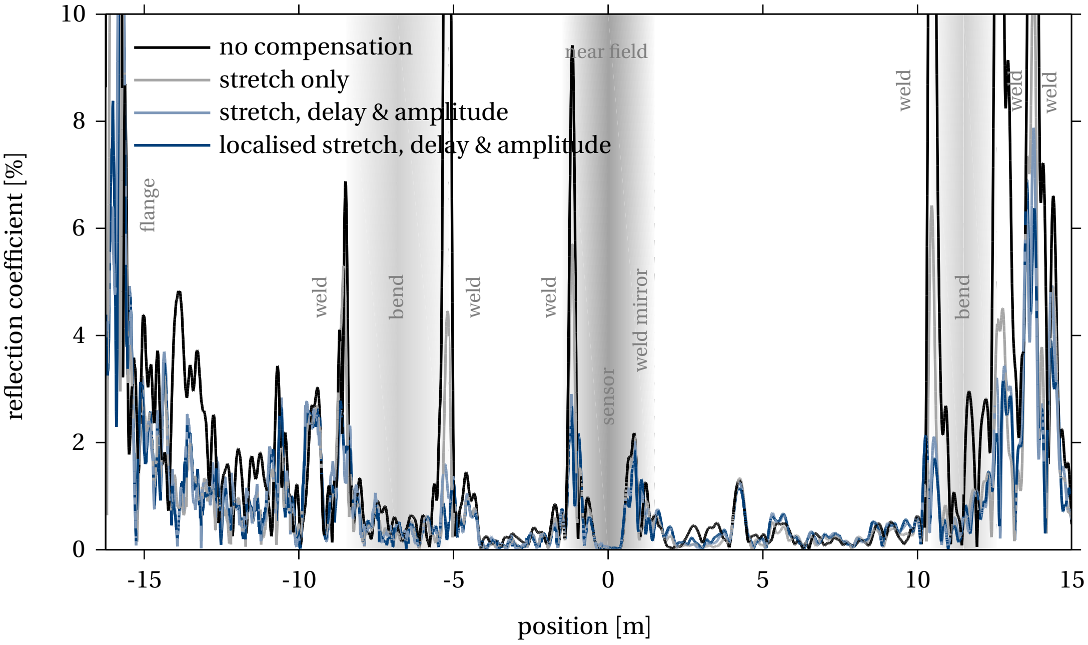

Figure 4.9: Reflection Coefficient (RC) envelopes of residual signals obtained from sensor gPIMS®-138 (inoperative pipeline) by subtracting baseline **C** from the current signal with different compensation approaches.

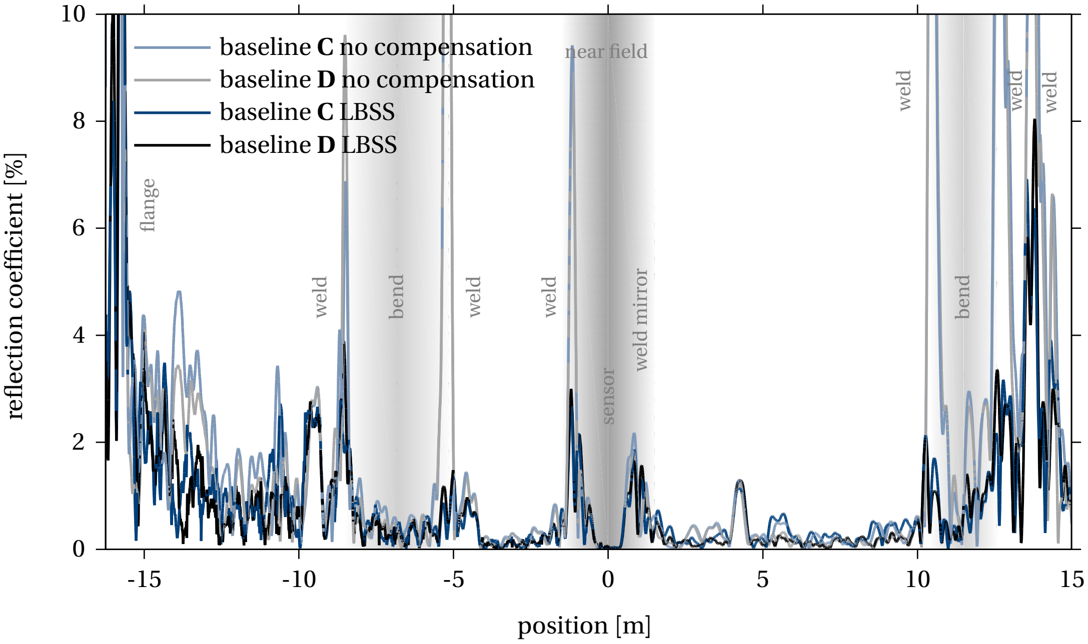

Figure 4.10: Reflection Coefficient (RC) envelopes of residual signals obtained from sensor gPIMS®-138 (inoperative pipeline) by subtracting baselines **C** and **D** from the current signal with different compensation approaches.

features such as welds and flanges are smaller when baseline **D** is subtracted from the current signal, once baseline subtraction compensation is enabled the artefact echoes in the residual signal in correspondence of pipeline features such as welds and flanges are smaller when baseline **C** is subtracted from the current signal. This analysis therefore suggests that baseline **C**, which was selected utilising the OBS methodology that minimises the SS of the residual signal after LBSS compensation, rather than baseline **D**, which was selected utilising the OBS methodology that minimises the SS of the residual signal without any LBSS compensation applied, is actually the optimal baseline for the current signal, thereby hinting that it could be advantageous to integrate OBS and LBSS to minimise the amplitude of the artefact echoes in the residual signal.

Summary

This section has presented two examples of a typical baseline subtraction scenario utilising the torsional $\mathrm{T}(0,1)$ signals recorded by the permanently installed guided wave sensor gPIMS®-138, which is deployed on a NPS 10 Schedule 40 carbon steel pipeline at the Wytch Farm oilfield. The two examples suggest that by integrating the OBS and BSS or LBSS techniques, rather than utilising them separately, their effect is maximised. Specifically, the amplitude of the artefact echoes in the residual signal are minimised when the optimal baseline for a given reading is chosen to be the one that minimises the SS of the residual signal after the effects of global and local differences in pipeline operating temperature as well as of variations in the transduction efficiency of permanently installed guided wave sensors have been compensated for utilising BSS or LBSS, as tables 4.1 and 4.2 appear to indicate.

Nevertheless, a more thorough and systematic experiment is required to obtain definitive proof of the advantages of integrating the OBS and BSS or LBSS techniques as well as of the capability of the LBSS technique to effectively compensate for local as well as global differences in pipeline operating temperature. For this purpose, the dedicated NPS 8 Schedule 40 pipe loop facility at BP's Naperville Campus, later described in chapter 6 and in particular in section 6.3, could prove very useful, since it can operate over a very wide temperature range and it enables to accurately control the temperature gradient along the length of the pipe.

4.4.4 Effect of Compensation on Damage Growth Echoes

It is crucial to understand whether, were damage to grow, the Baseline Signal Stretch (BSS) technique, and therefore the Localised Baseline Signal Stretch (LBSS) technique, would only minimise the amplitude of the artefact echoes or it would also hide the presence of any damage growth echo in the residual signal $r\left(t,\gamma,\tau,\kappa\right)$.

Consider a permanently installed guided wave sensor that records the baseline signal

$$u_b(t)=\sum_j h_j^b * s\left(t-t_j\right), \quad U_b(\omega)=S(\omega)\sum_j e^{-i\omega t_j}H_j^b(\omega) \tag{4.36}$$

Suppose after the baseline signal has been recorded damage grows and the operating temperature of the pipeline undergoes some uniform variation. The current signal subsequently recorded by the permanently installed guided wave sensor will be

$$u_{c+}(t)=u_c(t)+u_+(t), \quad U_{c+}(\omega)=U_c(\omega)+U_+(\omega) \tag{4.37}$$

with

$$u_c(t)=\sum_j h_j^c * s\left(t-t_j\gamma-\tau\right), \quad U_c(\omega)=S(\omega)\sum_j e^{-i\omega\left(t_j\gamma+\tau\right)}H_j^c(\omega) \tag{4.38}$$

and with the damage growth echo arriving at time $t_+\gamma+\tau$

$$u_+(t)=h_+ * s\left(t-t_+\gamma-\tau\right), \quad U_+(\omega)=S(\omega)e^{-i\omega\left(t_+\gamma+\tau\right)}H_+(\omega) \tag{4.39}$$

Consequently, the residual spectrum $R(\omega)$ will become

$$\begin{aligned}R(\omega)&=U_{c+}(\omega)-U_b(\omega)\\&=U_c(\omega)-U_b(\omega)+U_+(\omega)\\&=S(\omega)\left(\sum_j\left(e^{-i\omega\left(t_j\gamma+\tau\right)}H_j^c(\omega)-e^{-i\omega t_j}H_j^b(\omega)\right)+e^{-i\omega\left(t_+\gamma+\tau\right)}H_+(\omega)\right)\end{aligned} \tag{4.40}$$

As previously discussed, the expression

$$\sum_j\left(e^{-i\omega\left(t_j\gamma+\tau\right)}H_j^c(\omega)-e^{-i\omega t_j}H_j^b(\omega)\right) \tag{4.41}$$

will not in general nullify unless no uniform operating temperature variation occurs, in which case $\gamma=1$, $H_j^c(\omega)=H_j^b(\omega)$ and the expression can be nullified by delaying the baseline signal $u_b(t)$ by a time τ. Therefore, the residual signal will in general contain not just the damage growth echo but also artefact echoes because the echoes from pipeline features and pre-existing damage will not cancel out during baseline subtraction as a result of the uniform operating temperature variation.

To highlight the damage growth echo in the residual signal, one should minimise the amplitude of the artefact echoes. As previously proposed with the BSS technique, the amplitude of the artefact echoes can be minimised by finding the values of γ, τ and κ that minimise the Sum of the Squares (SS) of the residual signal

$$r_{SS}\left(\gamma,\tau,\kappa\right)=\int\left(r\left(t,\gamma,\tau,\kappa\right)\right)^2\mathrm{d}t,\quad r\left(t,\gamma,\tau,\kappa\right)=\int_{-\infty}^{\infty}R\left(\omega,\gamma,\tau,\kappa\right)e^{i\omega t}\,\mathrm{d}\omega \tag{4.42}$$

with

$$\begin{aligned}R\left(\omega,\gamma,\tau,\kappa\right)&=U_{c+}\left(\omega\right)-U_b^{\star}\left(\omega,\gamma,\tau,\kappa\right)\\&=U_c\left(\omega\right)-U_b^{\star}\left(\omega,\gamma,\tau,\kappa\right)+U_+\left(\omega\right)\\&=S(\omega)\left(\sum\nolimits_j e^{-i\omega\left(t_j\gamma+\tau\right)}\left(H_j^c\left(\omega\right)-\kappa H_j^b\left(\omega/\gamma\right)\right)+e^{-i\omega\left(t_+\gamma+\tau\right)}H_+\left(\omega\right)\right)\end{aligned} \tag{4.43}$$

The residual signal after compensation is therefore given by

$$r\left(t,\gamma,\tau,\kappa\right)=\sum\nolimits_j\left(h_j^c-\kappa h_j^{b\star}\right)*s\left(t-t_j\gamma-\tau\right)+h_+*s\left(t-t_+\gamma-\tau\right) \tag{4.44}$$

where the compensated baseline discontinuity impulse response is given by

$$h_j^{b\star}(t)=\int_{-\infty}^{\infty}H_j^b\left(\omega/\gamma\right)e^{i\omega t}\,\mathrm{d}\omega \tag{4.45}$$

It is of interest to show whether the BSS technique highlights or hides the damage growth echo. To do so, it is necessary to derive analytical expressions for the scaling factor κ, the stretch factor γ, and the delay time τ that minimise the SS $r_{SS}\left(\gamma,\tau,\kappa\right)$ of the residual signal, and show the outcome of substituting these expressions in the residual signal of equation 4.44.

From equations 4.42 and 4.44, it follows that the SS of the residual signal is given by

$$r_{SS}=\left(\gamma,\tau,\kappa\right)\int\left(\sum\nolimits_j\left(h_j^c-\kappa h_j^{b\star}\right)*s\left(t-t_j\gamma-\tau\right)+h_+*s\left(t-t_+\gamma-\tau\right)\right)^2\mathrm{d}t \tag{4.46}$$

Expanding the squared term inside the integral yields, after some manipulation

$$\begin{aligned}r_{SS}\left(\gamma,\tau,\kappa\right)=&\int\left(\sum\nolimits_j h_j^c*s\left(t-t_j\gamma-\tau\right)\right)^2\mathrm{d}t\\&+\kappa^2\int\left(\sum\nolimits_j h_j^{b\star}*s\left(t-t_j\gamma-\tau\right)\right)^2\mathrm{d}t\\&+\int\left(h_+*s\left(t-t_+\gamma-\tau\right)\right)^2\mathrm{d}t\\&-2\kappa\int\left(\sum\nolimits_j h_j^c*s\left(t-t_j\gamma-\tau\right)\right)\left(\sum\nolimits_j h_j^{b\star}*s\left(t-t_j\gamma-\tau\right)\right)\mathrm{d}t\\&+2\int\left(\sum\nolimits_j h_j^c*s\left(t-t_j\gamma-\tau\right)\right)\left(h_+*s\left(t-t_+\gamma-\tau\right)\right)\mathrm{d}t\\&-2\kappa\int\left(\sum\nolimits_j h_j^{b\star}*s\left(t-t_j\gamma-\tau\right)\right)\left(h_+*s\left(t-t_+\gamma-\tau\right)\right)\mathrm{d}t\end{aligned} \tag{4.47}$$

Because of the Leibniz integral rule it is easy to see that the first derivatives of $r_{SS}\left(\gamma,\tau,\kappa\right)$ with respect to γ and τ are of the form

$$\begin{aligned}\frac{\partial r_{SS}\left(\gamma,\tau,\kappa\right)}{\partial\gamma} = & -2\int\left(\sum\nolimits_j h_j^c * s\left(t-t_j\gamma-\tau\right)\right)\left(\sum\nolimits_j h_j^c * \frac{\partial s\left(t-t_j\gamma-\tau\right)}{\partial\gamma}t_j\right)\mathrm{d}t\\ & -2\kappa^2\int\left(\sum\nolimits_j h_j^{b\star} * s\left(t-t_j\gamma-\tau\right)\right)\left(\sum\nolimits_j h_j^{b\star} * \frac{\partial s\left(t-t_j\gamma-\tau\right)}{\partial\gamma}t_j\right)\mathrm{d}t\\ & -2\int\left(h_+ * s\left(t-t_+\gamma-\tau\right)\right)\left(h_+ * \frac{\partial s\left(t-t_+\gamma-\tau\right)}{\partial\gamma}t_+\right)\mathrm{d}t+\ldots\end{aligned}\tag{4.48}$$

$$\begin{aligned}\frac{\partial r_{SS}\left(\gamma,\tau,\kappa\right)}{\partial\tau} = & -2\int\left(\sum\nolimits_j h_j^c * s\left(t-t_j\gamma-\tau\right)\right)\left(\sum\nolimits_j h_j^c * \frac{\partial s\left(t-t_j\gamma-\tau\right)}{\partial\tau}\right)\mathrm{d}t\\ & -2\kappa^2\int\left(\sum\nolimits_j h_j^{b\star} * s\left(t-t_j\gamma-\tau\right)\right)\left(\sum\nolimits_j h_j^{b\star} * \frac{\partial s\left(t-t_j\gamma-\tau\right)}{\partial\tau}\right)\mathrm{d}t\\ & -2\int\left(h_+ * s\left(t-t_+\gamma-\tau\right)\right)\left(h_+ * \frac{\partial s\left(t-t_+\gamma-\tau\right)}{\partial\tau}\right)\mathrm{d}t+\ldots\end{aligned}\tag{4.49}$$

while it can be seen at once that the first derivative of $r_{SS}\left(\gamma,\tau,\kappa\right)$ with respect to κ is given by

$$\begin{aligned}\frac{\partial r_{SS}\left(\gamma,\tau,\kappa\right)}{\partial\kappa} = & \,2\kappa\int\left(\sum\nolimits_j h_j^{b\star} * s\left(t-t_j\gamma-\tau\right)\right)^2\mathrm{d}t\\ & -2\int\left(\sum\nolimits_j h_j^c * s\left(t-t_j\gamma-\tau\right)\right)\left(\sum\nolimits_j h_j^{b\star} * s\left(t-t_j\gamma-\tau\right)\right)\mathrm{d}t\\ & -2\int\left(\sum\nolimits_j h_j^{b\star} * s\left(t-t_j\gamma-\tau\right)\right)\left(h_+ * s\left(t-t_+\gamma-\tau\right)\right)\mathrm{d}t\end{aligned}\tag{4.50}$$

The SS of the residual signal $r_{SS}\left(\gamma,\tau,\kappa\right)$ will reach its minimum when its first derivatives nullify. This condition yields a system of three equations in three variables whose solution will yield analytical expressions for the scaling factor κ, the stretch factor γ and the delay time τ that minimise $r_{SS}\left(\gamma,\tau,\kappa\right)$ and that therefore should minimise the amplitude of the artefact echoes in the residual signal.

For illustrative purposes, assume that all pipeline discontinuities have a frequency independent response $H_j^b\left(\omega\right)=H_j^b\left(\omega/\gamma\right)=a_j^b$ and $H_j^c\left(\omega\right)=a_j^c$, with $0<a_j^b,a_j^c,a_+<1$. Then the above expressions simplify considerably, and the first derivative of $r_{SS}\left(\gamma,\tau,\kappa\right)$ with respect to κ becomes

$$\begin{aligned}\frac{\partial r_{SS}\left(\gamma,\tau,\kappa\right)}{\partial\kappa} = & \,2\kappa\int\left(\sum\nolimits_j a_j^b s\left(t-t_j\gamma-\tau\right)\right)^2\mathrm{d}t\\ & -2\int\left(\sum\nolimits_j a_j^c s\left(t-t_j\gamma-\tau\right)\right)\left(\sum\nolimits_j a_j^b s\left(t-t_j\gamma-\tau\right)\right)\mathrm{d}t\\ & -2\int\left(\sum\nolimits_j a_j^b s\left(t-t_j\gamma-\tau\right)\right)\left(a_+ s\left(t-t_+\gamma-\tau\right)\right)\mathrm{d}t\end{aligned}\tag{4.51}$$

or, after expanding the terms in the integrals

$$\begin{aligned}\frac{\partial r_{SS}(\gamma,\tau,\kappa)}{\partial\kappa} &= 2\kappa\sum\nolimits_j\left(a_j^b\right)^2\int\left(s\left(t-t_j\gamma-\tau\right)\right)^2\,\mathrm{d}t\\ &+2\kappa\sum\nolimits_{j\neq g}a_j^b a_g^b\int\left(s\left(t-t_j\gamma-\tau\right)s\left(t-t_g\gamma-\tau\right)\right)\mathrm{d}t\\ &-2\sum\nolimits_j a_j^c a_j^b\int\left(s\left(t-t_j\gamma-\tau\right)^2\right)\mathrm{d}t\\ &-2\sum\nolimits_{j\neq g}a_j^c a_g^b\int\left(s\left(t-t_j\gamma-\tau\right)s\left(t-t_g\gamma-\tau\right)\right)\mathrm{d}t\\ &-2a_+\sum\nolimits_j a_j^b\int\left(s\left(t-t_j\gamma-\tau\right)s\left(t-t_+\gamma-\tau\right)\right)\mathrm{d}t\end{aligned}\tag{4.52}$$

For any echo, after an appropriate change of variable $t\to t-t_j\gamma-\tau$ or $t\to t-t_+\gamma-\tau$, it is trivial to verify that

$$\Gamma=\int\left(s(t)\right)^2\,\mathrm{d}t=\int\left(s\left(t-t_j\gamma-\tau\right)\right)^2\,\mathrm{d}t=\int\left(s\left(t-t_+\gamma-\tau\right)\right)^2\,\mathrm{d}t\tag{4.53}$$

which is constant independent of the values of γ and τ. For convenience, define

$$\Gamma_{j,g}=\int\left(s\left(t-t_j\gamma-\tau\right)s\left(t-t_g\gamma-\tau\right)\right)\mathrm{d}t\tag{4.54}$$

and

$$\Gamma_{j,+}=\int\left(s\left(t-t_j\gamma-\tau\right)s\left(t-t_+\gamma-\tau\right)\right)\mathrm{d}t\tag{4.55}$$

The first derivative of $r_{SS}(\gamma,\tau,\kappa)$ with respect to κ then simplifies to

$$\begin{aligned}\frac{\partial r_{SS}(\gamma,\tau,\kappa)}{\partial\kappa} &= 2\kappa\left(\sum\nolimits_j\left(a_j^b\right)^2\Gamma+\sum\nolimits_{j\neq g}a_j^b a_g^b\Gamma_{j,g}\right)\\ &-2\left(\sum\nolimits_j a_j^c a_j^b\Gamma+\sum\nolimits_{j\neq g}a_j^c a_g^b\Gamma_{j,g}\right)\\ &-2a_+\sum\nolimits_j a_j^b\Gamma_{j,+}\end{aligned}\tag{4.56}$$

and by equating it to zero it is possible to derive at once an analytical expression

$$\hat{\kappa}=\frac{\sum\nolimits_j a_j^c a_j^b\Gamma+\sum\nolimits_{j\neq g}a_j^c a_g^b\Gamma_{j,g}+a_+\sum\nolimits_j a_j^b\Gamma_{j,+}}{\sum\nolimits_j\left(a_j^b\right)^2\Gamma+\sum\nolimits_{j\neq g}a_j^b a_g^b\Gamma_{j,g}}\tag{4.57}$$

for the estimate $\hat{\kappa}$ of κ that minimises the SS of the residual signal $r_{SS}(\gamma,\tau,\kappa)$ and therefore minimises the amplitude of the artefact echoes in the residual signal.

Under the simplifying assumption that all pipeline discontinuities have a frequency independent response $H_j^b(\omega)=H_j^b(\omega/\gamma)=a_j^b$ and $H_j^c(\omega)=a_j^c$, with $0<a_j^b,a_j^c,a_+<1$, and that the echoes $a_j^c = \kappa a_j^b \; \forall \; j$ in the current signal, other than the one from damage growth, are scaled, shifted and delayed versions of the echoes in the baseline signal, it follows that

$$\begin{aligned}\hat{\kappa} &= \frac{\kappa \sum_j \left(a_j^b\right)^2 \Gamma + \kappa \sum_{j \neq g} a_j^b a_g^b \Gamma_{j,g} + a_+ \sum_j a_j^b \Gamma_{j,+}}{\sum_j \left(a_j^b\right)^2 \Gamma + \sum_{j \neq g} a_j^b a_g^b \Gamma_{j,g}} \\ &= \kappa + \frac{a_+ \sum_j a_j^b \Gamma_{j,+}}{\sum_j \left(a_j^b\right)^2 \Gamma + \sum_{j \neq g} a_j^b a_g^b \Gamma_{j,g}} \end{aligned} \tag{4.58}$$

from which it can be concluded that the estimate $\hat{\kappa}$ of κ that minimises the SS of the residual signal $r_{SS}(\gamma, \tau, \kappa)$ differs from its true value by

$$\frac{a_+ \sum_j a_j^b \Gamma_{j,+}}{\sum_j \left(a_j^b\right)^2 \Gamma + \sum_{j \neq g} a_j^b a_g^b \Gamma_{j,g}} \tag{4.59}$$

It is easy to verify that were $\hat{\kappa}$ to be equal to $\kappa = a_j^c / a_j^b$, the residual signal after BSS compensation would become

$$\begin{aligned} r(t, \gamma, \tau, \hat{\kappa}) &= \sum_j \left(a_j^c - \kappa a_j^b\right) s\left(t - t_j \gamma - \tau\right) + a_+ s\left(t - t_+ \gamma - \tau\right) \\ &= a_+ s\left(t - t_+ \gamma - \tau\right) \end{aligned} \tag{4.60}$$

and therefore would include solely the echo from the damage growth.

It has therefore been proven that, even under the most simplifying of assumptions, in the presence of damage growth the estimate $\hat{\kappa}$ of the scaling factor κ that minimises the SS of the residual signal $r_{SS}(\gamma, \tau, \kappa)$ will differ from the ideal value that would minimise the amplitude of the artefact echoes and highlight the damage growth echo in the residual signal. It follows from equations 4.49 and 4.48 that the estimates $\hat{\gamma}$ and $\hat{\tau}$ of respectively the scaling factor γ and the delay τ that minimise the SS of the residual signal $r_{SS}(\gamma, \tau, \kappa)$ will also differ from their ideal values if only because they are also functions of the scaling factor κ. It can therefore be concluded that the estimates $\hat{\kappa}$, $\hat{\gamma}$ and $\hat{\tau}$ that minimise $r_{SS}(\gamma, \tau, \kappa)$ will in general differ from the ideal values, and consequently that the residual signal $r(t, \hat{\gamma}, \hat{\tau}, \hat{\kappa})$ will include artefact echoes as well as an altered version of the damage growth echo as a result of the attempt to minimise the amplitude of the artefact echoes in the residual signal by utilising BSS, a sub-optimal compensation technique for operating temperature variations. The sub-optimality of the BSS technique originates from a lack of knowledge of the frequency response of all pipeline features and pre-existing damage before and after a uniform operating temperature variation, as previously discussed.

Lastly, it is of interest to analyse the conditions under which the expression in equation 4.59 vanishes and therefore the difference between the estimate $\hat{\kappa}$ of the scaling factor κ and its ideal value disappears. The value of Γ has been shown to be constant irrespective of the values of γ and τ, and so are the frequency independent pipeline discontinuity responses a_j^b. Therefore the expression in equation 4.59 will increase when $\Gamma_{j,g}$ decreases, when $\Gamma_{j,+}$ increases and when the amplitude a_+ of the damage growth echo increases. Conversely, the expression in equation 4.59 will decrease when $\Gamma_{j,g}$ increases, when $\Gamma_{j,+}$ decreases and when the amplitude a_+ of the damage growth echo decreases.

Moreover, the value of

$$\Gamma_{j,+} = \int \left(s\left(t - t_j\gamma - \tau\right) s\left(t - t_+\gamma - \tau\right) \right) \mathrm{d}t \tag{4.61}$$

is a function of the difference $t_j - t_+$ between the arrival time of the damage growth echo and of the j^{th} echo. Clearly

$$\lim_{t_j - t_+ \to 0} s\left(t - t_j\gamma - \tau\right) = s\left(t - t_+\gamma - \tau\right) \tag{4.62}$$

and it follows that

$$\lim_{t_j - t_+ \to 0} \Gamma_{j,+} = \int \left(s\left(t - t_j\gamma - \tau\right) \right)^2 \mathrm{d}t = \Gamma \tag{4.63}$$

since in this case the damage growth echo would be perfectly in phase with the j^{th} echo. Conversely, if $\left|t_j - t_+\right| \geq \tau_s$, where τ_s is the length of the transmitted wave packet $s(t)$, then $\Gamma_{j,+} = 0$ since in this case the damage growth echo and the j^{th} echo would be distinct. Therefore, the expression in equation 4.59, and thus the difference between the estimate $\hat{\kappa}$ of the scaling factor κ and its ideal value, vanishes when the damage growth echo is distinct from all the other echoes, and therefore when damage growth occurs well away from pipeline features and pre-existing damage. However, such a scenario is unlikely to occur in practice because of the presence of coherent noise in the signal. Conversely, the expression in equation 4.59 is maximised when damage grows at or near pipeline features and pre-existing damage.

Figure 4.11 exemplifies the detrimental effect of BSS compensation combined with damage growth near pipeline features or pre-existing damage. The signals have been synthetically generated for illustrative purposes, and consist in the sum of several Hann-windowed tonebursts with different amplitudes. The baseline signal can therefore be expressed as

$$u_b(t) = \sum\nolimits_j a_j * s\left(t - t_j\right) \tag{4.64}$$

while the current signal can be expressed as

$$u_c(t) = \sum\nolimits_j a_j * s\left(t - t_j\gamma\right) + a_+ s\left(t - t_+\gamma\right) \tag{4.65}$$

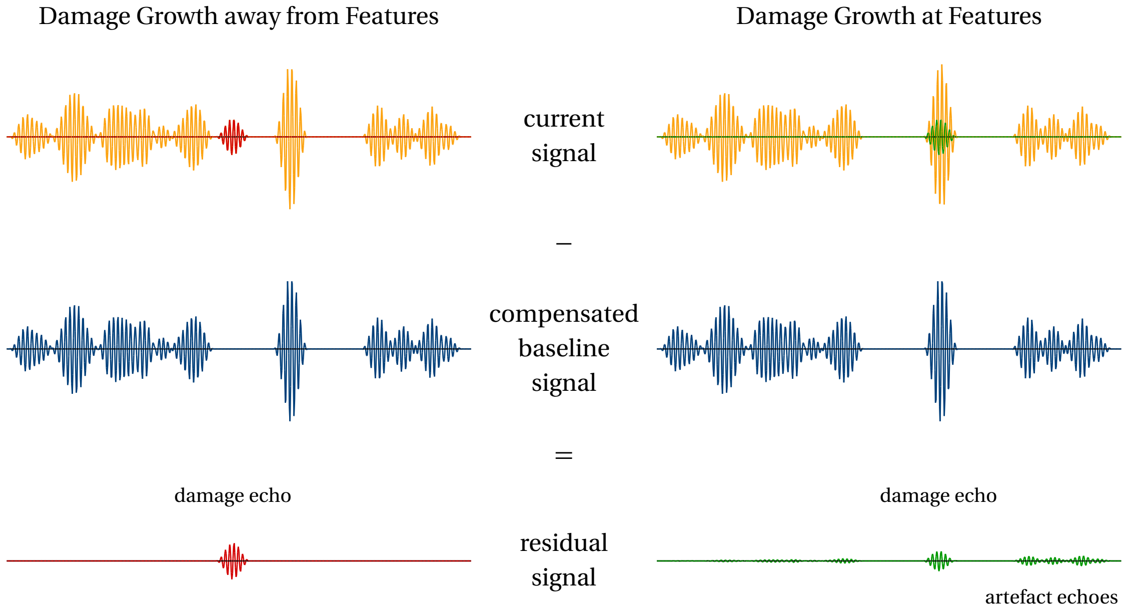

Figure 4.11: Diagram with synthetic signals exemplifying damage growth away from (left) and at (right) pipeline features: in the first case the amplitude of the damage growth echo in the residual signal after Baseline Signal Stretch (BSS) compensation remains unaltered, while in the other it is reduced and artefact echoes also appear.

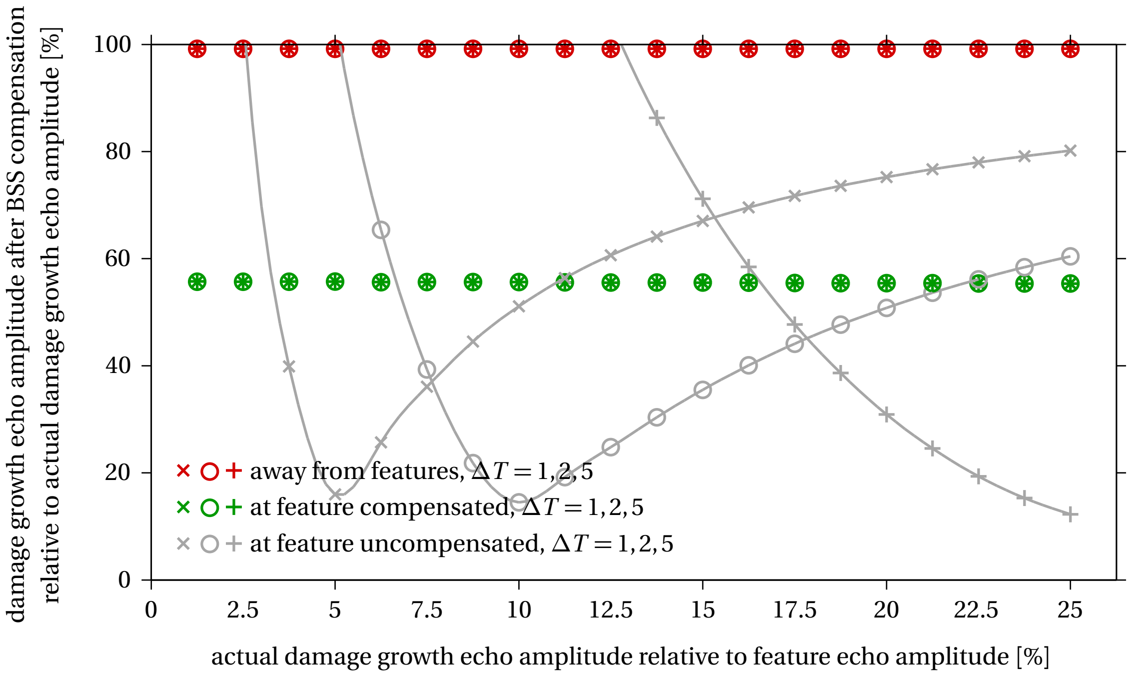

Figure 4.12: Amplitude of the damage growth echo in the residual signal after BSS compensation relative to the actual amplitude of the damage growth echo, as a function of damage growth location and of the temperature difference ΔT between current and baseline signals.

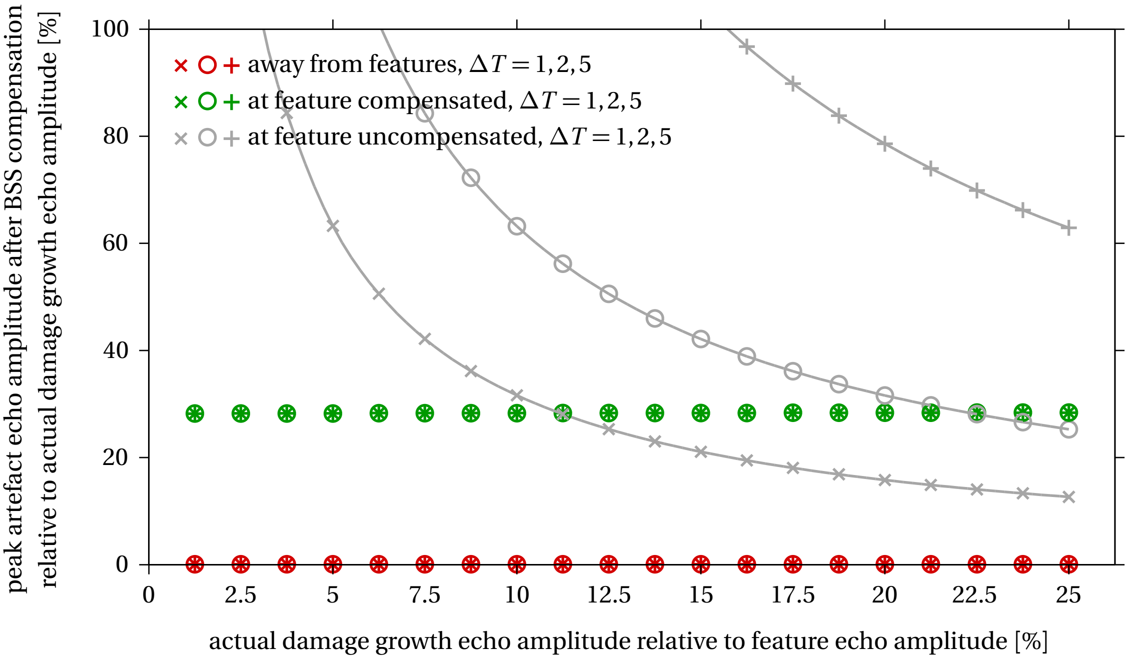

Figure 4.13: Peak amplitude of the artefact echoes in the residual signal with BSS compensation relative to the actual amplitude of the damage growth echo, as a function of damage growth location and of the temperature difference ΔT between current and baseline signals.

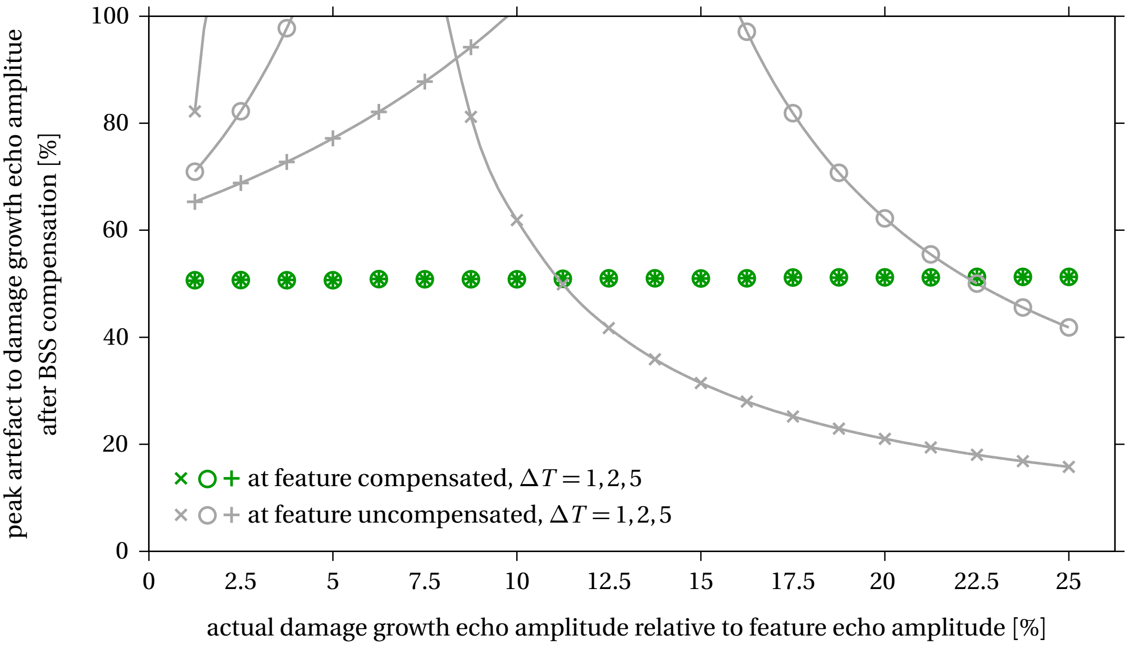

Figure 4.14: Relative amplitude of the peak artefact to the damage growth echo in the residual signal as a function of damage size, of the use of BSS compensation and of the temperature difference ΔT between current and baseline signals.

where a_+ and t_+ are respectively the amplitude and the time of arrival of the damage growth echo, and γ is the factor expressing the change in arrival time caused by a uniform operating temperature variation. Of the two examples in figure 4.11, in one case damage grows away from all pipeline discontinuities, while in the other case damage grows at a feature. It can be seen that the residual signal after BSS compensation in the first case contains solely the unaltered damage growth echo, while in the other case it contains a number of artefact echoes and the amplitude of the damage growth echo is significantly reduced.

Irrespective of the uniform operating temperature difference ΔT between current and baseline signals and of the amplitude a_+ of the damage growth echo, for the signals of figure 4.11 it is shown in figure 4.12 that when damage grows at a feature the amplitude of its echo in the residual signal after BSS compensation is about 55% of its actual value, and it is shown in figure 4.13 that the peak amplitude of the artefact echoes in the residual signal after BSS compensation is about 30% of the actual amplitude of the damage growth echo.

By comparison, provided that the damage echo is relatively big and the temperature difference ΔT between current and baseline signals remains small, it can be seen in figure 4.12 that when damage grows at a feature the amplitude of the damage growth echo in the residual signal is closer to its true value when no compensation for operating temperature differences is applied than when BSS compensation is applied. Moreover, figure 4.13 shows that under the same circumstances the peak amplitude of the artefact echoes in the residual signal is lower when no compensation for operating temperature differences is applied than when BSS compensation is applied.

Figure 4.14, which shows the relative amplitude of the peak artefact to the damage growth echo, indicates that when damage is relatively large and the temperature difference ΔT between current and baseline signals remains small, damage growing at a feature is more prominent among the artefact echoes in the residual signal when no operating temperature compensation is applied. Conversely, when damage is relatively small and the temperature difference ΔT between current and baseline signals becomes large, it can be seen from figure 4.14 that damage growing at a feature is more prominent among the artefact echoes in the residual signal when BSS compensation is applied.

In conclusion, figures 4.12, 4.13 and 4.14 indicate clearly that if one seeks to detect small damage at features then one is more likely to find indications of it by applying BSS compensation, and conversely that if one seeks to detect large damage at features then one is more likely to find indications of it by not applying operating temperature compensation provided that the operating temperature of the pipe under consideration remains roughly constant.

Note that the relative echo amplitude values, and therefore the actual benefit or hindrance of applying BSS compensation, will in general vary depending on the baseline component of the signals, and therefore on the pipeline, under consideration. The values presented in figures 4.12, 4.13 and 4.14 are for the baseline component of the signals of figure 4.11.

Finally, the value of

$$\Gamma_{j,g} = \int \left(s\left(t - t_j\gamma - \tau\right) s\left(t - t_g\gamma - \tau\right)\right) \mathrm{d}t \tag{4.66}$$

is a function of the difference $t_j - t_g$ between the arrival time of the j^{th} and g^{th} echoes. Clearly

$$\lim_{t_j - t_g \to 0} s\left(t - t_j\gamma - \tau\right) = s\left(t - t_g\gamma - \tau\right) \tag{4.67}$$

and it follows that

$$\lim_{t_j - t_g \to 0} \Gamma_{j,g} = \int \left(s\left(t - t_j\gamma - tau\right)\right)^2 \mathrm{d}t = \Gamma \tag{4.68}$$

since in this case the j^{th} and g^{th} echoes would be perfectly in phase. Conversely, if $\left|t_j - t_g\right| \geq \tau_s$, where τ_s is the length of the transmitted wave packet $s(t)$, then $\Gamma_{j,g} = 0$ since in this case the j^{th} and g^{th} echoes would be distinct. Therefore, the expression in equation 4.59, and thus the difference between the estimate $\hat{\kappa}$ of the scaling factor κ and its ideal value, is maximised when pipeline discontinuity echoes are distinct from each other, and is minimised when pipeline discontinuity echoes are very close to each other.

Figure 4.15 exemplifies the detrimental effect of BSS compensation combined with damage growth near pipeline features or pre-existing damage when pipeline features are sparse. The signals have been synthetically generated for illustrative purposes, and consist in the sum of six Hann-windowed tone-bursts with different amplitudes. The baseline signal can therefore be expressed as

$$u_b(t) = \sum\nolimits_j a_j * s\left(t - t_j\right) \tag{4.69}$$

while the current signal can be expressed as

$$u_c(t) = \sum\nolimits_j a_j * s\left(t - t_j\gamma\right) + a_+ s\left(t - t_+\gamma\right) \tag{4.70}$$

where a_+ and t_+ are respectively the amplitude and the time of arrival of the damage growth echo, and γ is the factor expressing the change in arrival time caused by a uniform operating temperature variation. Of the two examples in figure 4.15, in one case five of the tone-bursts overlap to simulate closely-spaced pipeline features, while in the other case the same five tone-bursts are distinct from each other to simulate sparse pipeline features. It can be seen

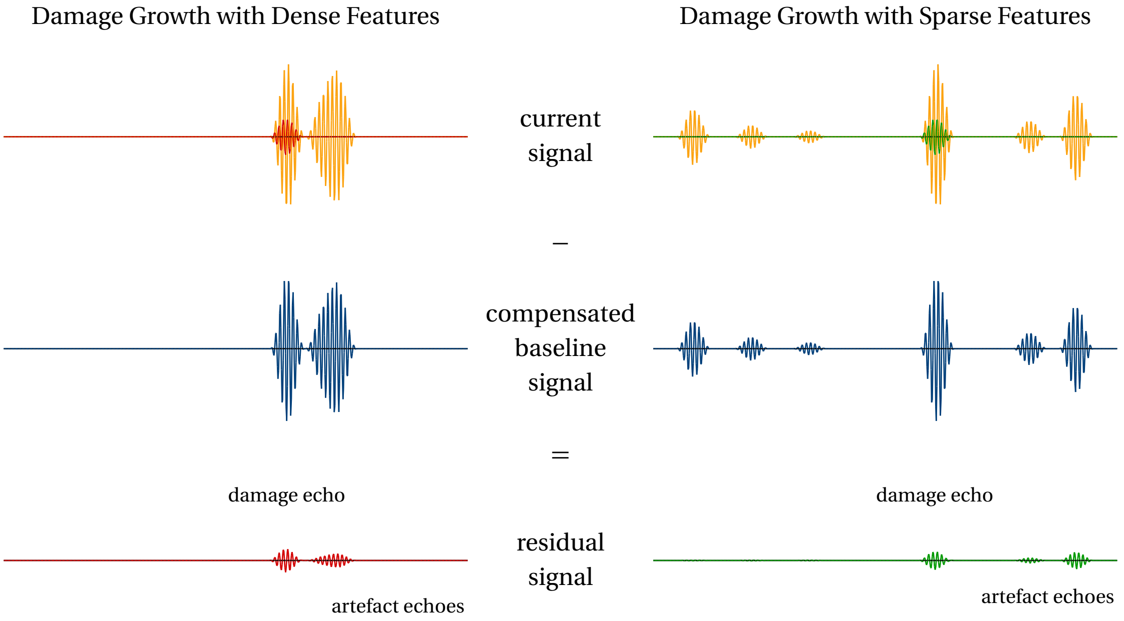

Figure 4.15: Diagram with synthetic signals exemplifying damage growth with dense (left) and sparse (right) pipeline features: in both cases the amplitude of the damage growth echo in the residual signal after Baseline Signal Stretch (BSS) compensation is reduced and artefact echoes appear, but in the first case these effects are less severe.

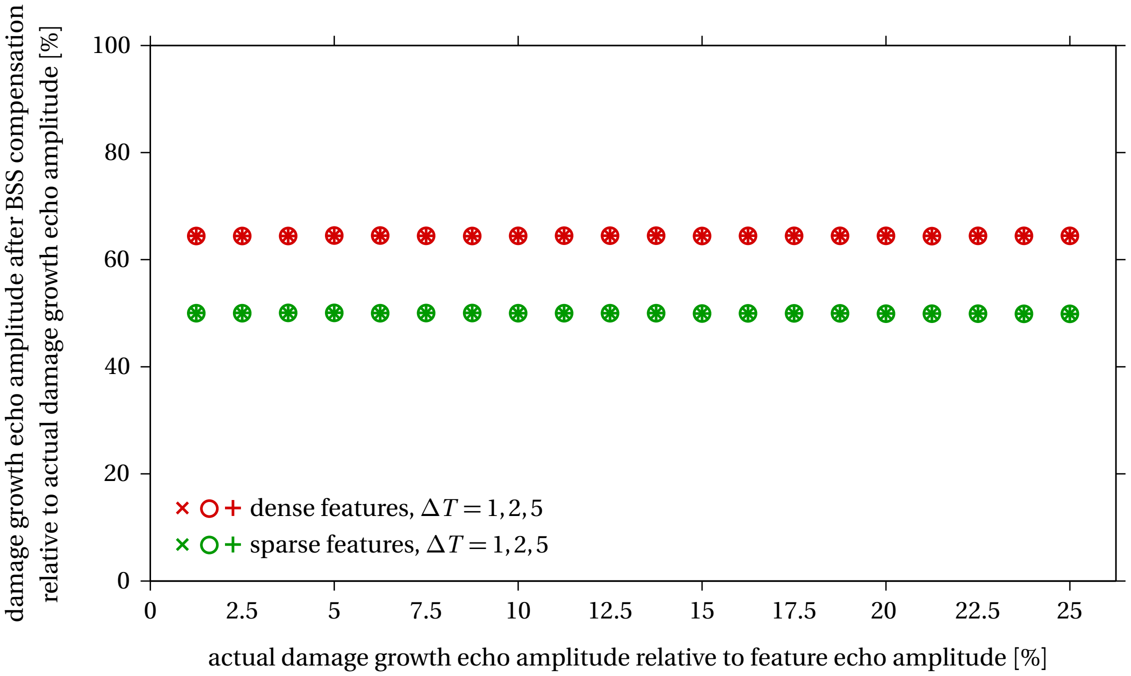

Figure 4.16: Amplitude of the damage growth echo in the residual signal after BSS compensation relative to the actual amplitude of the damage growth echo, as a function of the density of features and of the temperature difference ΔT between current and baseline signals.

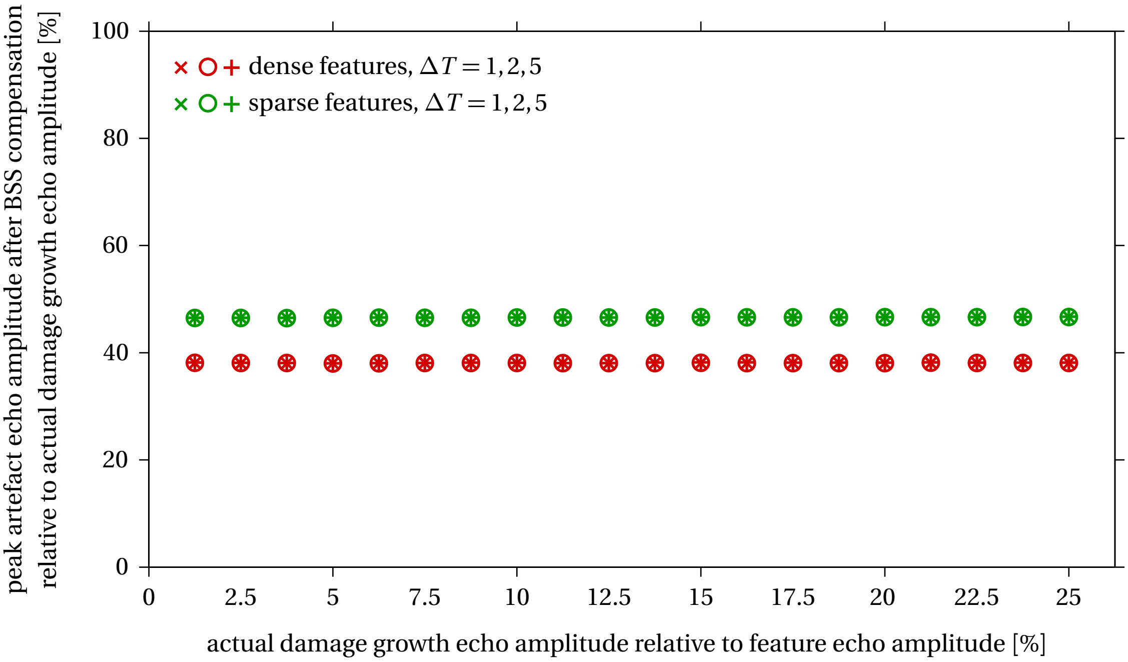

Figure 4.17: Peak amplitude of the artefact echoes in the residual signal with BSS compensation relative to the actual amplitude of the damage growth echo, as a function of the density of features and of the temperature difference ΔT between current and baseline signals.

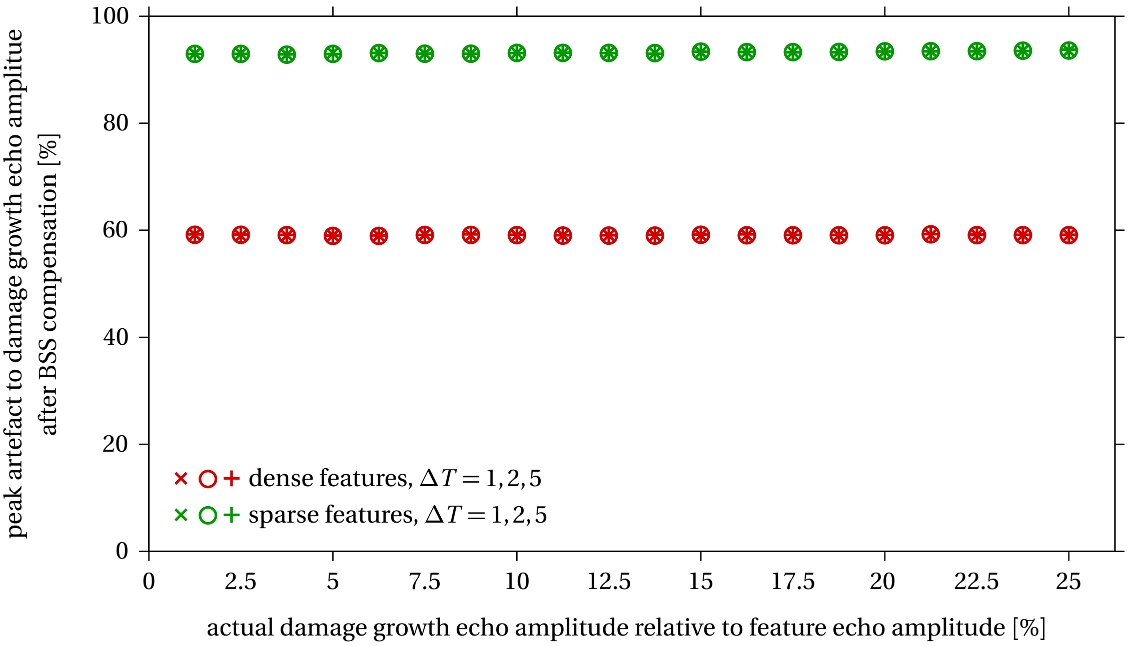

Figure 4.18: Relative amplitude of the peak artefact to the damage growth echo in the residual signal as a function of damage size, of the density of features and of the temperature difference ΔT between current and baseline signals.

that in both cases residual signal obtained after BSS compensation contains an altered damage growth echo as well as a number of artefact echoes. However, in the first case these effect are less severe.

Irrespective of the temperature difference ΔT between current and baseline signals and of the amplitude a_+ of the damage growth echo, for the signals of figure 4.15 it is shown in figure 4.16 that when damage grows at a feature and pipeline features are dense the amplitude of the damage echo in the residual signal after BSS compensation is about 65% of its actual value, while when those same pipeline features are sparse the amplitude of the damage growth echo falls to about 50% of its actual value. Moreover, figure 4.17 indicates that the peak amplitude of the artefact echoes in the residual signal after BSS compensation is about 37% of the actual amplitude of the damage growth echo when pipeline features are dense, and about 45% of the actual amplitude of the damage growth echo when those same pipeline features are sparse.

Therefore, it can be concluded from figure 4.18, which shows the relative amplitude of the peak artefact to the damage growth echo, that damage growing at a feature is more prominent among the artefact echoes in the residual signal after BSS compensation when pipeline discontinuities are dense than when they sparse, irrespective of the temperature difference ΔT between current and baseline signals and of damage size.

In summary, it has been proven that compensating for changes in transduction efficiency and for jitter, and partially compensating for variations in echo arrival time can have a detrimental impact as it could in general alter the damage growth echo and introduce artefact echoes in the residual signal. The impact is minimised when the damage growth echo has an amplitude that is small relative to the amplitude of all the other pipeline discontinuity echoes and when damage grows away from other pipeline discontinuities, in which case the impact is further reduced if the pipeline discontinuities are closely-spaced and their echoes overlap each other. It has also been exemplified that the use of BSS compensation is especially beneficial when damage is relatively small and the temperature difference between the current and baseline signals becomes large, and that when damage is extensive and the temperature difference between the current and baseline signals remains limited then the use of BSS compensation could prove to be detrimental.

There is a fundamental practical implication that stems from this analysis. Clearly, the expression in equation 4.59 will tend to zero when $a_j \gg a_+ \; \forall \; j$, or in other words when the amplitude of the damage growth echo is much smaller than the amplitude of all the other pipeline discontinuity echoes. It follows that for the Localised Baseline Signal Stretch (LBSS) technique to be successful, the gate functions must be chosen so that each contains at least one major reflector so that the condition $a_j \gg a_+ \ \forall \ j$ holds and therefore the difference between the estimate $\hat{\kappa}$ of the scaling factor κ and its ideal value disappears.

There is also another subtle practical implication that stem from this analysis. Note that in principle, when there is no damage growth, and therefore when $a_+ = 0$, the expression in equation 4.59 nullifies and the estimate $\hat{\kappa}$ of the scaling factor κ is equal to its ideal value. Conversely, if the damage growth echo is of a comparable size to the echoes from pipeline features and pre-existing damage, then the estimate $\hat{\kappa}$ will be significantly different from its true value. As was previously discussed in section 4.4.1, echoes from all pipeline features and pre-existing damage are in practice temperature dependent, if only because they are a function of material damping which is notoriously temperature dependent. Such dependence is equivalent, from a mathematical standpoint, to damage growth at a feature, since the current feature echo following a change in operating temperature can be thought of as the sum of the baseline feature echo plus a damage growth echo. It follows that the use of BSS compensation will in general introduce artefact echoes in the residual signal. As figure 4.13 exemplifies, the greater the amplitude of the damage-equivalent echo, *i.e.* the variability of the echo from a pipeline features or pre-existing damage, the bigger the peak amplitude of artefact echoes in the residual signal.

4.4.5 Summary

In this section the formal mathematical foundations for analysing the effects of operating temperature variations on the signals recorded by permanently installed guided wave sensors have been laid and have been utilised to introduce the novel Localised Baseline Signal Stretch (LBSS) technique, which is an extension of the Baseline Signal Stretch (BSS) technique already discussed by other authors [115–117, 119] designed to compensate for uniform and non-uniform operating temperature variations along a pipeline.

Interestingly, the examples of typical baseline subtraction scenarios presented in this section suggest that the two distinct Optimal Baseline Selection (OBS) and BSS or LBSS steps that form the basis of common baseline subtraction compensation procedures [115–117, 119] should be integrated to maximise their effect, although a thorough systematic test is still required to obtain definitive proof.

Notably, a thorough analysis has been made of the side-effects that baseline subtraction compensation procedures, and in particular BSS and LBSS, might have in practical situations. It has been proven and extensively exemplified that baseline subtraction compensation may need to be utilised with care since it is only effective when the echoes from damage growth in the recorded signals are small compared to the echoes from features and pre-existing damage. In a practical SHM application, such as a permanently installed guided wave sensor monitoring a petrochemical pipeline, the use of baseline subtraction compensation is therefore always advisable because the typical petrochemical damage mechanisms operate relatively slowly, and consequently the echoes from damage growth will tend to remain quite small compared to the echoes from features and pre-existing damage. As will be discussed in chapter 6 and in section 6.3 in particular, when damage growth is very small the use of BSS compensation can be crucial to successfully detect it even when the Environmental and Operational Conditions (EOC) are precisely controlled.

Importantly, as previously discussed the outlined baseline subtraction procedure involving OBS and LBSS cannot compensate exactly for EOC variations such as operating temperature variations, changes in coherent noise and the changing echoes from certain types of pipeline features, and therefore **uncompensated EOC effects** in the form of artefact echoes will always be present in residual signals.

4.5 Uncompensated EOC Effects

As previously discussed, the effect of EOC variations on a signal recorded by a permanently installed guided wave sensor is extremely complex and unpredictable, and although compensation procedures such as OBS and LBSS exist, it has been demonstrated that these can at best only compensate partially for EOC variations, which can nevertheless be just as strong a source of change in the baseline component of recorded signals as actual damage growth [103]. For example, it was proven that it is in practice impossible to compensate even for uniform changes in the propagation distance and velocity of guided waves caused by an idealised uniform temperature variation, let alone temperature gradients and other more complex EOC effects, because of an inherent lack of knowledge of the frequency response of all pipeline features and pre-existing damage.

Consequently, permanently installed guided wave sensors just as any other SHM sensor will to an extent measure EOC variations as well as damage growth, and although it is possible to partially compensate for some EOC variations [2, 102, 103, 115–124, 130, 131], it remains nevertheless true that **uncompensated EOC effects** will always feature in SHM sensor measurements together with any damage growth.

One way to address the issue of uncompensated EOC effects is through some form of intelligent feature extraction [2], which loosely speaking consists in identifying subsets or particular combinations of the damage-sensitive properties of a system that are solely sensitive to damage growth but not to EOC variations. Several intelligent feature extraction approaches have been tried in laboratory conditions with varying degrees of success [2, 103, 122, 130, 131]. However, to identify features that are insensitive to EOC variations these approaches rely on having hundreds of samples that in an industrial SHM scenario, such as in the case of a permanently installed guided wave sensor monitoring a pipeline, are unlikely to be available.

Alternatively, given a set of baseline samples one could feed these samples to a supervised learning algorithm to create a statistical model of the EOC effects [109, 130, 131]. Such a model could then in principle be utilised to remove EOC effects from future SHM sensor measurements. There are however several limitations to this approach. Importantly, this approach assumes that one is measuring the entire set of system parameters, such as temperature, loading, and others, that completely describe the behaviour of EOC effects so that for any value of these parameters the EOC effects could be exactly predicted and therefore removed from SHM sensor measurements. Moreover, this approach makes the no less important assumptions that enough baseline samples are available to capture and appropriately represent the vast majority of EOC effects so that the statistical model is truly descriptive of them. In practice these two assumptions quickly fall apart in an industrial SHM scenario, rendering this approach not viable. For example, in the case of a permanently installed guided wave sensor monitoring a pipeline many industrially observed EOC effects, particularly those involving changing echoes from complex features and supports, have sources that are in general not entirely clear, that typically vary from one pipeline to another and whose description therefore involves a vast yet incomplete set of parameters that is simply unfeasible to measure and control. It follows that even in principle it is extremely unlikely that enough baseline samples will be available to completely capture and represent EOC effects.

In conclusion, a different and more viable approach is therefore needed to address the issue of uncompensated EOC effects and enable effective damage detection in pipelines. The novel approach introduced in this thesis will be presented and demonstrated in chapter 6.

4.6 Conclusions

In this chapter, permanently installed guided wave sensors and baseline subtraction were introduced in section 4.1. Successively, section 4.2 introduced and explained the fundamental problem of damage detection, while section 4.3 explained the challenge that Environmental and Operational Conditions (EOC) variations represent to effective damage detection and ultimately effective SHM.

Successively, in section 4.4 the formal mathematical foundations for analysing the effects of operating temperature variations on the signals recorded by permanently installed guided wave sensors have been laid and have been utilised to introduce the novel Localised Baseline Signal Stretch (LBSS) technique, which is an extension of the Baseline Signal Stretch (BSS) technique already discussed by other authors [115–117, 119] designed to compensate for uniform and non-uniform operating temperature variations along a pipeline, and, more importantly, to conduct a thorough analysis of the side-effects that baseline subtraction compensation procedures, and in particular BSS and LBSS, might have in practical situations. It has been proven and extensively exemplified that baseline subtraction compensation may need to be utilised with care since it is only effective when the echoes from damage growth in the recorded signals are small compared to the echoes from features and pre-existing damage. In a practical SHM application, such as a permanently installed guided wave sensor monitoring a petrochemical pipeline, the use of baseline subtraction compensation is therefore always advisable because the typical petrochemical damage mechanisms operate relatively slowly, and consequently the echoes from damage growth will tend to remain quite small compared to the echoes from features and pre-existing damage. As will be discussed in chapter 6, and in section 6.3 in particular, when damage growth is very small the use of BSS compensation can be crucial to successfully detect it even when the EOC are precisely controlled.

Finally, section 4.5 summarised why uncompensated variations in EOC will invariably feature in the measurements from any SHM sensor, and illustrated what challenge this represents for effective SHM.

Chapter 5

Change Detection

Over the last few decades the development and increasing availability of sophisticated sensors and powerful information processing systems has resulted in a multiplication of monitoring and change detection applications [132, 133], many of which are of critical importance. Examples include production process quality control, condition-based maintenance of complex systems, monitoring of patient health condition, as well as the tracking of local and global environmental changes including catastrophic natural events such as earthquakes. The common problem of interest across all applications is the detection of anomalous or unexpected changes in the response of the sensors monitoring a system which may indicate that malfunctions or damage are developing.

In Structural Health Monitoring (SHM) applications, such as the health monitoring of petrochemical pipelines, the early detection and tracking of anomalous changes, and therefore of damage growth, is a fundamental prerequisite to enable the use of condition-based maintenance and consequently to reduce down-time and total cost of ownership. The earlier anomalous changes in the response of a SHM sensor are detected, the more time will be available to plan adequate maintenance interventions before failure occurs. Furthermore, by accurately tracking these changes over time it may become possible to estimate the remaining life of the monitored structure. The key challenge lies in detecting anomalous changes in the response of SHM sensors that may or may not be directly observable and that are invariably sampled together with other kinds of perturbations.

Typically, the response of a SHM sensor consists of a variable y. In the case of a permanently installed guided wave sensor the variable y is a vector representing the signal composed of the echoes originating from pipeline features as well as from damage. In general, when sampling a variable y over time t each gathered sample will be corrupted by some random noise ϵ. If μ represents its underlying true value, then y can be expressed as

$$y = \mu + \epsilon \tag{5.1}$$

Because the noise ϵ is a random variable, and μ is a deterministic if unknown variable, it follows that the sensor response y will also be a random variable with a certain probability distribution. Therefore, changes in the response of a sensor will be reflected by changes in the probability distribution of y.

In this chapter the most powerful algorithms for detecting changes in the probability distribution of random variables are reviewed in section 5.1, while sections 5.2 and 5.3 exemplify respectively step and gradual change detection in the case of a normally distributed random variable.

5.1 Change Detection Algorithms

Consider a random variable y, and assume that before an unknown change time t_c the probability density function of y is given by $p_0(y)$, and that after t_c the probability density function of y is given by $p_1(y)$. A change detection algorithm is a procedure to detect the onset of change in the probability density function of y and to estimate t_c. Formally, there are two possible change detection scenarios:

- **Simple Change Detection.** The first and simplest scenario is based on the principle of **simple hypothesis testing** and assumes that both $p_0(y)$ and $p_1(y)$ are known. Section 5.1.2 presents the Cumulative Sum (CUSUM) algorithm and describes how it can be utilised to detect the onset of simple change and estimate t_c.
- **Composite Change Detection.** The second, more complex scenario is based on the principle of **composite hypothesis testing** and assumes only $p_0(y)$ is known. Then, under the assumption that $p_1(y) = p(y \mid \theta_1)$ is a differently parameterised version of $p_0(y) = p(y \mid \theta_0)$, section 5.1.3 introduces the Generalised Likelihood Ratio (GLR) algorithm and shows how it can be utilised to estimate $p_1(y)$ as well as to detect the onset of change and estimate t_c.

Both the CUSUM and the GLR algorithms essentially consist of a repeated Sequential Probability Ratio Test (SPRT). The SPRT, summarised in section 5.1.1 and discussed in appendix

B, has been shown [134–136] to require the minimum amount of samples y_i to discriminate between hypotheses on the underlying probability density function of a random variable y for prescribed probabilities of error. In this sense, the SPRT is said to be **optimal**. Consequently, the CUSUM and the GLR algorithms are also **optimal**, in the sense that they require the minimum amount of samples y_i to detect whether the probability density function of y has changed from $p_0(y)$ to $p_1(y)$ for prescribed probabilities of error, thereby minimising the delay δ between change time t_c and detection time t_d.

5.1.1 Sequential Probability Ratio Test

Consider a random variable y, and consider the hypothesis $\mathbf{H}_0$ that the probability density function of y is given by $p_0(y)$ and an alternative hypothesis $\mathbf{H}_1$ that the probability density function of y is given by $p_1(y)$. Given these hypotheses, the log likelihood ratio

$$z = \ln \frac{p_1(y)}{p_0(y)} \tag{5.2}$$

is a function of y that will be negative if hypothesis $\mathbf{H}_0$ is true and positive if hypothesis $\mathbf{H}_1$ is true. The Neyman-Pearson lemma [137] implies that for a given amount of information the log likelihood ratio z is the most powerful test to discriminate between hypotheses $\mathbf{H}_0$ and $\mathbf{H}_1$. If $Y_m = \{y_1, y_2, \ldots, y_m\}$ is a finite set of samples y_i of y, and A and B are two positive constants such that $B < A$, at each sampling stage m the SPRT consists in evaluating the cumulative log likelihood ratio [138]

$$Z_m = \sum_{i=1}^{m} z_i = \sum_{i=1}^{m} \ln \frac{p_1(y_i)}{p_0(y_i)} \tag{5.3}$$

Hypothesis $\mathbf{H}_1$ is accepted if $Z_m \geq \ln A$, and hypothesis $\mathbf{H}_0$ is accepted if $Z_m \leq \ln B$. If $\ln B < Z_m < \ln A$ then sample y_{m+1} is collected and Z_{m+1} is evaluated for the extended sample set $Y_{m+1} = \{Y_m, y_{m+1}\}$. The SPRT will eventually terminate if the samples y_i are distributed independently and identically, but otherwise it might not terminate [138]. If it terminates, the SPRT is **optimal** in the sense that it minimises the amount of samples y_i required to accept either hypothesis $\mathbf{H}_0$ or $\mathbf{H}_1$ utilising the log likelihood ratio, which for a given amount of information, *i.e.* samples y_i and probability density functions $p_0(y)$ and $p_1(y)$, is the most powerful test to discriminate between hypotheses $\mathbf{H}_0$ and $\mathbf{H}_1$ [134–137, 139]. Further details can be found in appendix B.

Test Boundaries

Under the assumption that when the SPRT ends the excess of Z_m over either boundary $\ln A$ or $\ln B$ is negligible, it is shown in appendix section B.3 that the value of constants A and B is given by the **Wald boundaries**

$$A = \frac{1-\beta}{\alpha} \quad \text{and} \quad B = \frac{\beta}{1-\alpha} \tag{5.4}$$

A SPRT with **Wald boundaries** will have a probability equal to or lower than α of committing an error of the first kind, and a probability equal to or lower than β of committing an error of the second kind [135, 138]. An error of the first kind is the rejection of hypothesis $\mathbf{H}_0$ when it is true, while an error of the second kind is the rejection of hypothesis $\mathbf{H}_1$ when it is true. If hypothesis $\mathbf{H}_0$ represents the no change condition, then the probability α of rejecting the hypothesis $\mathbf{H}_0$ when it is true corresponds to the probability of detecting a change when there is none, *i.e.* to the probability of **false-calling**. Conversely, the probability β of rejecting hypothesis $\mathbf{H}_1$ when it is true corresponds to the probability of not detecting a change when there is one, *i.e.* to the probability of **non-detection**. It follows that $1-\beta$ represents the probability of **detection**.

Importantly, equation 5.4 reveals that decreasing the probabilities of **false-calling** α and of **non-detection** β increases the value of A and decreases the value of B, *i.e.* any decrease in the probabilities of committing an error widens the interval between A and B. Consequently, more samples y_i are needed for the SPRT to terminate with lower probabilities of committing an error because, intuitively, more information is required to take a decision with a lower probabilities of making a mistake. Note that $A \to \infty$ for $\alpha \to 0$, thereby obtaining a SPRT that can only accept of hypothesis $\mathbf{H}_0$. It follows that a SPRT will need to have a probability $\alpha > 0$ of **false-calling** for it to be able to accept hypothesis $\mathbf{H}_1$, and therefore be able to discriminate between hypotheses $\mathbf{H}_0$ and $\mathbf{H}_1$ and be useful for change detection purposes.

Finally, the assumption of negligible excess of Z_m over either boundary $\ln A$ or $\ln B$ is trivial, since the probabilities α of **false-calling** and β of **non-detection** can be reduced as needed to minimise any excess without negatively affecting the performance of the SPRT.

Average Sample Number

Assuming that when the SPRT ends the excess of Z_m over either boundary $\ln A$ or $\ln B$ is negligible, it is possible to calculate the expected value $\mathrm{E}[m]$ of the cardinality m of the finite sample set Y_m required for the SPRT to terminate with the acceptance of either hypothesis $\mathbf{H}_0$ or $\mathbf{H}_1$ when they are true. In appendix section B.4.1 it is shown that the expected value $\mathrm{E}[m]$, known as the Average Sample Number (ASN), is approximated by

$$\mathrm{E}[m] \approx \frac{L \ln B + (1-L) \ln A}{\mathrm{E}[z]} \tag{5.5}$$

where $\mathrm{E}[z]$ is the expected value of the log likelihood ratio z, and L, known as the Operating Characteristic (OC), describes the probability that the SPRT will terminate with the acceptance of hypothesis $\mathbf{H}_0$ as a function of whether hypothesis $\mathbf{H}_0$ or $\mathbf{H}_1$ is actually true. Since the probability of accepting hypothesis $\mathbf{H}_1$ when it is true, *i.e.* the probability of **detection**, is $1-\beta$, it follows that the hypothesis of accepting $\mathbf{H}_0$ when it is false is β. Similarly, the probability of accepting hypothesis $\mathbf{H}_1$ when it is false, *i.e.* the probability of **false-calling**, is α, it follows that the hypothesis of accepting $\mathbf{H}_0$ when it is true is $1-\alpha$. Therefore, if hypothesis $\mathbf{H}_0$ is true then $L = 1-\alpha$, while if hypothesis $\mathbf{H}_1$ is true then $L = \beta$. If the values $\mathrm{E}_0[z]$ and $\mathrm{E}_1[z]$ represent the expected values of the log likelihood ratio z assuming respectively hypothesis $\mathbf{H}_0$ and $\mathbf{H}_1$ are true, then if hypothesis $\mathbf{H}_0$ is actually true it will take on average

$$\mathrm{E}_0[m] \approx \frac{(1-\alpha) \ln B + \alpha \ln A}{\mathrm{E}_0[z]} \tag{5.6}$$

samples to accept it, and if hypothesis $\mathbf{H}_1$ is actually true it will take on average

$$\mathrm{E}_1[m] \approx \frac{\beta \ln B + (1-\beta) \ln A}{\mathrm{E}_1[z]} \tag{5.7}$$

samples to accept it. In practice $\alpha \ll 1\%$ and $\beta \ll 1\%$. It follows that $\ln A \gg 0$ and $\ln B \ll 0$, and that if hypothesis $\mathbf{H}_0$ is true then $L = 1-\alpha \approx 1$, while if hypothesis $\mathbf{H}_1$ is true then $L = \beta \approx 0$. Then if hypothesis $\mathbf{H}_0$ is actually true it will take on average

$$\mathrm{E}_0[m] \approx \frac{\ln B}{\mathrm{E}_0[z]} \tag{5.8}$$

samples to accept it, and if hypothesis $\mathbf{H}_1$ is actually true it will take on average

$$\mathrm{E}_1[m] \approx \frac{\ln A}{\mathrm{E}_1[z]} \tag{5.9}$$

samples to accept it. As previously discussed, decreasing the probabilities of committing an error increases the value of A and decreases the value of B. It follows that, as previously noted, the ASN will also increase as the probabilities of committing an error decrease.

Minimum Detectable Change

The Average Sample Number (ASN) is particularly useful in the case of parameterised distributions. Assume the random variable y has a probability density function $p(y \mid \theta)$ parameterised by the parameter vector θ, and consider the hypothesis $\mathbf{H}_0$ that the parameter vector θ is equal to some value θ_0 and an alternative hypothesis $\mathbf{H}_1$ that the parameter vector θ is equal to some other value $\theta_1 \neq \theta_0$. Consequently, if hypothesis $\mathbf{H}_0$ is true then the probability density function of y is given by $p\left(y \mid \theta_0\right)$, and if hypothesis $\mathbf{H}_1$ is true then the probability density function of y is given by $p\left(y \mid \theta_1\right)$. It is possible to calculate the expected value $\mathrm{E}[m \mid \theta]$ of the cardinality m of the finite sample set Y_m required for the SPRT to terminate with the acceptance of either hypothesis $\mathbf{H}_0$ or $\mathbf{H}_1$ when the true parameter vector is θ which may or may not be equal to either θ_0 or θ_1. In appendix section B.4.2 it is shown that the expected value $\mathrm{E}[m \mid \theta]$ is approximated by

$$\mathrm{E}[m \mid \theta] \approx \frac{L(\theta) \ln B + (1 - L(\theta)) \ln A}{\mathrm{E}[z \mid \theta]} \tag{5.10}$$

The Operating Characteristic (OC) $L(\theta)$ describes the probability that the SPRT will terminate with the acceptance of hypothesis $\mathbf{H}_0$ as a function of the true parameter vector θ. As a special case, if hypothesis $\mathbf{H}_0$ is true then $L(\theta_0) = 1 - \alpha$, while if hypothesis $\mathbf{H}_1$ is true then $L(\theta_1) = \beta$, as previously discussed. If $\mathrm{E}[z \mid \theta]$ is the expected value of the log likelihood ratio z when the true parameter vector is θ, then it will take on average $\mathrm{E}[m \mid \theta]$ samples for the SPRT to terminate, with a probability $L(\theta)$ of accepting hypothesis $\mathbf{H}_0$ that the parameter vector θ is equal to some value θ_0, and a probability $1 - L(\theta)$ of accepting hypothesis $\mathbf{H}_1$ that the parameter vector θ is equal to some value θ_1.

It is often of interest to find the minimum absolute element-wise change $|v| = |\theta_1 - \theta_0|$ between parameter vectors θ_1 and θ_0 that can be detected with a given finite sample set Y_m of cardinality m. Then, given parameter vector θ_0, solving $\mathrm{E}[m \mid \theta_1] = m$ for θ_1 will yield a value for parameter vector θ_1 such that the minimum absolute element-wise change $|v| = |\theta_1 - \theta_0|$ detectable is minimised for a probability equal to or higher than $1 - \beta$ of **detection**, and a probability equal to or smaller than α of **false-calling**. Because in practice $\alpha \ll 1\%$ and $\beta \ll 1\%$, as previously noted the equation

$$\mathrm{E}[m \mid \theta_1] \approx \frac{L(\theta_1) \ln B + (1 - L(\theta_1)) \ln A}{\mathrm{E}[z \mid \theta_1]} \tag{5.11}$$

in practice simplifies to

$$\mathrm{E}[m \mid \theta_1] \approx \frac{\ln A}{\mathrm{E}[z \mid \theta_1]} \tag{5.12}$$

Solving $\mathrm{E}[m \mid \theta_1] = m$ implies that

$$\frac{\ln A}{m} = \mathrm{E}[z \mid \theta_1] = \ln \frac{\mathrm{E}\left[p\left(y \mid \theta_1\right)\right]}{\mathrm{E}\left[p\left(y \mid \theta_0\right)\right]} \tag{5.13}$$

Decreasing the probabilities of committing an error increases the value of A. Consequently, given parameter vector θ_0, for a fixed m the value z must increase and so does the minimum absolute element-wise change $|v| = |\theta_1 - \theta_0|$ between parameter vectors θ_1 and θ_0.

5.1.2 Cumulative Sum Algorithm

The Cumulative Sum (CUSUM) algorithm is a repeated SPRT designed to detect changes in the probability density function of a random variable y from $p_0(y)$ to $p_1(y)$. Its main advantage is that it can be used with any probability density function. However, both probability density functions before and after change must be known in advance.

Consider a finite set $Y_n = \{y_1, y_2, \ldots, y_n\}$ of samples y_i of the random monitored variable y gathered at known times $t_1, t_2, \ldots, t_n$, and assume that before an unknown change time t_c the probability density function of y is given by $p_0(y)$, and that after t_c the probability density function of y is given by $p_1(y)$. It is of interest to detect the onset of change in the probability density function of y and to estimate t_c.

Consider hypothesis $\mathbf{H}_0$ which states that the probability density function of y is given by $p_0(y)$, and hypothesis $\mathbf{H}_1$ which states that the probability density function of y is given by $p_1(y)$. The log likelihood ratio

$$z_i = \ln \frac{p_1(y_i)}{p_0(y_i)} \tag{5.14}$$

will generally be negative if hypothesis $\mathbf{H}_0$ is true, and positive if hypothesis $\mathbf{H}_1$ is true. Intuitively, to detect a change from hypothesis $\mathbf{H}_0$ to hypothesis $\mathbf{H}_1$ only the positive values of z_i are of interest. With the cumulative log likelihood ratio defined as

$$Z_{j+m}^{j} = \sum_{i=j}^{j+m} z_i = \sum_{i=j}^{j+m} \ln \frac{p_1(y_i)}{p_0(y_i)} \tag{5.15}$$

set $j = 1$ and $m = 1$, and start a SPRT with Z_{j+m}^{j}. If $Z_{j+m}^{j} \geq \ln A$ then hypothesis $\mathbf{H}_1$ is accepted and change is detected. Else, if $0 \leq Z_{j+m}^{j} \leq \ln A$ continue the SPRT by setting $m = m + 1$ and re-evaluate Z_{j+m}^{j}. Finally, because only positive values of z_i and therefore of Z_{j+m}^{j} are of interest for change detection purposes, if $Z_{j+m}^{j} \leq 0$ then set $j = j + 1$ and $m = 1$, and re-evaluate Z_{j+m}^{j}, which is equivalent to re-starting the SPRT with $j = j + 1$ and $m = 1$. This repeated SPRT procedure, known as the CUSUM algorithm [140], can be expressed recursively as

$$u_i = \sup(u_{i-1} + z_i, 0), \quad u_0 = 0 \tag{5.16}$$

With prescribed probabilities $1 - \beta$ of **detection** and α of **false-calling**, hypothesis $\mathbf{H}_1$ is accepted and change is detected at sample y_d and detection time t_d, where d is the smallest positive integer for which $u_d \geq \ln A$. If $u_n < \ln A$ then hypothesis $\mathbf{H}_1$ is not accepted and change is not detected within the sample set Y_n, and further samples of y might be required if there is reason to believe change has actually occurred. Importantly, change detection is not equivalent to change occurrence since, subject to probabilities $1-\beta < 1$ of **detection** and $\alpha > 0$ of **false-calling**, change may occur but not be detected and may be detected but not have occurred. By definition $t_c \leq t_d$, since at least one sample of the random variable y must be collected at or after change time t_c for change to be detected. Once change has been detected, the maximum likelihood estimate of t_c is given by t_e, where e is a positive integer smaller or equal to d that maximises the log likelihood function $l(e)$

$$e = \arg\max_{1\leq e\leq d} l(e), \quad l(e) = \ln\left(\prod_{i=1}^{e-1} p_0(y_i) \prod_{i=e}^{d} p_1(y_j)\right) \tag{5.17}$$

The CUSUM algorithm has been shown [141–144] to be **optimal** as it minimises the detection delay $\delta = t_d - t_c$ for prescribed probabilities $1-\beta$ of **detection** and α of **false-calling**.

5.1.3 Generalised Likelihood Ratio Algorithm

The Generalised Likelihood Ratio (GLR) algorithm is a repeated SPRT designed to detect changes in the probability density function of a random variable y from $p(y \mid \theta_0)$ to $p(y \mid \theta_1)$. The GLR assumes that the probability density functions before and after change are differently parameterised versions of the same probability density function, and its main advantage is that the parameter θ_1 after the change does not have to be known in advance but can be estimated from the available samples of y.

Consider a finite set $Y_n = \{y_1, y_2, \ldots, y_n\}$ of samples y_i of the random monitored variable y gathered at known times $t_1, t_2, \ldots, t_n$, and assume that before an unknown change time t_c the probability density function of y is given by $p(y \mid \theta_0)$, and that after t_c the probability density function of y is given by $p(y \mid \theta_1)$ with θ_1 unknown. It is of interest to detect the onset of change in the probability density function of y and to estimate t_c and θ_1.

Consider hypothesis $\mathbf{H}_0$ which states that the probability density function of y is given by $p(y \mid \theta_0)$, and hypothesis $\mathbf{H}_1$ which states that the probability density function of y is given by $p(y \mid \theta_1)$. The value of the log likelihood ratio

$$z_i(v) = \ln \frac{p(y_i \mid \theta_0 + v)}{p(y_i \mid \theta_0)}, \quad v = \theta_1 - \theta_0 \tag{5.18}$$

will be a function of the value of the sample y_i as well as of the value of the change vector v. For a given sample y_i, the value of $z_i(v)$ can therefore be maximised with respect to the change vector v. Similarly, the cumulative log likelihood ratio

$$Z_k^j(v) = \sum_{i=j}^{k} z_i(v) \tag{5.19}$$

can also be maximised with respect to the change vector v. For a given value of the change vector v the maximisation

$$\max_{1 \le j \le k} Z_k^j(v) \tag{5.20}$$

will find which samples $y_j, \ldots, y_k$ are most likely to have probability density function $p\left(y \mid \theta_1\right) = p\left(y \mid \theta_0 + v\right)$, under the assumption that samples $y_1, \ldots, y_{j-1}$ have probability density function $p\left(y \mid \theta_0\right)$. It follows that the double maximisation

$$g_k = \max_{1 \le j \le k} \sup_{v} Z_k^j(v) \tag{5.21}$$

will find the likeliest change vector v for which samples $y_j, \ldots, y_k$ are most likely to have probability density function $p\left(y \mid \theta_1\right) = p\left(y \mid \theta_0 + v\right)$ under the assumption that samples $y_1, \ldots, y_{j-1}$ have probability density function $p\left(y \mid \theta_0\right)$. With prescribed probabilities $1 - \beta$ of **detection** and α of **false-calling**, hypothesis $\mathbf{H}_1$ is accepted and change is detected at sample y_d and detection time t_d, where d is the smallest positive integer for which $g_d \ge \ln A$. This procedure is known as the GLR algorithm [141]. As previously noted, $t_c \le t_d$ since at least one sample of the random variable y must be collected at or after change time t_c for change to be detected. Once change has been detected the arguments of the double maximisation

$$e, v = \arg \max_{1 \le e \le k} \sup_{v} Z_k^e(v) \ge \ln A \tag{5.22}$$

will give the the maximum likelihood estimates $\theta_0 + v$ of the parameter vector θ_1, and t_e of the change time t_c. Note that if $g_n < \ln A$ then hypothesis $\mathbf{H}_1$ is not accepted and change is not detected within the sample set Y_n, and further samples of y might be required if there is reason to believe change has actually occurred. As previously discussed, change detection is not equivalent to change occurrence since, subject to probabilities $1 - \beta < 1$ of **detection** and $\alpha > 0$ of **false-calling**, change may occur but not be detected and may be detected but not have occurred.

5.2 Step Change Detection

Consider a normally distributed random variable $y \in \mathbb{R}$ with probability density function

$$p\left(y \mid \theta\right) = p\left(y \mid \mu, \sigma^2\right) = \left(2\pi\sigma^2\right)^{-1/2} e^{-\left(y-\mu\right)^2/2\sigma^2} \tag{5.23}$$

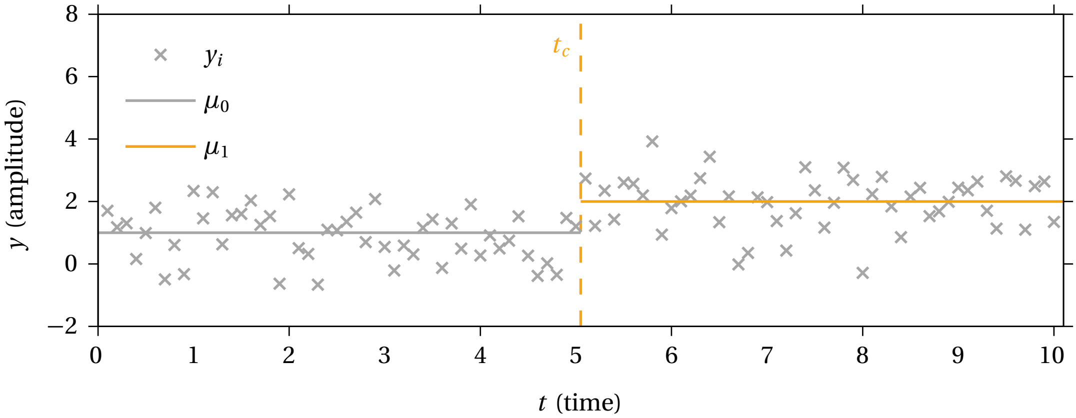

Figure 5.1: Time series of independent samples y_i of the random variable y undergoing a step change in its mean from μ_0 to μ_1 at t_c.

parameterised by the parameter vector $\theta = (\mu, \sigma^2)$ with mean μ and variance σ^2. Assume that a finite set $Y_n = \{y_1, y_2, \cdots, y_n\}$ of $n = 100$ independent samples y_i have been gathered every $\lambda = 0.1$s at known times $t_1, t_2, \cdots, t_n = 0.1\text{s}, 0.2\text{s}, \cdots, 10\text{s}$ resulting in the time series shown in figure 5.1. It is known that y has a constant variance $\sigma^2 = 1$, and it is of interest to detect if the mean of the probability density function of y changes from its initial value $\mu_0 = 1$ and in such case it is of interest to estimate the change time t_c and its value μ_1 after the change has occurred. Consider hypothesis $\mathbf{H}_0$ that the probability density function of y is given by $p\left(y \mid \mu_0, \sigma^2\right)$, and the alternative hypothesis $\mathbf{H}_1$ that the probability density function of y is given by $p\left(y \mid \mu_1, \sigma^2\right)$. The log likelihood ratio will therefore be a function of the value of μ_1 after the change and will given by

$$z\left(\mu_1\right) = \ln \frac{p\left(y \mid \mu_1, \sigma^2\right)}{p\left(y \mid \mu_0, \sigma^2\right)} = \frac{2\left(\mu_1 - \mu_0\right) y + \mu_0^2 - \mu_1^2}{2\sigma^2} \tag{5.24}$$

Any onset of change can be detected utilising the double GLR maximisation

$$g_k = \max_{1 \le j \le k} \sup_{\nu} Z_k^j(\nu), \quad Z_k^j(\nu) = \sum_{i=j}^{k} z_i(\nu), \quad \nu = \mu_1 - \mu_0 \tag{5.25}$$

or explicitly

$$g_k = \max_{1 \le j \le k} \sup_{\nu} \sum_{i=j}^{k} \frac{2\nu_j\left(y_i - \mu_0\right) - \nu^2}{2\sigma^2} \tag{5.26}$$

since substituting $\mu_0 + \nu$ for μ_1 in equation 5.24 yields

$$z(\nu) = \frac{2\nu\left(y - \mu_0\right) - \nu^2}{2\sigma^2} \tag{5.27}$$

If μ_1 after t_c is known in advance, then so is ν and the GLR reduces to the CUSUM. Otherwise because $Z_k^j(\nu)$ is a concave quadratic form in ν, it will reach its maximum when its first derivative

$$\begin{aligned}\frac{\partial Z_k^j(\nu)}{\partial \nu} &= \frac{\partial}{\partial \nu}\sum_{i=j}^{k}\frac{2\nu\left(y_i-\mu_0\right)-\nu^2}{2\sigma^2}\\ &= \frac{\partial}{\partial \nu}\left(\nu\sum_{i=j}^{k}\frac{y_i-\mu_0}{\sigma^2}-\nu^2\sum_{i=j}^{k}\frac{1}{2\sigma^2}\right)\\ &= \sum_{i=j}^{k}\frac{y_i-\mu_0}{\sigma^2}-\nu\frac{k-j+1}{\sigma^2}\end{aligned} \tag{5.28}$$

nullifies, from which it follows at once that the value of ν that maximises $Z_k^j(\nu)$ is

$$\nu = \sum_{i=j}^{k}\frac{y_i-\mu_0}{k-j+1} \tag{5.29}$$

Figure 5.2 shows that g_k first crosses the change detection threshold $\ln A = 4.60$ at detection time $t_d = t_{57} = 5.7$s, with $A = \left(1-\beta\right)/\alpha = 99$ for $1-\beta = 99\%$ and $\alpha = 1\%$. The true change time t_c is 5.05s, so y_{51} is the first sample collected after the mean changes, and the detection delay is therefore seven samples. In general the average number m of samples y_i of y required to accept hypothesis $\mathbf{H}_1$, and therefore the detection delay to detect a change in the mean should there be one, can be calculated in advance and is given by the Average Sample Number (ASN)

$$\begin{aligned}\mathrm{E}\left[m \mid \mu_1\right] &\approx \frac{L\left(\mu_1\right)\ln B+\left(1-L\left(\mu_1\right)\right)\ln A}{\mathrm{E}\left[z \mid \mu_1\right]}\\ &\approx 2\sigma^2\,\frac{\beta\ln B+\left(1-\beta\right)\ln A}{2\left(\mu_1-\mu_0\right)\mu_1+\mu_0^2-\mu_1^2}\end{aligned} \tag{5.30}$$

since

$$\mathrm{E}\left[z \mid \mu_1\right] = \frac{2\left(\mu_1-\mu_0\right)\mu_1+\mu_0^2-\mu_1^2}{2\sigma^2} \tag{5.31}$$

Given that the true value of μ_1 after t_c is 2, then $\mathrm{E}\left[m \mid \mu_1\right] \approx 9$ for a $1-\beta = 99\%$ probability of **detection** and a $\alpha = 1\%$ probability of **false-calling**. It follows that nine samples would on average have to be collected after t_c for the change in the mean to be detected, resulting in an expected detection time $\mathrm{E}\left[t_d\right] = t_c + 9$ samples $= t_{59} = 5.9s$. Figure 5.3 indicates that the estimate $\mu_0+\nu$ of μ_1 quickly converges to its true value of 2 after t_c, and that $\mu_0+\nu = 2.16$ at t_d. Finally, when the GLR terminates at t_d figure 5.4 shows that the estimated change time is $t_e = t_{51} = 5.1$s, which is just one sample after, and therefore the closest it can possibly be, to the actual change time $t_c = 5.05s$.

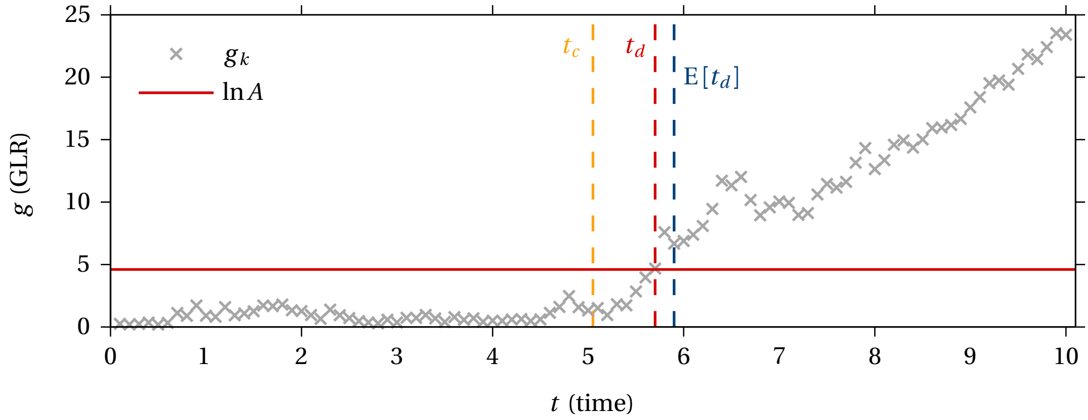

Figure 5.2: GLR g_k for $\mu_0 = 1$ and $\sigma^2 = 1$, with the detection time t_d at which g_k first crosses change threshold $\ln A = 4.60$ and its estimate $\mathrm{E}[t_d]$.

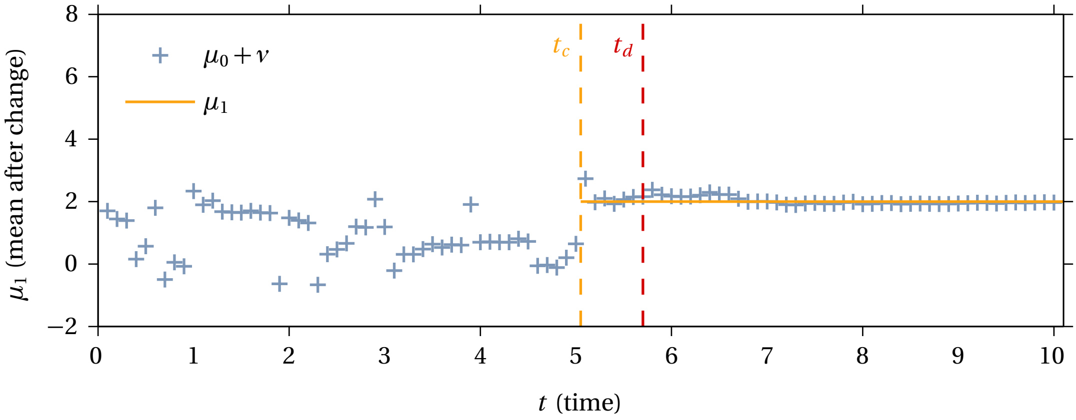

Figure 5.3: Estimate $\mu_0 + \nu$ of the mean μ_1 after t_c, with its true value $\mu_1 = 2$.

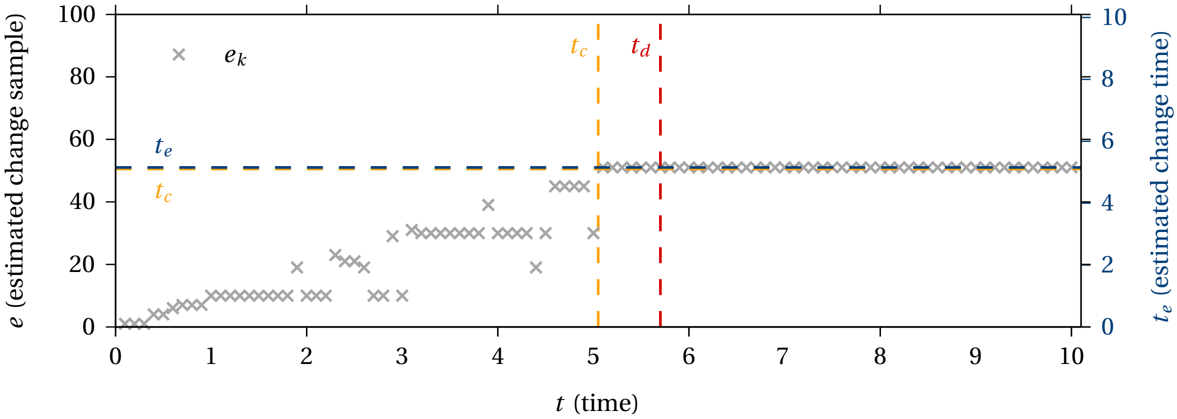

Figure 5.4: Estimated change sample e and corresponding estimate t_e of t_c.

5.2.1 General Detectability Charts

General detectability charts can be created for use with the GLR algorithm. The ASN

$$\begin{aligned} \mathrm{E}[m \mid \nu] &\approx \frac{L(\mu_0+\nu)\ln B + (1-L(\mu_0+\nu))\ln A}{\mathrm{E}[z(\nu)\mid \nu]} \\ &\approx 2\sigma^2\,\frac{\beta \ln B + (1-\beta)\ln A}{\nu^2} \end{aligned} \tag{5.32}$$

indicates the number m of independent samples y_i that will on average need to be collected in order to detect an absolute step change $|\nu|$ in the mean μ of the probability density function of y with probabilities $1-\beta$ of **detection** and α of **false-calling**, and it can be plotted as a function of the absolute step change $|\nu|$ and of the standard deviation σ.

With probabilities $1-\beta = 99\%$ of **detection** and $\alpha = 1\%$ of **false-calling**, figure 5.5(a), which plots the average sample number $\mathrm{E}[m \mid \nu]$ as a function of the absolute step change $|\nu|$ for different values of the standard deviation σ, indicates that to detect a step change of 0.3 one would need on average four samples for a standard deviation of 0.2, 35 samples for a standard deviation of 0.6, and as many as 100 samples for a standard deviation of 1.0. Similarly, to detect a step change of 0.6 one would need on average just one sample for a standard deviation of 0.2, nine samples for a standard deviation of 0.6 and 24 samples for a standard deviation of 1.0. Figure 5.5(b), which plots the average sample number $\mathrm{E}[m \mid \nu]$ as a function of the standard deviation σ for different values of the absolute step change $|\nu|$, indicates that for a standard deviation of 0.6 one would need on average just over three samples to detect a step change of 1.0, five samples to detect a step change of 0.8, nine samples to detect a step change of 0.6, 11 samples to detect a step change of 0.4, and finally 18 samples to detect a step change of 0.2.

Predictably, higher values of standard deviation require on average higher numbers of samples in order to confirm whether a given step change in mean has occurred or not, and similarly for a given standard deviation higher numbers of samples are on average required to confirm whether smaller step changes in mean have occurred or not. Conversely, lower values of standard deviation require on average lower numbers of samples in order to confirm whether a given step change in mean has occurred or not, and similarly for a given standard deviation lower numbers of samples are on average required to confirm whether bigger step changes in mean have occurred or not. Defining the detectability ratio υ as

$$\upsilon = \frac{|\nu|}{\sigma} = \frac{|\mu_1 - \mu_0|}{\sigma} \tag{5.33}$$

it can be seen from figure 5.5(c) that higher values of the detectability ratio υ, caused by higher values of the absolute step change $|\nu|$ or lower values of the standard deviation σ, re-

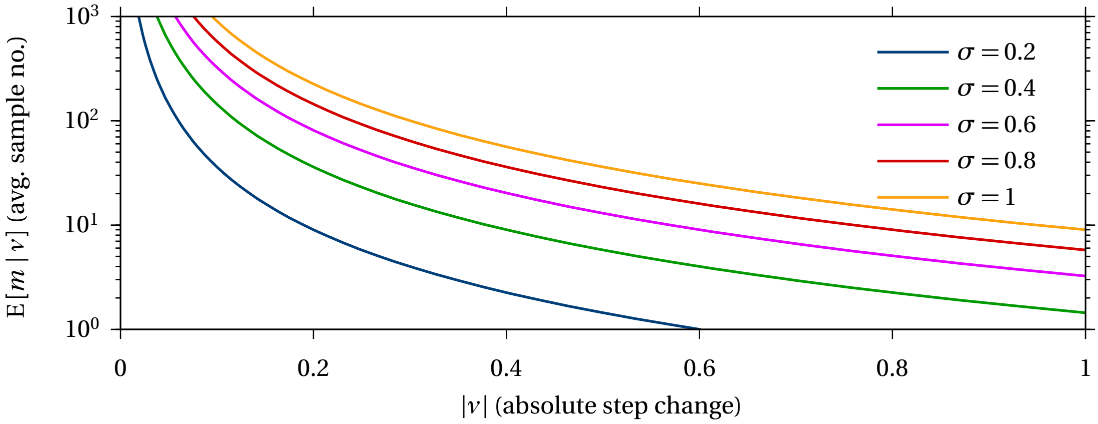

(a) ASN as a function of the absolute step change $|v|$ for different values of σ.

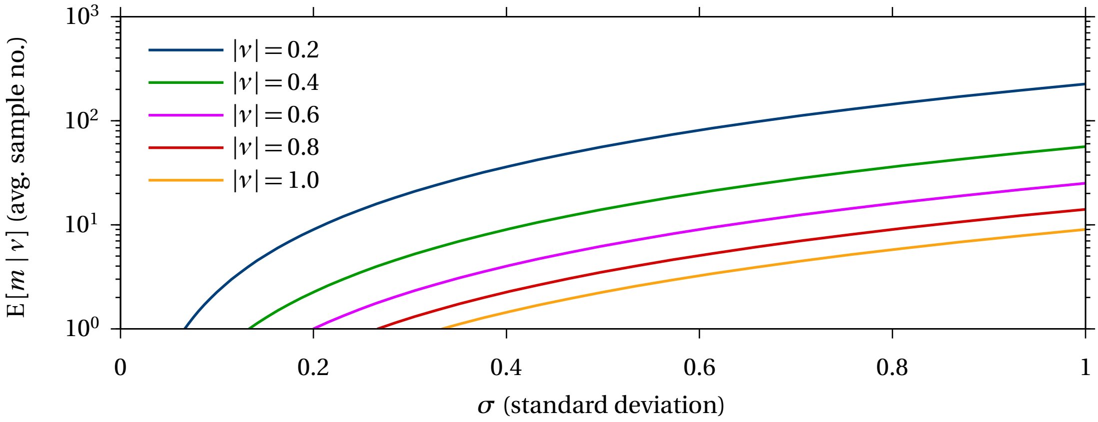

(b) ASN as a function of σ for different values of the absolute step change $|v|$.

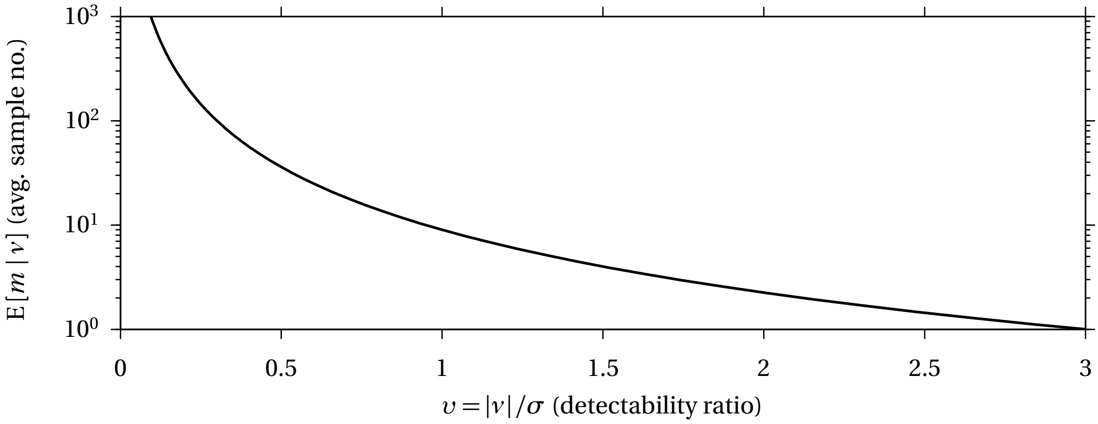

(c) ASN as a function of the detectability ratio υ.

Figure 5.5: $\mathrm{E}[m \mid v]$ as function (a) of $|v|$ for different values of σ, (b) of σ for different values of the absolute step change $|v|$, and (c) of the detectability ratio υ; for given standard deviation σ, detecting an absolute step change $|v| = \left|\mu_1 - \mu_0\right|$ in the mean μ of the probability density function of y requires on average $\mathrm{E}[m \mid v]$ samples ($1 - \beta = 99\%$, $\alpha = 1\%$).

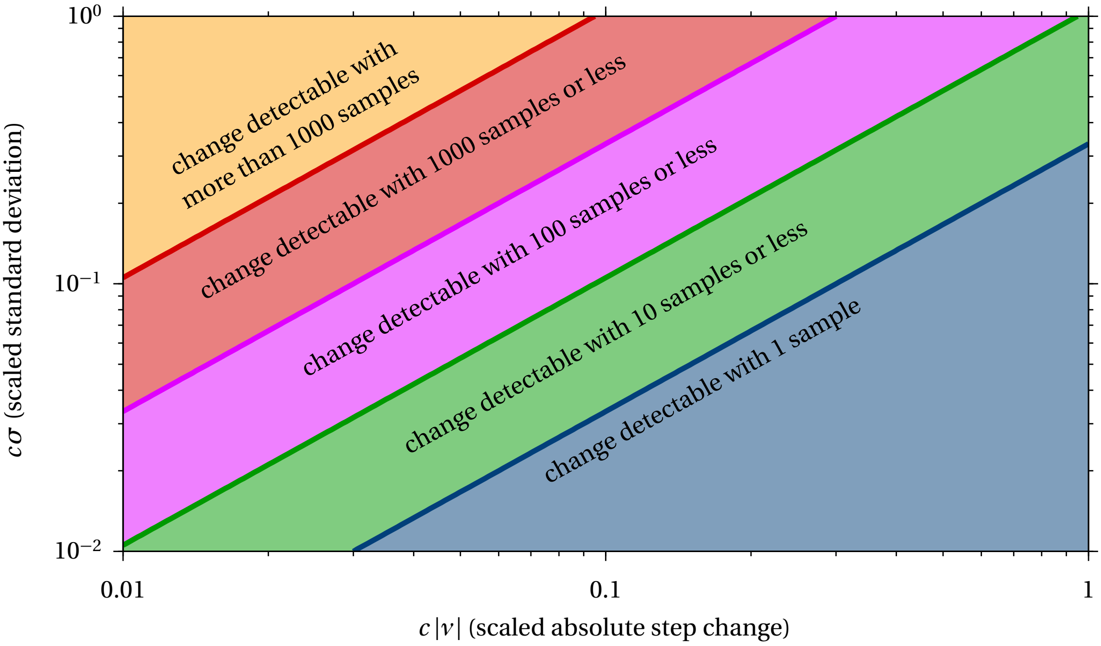

Figure 5.6: Average number of samples required to detect an absolute step change in mean $c\,|v|$ when the standard deviation is $c\sigma$ ($1-\beta = 99\%$, $\alpha = 1\%$).

quire on average lower numbers of samples in order to confirm whether a given step change in mean has occurred or not. Conversely, lower values of the detectability ratio υ, caused by lower values of the absolute step change $|v|$ or higher values of the standard deviation σ, require on average higher numbers of samples in order to confirm whether a given step change in mean has occurred or not. The detectability ratio υ is of key importance because it expresses the general relationship that ties the number of samples that are on average required to confirm whether a step change in mean has occurred or not to the absolute step change in mean $|v|$ itself and the standard deviation σ, irrespectively of their actual values and for probabilities $1-\beta$ of **detection** and α of **false-calling**.

Often, rather than knowing how many samples are required to detect some absolute step change $|v|$ given some standard deviation σ, it is of practical importance to know how small a step change in mean can be detected with a given number of samples, say 10 or less, and a given standard deviation σ, say 0.1. From figure 5.6 it can be seen that, for a positive real number c, given a standard deviation $c\sigma = 0.1$ any absolute step change $c\,|v|$ of 0.1 or more can on average be detected with 10 samples or less, and that any absolute step change $c\,|v|$ of 0.3 or more can be detected on average with just one sample; however, it could take on average up to 100 samples to detect absolute step changes $c\,|v|$ as small as 0.03. Moreover, figure 5.6 clearly presents the link between the number of samples that are on average required to

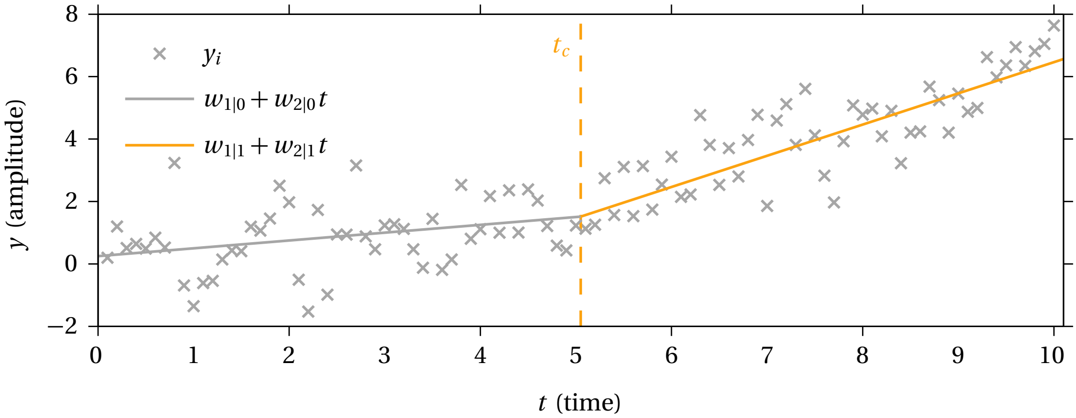

Figure 5.7: Time series of independent samples y_i of the random variable y undergoing a change in the slope of its mean $\mu = w_1 + w_2 t$ from $w_{1|0} + w_{2|0}t$ to $w_{1|1} + w_{2|1}t$ at t_c.

confirm whether a step change in mean has occurred or not, the standard deviation and the absolute step change in mean $|\nu|$ itself.

5.3 Gradual Change Detection

Consider a normally distributed random variable $y \in \mathbb{R}$ with probability density function

$$p(y \mid \theta) = p\left(y \mid \mu, \sigma^2\right) = \left(2\pi\sigma^2\right)^{-1/2} e^{-(y-\mu)^2/2\sigma^2} \tag{5.34}$$

parameterised by the parameter vector $\theta = (\mu, \sigma^2)$ with mean μ and variance σ^2. Assume the mean $\mu = w_1 + w_2 t$ is a linear function of t with intercept w_1 and slope w_2. Then the probability density function of y becomes

$$p(y \mid \theta) = p\left(y \mid w_1 + w_2 t, \sigma^2\right) = \left(2\pi\sigma^2\right)^{-1/2} e^{-(y-w_1-w_2 t)^2/2\sigma^2} \tag{5.35}$$

parameterised by the parameter vector $\theta = (w_1, w_2, \sigma^2)$. Assume that $Y_n = \{y_1, y_2, \cdots, y_n\}$ is a finite set of $n = 100$ independent samples y_i gathered every $\lambda = 0.1$s at known times $t_1, t_2, \cdots, t_n = 0.1$s, 0.2s, $\cdots$, 10s resulting in the time series shown in figure 5.7. It is known that y has a constant variance $\sigma^2 = 1$, and it is of interest to detect if the slope w_2 of the mean of the probability density function of y changes from its initial value $w_{2|0} = 0.25$ and in such case it is of interest to estimate the change time t_c and its value $w_{2|1}$ after the change has occurred. Consider hypothesis $\mathbf{H}_0$ that the probability density function of y is given by $p\left(y \mid w_{1|0} + w_{2|0}t, \sigma^2\right)$, and the alternative hypothesis $\mathbf{H}_1$ that the probability density function of y is given by $p\left(y \mid w_{1|1} + w_{2|1}t, \sigma^2\right)$. The log likelihood ratio will therefore be a function of the value of $w_{1|1}$ and $w_{2|1}$ after the change and will given by

$$\begin{aligned} z\left(w_{1|1}, w_{2|1}\right) &= \ln \frac{p\left(y \mid w_{1|1} + w_{2|1}t, \sigma^2\right)}{p\left(y \mid w_{1|0} + w_{2|0}t, \sigma^2\right)} \\ &= \frac{2\left(w_{1|1} + w_{2|1}t - w_{1|0} - w_{2|0}t\right)y + \left(w_{1|0} + w_{2|0}t\right)^2 - \left(w_{1|1} + w_{2|1}t\right)^2}{2\sigma^2} \end{aligned} \tag{5.36}$$

Any onset of change can be detected utilising the double GLR maximisation

$$g_k = \max_{1 \le j \le k} \sup_{\eta} Z_k^j(\eta), \quad Z_k^j(\eta) = \sum_{i=j}^{k} z_i(\eta), \quad \eta = w_{2|1} - w_{2|0} \tag{5.37}$$

or explicitly

$$g_k = \max_{1 \le j \le k} \sup_{\eta} \sum_{i=j}^{k} \frac{2\eta_j\left(t_i - t_j\right)\left(y_i - w_{1|0} - w_{2|0}t_i\right) - \eta_j^2\left(t_i - t_j\right)^2}{2\sigma^2} \tag{5.38}$$

since substituting $w_{2|0} + \eta$ for $w_{2|1}$ in equation 5.36 yields

$$z_i(\eta) = \frac{2\eta\left(t_i - t_j\right)\left(y_i - w_{1|0} - w_{2|0}t_i\right) - \eta^2\left(t_i - t_j\right)^2}{2\sigma^2} \tag{5.39}$$

with

$$\hat{w}_{2|1} = w_{2|0} + \eta, \quad \hat{w}_{1|1} = w_{1|0} - \eta t_j \tag{5.40}$$

If $w_{2|1}$ after t_c is known in advance, then so is η and the GLR reduces to the CUSUM. Otherwise because $Z_k^j(\eta)$ is a concave quadratic form in η, it will reach its maximum when its first derivative

$$\begin{aligned} \frac{\partial Z_k^j(\eta)}{\partial \eta} &= \frac{\partial}{\partial \eta} \sum_{i=j}^{k} \frac{2\eta\left(t_i - t_j\right)\left(y_i - w_{1|0} - w_{2|0}t_i\right) - \eta^2\left(t_i - t_j\right)^2}{2\sigma^2} \\ &= \frac{\partial}{\partial \eta}\left(\eta \sum_{i=j}^{k} \frac{\left(t_i - t_j\right)\left(y_i - w_{1|0} - w_{2|0}t_i\right)}{\sigma^2} - \eta^2 \sum_{i=j}^{k} \frac{\left(t_i - t_j\right)^2}{2\sigma^2}\right) \\ &= \sum_{i=j}^{k} \frac{\left(t_i - t_j\right)\left(y_i - w_{1|0} - w_{2|0}t_i\right)}{\sigma^2} - \eta \sum_{i=j}^{k} \frac{\left(t_i - t_j\right)^2}{\sigma^2} \end{aligned} \tag{5.41}$$

nullifies, from which it follows at once that the value of η that maximises $Z_k^j(\eta)$ is

$$\eta = \frac{\sum_{i=j}^{k} \left(t_i - t_j\right)\left(y_i - w_{1|0} - w_{2|0}t_i\right)}{\sum_{i=j}^{k} \left(t_i - t_j\right)^2} \tag{5.42}$$

Figure 5.8 shows that g_k first crosses the change detection threshold $\ln A = 4.60$ at detection time $t_d = t_{63} = 6.3$s, with $A = (1-\beta)/\alpha = 99$ for $1-\beta = 99\%$ and $\alpha = 1\%$. The true change time t_c is 5.05s, so y_{51} is the first sample collected after the mean changes, and the detection delay is therefore 13 samples. In general the average number m of samples y_i of y required to accept hypothesis $\mathbf{H}_1$, and therefore the detection delay to detect a change in the slope of the mean should there be one, can be calculated in advance and is given by the Average Sample Number (ASN)

$$\mathrm{E}\left[m \mid w_{1|1} + w_{2|1} t\right] \approx \frac{L\left(w_{1|1} + w_{2|1} t\right) \ln B + \left(1 - L\left(w_{1|1} + w_{2|1} t\right)\right) \ln A}{\mathrm{E}\left[z \mid w_{1|1} + w_{2|1} t\right]} \tag{5.43}$$

Because it is of interest to detect just a change in the slope w_2 from $w_{2|0}$ to $w_{2|1}$ independently from the time t_c at which it may happen, one can assume that $t_c = 0$ or shift the time axis appropriately. Since at $t_c = 0$ by definition $w_{1|0} + w_{2|0} t_c = w_{1|1} + w_{2|1} t_c$, it follows that $w_{1|0} = w_{1|1}$, and one can assume that $w_{1|0} = w_{1|1} = 0$ or shift the amplitude axis appropriately. Then

$$\begin{aligned}\mathrm{E}\left[z \mid w_{2|1} t\right] &= \frac{2\left(w_{2|1} t - w_{2|0} t\right) w_{2|1} t + w_{2|0}^2 t^2 - w_{2|1}^2 t^2}{2\sigma^2} \\ &= t^2 \left(w_{2|1} - w_{2|0}\right)^2 / 2\sigma^2\end{aligned} \tag{5.44}$$

and the ASN then becomes

$$\begin{aligned}\mathrm{E}\left[m \mid w_{2|1} t\right] &\approx 2\sigma^2 \frac{L\left(w_{2|1} t\right) \ln B + \left(1 - L\left(w_{2|1} t\right)\right) \ln A}{\left(w_{2|1} - w_{2|0}\right)^2 t^2} \\ &\approx 2\sigma^2 \frac{\beta \ln B + (1-\beta) \ln A}{\left(w_{2|1} - w_{2|0}\right)^2 t^2}\end{aligned} \tag{5.45}$$

In general the ASN of equation 5.45 will indicate the number m of independent samples y_i that will on average need to be collected at or after time $t + t_c > t_c$ in order to detect a change in the slope w_2 from $w_{2|0}$ to $w_{2|1}$. To explain this, consider the expected value $\mathrm{E}\left[z \mid w_{2|1} t\right]$ of the log likelihood ratio z assuming $p\left(y \mid w_{2|1} t, \sigma^2\right)$ is the true probability density function of y, presented in equation 5.44. Equation 5.44 shows that the expected value of z increases monotonically for $t + t_c > t_c$. Intuitively, this is because, for a given variance σ^2, as time t increases it becomes easier to distinguish whether y has a probability density function $p\left(y \mid w_{2|0} t, \sigma^2\right)$ or $p\left(y \mid w_{2|1} t, \sigma^2\right)$, as the absolute difference $\left|w_{2|0} - w_{2|1}\right| t$ in the mean of the two distributions increases monotonically for $t + t_c > t_c$. It follows that if a number m of independent samples y_i collected at time $t + t_c > t_c$ are on average required to detect a change in the slope w_2 from $w_{2|0}$ to $w_{2|1}$, then a number $m_+ < m$ of independent samples y_i collected at time $t_+ > t$ will on average be required to detect the same change since it becomes more evident, and a number $m_- > m$ of independent samples y_i collected at time $t_c < t_- < t$ will on average be required to detect the same change since it becomes less evident. Consequently if m samples y_i are collected at or after time t they will on average be sufficient to detect a change in the slope w_2 from $w_{2|0}$ to $w_{2|1}$. However, in the present case it is known that $t = \lambda m$ because the samples y_i are gathered with sampling interval λ. Therefore, equation 5.45 becomes

$$\mathrm{E}\left[m \mid w_{2|1} t\right] \approx 2\sigma^2 \frac{\beta \ln B + (1-\beta) \ln A}{\left(w_{2|1} - w_{2|0}\right)^2 \lambda^2 m^2} \tag{5.46}$$

from which

$$m^3 \approx 2\sigma^2 \frac{\beta \ln B + (1-\beta) \ln A}{\left(w_{2|1} - w_{2|0}\right)^2 \lambda^2} \tag{5.47}$$

and ultimately

$$\mathrm{E}\left[m \mid w_{2|1} t\right] \approx \left(2\sigma^2 \frac{\beta \ln B + (1-\beta) \ln A}{\left(w_{2|1} - w_{2|0}\right)^2 \lambda^2}\right)^{1/3} \tag{5.48}$$

Given that the true value of $w_{2|1}$ after t_c is 1, then $\mathrm{E}\left[m \mid w_{2|1} t\right] \approx 12$ for a $1-\beta = 99\%$ probability of **detection** and a $\alpha = 1\%$ probability of **false-calling**. It follows that 12 samples would on average have to be collected after t_c for the change in the slope of the mean to be detected, resulting in an expected detection time $\mathrm{E}[t_d] = t_c + 12 \text{ samples} = t_{59} = 6.2s$. Figure 5.9 indicates that the estimate $w_{2|0} + v$ of $w_{2|1}$ quickly converges to its true value of 1 after t_c, and that $w2 \mid 0 + \eta = 1.02$ at t_d. Finally, when the GLR terminates at t_d figure 5.10 shows that the estimated change time is $t_e = t_{51} = 5.1$s, which is just one sample after, and therefore the closest it can possibly be, to the actual change time $t_c = 5.05s$.

5.3.1 General Detectability Charts

General detectability charts can be created for use with the GLR algorithm. The ASN

$$\begin{aligned}\mathrm{E}[m \mid \eta] &\approx 2\sigma^2 \frac{L\left(\left(w_{2|0} + \eta\right) t\right) \ln B + \left(1 - L\left(\left(w_{2|0} + \eta\right) t\right)\right) \ln A}{\eta^2 t^2} \\ &\approx 2\sigma^2 \frac{\beta \ln B + (1-\beta) \ln A}{\eta^2 t^2}\end{aligned} \tag{5.49}$$

indicates the number m of independent samples y_i that will on average need to be collected at or after time $t + t_c > t_c$ in order to detect an absolute slope change $\left|\eta\right|$ in the mean μ of the probability density function of y with probabilities $1-\beta$ of **detection** and α of **false-calling**, as previously explained. However, if the samples y_i are regularly gathered with sampling interval λ, the ASN becomes

$$\mathrm{E}[m \mid \eta] \approx \left(2\sigma^2 \frac{\beta \ln B + (1-\beta) \ln A}{\eta^2 \lambda^2}\right)^{1/3} \tag{5.50}$$

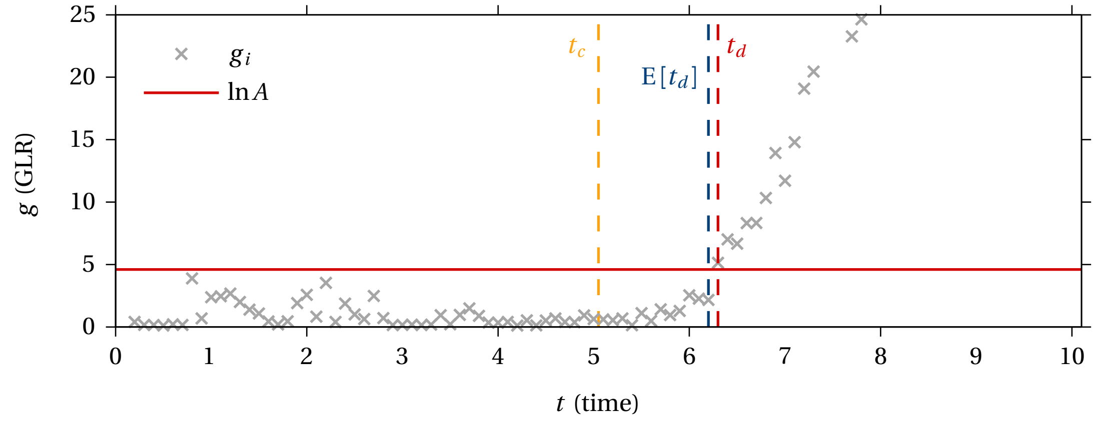

Figure 5.8: GLR g_k for $w_{2|0} = 0.25$, $w_{1|0} = 0.25$ and $\sigma^2 = 1$, with the detection time t_d at which g_k first crosses change threshold $\ln A = 4.60$ and its estimate $\mathrm{E}[t_d]$.

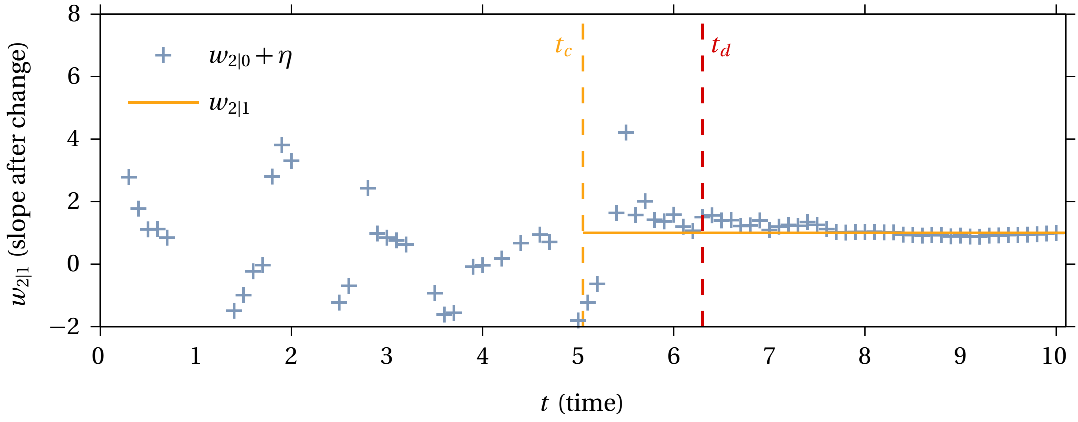

Figure 5.9: Estimate $w_{2|0} + \eta_k$ of the slope of the mean $w_{2|1}$ after t_c, with its true value $w_{2|1} = 1$.

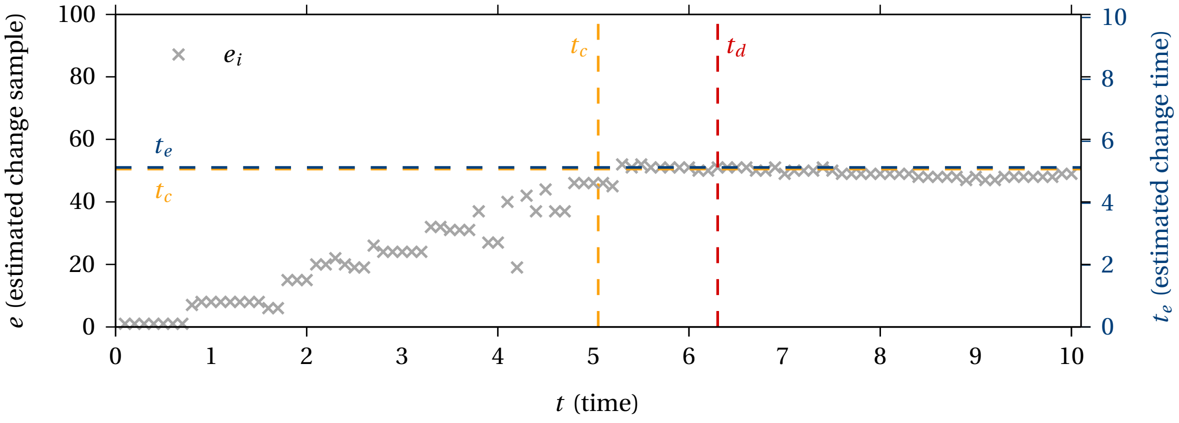

Figure 5.10: Estimated change sample e and corresponding estimate t_e of t_c.

and it can be plotted as a function of the sampling interval λ, the absolute slope change $\left|\eta\right|$ and of the standard deviation σ. Naturally, the number m of independent samples y_i that will on average need to be collected at or after time $t + t_c > t_c$ in order to detect an absolute slope change $\left|\eta\right|$ is inversely proportional to the sampling interval λ. In other words, if the sampling interval is large fewer samples will on average be needed to detect a given absolute slope change $\left|\eta\right|$. Intuitively, this is because, for a given variance σ^2 and a given number m of independent samples y_i, as the sampling interval λ increases then do does $t = \lambda m$ and it becomes easier to distinguish whether y has a probability density function $p\left(y \mid w_{2|0}t, \sigma^2\right)$ or $p\left(y \mid w_{2|1}t, \sigma^2\right)$, since the absolute difference $\left|w_{2|0} - w_{2|1}\right| t$ in the mean of the two distributions increases monotonically for $t + t_c > t_c$. Consider the variable $v = \left|\eta\right| \lambda$. Because $\left|\eta\right|$ is an absolute slope change and λ is an interval, it follows that v is an absolute step change.

With probabilities $1-\beta = 99\%$ of **detection** and $\alpha = 1\%$ of **false-calling**, figure 5.11(a), which plots the average sample number $\mathrm{E}\left[m \mid \eta\right]$ as a function of the absolute slope change $\left|\eta\right|$ and of the sampling interval λ for different values of the standard deviation σ, indicates that to detect an absolute step change $v = \left|\eta\right| \lambda$ of 0.1 one would need on average three samples for a standard deviation of 0.2, seven samples for a standard deviation of 0.6, and ten samples for a standard deviation of 1.0. Figure 5.11(b), which plots the average sample number $\mathrm{E}\left[m \mid \eta\right]$ as a function of the standard deviation σ for different values of the absolute slope change $\left|\eta\right|$ and of the sampling interval λ, indicates that for a standard deviation of 1.0 one would need on average 2 samples to detect an absolute step change $v = \left|\eta\right| \lambda$ change of 1.0, 3 samples to detect an absolute step change of 0.6, 4 samples to detect an absolute step change of 0.4, and 6 samples to detect an absolute step change of 0.2.

Predictably, higher values of standard deviation require on average higher numbers of samples in order to confirm whether a given slope change has occurred or not, and similarly for a given standard deviation higher numbers of samples are on average required to confirm whether smaller slope changes have occurred or not. Conversely, lower values of standard deviation require on average lower numbers of samples in order to confirm whether a given slope change has occurred or not, and similarly for a given standard deviation lower numbers of samples are on average required to confirm whether bigger slope changes have occurred or not. Defining the detectability ratio υ as

$$\upsilon = \frac{\left|\eta\right| \lambda}{\sigma} = \frac{\left|w_{2|1} - w_{2|0}\right| \lambda}{\sigma} \tag{5.51}$$

it can be seen from figure 5.11(c) that, for a given value of the sampling interval λ, higher values of the detectability ratio υ, caused by higher values of the absolute slope change $\left|\eta\right|$

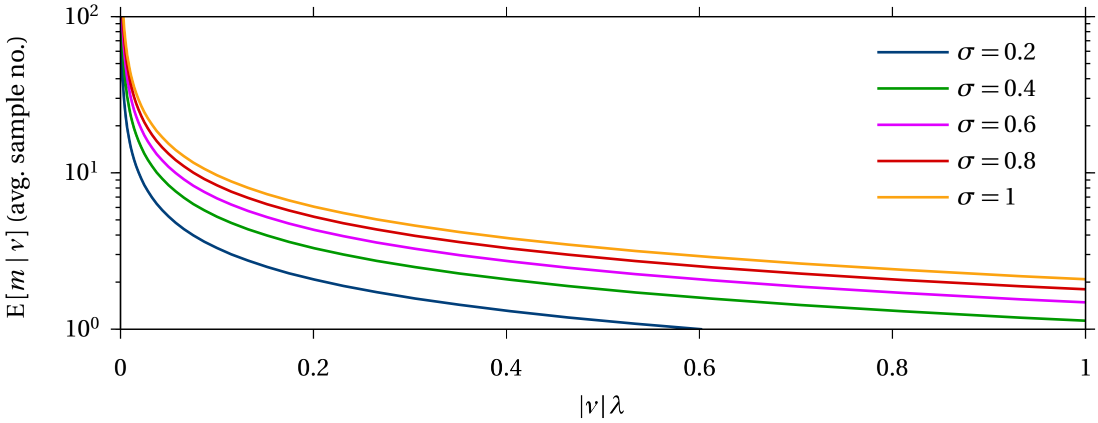

(a) ASN as a function of $|\eta|$ and λ for different values of σ.

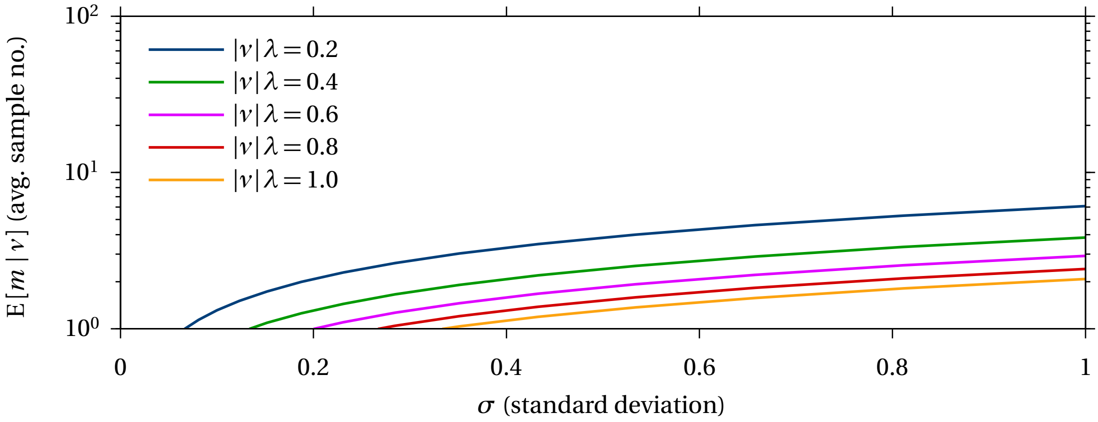

(b) ASN as a function of σ for different values of $|\eta|$ and λ.

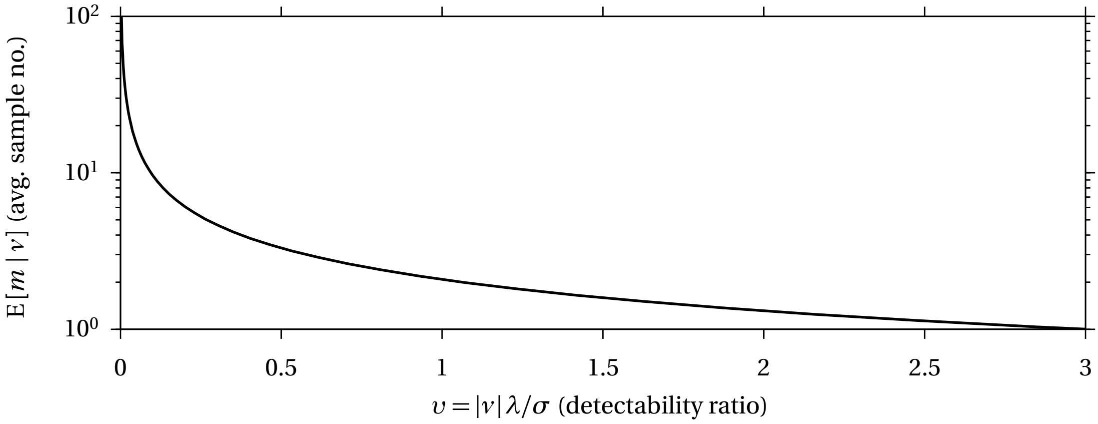

(c) ASN as a function of the detectability ratio υ.

Figure 5.11: $E[m \mid \eta]$ as function (a) of the absolute slope change $|\eta|$ and of the sampling interval λ for different values of the standard deviation σ, (b) of σ for different values of $|\eta|$ and λ, and (c) of the detectability ratio υ; for given sampling interval λ and standard deviation σ, detecting an absolute slope change $|\eta| = |w_{2|0} - w_{2|1}|$ in the mean μ of the probability density function of y requires on average $E[m \mid \eta]$ samples $(1 - \beta = 99\%,\ \alpha = 1\%)$.

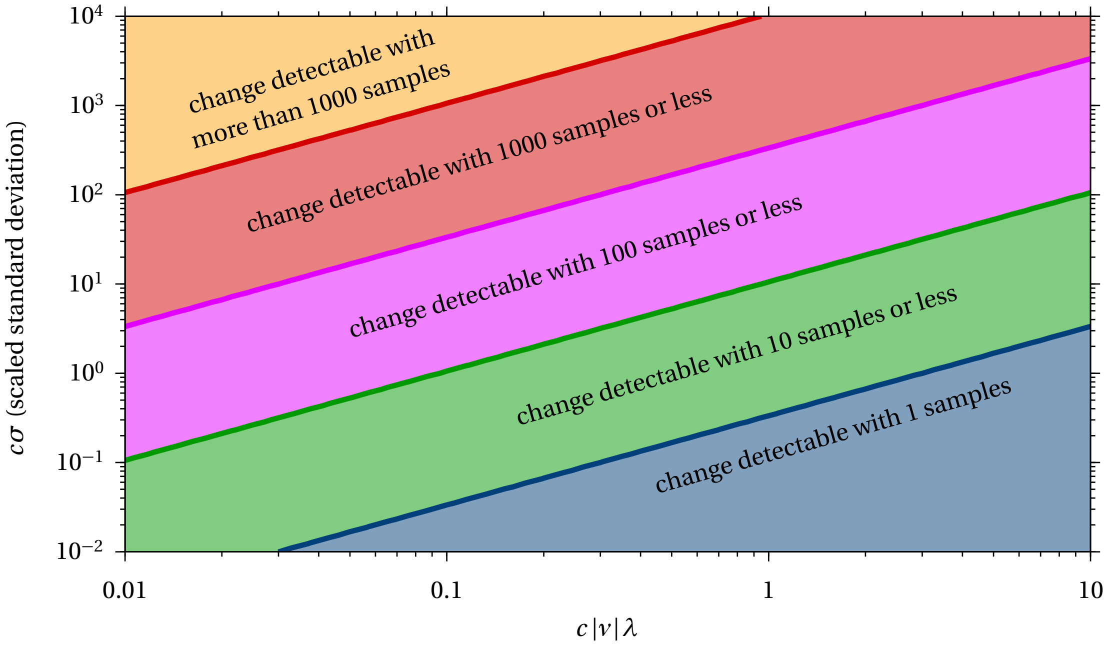

Figure 5.12: Average number of samples required to detect an absolute slope change $c\left|\eta\right|$ when the standard deviation is $c\sigma$ and the sampling interval is λ ($1-\beta = 99\%$, $\alpha = 1\%$).

or lower values of the standard deviation σ, require on average lower numbers of samples in order to confirm whether a given slope change has occurred or not. Conversely, lower values of the detectability ratio υ, caused by lower values of the absolute slope change $\left|\eta\right|$ or higher values of the standard deviation σ, require on average higher numbers of samples in order to confirm whether a given slope change has occurred or not. The detectability ratio υ is of key importance because it expresses the general relationship that ties the number of samples that are on average required to confirm whether a slope change has occurred or not to the absolute slope change $\left|\eta\right|$ itself, the standard deviation σ and the sampling interval λ, irrespectively of their actual values and with probabilities $1-\beta$ of **detection** and α of **false-calling**.

Often, rather than knowing how many samples are required to detect some absolute slope change $\left|\eta\right|$ given some standard deviation σ, it is of practical importance to know how small a slope change can be detected with a given number of samples, say ten or less, a given sampling interval λ, say 1s, and a given standard deviation σ, say 0.1. From figure 5.12 it can be seen that, for a positive real number c, any absolute slope change $c\left|\eta\right|$ of 0.1 or more can on average be detected with ten samples or less, and that any absolute slope change $c\left|\eta\right|$ of 0.3 or more can be detected on average with one samples; however, it could take on average up to 100 samples to detect absolute slope changes $c\left|\eta\right|$ as small as 0.03. Moreover, figure

5.12 clearly presents the link between the number of samples that are on average required to confirm whether a slope change has occurred or not, the sampling interval, the standard deviation and the absolute slope change $\left|\eta\right|$ itself.

5.4 Conclusions

In this chapter the most powerful algorithms for detecting changes in the probability distribution of random variables, and in particular the GLR, have been reviewed in section 5.1. Sections 5.2 and 5.3 exemplified respectively step and gradual change detection in the case of a normally distributed random variable utilising the GLR algorithm.

Chapter 6

Damage Detection in Pipelines

The detection of damage growth is the fundamental part of any Structural Health Monitoring (SHM) strategy. However, the sensors that SHM relies upon do not directly measure damage growth, but rather measure a set of damage-sensitive system properties from which the growth of damage can be inferred. The detection of damage growth is therefore a change detection problem that consists in identifying changes over time in the damage-sensitive properties of a monitored system, and that by definition requires the comparison between two system states before and after the occurrence of change, *i.e.* the growth of damage. The state of the system before the occurrence of change, *i.e.* the growth of damage, is commonly referred to as **baseline**, and any properties sample collected while the system is in its baseline state is referred to as **baseline sample**. Note that in its baseline state the system might be undamaged or may present some pre-existing damage.

In the case of pipelines, the damage-sensitive property that permanently installed guided wave sensors measure is the response to a guided wave excitation of all discontinuities in the waveguide under consideration, *i.e.* the pipeline. Should damage grow then either a new response will appear or the response from an existing discontinuity will change. Moreover, permanently installed guided wave sensors rely on baseline subtraction to enhance sensitivity and detect the presence of damage whose response would normally be masked by coherent noise or by the large responses of pipeline features and pre-existing damage. Therefore, the damage-sensitive property that permanently installed guided wave sensors actually measure is the residual signal obtained from baseline subtraction, and the detection of damage growth consists in identifying the presence of new responses as well as changes in existing responses over time in the residual signal.

The detection of damage growth presents two fundamental challenges. Firstly, as discussed in section 4.2, one of the biggest challenges of damage detection, and thence of SHM, is that the values of the damage-sensitive properties measured by a SHM sensor monitoring a system while the system remains in its baseline state often cannot be computed in advance but rather have to be modelled from a set of baseline samples utilising some form of machine learning [108, 109]. Secondly, as discussed in section 4.3, because of Environmental and Operational Conditions (EOC) effects the value of the damage-sensitive properties of a system will vary significantly even when the underlying structural integrity conditions of the system remain unaltered. In particular, the discontinuity responses measured by permanently installed guided wave sensors will change over time as a function of many EOC variations, and primarily as a function of changes in the operating temperature of the monitored pipeline. In the context of SHM, EOC refer to the conditions the monitored system is operating at and in when its damage-sensitive properties are measured, while EOC effects refer to the influence EOC variations have on the damage-sensitive properties. In the case of petrochemical pipelines EOC include factors such as operating temperature, environmental temperature, type of petrochemical product transported, and many others.

EOC effects represent arguably the major issue hindering practical large-scale SHM deployment [1, 2, 102, 115] and raise issues both when creating a model of the damage-sensitive properties of a system while it remains in its baseline state, and when detecting damage-induced changes, since if the damage-sensitive properties were to change following not only damage growth but also EOC variations then these two sources of change could be mistaken for one another.

In section 4.4 it was shown that although in theory it is possible to compensate for EOC variations in the residual signal from permanently installed guided wave sensors, in practice any compensation is bound to remain partial. It follows that the residual signal from permanently installed guided wave sensors will always vary over time even when there is no damage growth because of uncompensated EOC effects.

This chapter will introduce, explain and exemplify a novel approach to enable the effective detection of damage growth in pipelines even with a limited amount of baseline samples. While previous approaches sought to create actual statistical models of the EOC effects and utilise these to essentially purge the damage-sensitive properties of any EOC effect [109, 130, 131], by contrast the proposed approach seeks first to compensate as much as possible for EOC variations utilising the baseline subtraction compensation methodology discussed in section 4.4, and successively to treat all remaining uncompensated EOC effects as a random noise source that corrupts the true underlying value of the residual signal from permanently installed guided wave sensors. Because the combined residual signal variations are the sum of many different uncompensated EOC effects, including benign changes in feature echoes and in coherent noise, each of which has an unknown probability distribution, by the central limit theorem it will be assumed throughout this chapter that uncompensated EOC effects are equivalent to normally distributed noise with a variance that remains nominally constant across all residual signals. Note, importantly, that such assumption implies that the proposed approach would not work were the magnitude of the uncompensated EOC effects to grow steadily, *i.e.* drift, as more and more residual signals from permanently installed guided wave sensor become available.

The approach described in this chapter therefore regards SHM with permanently installed guided wave sensors as a machine learning problem the goal of which is not to reconstruct a statistical model of EOC effects, but instead to reconstruct a statistical model that represents the true underlying value of the damage-sensitive property, *i.e.* the residual signal, while the monitored system, *i.e.* the pipeline, remains in its baseline state. All uncompensated EOC effects left after baseline subtraction compensation are confined to the noise term of the statistical model.

Utilising such a statistical model it becomes possible to predict the likely future underlying value of the damage-sensitive property, *i.e.* the residual signal, were the system, *i.e.* the pipeline, to remain in its baseline state. The detection of damage growth therefore reduces to a composite change detection problem in which it is sought to determine whether a newly gathered property sample, *i.e.* a new residual signal, is consistent or not with the statistical model and therefore with the baseline state of the system. In this way it becomes possible to establish whether variations in the residual signal from permanently installed guided wave sensors over time are due to uncompensated EOC effects or to damage growth.

The proposed approach therefore fundamentally differs from previous ones [109, 130, 131] because it is chosen to explicitly avoid any attempt at modelling the behaviour of the EOC effects that influence the damage-sensitive properties measured by SHM sensors, and offers multiple advantages, the most important of which is that it enables effective operation even when the availability of baseline samples is limited as a result of the integration of baseline subtraction compensation with statistical modelling.

Because in previous approaches [109, 130, 131] attempts were made to create actual statistical models of the EOC effects that influence the damage-sensitive properties measured by a SHM sensor, a large number of baseline samples were required to learn to a satisfactory level the relationships between EOC effects and measurable EOC parameters such as operating temperature, environmental temperature, and others. As previously discussed in section 4.5, constructing a statistical model of the EOC effects would require an amount of baseline samples that is proportional to the complexity of the EOC effects and that is simply too large to be practical in an industrial SHM scenario, and even though there exist methods, such as sparse sampling theory, to limit the amount of samples needed, these methods are nevertheless based on a number of assumptions that may or may not prove realistic.

The proposed approach utilises baseline subtraction compensation to minimise the impact of EOC effects. Specifically, the baseline subtraction compensation approach described in section 4.4 minimises the impact of any EOC effect whose physics is well understood and that therefore presents a clear trend against measurable EOC parameters such as operating temperature, environmental temperature, and others. Any uncompensated EOC effect left in the residual signal after baseline subtraction compensation does not by definition present a clear trend against measurable EOC parameters, because otherwise it would have been possible to create and validate a physical model that explains it. Consequently, it is reasonable to treat unexplained, uncompensated EOC effects as measurement noise, as in practice has been done in previous approaches [109, 130, 131]. Importantly, because by utilising baseline subtraction compensation, and therefore by making full use of all available information about the physics of EOC effects to minimise their impact, there is no need to learn the relationships between measurable EOC parameters and EOC effects, there is also no need to have a large number of baseline samples from which to learn such relationships. In other words, while previous approaches [109, 130, 131] utilised the information contained in the baseline samples to both learn the physical models that govern the relationships between measurable EOC parameters and EOC effects and to estimate the measurement noise, the proposed approach requires baseline samples only to estimate the measurement noise, *i.e.* the uncompensated EOC effects. As a result, the minimum number of baselines samples required by the proposed approach to operate effectively is much reduced.

As previously discussed in chapter 4, SHM in general seeks to:

1. **Detect** the development and growth of damage.
2. **Locate** the system region or component where damage has developed.
3. **Diagnose** the type and severity of damage and potentially its growth rate.
4. **Monitor** the damage growth rate.

The approach presented in this chapter therefore seeks to address the **detection**, **location** and, to a partial extent, **diagnosis** aspects of SHM when the system under consideration is a petrochemical pipeline being monitored by a permanently installed guided wave sensor. More specifically, the primary goal of the proposed approach is to determine whether new responses as well as changes in existing responses over time in the residual signal have been produced by damage growth or not. Once that has been established, locating damage becomes a simple heuristic problem because the velocity of propagation of guided waves in pipes is known and therefore so is the location of origin of each echo. Diagnosis is then straightforward and consists in evaluating the magnitude of any new response as well as of any change in existing responses over time, in a similar way to and subject to similar limitations as conventional guided wave inspection procedures described in section 2.2 [8, 9, 51–53, 55, 57–60]. Notably, there have recently been parallel efforts seeking to utilise an approach similar to the proposed one that combines baseline subtraction compensation with statistical modelling to address the **detection**, **location** and, to a partial extent, **diagnosis** aspects of SHM when the system under consideration is a plate-like structure being monitored by an array of ultrasonic transducers [145, 146].

The true response from pipeline features as well as from pre-existing damage should in principle remain constant during the period over which baseline signals are being collected, and any variation observed between the baseline residuals must be caused by uncompensated EOC effects. The evolution over time of the damage-sensitive properties, *i.e.* the residual signal, of the monitored system, *i.e.* the pipeline, were the system to remain in its baseline state can therefore be modelled as a linear process whose mean remains constant over time and whose variance represents the variation between baseline residuals caused by uncompensated EOC effects.

Under the assumption that the true response from pipeline features as well as from pre-existing damage will generally remain constant in the future unless damage grows, utilising the linear process model it becomes possible to predict the likely future magnitude of variations caused by uncompensated EOC effects, *i.e.* the measurement noise, and therefore to structure a composite change detection problem which seeks to determine the likelihood that the variations observed between a newly gathered damage-sensitive properties sample, *i.e.* a new residual signal, and the linear process model are due to damage growth.

Throughout this chapter the column vector $\mathbf{y} \in \mathbb{R}^q$ will represent a residual signal consisting of q samples collected with sampling frequency λ. Note that the sampling frequency λ refers to the actual sampling frequency of the instrumentation utilised to record the signals from which the residual signal represented by $\mathbf{y} \in \mathbb{R}^q$ has been obtained. Typically, after a permanently installed guided wave sensor has been installed on a pipeline, a number b of baseline signals will be gathered while the pipeline is operative and in a known, stable health condition, whether undamaged or partially damaged, that is being ascertained through means other than the permanently installed guided wave sensor. From these baseline signals it is possible to obtain b residual signals $\mathbf{y}_i$, referred to as baseline residuals, utilising the baseline subtraction compensation methodology discussed in section 4.4. Specifically, each of the baseline signals can in turn be regarded as a newly collected signal from which one of the remaining baseline signals can be subtracted utilising the baseline subtraction compensation procedure discussed in section 4.4.

This chapter will first introduce the linear regression model, which has been identified as the preferred method to model the behaviour of the uncompensated EOC effects, in section 6.1 together with a discussion on the methodology and implications of estimating such model from a set of b baseline residuals. Successively, in section 6.2 it will be shown how it is in general possible to determine whether a new sample, such as a new residual signal, is consistent or not with a given linear regression model, such as the one estimated from a set of b baseline residuals, thereby enabling the possibility of establishing whether variations in the residual signal from permanently installed guided wave sensors over time are due to uncompensated EOC effects or to damage growth. Finally, in section 6.3 it will be exemplified, utilising experimental data, how the concepts presented in sections 6.1 and 6.2 can be combined to detect damage growth in practical circumstances.

6.1 Linear Regression for Damage Detection

Let $\mathbf{y} \in \mathbb{R}^q$ be a column vector representing a residual signal from a permanently installed guided wave sensor obtained utilising the baseline subtraction compensation methodology introduced in section 4.4. As previously discussed, a residual signal can be thought of as the sum of its true underlying value and of some measurement noise originating from uncompensated EOC effects. The column vector $\mathbf{y}$ representing the residual signal can therefore be though of as a random column vector fluctuating around a column vector $\boldsymbol{\mu} \in \mathbb{R}^q$ that represents the true underlying value of the residual signal when there is no damage growth.

Because the evolution over time of the residual signal $\mathbf{y}$ in the absence of damage growth can be modelled as a linear process, it follows that the column vector $\boldsymbol{\mu}$ can be modelled as a linear function

$$\boldsymbol{\mu} = f(\mathbf{X}) = \mathbf{X}\mathbf{w} \tag{6.1}$$

of a matrix $\mathbf{X} \in \mathbb{R}^{q \times p}$ composed of q known row vectors $\mathbf{x}_k$ and parameterised by the column vector $\mathbf{w} \in \mathbb{R}^p$, or explicitly

$$\begin{bmatrix} \mu_1 \\ \mu_2 \\ \vdots \\ \mu_q \end{bmatrix} = \boldsymbol{\mu} = \mathbf{X}\mathbf{w} = \begin{bmatrix} \mathbf{x}_1 \\ \mathbf{x}_2 \\ \vdots \\ \mathbf{x}_q \end{bmatrix} \begin{bmatrix} w_1 \\ w_2 \\ \vdots \\ w_p \end{bmatrix} = \begin{bmatrix} x_{1,1}w_1 + x_{1,2}w_2 + \cdots + x_{1,p}w_p \\ x_{2,1}w_1 + x_{2,2}w_2 + \cdots + x_{2,p}w_p \\ \vdots \\ x_{q,1}w_1 + x_{q,2}w_2 + \cdots + x_{q,p}w_p \end{bmatrix} \tag{6.2}$$

Each row vector $\mathbf{x}_k$ is composed of independent inputs $x_{k,j}$ each of which represents a quantity such as the time at which the residual signal $\mathbf{y}$ has been gathered, the distance along the pipe to which the signal sample y_k corresponds to, and others, as shall be discussed in section 6.3. The residual signal $\mathbf{y}$ can then in general be expressed as

$$\mathbf{y} = \boldsymbol{\mu} + \boldsymbol{\epsilon} = f(\mathbf{X}) + \boldsymbol{\epsilon} = \mathbf{X}\mathbf{w} + \boldsymbol{\epsilon} \tag{6.3}$$

where $\boldsymbol{\epsilon} \in \mathbb{R}^q$ is a zero-mean random column vector representing the uncompensated EOC effects which, as previously discussed, are assumed to have a non-degenerate normal probability density function

$$p(\boldsymbol{\epsilon} \mid \mathbf{0}, \boldsymbol{\Psi}) = (2\pi)^{-q/2} |\boldsymbol{\Psi}|^{-1/2} \exp\left(-\boldsymbol{\epsilon}^\top \boldsymbol{\Psi}^{-1} \boldsymbol{\epsilon}/2\right) \tag{6.4}$$

and symmetric positive-definite covariance matrix $\boldsymbol{\Psi} \in \mathbb{R}^{q \times q}$. Then by affinity the residual signal $\mathbf{y}$ is also a random column vector with a non-degenerate normal probability density function

$$p\left(\mathbf{y} \mid \mathbf{X}\mathbf{w}, \boldsymbol{\Psi}\right) = |2\pi\boldsymbol{\Psi}|^{-1/2} \exp\left(-\left(\mathbf{y} - \mathbf{X}\mathbf{w}\right)^\top \boldsymbol{\Psi}^{-1} \left(\mathbf{y} - \mathbf{X}\mathbf{w}\right)/2\right), \quad \mathbf{y} \sim \mathcal{N}(\mathbf{X}\mathbf{w}, \boldsymbol{\Psi}) \tag{6.5}$$

since it can be easily verified [147] that

$$f : \mathbf{z} \to \mathbf{c} + \mathbf{B}\mathbf{z} \Longleftrightarrow \mathcal{N}\left(\boldsymbol{\mu}, \boldsymbol{\Psi}\right) \to \mathcal{N}\left(\mathbf{c} + \mathbf{B}\boldsymbol{\mu}, \mathbf{B}\boldsymbol{\Psi}\mathbf{B}^\top\right) \tag{6.6}$$

for any affine transformation f and any normal probability density function

$$p\left(\mathbf{z} \mid \boldsymbol{\mu}, \boldsymbol{\Psi}\right) = |2\pi\boldsymbol{\Psi}|^{-1/2} \exp\left(-\left(\mathbf{z} - \boldsymbol{\mu}\right)^\top \boldsymbol{\Psi}^{-1} \left(\mathbf{z} - \boldsymbol{\mu}\right)/2\right), \quad z \sim \mathcal{N}\left(\boldsymbol{\mu}, \boldsymbol{\Psi}\right) \tag{6.7}$$

with $\mathbf{c} \in \mathbb{R}^m$ and $\mathbf{B} \in \mathbb{R}^{m \times q}$, as discussed in appendix C.

Assume a column vector $\mathring{\mathbf{Y}} \in \mathbb{R}^r$, with $r = qb$, consisting of a concatenation of b nominally independent baseline samples $\mathbf{y}_i$ of the residual signal $\mathbf{y}$ has been gathered for a matrix $\mathring{\mathbf{X}}$ of b known input matrices $\mathbf{X}_i$. Then

$$\mathring{\mathbf{Y}} = \mathring{\mathbf{X}}\mathbf{w} + \mathring{\mathbf{E}} \tag{6.8}$$

or, explicitly

$$\begin{bmatrix}\mathbf{y}_1\\\mathbf{y}_2\\\vdots\\\mathbf{y}_b\end{bmatrix}=\begin{bmatrix}\mathbf{X}_1\\\mathbf{X}_2\\\vdots\\\mathbf{X}_b\end{bmatrix}\begin{bmatrix}w_1\\w_2\\\vdots\\w_p\end{bmatrix}+\begin{bmatrix}\boldsymbol{\epsilon}_1\\\boldsymbol{\epsilon}_2\\\vdots\\\boldsymbol{\epsilon}_b\end{bmatrix},\quad \mathbf{y}_i\sim\mathscr{N}(\mathbf{X}_i\mathbf{w},\boldsymbol{\Psi}),\quad \boldsymbol{\epsilon}_i\sim\mathscr{N}(\mathbf{0},\boldsymbol{\Psi}) \tag{6.9}$$

where $\mathring{\mathbf{X}}\in\mathbb{R}^{r\times p}$ is a matrix of b input matrices $\mathbf{X}_i$. In general neither the vector $\mathbf{w}$ that parameterises the linear regression model f, which represents the true underlying value of the residual signal $\mathbf{y}$, nor the covariance matrix $\boldsymbol{\Psi}$, that parameterises the measurement noise originating from uncompensated EOC effects, will be known in advance. It is therefore of interest to obtain their joint estimates $\hat{\mathbf{w}}$ and $\hat{\boldsymbol{\Psi}}$.

In appendix section C.3 it is shown that, for known $\boldsymbol{\Psi}$, the maximum-likelihood estimate $\hat{\mathbf{w}}$ of the parameter vector $\mathbf{w}$ given baseline data $\mathring{\mathbf{Y}}$ and $\mathring{\mathbf{X}}$ is a random column vector given by

$$\hat{\mathbf{w}}=\boldsymbol{\Omega}\sum_{i=1}^{b}\mathbf{X}_i^\top\boldsymbol{\Psi}^{-1}\mathbf{y}_i,\quad \boldsymbol{\Omega}^{-1}=\sum_{i=1}^{b}\mathbf{X}_i^\top\boldsymbol{\Psi}^{-1}\mathbf{X}_i,\quad \hat{\mathbf{w}}\sim\mathscr{N}(\mathbf{w},\boldsymbol{\Omega}) \tag{6.10}$$

with a non-degenerate normal probability density function

$$p(\hat{\mathbf{w}}\mid\mathbf{w},\boldsymbol{\Omega})=|2\pi\boldsymbol{\Omega}|^{-1/2}\exp\left(-(\hat{\mathbf{w}}-\mathbf{w})^\top\boldsymbol{\Omega}^{-1}(\hat{\mathbf{w}}-\mathbf{w})/2\right) \tag{6.11}$$

and that, for known $\mathbf{w}$, the maximum-likelihood estimate $\hat{\boldsymbol{\Psi}}$ of the covariance matrix $\boldsymbol{\Psi}$ given baseline data $\mathring{\mathbf{Y}}$ and $\mathring{\mathbf{X}}$ is a random matrix given by

$$\hat{\boldsymbol{\Psi}}=\frac{1}{b}\sum_{i=1}^{b}(\mathbf{y}_i-\mathbf{X}_i\mathbf{w})(\mathbf{y}_i-\mathbf{X}_i\mathbf{w})^\top,\quad \hat{\boldsymbol{\Psi}}\sim\mathscr{W}_b(\boldsymbol{\Psi}/b) \tag{6.12}$$

with a Wishart probability density function

$$p\left(\hat{\boldsymbol{\Psi}}\mid\boldsymbol{\Psi}/b\right)=\frac{|\boldsymbol{\Psi}/b|^{-b/2}}{2^{kb/2}\Gamma_k(b/2)}\left|\hat{\boldsymbol{\Psi}}\right|^{(b-q-1)/2}\exp\left(-\operatorname{tr}\left(\boldsymbol{\Psi}^{-1}\hat{\boldsymbol{\Psi}}/b\right)/2\right) \tag{6.13}$$

with b degrees of freedom and mean $\boldsymbol{\Psi}$. It then follows, as demonstrated in appendix section C.3, that the maximum-likelihood estimate $\hat{\boldsymbol{\Omega}}$ of the covariance matrix $\boldsymbol{\Omega}$

$$\hat{\boldsymbol{\Omega}}=\left(\sum_{i=1}^{b}\mathbf{X}_i^\top\hat{\boldsymbol{\Psi}}^{-1}\mathbf{X}_i\right)^{-1},\quad \hat{\boldsymbol{\Omega}}\sim\mathscr{W}_b(\boldsymbol{\Omega}/b) \tag{6.14}$$

also follows a Wishart distribution with b degrees of freedom and mean $\boldsymbol{\Omega}$.

It is shown in appendix section C.3 that if both $\mathbf{w}$ and $\boldsymbol{\Psi}$ are unknown then the joint distribution of their estimates $\hat{\mathbf{w}}$ and $\hat{\boldsymbol{\Psi}}$ will be given by the normal-Wishart distribution

$$\left(\hat{\mathbf{w}},\hat{\boldsymbol{\Psi}}\right)\sim\mathscr{N}\mathscr{W}_b(\mathbf{w},\boldsymbol{\Psi})=\mathscr{N}(\mathbf{w},\boldsymbol{\Omega})\mathscr{W}_b(\boldsymbol{\Psi}/b) \tag{6.15}$$

Similarly, the joint distribution of the estimates $\hat{\mathbf{w}}$ and $\hat{\boldsymbol{\Omega}}$ of $\mathbf{w}$ and $\boldsymbol{\Omega}$ will be given by the normal-Wishart distribution

$$\left(\hat{\mathbf{w}},\hat{\boldsymbol{\Omega}}\right) \sim \mathscr{N}\mathscr{W}_b\left(\mathbf{w},\boldsymbol{\Omega}\right) = \mathscr{N}\left(\mathbf{w},\boldsymbol{\Omega}\right)\mathscr{W}_b\left(\boldsymbol{\Omega}/b\right) \tag{6.16}$$

which, as shown in appendix section C.3, after some manipulation can be written as

$$\begin{aligned} p\left(\hat{\mathbf{w}}\,|\,\hat{\boldsymbol{\Omega}}\right)p\left(\hat{\boldsymbol{\Omega}}\right) = {} & \frac{\left|b\boldsymbol{\Omega}^{-1}\right|^{1/2}}{2^{p(b+1)/2}\pi^{p/2}\Gamma_p\left(b/2\right)} \\ & \left|\hat{\boldsymbol{\Omega}}^{-1}\right|^{(-b-p)/2}\exp\left(-\operatorname{tr}\left(\left(b\boldsymbol{\Omega}+(\hat{\mathbf{w}}-\mathbf{w})(\hat{\mathbf{w}}-\mathbf{w})^{\top}\right)\hat{\boldsymbol{\Omega}}^{-1}\right)/2\right) \end{aligned} \tag{6.17}$$

Then, the marginal distribution of $p\left(\hat{\mathbf{w}}\right)$ of $\hat{\mathbf{w}}$ over all values of $\hat{\boldsymbol{\Omega}}$ is given by [148]

$$\begin{aligned} p\left(\hat{\mathbf{w}}\right) &= \int p\left(\hat{\mathbf{w}}\,|\,\hat{\boldsymbol{\Omega}}\right)p\left(\hat{\boldsymbol{\Omega}}\right)\,\mathrm{d}\hat{\boldsymbol{\Omega}} \\ &\propto \int\left|\hat{\boldsymbol{\Omega}}^{-1}\right|^{(-b-p)/2}\exp\left(-\operatorname{tr}\left(\left(b\boldsymbol{\Omega}+(\hat{\mathbf{w}}-\mathbf{w})(\hat{\mathbf{w}}-\mathbf{w})^{\top}\right)\hat{\boldsymbol{\Omega}}^{-1}\right)/2\right)\,\mathrm{d}\hat{\boldsymbol{\Omega}} \\ &\propto \left|b\boldsymbol{\Omega}+(\hat{\mathbf{w}}-\mathbf{w})(\hat{\mathbf{w}}-\mathbf{w})^{\top}\right|^{(-b-p)/2} \\ &\propto \left(1+(\hat{\mathbf{w}}-\mathbf{w})\boldsymbol{\Omega}^{-1}(\hat{\mathbf{w}}-\mathbf{w})^{\top}/b\right)^{(-b-p)/2} \end{aligned} \tag{6.18}$$

since the theory of determinants shows that for any square matrix $\mathbf{A}\in\Re^{k\times k}$ and column vector $\mathbf{v}\in\Re^{k}$

$$\left|\mathbf{A}+\mathbf{v}\mathbf{v}^{\top}\right| = |\mathbf{A}|\left(1+\mathbf{v}\mathbf{A}^{-1}\mathbf{v}^{\top}\right) \tag{6.19}$$

from which it can be concluded that the estimate $\hat{\mathbf{w}}$ of the parameter vector $\mathbf{w}$ is a random column vector with a t probability density function with b degrees of freedom

$$p\left(\hat{\mathbf{w}}\right) = \frac{\Gamma_p\left(\left(b+p\right)/2\right)}{\Gamma_p\left(b/2\right)\left(b\pi\right)^{p/2}|\boldsymbol{\Omega}|^{1/2}}\left(1+(\hat{\mathbf{w}}-\mathbf{w})^{\top}\boldsymbol{\Omega}^{-1}(\hat{\mathbf{w}}-\mathbf{w})/b\right)^{(-b-p)/2}, \quad \hat{\mathbf{w}}\sim\mathscr{T}_b\left(\mathbf{w},\boldsymbol{\Omega}\right) \tag{6.20}$$

Practical estimates $\hat{\mathbf{w}}$, $\hat{\boldsymbol{\Psi}}$ and $\hat{\boldsymbol{\Omega}}$ of respectively $\mathbf{w}$, $\boldsymbol{\Psi}$ and $\boldsymbol{\Omega}$ can be obtained by iterating

$$\hat{\boldsymbol{\Psi}}_n = \frac{1}{b}\sum_{i=1}^{b}\left(\mathbf{y}_i-\mathbf{X}_i\hat{\mathbf{w}}_{n-1}\right)\left(\mathbf{y}_i-\mathbf{X}_i\hat{\mathbf{w}}_{n-1}\right)^{\top}, \quad \boldsymbol{\Psi}_0=\mathbf{I} \tag{6.21}$$

with

$$\hat{\mathbf{w}}_{n-1} = \hat{\boldsymbol{\Omega}}_{n-1}\sum_{i=1}^{b}\mathbf{X}_i^{\top}\hat{\boldsymbol{\Psi}}_{n-1}^{-1}\mathbf{y}_i \tag{6.22}$$

and

$$\hat{\boldsymbol{\Omega}}_{n-1} = \left(\sum_{i=1}^{b}\mathbf{X}_i^{\top}\hat{\boldsymbol{\Psi}}_{n-1}^{-1}\mathbf{X}_i\right)^{-1} \tag{6.23}$$

until a satisfactory convergence has been reached.

Because the parameter vector $\mathbf{w}$ is what characterises the linear regression model f, obtaining an estimate $\hat{\mathbf{w}}$ is equivalent to fitting the linear regression model f to the baseline data $\mathring{\mathbf{Y}}$ and $\mathring{\mathbf{X}}$. The function

$$\hat{f}(\mathbf{X}) = \mathbf{X}\hat{\mathbf{w}}, \quad \hat{f}(\mathbf{X}) \sim \mathcal{N}\left(\mathbf{X}\mathbf{w}, \mathbf{X}\boldsymbol{\Omega}\mathbf{X}^{\top}\right) = \mathcal{N}\left(f(\mathbf{X}), \boldsymbol{\Theta}\right) \tag{6.24}$$

parameterised by the estimate $\hat{\mathbf{w}}$ of the parameter vector $\mathbf{w}$ therefore represents an estimate of the linear regression model f fitted to the baseline data $\mathring{\mathbf{Y}}$ and $\mathring{\mathbf{X}}$. Equivalently, the estimate $\hat{f}$ of the linear regression model f indicates what, according to the information provided by the baseline data, appears to be the true underlying value of the residual signal from a permanently installed guided wave sensor in absence of damage growth for any input matrix $\mathbf{X}$, *i.e.* at any position along the pipe and at any moment in time. The estimate $\hat{f}$ is clearly an affine transformation of $\hat{\mathbf{w}}$, and it follows that for known $\boldsymbol{\Psi}$, and therefore known $\boldsymbol{\Omega}$ and $\boldsymbol{\Theta}$, it is also a normally distributed random column vector with symmetric covariance matrix

$$\boldsymbol{\Theta} = \mathbf{X}\boldsymbol{\Omega}\mathbf{X}^{\top} = \mathbf{X}\boldsymbol{\Omega}^{\top}\mathbf{X}^{\top} = \left(\mathbf{X}\boldsymbol{\Omega}\mathbf{X}^{\top}\right)^{\top} = \boldsymbol{\Theta}^{-\top} \tag{6.25}$$

If $\hat{\boldsymbol{\Theta}}$ is an estimate of $\boldsymbol{\Theta}$, then from the properties of the Wishart distribution

$$\hat{\boldsymbol{\Theta}} = \mathbf{X}\hat{\boldsymbol{\Omega}}\mathbf{X}^{\top} \sim \mathcal{W}_b\left(\mathbf{X}\boldsymbol{\Omega}\mathbf{X}^{\top}/b\right) = \mathcal{W}_b(\boldsymbol{\Theta}/b) \tag{6.26}$$

The joint distribution of the estimates $\hat{f}$ and $\hat{\boldsymbol{\Theta}}$ of f and $\boldsymbol{\Theta}$ will be given by the normal-Wishart distribution

$$\left(\hat{f}, \hat{\boldsymbol{\Theta}}\right) \sim \mathcal{N}\mathcal{W}_b\left(f, \boldsymbol{\Theta}\right) = \mathcal{N}\left(f, \boldsymbol{\Theta}\right)\mathcal{W}_b(\boldsymbol{\Theta}/b) \tag{6.27}$$

which, as shown in appendix section C.3, after some manipulation can be written as

$$\begin{aligned} p\left(\hat{f} \mid \hat{\boldsymbol{\Theta}}\right) p\left(\hat{\boldsymbol{\Theta}}\right) = {} & \frac{\left|b\boldsymbol{\Theta}^{-1}\right|^{1/2}}{2^{q(b+1)/2}\pi^{q/2}\Gamma_q(b/2)} \\ & \left|\hat{\boldsymbol{\Theta}}^{-1}\right|^{(-b-q)/2} \exp\left(-\operatorname{tr}\left(\left(b\boldsymbol{\Theta} + \left(\hat{f}-f\right)\left(\hat{f}-f\right)^{\top}\right)\hat{\boldsymbol{\Theta}}^{-1}\right)/2\right) \end{aligned} \tag{6.28}$$

Then, the marginal distribution of $p\left(\hat{f}\right)$ of $\hat{f}$ over all values of $\hat{\boldsymbol{\Theta}}$ is given by [148]

$$\begin{aligned} p\left(\hat{f}\right) &= \int p\left(\hat{f} \mid \hat{\boldsymbol{\Theta}}\right) p\left(\hat{\boldsymbol{\Theta}}\right) \mathrm{d}\hat{\boldsymbol{\Theta}} \\ &\propto \int \left|\hat{\boldsymbol{\Theta}}^{-1}\right|^{(-b-q)/2} \exp\left(-\operatorname{tr}\left(\left(b\boldsymbol{\Theta} + \left(\hat{f}-f\right)\left(\hat{f}-f\right)^{\top}\right)\hat{\boldsymbol{\Theta}}^{-1}\right)/2\right) \mathrm{d}\hat{\boldsymbol{\Theta}} \\ &\propto \left|b\boldsymbol{\Theta} + \left(\hat{f}-f\right)\left(\hat{f}-f\right)^{\top}\right|^{(-b-q)/2} \\ &\propto \left(1 + \left(\hat{f}-f\right)\boldsymbol{\Theta}^{-1}\left(\hat{f}-f\right)^{\top}/b\right)^{(-b-q)/2} \end{aligned} \tag{6.29}$$

from which it can be concluded at once that the function

$$\hat{f}(\mathbf{X}) = \mathbf{X}\hat{\mathbf{w}}, \quad \hat{f}(\mathbf{X}) \sim \mathscr{T}_b\left(\mathbf{X}\mathbf{w}, \mathbf{X}\boldsymbol{\Omega}\mathbf{X}^\top\right) = \mathscr{T}_b\left(f(\mathbf{X}), \boldsymbol{\Theta}\right) \tag{6.30}$$

parameterised by the estimate $\hat{\mathbf{w}}$ of the parameter vector $\mathbf{w}$ that represents an estimate of the linear regression model f fitted to the baseline data $\mathring{\mathbf{Y}}$ and $\mathring{\mathbf{X}}$ is also a random column vector with a t probability density function with b degrees of freedom.

In conclusion, in this section it has been shown how it is in general possible to represent the true underlying value of the residual signal $\mathbf{y}$ at any position along the pipe and at any moment in time utilising a linear regression model f, and an iterative procedure has been presented to derive an estimate $\hat{f}$ of the linear regression model starting from a set of b baseline samples $\mathbf{y}_i$ of the residual signal $\mathbf{y}$. Specifically, the iterative procedure enables the estimation of the parameter vector $\mathbf{w}$ that characterises the regression model, and of the covariance matrix $\boldsymbol{\Psi}$ that models the uncompensated EOC effects which, as previously discussed, are assumed to have a non-degenerate normal probability density function. Importantly, it has been shown that the estimate $\hat{f}$ of the linear regression model f derived from b baseline samples $\mathbf{y}_i$ of the residual signal $\mathbf{y}$ is actually a random column vector with a t probability density function with b degrees of freedom. As a result, the true underlying value of the residual signal $\mathbf{y}$ at any position along the pipe and at any moment in time is not known absolutely, but instead only its probability density function is actually known. In the next section it will be shown how the information encoded in the probability density function can be effectively utilised to establish whether a given sample, such as a new residual signal, is consistent or not with the estimate of the linear regression model.

6.2 Change Detection with Linear Regression

Suppose a new sample $\mathbf{y}_\star$ of the random column vector $\mathbf{y} \in \mathbb{R}^q$, *i.e.* a new residual signal from a permanently installed guided wave sensor obtained utilising the baseline subtraction compensation methodology introduced in section 4.4, has been gathered at some time $t_\star$ for some input matrix $\mathbf{X}_\star$. As previously discussed, a residual signal can be thought of as the sum of its true underlying value and of the measurement noise originating from uncompensated EOC effects. Therefore it also has a non-degenerate normal probability density function

$$\mathbf{y}_\star \sim \mathscr{N}\left(f(\mathbf{X}_\star), \boldsymbol{\Psi}\right) \tag{6.31}$$

with symmetric positive-definite covariance matrix $\boldsymbol{\Psi}$. It is of interest to establish whether the new sample $\mathbf{y}_\star$ is consistent or inconsistent with the baseline data $\mathring{\mathbf{Y}}$ and $\mathring{\mathbf{X}}$, *i.e.* whether damage has grown in the period of time between the baseline data and the new sample were collected. The information contained in the baseline data is encoded by the estimate $\hat{f}$ of the linear regression model f that indicates what, in the absence of damage growth, should be the true underlying value of the residual signal $\mathbf{y}$ at any position along the pipe and at any moment in time. Then, were there no damage growth one would have

$$\mathbf{y}_\star = \hat{f}(\mathbf{X}_\star) + \boldsymbol{\epsilon} = \mathbf{X}_\star \hat{\mathbf{w}} + \boldsymbol{\epsilon} \tag{6.32}$$

or in other words the new sample $\mathbf{y}_\star$ will be equal to the estimate $\hat{f}(\mathbf{X}_\star)$ of the linear regression model $f(\mathbf{X}_\star)$ plus the zero-mean random column vector $\boldsymbol{\epsilon}$ that represents the uncompensated EOC effects that, as previously discussed, are assumed to have a non-degenerate normal probability density function and symmetric positive-definite covariance matrix $\boldsymbol{\Psi}$. Conversely, were any damage to grow, then

$$\mathbf{y}_\star = \hat{f}(\mathbf{X}_\star) + \boldsymbol{\epsilon} + \boldsymbol{\nu} = \mathbf{X}_\star \hat{\mathbf{w}} + \boldsymbol{\epsilon} + \boldsymbol{\nu} \tag{6.33}$$

or in other words the new sample $\mathbf{y}_\star$ will be equal to the estimate $\hat{f}(\mathbf{X}_\star)$ of the linear regression model $f(\mathbf{X}_\star)$ plus the zero-mean random column vector $\boldsymbol{\epsilon}$ plus the vector $\boldsymbol{\nu} \in \mathbb{R}^q$ that represents the response from the damage that has grown.

If $\boldsymbol{\Psi}$ is known in advance, then so is $\boldsymbol{\Theta}$ and, as previously discussed, one has

$$\hat{f}(\mathbf{X}_\star) \sim \mathcal{N}\left(f(\mathbf{X}_\star), \boldsymbol{\Theta}\right), \quad \boldsymbol{\epsilon} \sim \mathcal{N}(\mathbf{0}, \boldsymbol{\Psi}) \tag{6.34}$$

It follows from the definition of the normal probability density function of equation 6.7 that

$$\mathbf{y}_\star = \hat{f}(\mathbf{X}_\star) + \boldsymbol{\epsilon}, \quad \mathbf{y}_\star \sim \mathcal{N}\left(f(\mathbf{X}_\star), \boldsymbol{\Psi} + \boldsymbol{\Theta}\right) = \mathcal{N}\left(f(\mathbf{X}_\star), \boldsymbol{\Delta}\right) \tag{6.35}$$

and that by affine transform

$$\mathbf{y}_\star - \boldsymbol{\nu} = \hat{f}(\mathbf{X}_\star) + \boldsymbol{\epsilon}, \quad (\mathbf{y}_\star - \boldsymbol{\nu}) \sim \mathcal{N}\left(f(\mathbf{X}_\star) - \boldsymbol{\nu}, \right) = \mathcal{N}\left(f(\mathbf{X}_\star) - \boldsymbol{\nu}, \boldsymbol{\Delta}\right) \tag{6.36}$$

In other words, it has just been shown that because only the estimate $\hat{f}$ of the linear regression model f is known, the apparent probability distribution of $\mathbf{y}_\star$ differs from the true one of equation 6.31 by the addition of the covariance matrix $\boldsymbol{\Theta}$ which intuitively represents the uncertainty on the estimate $\hat{f}$ of the linear regression model f derived from the baseline data $\mathring{\mathbf{Y}}$ and $\mathring{\mathbf{X}}$.

In practical situations however $\boldsymbol{\Psi}$, and therefore $\boldsymbol{\Theta}$, will not in general be known and will have to be estimated from the baseline data $\mathring{\mathbf{Y}}$ and $\mathring{\mathbf{X}}$. Then, as previously discussed, their estimates $\hat{\boldsymbol{\Psi}}$ and $\hat{\boldsymbol{\Theta}}$ will have a Wishart distribution with b degrees of freedom

$$\hat{\boldsymbol{\Psi}} \sim \mathcal{W}_b(\boldsymbol{\Psi}/b), \quad \hat{\boldsymbol{\Theta}} \sim \mathcal{W}_b(\boldsymbol{\Theta}/b) \tag{6.37}$$

and since the Wishart distribution is co-additive it follows that

$$\hat{\mathbf{\Delta}} = \hat{\mathbf{\Psi}} + \hat{\mathbf{\Theta}}, \quad \hat{\mathbf{\Delta}} \sim \mathscr{W}_b\left((\mathbf{\Psi}+\mathbf{\Theta})/b\right) = \mathscr{W}_b\left(\mathbf{\Delta}/b\right) \tag{6.38}$$

The joint distribution of $\mathbf{y}_\star$ and of the estimate $\hat{\mathbf{\Delta}}$ of $\mathbf{\Delta}$ will therefore be given by the normal-Wishart distribution

$$\left(\mathbf{y}_\star, \hat{\mathbf{\Delta}}\right) \sim \mathscr{N}\mathscr{W}_b\left(f\left(\mathbf{X}_\star\right), \mathbf{\Delta}\right) = \mathscr{N}\left(f\left(\mathbf{X}_\star\right), \mathbf{\Delta}\right) \mathscr{W}_b\left(\mathbf{\Delta}/b\right) \tag{6.39}$$

which after some manipulation can be written as

$$\begin{aligned} p\left(\mathbf{y}_\star \mid \hat{\mathbf{\Delta}}\right) p\left(\hat{\mathbf{\Delta}}\right) = {} & \frac{\left|b\mathbf{\Delta}^{-1}\right|^{1/2}}{2^{q(b+1)/2}\pi^{q/2}\Gamma_q\left(b/2\right)} \left|\hat{\mathbf{\Delta}}^{-1}\right|^{-(b+q)/2} \\ & \exp\left(-\operatorname{tr}\left(\left(b\mathbf{\Delta} + \left(\mathbf{y}_\star - f\left(\mathbf{X}_\star\right)\right)\left(\mathbf{y}_\star - f\left(\mathbf{X}_\star\right)\right)^\top\right)\hat{\mathbf{\Delta}}^{-1}\right)/2\right) \end{aligned} \tag{6.40}$$

It follows that the marginal distribution of $p\left(\mathbf{y}_\star\right)$ of $\mathbf{y}_\star$ over all values of $\hat{\mathbf{\Delta}}$ is given by [148]

$$\begin{aligned} p\left(\mathbf{y}_\star\right) &= \int p\left(\mathbf{y}_\star \mid \hat{\mathbf{\Delta}}\right) p\left(\hat{\mathbf{\Delta}}\right) \mathrm{d}\hat{\mathbf{\Delta}} \\ &\propto \int \left|\hat{\mathbf{\Delta}}^{-1}\right|^{-(b+q)/2} \exp\left(-\operatorname{tr}\left(\left(b\mathbf{\Delta} + \left(\mathbf{y}_\star - f\left(\mathbf{X}_\star\right)\right)\left(\mathbf{y}_\star - f\left(\mathbf{X}_\star\right)\right)^\top\right)\hat{\mathbf{\Delta}}^{-1}\right)/2\right) \mathrm{d}\hat{\mathbf{\Delta}} \\ &\propto \left|b\mathbf{\Delta} + \left(\mathbf{y}_\star - f\left(\mathbf{X}_\star\right)\right)\left(\mathbf{y}_\star - f\left(\mathbf{X}_\star\right)\right)^\top\right|^{-(b+q)/2} \\ &\propto \left(1 + \left(\mathbf{y}_\star - f\left(\mathbf{X}_\star\right)\right)\mathbf{\Delta}^{-1}\left(\mathbf{y}_\star - f\left(\mathbf{X}_\star\right)\right)^\top/b\right)^{-(b+q)/2} \end{aligned} \tag{6.41}$$

from which it can be concluded at once that

$$\mathbf{y}_\star = \hat{f}\left(\mathbf{X}_\star\right) + \boldsymbol{\epsilon}, \quad \mathbf{y}_\star \sim \mathscr{T}_b\left(f\left(\mathbf{X}_\star\right), \mathbf{\Psi}+\mathbf{\Theta}\right) = \mathscr{T}_b\left(f\left(\mathbf{X}_\star\right), \mathbf{\Delta}\right) \tag{6.42}$$

and that by affine transform

$$\mathbf{y}_\star - \boldsymbol{\nu} = \hat{f}\left(\mathbf{X}_\star\right) + \boldsymbol{\epsilon}, \quad \left(\mathbf{y}_\star - \boldsymbol{\nu}\right) \sim \mathscr{T}_b\left(f\left(\mathbf{X}_\star\right) - \boldsymbol{\nu}, \mathbf{\Psi}+\mathbf{\Theta}\right) = \mathscr{T}_b\left(f\left(\mathbf{X}_\star\right) - \boldsymbol{\nu}, \mathbf{\Delta}\right) \tag{6.43}$$

In other words, it has just been shown that because only the estimate $\hat{f}$ of the linear regression model f is known, when $\mathbf{\Psi}$, and therefore $\mathbf{\Theta}$, are not known in advance the apparent probability distribution of $\mathbf{y}_\star$ differs from the true one of equation 6.31 not only by the addition of the covariance matrix $\mathbf{\Theta}$, but also ceases to be a normal probability density function and becomes a t probability density function

$$p\left(\mathbf{y}_\star\right) = \frac{\Gamma_q\left(\left(b+q\right)/2\right)}{\Gamma_q\left(b/2\right)\left(b\pi\right)^{q/2}\left|\mathbf{\Delta}\right|^{1/2}} \left(1 + \left(\mathbf{y}_\star - f\left(\mathbf{X}_\star\right)\right)^\top \mathbf{\Delta}^{-1}\left(\mathbf{y}_\star - f\left(\mathbf{X}_\star\right)\right)/b\right)^{(-b-q)/2} \tag{6.44}$$

with b degrees of freedom.

Establishing whether the new sample $\mathbf{y}_\star$ is consistent or inconsistent with the baseline data $\mathring{\mathbf{Y}}$ and $\mathring{\mathbf{X}}$, *i.e.* whether damage has grown in the period of time between the baseline data and the new sample were collected, is equivalent to a composite change detection problem in which the goal is to determine whether the probability density function $p\left(y\right)$ of the random variable $\mathbf{y}_\star$ has undergone a change in mean from $\hat{f}\left(\mathbf{X}_\star\right)$ to $\hat{f}\left(\mathbf{X}_\star\right)+\boldsymbol{\nu}$, where $\boldsymbol{\nu}$ represents the echo from the damage that has grown.

For the special case of a random variable with a t probability density function, sections 6.2.1 and 6.2.2 will introduce respectively the Sequential Probability Ratio Test (SPRT), originally summarised in section 5.1.1 and discussed in appendix B, and the SPRT-based Generalised Likelihood Ratio (GLR) algorithm for the solution of composite change detection problems, originally discussed in section 5.1.3. The SPRT has been shown [134–136] to require the minimum number of samples $\mathbf{y}_{\star i}$ to discriminate between hypotheses on the underlying probability density function of a random variable $\mathbf{y}_\star$ for prescribed probabilities of error. In this sense, the SPRT is said to be **optimal**. Consequently, the GLR algorithm is also **optimal**, in the sense that for prescribed probabilities of error it requires the minimum number of samples $\mathbf{y}_{\star i}$ to detect whether the probability density function of $\mathbf{y}_\star$ has changed, thereby minimising the delay between change time, *i.e.* the time at which damage grows, and detection time.

6.2.1 Sequential Probability Ratio Test

Consider a random column vector $\mathbf{y}_\star$, and consider the hypothesis $\mathbf{H}_0$ that the probability density function of $\mathbf{y}_\star$ is given by $p\left(\mathbf{y}_\star \mid \boldsymbol{\mu}_0, \boldsymbol{\Delta}_0\right) = \mathscr{T}_b\left(\boldsymbol{\mu}_0, \boldsymbol{\Delta}_0\right)$ and an alternative hypothesis $\mathbf{H}_1$ that the probability density function of y is given by $p\left(\mathbf{y}_\star \mid \boldsymbol{\mu}_1, \boldsymbol{\Delta}_1\right) = \mathscr{T}_b\left(\boldsymbol{\mu}_1, \boldsymbol{\Delta}_1\right)$. The log likelihood ratio

$$z = \ln \frac{p\left(\mathbf{y}_\star \mid \boldsymbol{\mu}_1, \boldsymbol{\Delta}_1\right)}{p\left(\mathbf{y}_\star \mid \boldsymbol{\mu}_0, \boldsymbol{\Delta}_0\right)} = \frac{\left|\boldsymbol{\Delta}_0\right|^{1/2}}{\left|\boldsymbol{\Delta}_1\right|^{1/2}} \left(\frac{1 + \left(\mathbf{y}_\star - \boldsymbol{\mu}_0\right)^\top \boldsymbol{\Delta}_0^{-1} \left(\mathbf{y}_\star - \boldsymbol{\mu}_0\right)/b}{1 + \left(\mathbf{y}_\star - \boldsymbol{\mu}_1\right)^\top \boldsymbol{\Delta}_1^{-1} \left(\mathbf{y}_\star - \boldsymbol{\mu}_1\right)/b} \right)^{(b+q)/2} \tag{6.45}$$

will be negative if hypothesis $\mathbf{H}_0$ is true and positive if hypothesis $\mathbf{H}_1$ is true. Given a finite set $Y_m = \left\{\mathbf{y}_{\star 1}, \mathbf{y}_{\star 2}, \ldots, \mathbf{y}_{\star m}\right\}$ of samples $\mathbf{y}_{\star i}$ of $\mathbf{y}_\star$, at each sampling stage m the SPRT consists in evaluating the cumulative log likelihood ratio [138]

$$Z_m = \sum_{i=1}^{m} z_i = \sum_{i=1}^{m} \ln \frac{p\left(\mathbf{y}_{\star i} \mid \boldsymbol{\mu}_1, \boldsymbol{\Delta}_1\right)}{p\left(\mathbf{y}_{\star i} \mid \boldsymbol{\mu}_0, \boldsymbol{\Delta}_0\right)} \tag{6.46}$$

Hypothesis $\mathbf{H}_1$ is accepted if $Z_m \geq \ln A$, and hypothesis $\mathbf{H}_0$ is accepted if $Z_m \leq \ln B$. If $\ln B < Z_m < \ln A$ then sample $\mathbf{y}_{\star m+1}$ is collected and Z_{m+1} is evaluated for the extended sample set $Y_{m+1} = \left\{Y_m, \mathbf{y}_{\star m+1}\right\}$.

6.2.2 Generalised Likelihood Ratio Algorithm

Consider a finite set $Y_{star} = \{\mathbf{y}_{\star 1}, \mathbf{y}_{\star 2}, \ldots, \mathbf{y}_{\star n}\}$ of samples $\mathbf{y}_{\star i}$ of the random column vector $\mathbf{y}_\star$ gathered at known times $t_1, t_2, \ldots, t_n$, and assume that before an unknown change time t_c the probability density function of $\mathbf{y}_\star$ is given by $p\left(\mathbf{y}_\star \mid \boldsymbol{\mu}_0, \boldsymbol{\Delta}_0\right) = \mathcal{T}_b\left(\boldsymbol{\mu}_0, \boldsymbol{\Delta}_0\right)$, and that after t_c the probability density function of $\mathbf{y}_\star$ is given by $p\left(\mathbf{y}_\star \mid \boldsymbol{\mu}_1, \boldsymbol{\Delta}_1\right) = \mathcal{T}_b\left(\boldsymbol{\mu}_1, \boldsymbol{\Delta}_1\right)$ with $\boldsymbol{\mu}_1$ and $\boldsymbol{\Delta}_1$ unknown. It is of interest to detect the onset of change in the probability density function of $\mathbf{y}$ and to estimate t_c, $\boldsymbol{\mu}_1$ and $\boldsymbol{\Delta}_1$.

Consider hypothesis $\mathbf{H}_0$ which states that the probability density function of $\mathbf{y}_\star$ is given by $p\left(\mathbf{y}_\star \mid \boldsymbol{\mu}_0, \boldsymbol{\Delta}_0\right) = \mathcal{T}_b\left(\boldsymbol{\mu}_0, \boldsymbol{\Delta}_0\right)$, and hypothesis $\mathbf{H}_1$ which states that the probability density function of $\mathbf{y}$ is given by $p\left(\mathbf{y}_\star \mid \boldsymbol{\mu}_1, \boldsymbol{\Delta}_1\right) = \mathcal{T}_b\left(\boldsymbol{\mu}_1, \boldsymbol{\Delta}_1\right)$. The value of the log likelihood ratio

$$z_i\left(\boldsymbol{v}_\mu, \boldsymbol{v}_\Delta\right) = \ln \frac{p\left(\mathbf{y}_{\star i} \mid \boldsymbol{\mu}_0 + \boldsymbol{v}_\mu, \boldsymbol{\Delta}_0 + \boldsymbol{v}_\Delta\right)}{p\left(\mathbf{y}_{\star i} \mid \boldsymbol{\mu}_0, \boldsymbol{\Delta}_0\right)} \tag{6.47}$$

where

$$\boldsymbol{v}_\mu = \boldsymbol{\mu}_1 - \boldsymbol{\mu}_0, \quad \boldsymbol{v}_\Delta = \boldsymbol{\Delta}_1 - \boldsymbol{\Delta}_0 \tag{6.48}$$

will be a function of the value of the sample $\mathbf{y}_{\star i}$ as well as of the value of the mean change vector $\boldsymbol{v}_\mu$ and of the covariance change matrix $\boldsymbol{v}_\Delta$. For a given sample $\mathbf{y}_{\star i}$, the value of $z_i\left(\boldsymbol{v}_\mu, \boldsymbol{v}_\Delta\right)$ can therefore be maximised with respect to the mean change vector $\boldsymbol{v}_\mu$ and to the covariance change matrix $\boldsymbol{v}_\Delta$. Similarly, the cumulative log likelihood ratio

$$Z_k^j\left(\boldsymbol{v}_\mu, \boldsymbol{v}_\Delta\right) = \sum_{i=j}^{k} z_i\left(\boldsymbol{v}_\mu, \boldsymbol{v}_\Delta\right) \tag{6.49}$$

can also be maximised with respect to the mean change vector $\boldsymbol{v}_\mu$ and to the covariance change matrix $\boldsymbol{v}_\Delta$. For given values of $\boldsymbol{v}_\mu$ and $\boldsymbol{v}_\Delta$ the maximisation

$$\max_{1 \le j \le k} Z_k^j\left(\boldsymbol{v}_\mu, \boldsymbol{v}_\Delta\right) \tag{6.50}$$

will find, under the assumption that samples $\mathbf{y}_{\star 1}, \ldots, \mathbf{y}_{\star j-1}$ have probability density function $p\left(\mathbf{y}_{\star j} \mid \boldsymbol{\mu}_0, \boldsymbol{\Delta}_0\right)$, which samples $\mathbf{y}_{\star j}, \ldots, \mathbf{y}_{\star k}$ are most likely to have probability density function $p\left(\mathbf{y}_\star \mid \boldsymbol{\mu}_1, \boldsymbol{\Delta}_1\right) = p\left(\mathbf{y}_\star \mid \boldsymbol{\mu}_0 + \boldsymbol{v}_\mu, \boldsymbol{\Delta}_0 + \boldsymbol{v}_\Delta\right)$. It follows that the double maximisation

$$g_k = \max_{1 \le j \le k} \sup_{\boldsymbol{v}_\mu, \boldsymbol{v}_\Delta} Z_k^j\left(\boldsymbol{v}_\mu, \boldsymbol{v}_\Delta\right) \tag{6.51}$$

will find, under the assumption that samples $\mathbf{y}_{\star 1}, \ldots, \mathbf{y}_{\star j-1}$ have probability density function $p\left(\mathbf{y}_{\star j} \mid \boldsymbol{\mu}_0, \boldsymbol{\Delta}_0\right)$, the likeliest mean change vector $\boldsymbol{v}_\mu$ and covariance change matrix $\boldsymbol{v}_\Delta$ for which samples $\mathbf{y}_{\star j}, \ldots, \mathbf{y}_{\star k}$ are most likely to have probability density function $p\left(\mathbf{y}_\star \mid \boldsymbol{\mu}_1, \boldsymbol{\Delta}_1\right) =$

$p\left(\mathbf{y}_\star \mid \boldsymbol{\mu}_0 + \boldsymbol{\nu}_\mu, \boldsymbol{\Delta}_0 + \boldsymbol{\nu}_\Delta\right)$. With prescribed probabilities $1-\beta$ of **detection** and α of **false-calling**, hypothesis $\mathbf{H}_1$ is accepted and change is detected at sample $\mathbf{y}_{\star d}$ and detection time t_d, where d is the smallest positive integer for which $g_d \geq \ln A$. As previously noted, $t_c \leq t_d$ since at least one sample of the random variable $\mathbf{y}_\star$ must be collected at or after change time t_c for change to be detected. Once change has been detected the arguments of the double maximisation

$$e, \boldsymbol{\nu}_\mu, \boldsymbol{\nu}_\Delta = \arg \max_{1 \leq e \leq k} \sup_{\boldsymbol{\nu}_\mu, \boldsymbol{\nu}_\Delta} Z_k^e\left(\boldsymbol{\nu}_\mu, \boldsymbol{\nu}_\Delta\right) \geq \ln A \tag{6.52}$$

will give the the maximum likelihood estimates $\boldsymbol{\mu}_0 + \boldsymbol{\nu}_\mu$ of $\boldsymbol{\mu}_1$, $\boldsymbol{\Delta}_0 + \boldsymbol{\nu}_\Delta$ of $\boldsymbol{\Delta}_1$, and t_e of the change time t_c. Note that if $g_n < \ln A$ then hypothesis $\mathbf{H}_1$ is not accepted and change is not detected within the sample set Y_n, and further samples of $\mathbf{y}_\star$ might be required if there is reason to believe change has actually occurred. As previously discussed, change detection is not equivalent to change occurrence since, subject to probabilities $1-\beta < 1$ of **detection** and $\alpha > 0$ of **false-calling**, change may occur but not be detected and may be detected but not have occurred.

6.3 Practical Pipeline Damage Detection

In this section it will be exemplified, utilising experimental data, how the concepts presented in sections 6.1 and 6.2 can be combined to detect damage growth in practical circumstances utilising permanently installed guided wave sensors. The experimental data originates from two Guided Wave Permanently-Installed Monitoring System (gPIMS®) sensors that have been installed on a purpose-built NPS 8 Schedule 40 pipe loop facility at BP's Naperville Campus. A diagram of the pipe loop is presented in figure 6.1.

The installed gPIMS® sensors, produced and commercialised by Guided Ultrasonics Ltd. [20], are permanently installed guided wave sensors of the kind described in sections 2.2.3 and 4.1 and were attached to the pipe loop utilising a polyurethane-based adhesive. Figure 6.2 presents the gPIMS® P1 sensor before and after its installation on the pipe loop. The thickness of adhesive bond layer between the piezo-electric transducers and the pipe was minimised by closing the spring-loaded clamping mechanism of the gPIMS® sensors. After attachment, the clamping mechanism was sealed under a protective cover. The two gPIMS® sensors are nominally identical except that sensor P1 was sealed by packing the region around the clamping mechanism with Stopaq® CZH paste [149] prior to the attachment of the cover, while the clamping mechanism of sensor P2 was encapsulated with a polyurethane sealant

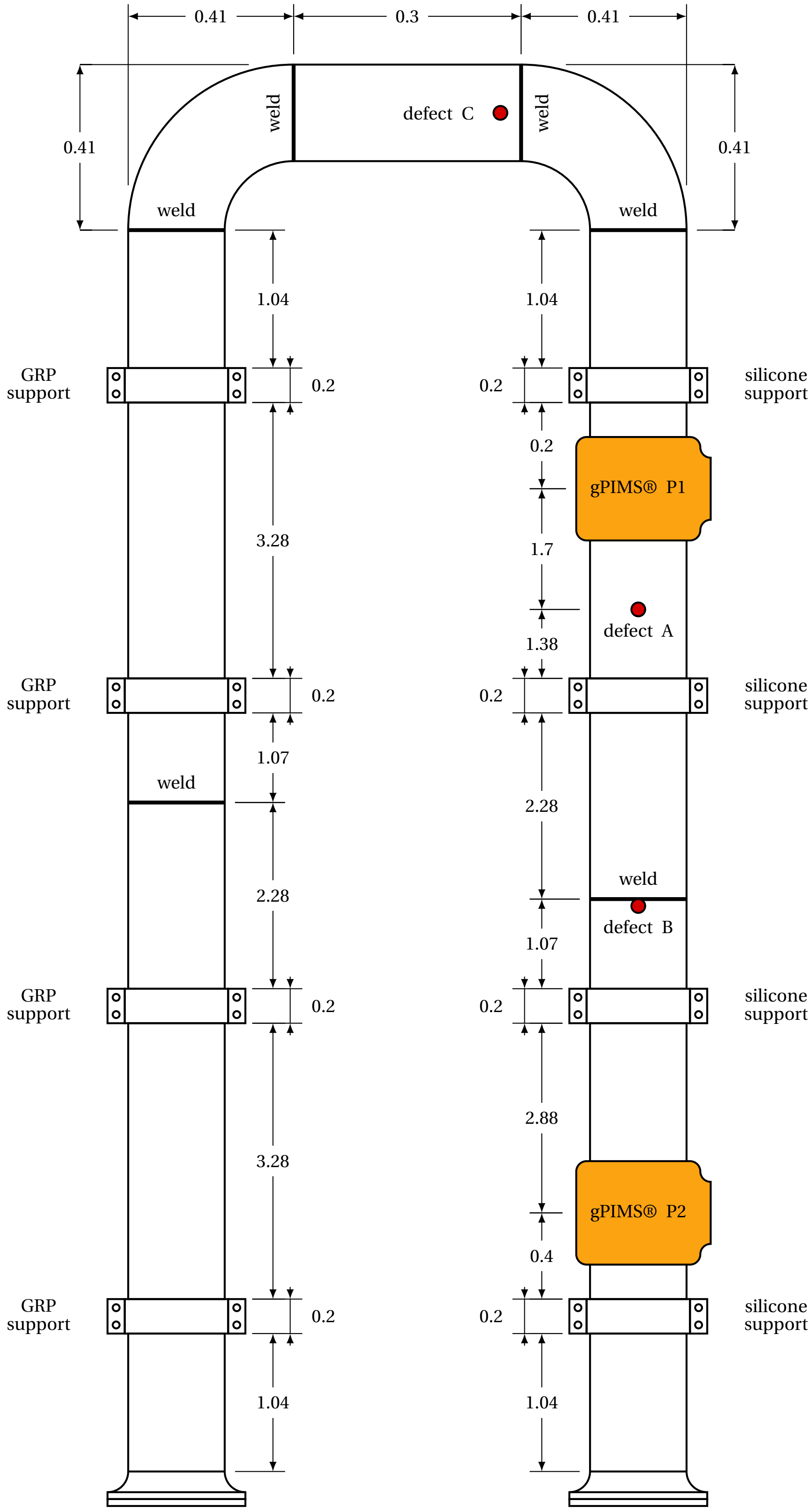

Figure 6.1: Diagram of the 8" pipe loop facility at BP's Naperville Campus with two pre-moulded gPIMS® sensors; all dimensions in metres (not to scale).

Figure 6.2: gPIMS® P1 sensor before and after its installation on the pipe loop.

that was pumped under the protective cover after its attachment. The two methods demonstrate different possibilities that can be chosen for convenience of installation in the field, and are very unlikely to influence the performance of the sensors.

As figure 6.1 indicates, the pipe loop rests on eight clamped supports. Originally, stiff GRP pads had been placed between the clamped supports and the pipe which produced very large echoes and induced significant attenuation on the guided waves propagating past them as a result of the high stiffness of the interfaces between the pipe and the GRP pads, as discussed in chapter 3. To address this issue, the support configuration was modified by replacing the stiff GRP pads with soft silicone rubber pads on the four supports on the side of the pipe loop where the sensors were placed, as shown in figure 6.1. As a result of this modification the magnitude of the echoes from silicone rubber padded supports has become negligible, and so has the induced attenuation on propagating guided waves. All reported readings were gathered after the stiff GRP pads were replaced with soft silicone rubber pads.

The temperature of the pipe loop is computer controlled, and can be precisely varied between 100°F (37.8°C) and 194°F (90°C). Initially, a set of four readings were collected from the gPIMS® P1 sensor while the pipe loop was at 100°F and in a baseline, damage-free condition. Subsequently, damage in the form of 1” diameter machined flat-bottomed holes was introduced in the pipe loop at locations A, B and C indicated in figure 6.1. The three locations were chosen to simulate three different damage detection scenarios of increasing difficulty. At location A, damage is introduced in a free section of pipe and therefore its echo should be easy to detect because it can only be masked by coherent noise but not by the large echoes of pipeline features and pre-existing damage. At location B, damage is introduced a few millimetres after a weld, and therefore it should be more difficult because its echo is masked by the large echo of the weld. Finally, at location C, not only damage is introduced in the vicinity of two welds, but it also located past two welds and a bend. Specifically, while it should in principle be possible to detect the echo from damage A in the raw reading signals under the assumption that coherent noise is very low, the detection of the echo from damage B and C requires by definition the utilisation of baseline subtraction. Moreover, at location C damage should in general be more difficult to detect than at location B as a result of the complex guided wave propagation effects along the preceding bend that are likely to magnify the effect of any minor change in Environmental and Operational Conditions (EOC) and in sensor behaviour and hence compromise the effectiveness of baseline subtraction. The depth of the flat-bottomed holes was increased in three successive 0.25% cross-sectional area increments, removing a nominal total 0.25%, 0.5% and 0.75% cross-sectional area at each of three locations, as detailed in table 6.1. After each damage increment the temperature of the pipe loop was increased to 194°F and subsequently returned to 100°F before collecting a set of readings so to thermally stress the gPIMS® P1 sensor and trigger the complex changes in sensor behaviour typically observed in the field. Finally, after the 0.75% cross-sectional area loss damage had been introduced and the last set of readings at 100°F had been collected, the temperature of the pipe loop was increased in 10°F (5.56°C) steps from 100°F to 194°F, and a set of readings was collected after each temperature increase with the purpose of assessing the performance of the sensor at high temperatures, and of testing the capabilities of the baseline subtraction compensation procedure discussed in section 4.4 and of the proposed automated damage detection procedure when large temperature differences occur between the baseline readings and any later collected reading. Table 6.2 presents a list of all the readings gathered from the gPIMS® P1 sensor, together with the time, temperature and damage condition at which they were collected.

During each reading, the gPIMS® P1 sensor transmits a torsional $T(0,1)$ guided wave packet in both directions along the pipe and listens for echoes. Echoes can be composed of the torsional $T(0,1)$ mode and mode converted flexural $F(1,2)$ mode. Figure 6.3 shows the received torsional $T(0,1)$ signal recorded by the gPIMS® P1 sensor. The transmitted signal is an eight-cycle 27kHz Hann-windowed toneburst. The sensor lies at the origin, and each echo originates from the indicated pipe loop feature. Because the velocity of propagation of the $T(0,1)$ mode is known, the time of arrival of each echo can be correlated to the position along the pipe relative to the sensor where it originates, and thus to the pipe feature that produced it. For example, the echo at -5.6m originates from a weld.

For a given amplitude of the incident $T(0,1)$ guided wave packet, the typical amplitude of the $T(0,1)$ echo from features such as welds or flanges is known. Therefore, from an observed $T(0,1)$ echo amplitude it is possible to infer the amplitude of the incident $T(0,1)$ guided wave

Table 6.1: Details of the damage introduced in the BP Naperville gPIMS® pipe loop; all holes were nominally 1” diameter and flat-bottomed; however, cutters produced a slightly domed shape with a minimum depth in the middle of the defect; the remaining wall thickness was measured ultrasonically at the middle of the defect and was corrected for the dome shape; the wall thickness loss consists of the pipe wall thickness before damage introduction less the corrected remaining wall thickness.

damage location	cross-sectional area loss nominal [%]	cross-sectional area loss corrected [%]	wall thickness loss [mm]	wall thickness remaining [mm]
A	0.25	0.35	1.0	7.3
	0.50	0.59	1.5	6.8
	0.75	0.78	1.9	6.4
B	0.25	0.38	0.7	7.2
	0.50	0.72	1.4	6.5
	0.75	0.89	1.8	6.2
C	0.25	0.14	0.6	7.7
	0.50	0.45	1.2	7.1
	0.75	0.84	2.1	6.2

packet at that feature. Furthermore, the typical reduction in transmission of the $T(0,1)$ wave mode caused by features such as welds and bends is also known. Consequently, as discussed in section 2.2.3, assuming the attenuation due to material damping and contents viscosity remains constant along the pipe, the amplitude of the incident $T(0,1)$ guided wave packet can be reconstructed at all positions along the pipe, obtaining the Distance Amplitude Correction (DAC) curve shown in figure 6.3. Dividing the $T(0,1)$ signal by the DAC curve results in a Reflection Coefficient (RC) signal, shown in figure 6.4, that expresses the amplitude of each $T(0,1)$ echo as a percentage of the amplitude of the incident $T(0,1)$ guided wave packet. Figure 6.5 presents the $T(0,1)$ RC signals for all the readings listed in table 6.2 collected while the pipe loop was at 100°F (37.8°C).

Baseline subtraction is performed utilising the four initial baseline readings after appropriately compensating for EOC effects, as described in section 4.4. Figure 6.6 presents the $T(0,1)$ residual RC signals for all the readings listed in table 6.2 collected while the pipe loop was at 100°F (37.8°C). As previously discussed, it is possible to obtain residual signals for each of the baseline readings by regarding each of the baseline signals in turn as a newly collected signal from which one of the remaining baseline signals can be subtracted utilising the baseline subtraction compensation procedure discussed in section 4.4.

Table 6.2: List of the gPIMS® P1 sensor readings gathered between July and August 2011.

damage condition	temp [°F] ([°C])	reading ID	reading time	reading ID	reading time
baseline	100.0 (37.8)	1310 1314	Jul 25, 13:55 Jul 25, 15:46	1312 1316	Jul 25, 14:56 Jul 26, 07:34
0.25% nominal	100.0 (37.8)	1319 1323	Jul 26, 09:34 Jul 26, 11:29	1321 1325	Jul 26, 10:20 Jul 26, 12:23
0.50% nominal	100.0 (37.8)	1337 1341	Jul 27, 11:07 Jul 27, 14:00	1339 1343	Jul 27, 12:24 Jul 27, 14:50
0.75% nominal	100.0 (37.8)	1357 1362	Jul 28, 12:20 Jul 28, 14:09	1359	Jul 28, 13:24
0.75% nominal	110.0 (43.3)	1364 1368	Jul 28, 15:33 Jul 28, 16:33	1366	Jul 28, 16:03
0.75% nominal	120.0 (48.9)	1370 1374	Jul 29, 06:20 Jul 29, 07:30	1372	Jul 29, 06:58
0.75% nominal	130.0 (54.4)	1376 1380	Jul 29, 08:34 Jul 29, 09:26	1378	Jul 29, 08:39
0.75% nominal	140.0 (60.0)	1382 1386	Jul 29, 10:34 Jul 29, 11:31	1384	Jul 29, 11:06
0.75% nominal	150.0 (65.6)	1388 1392	Jul 29, 12:37 Jul 29, 13:36	1390	Jul 29, 13:01
0.75% nominal	160.0 (71.1)	1394 1398	Jul 29, 14:38 Jul 29, 15:25	1396	Jul 29, 14:56
0.75% nominal	170.0 (76.7)	1400 1404	Jul 29, 16:37 Jul 29, 17:26	1402	Jul 29, 16:57
0.75% nominal	180.0 (82.2)	1406 1410	Aug 01, 07:43 Aug 01, 08:35	1408	Aug 01, 08:10
0.75% nominal	190.0 (87.8)	1412 1416	Aug 01, 09:49 Aug 01, 11:06	1414	Aug 01, 10:30
0.75% nominal	194.0 (90.0)	1418 1422	Aug 01, 12:13 Aug 01, 13:49	1420	Aug 01, 12:40

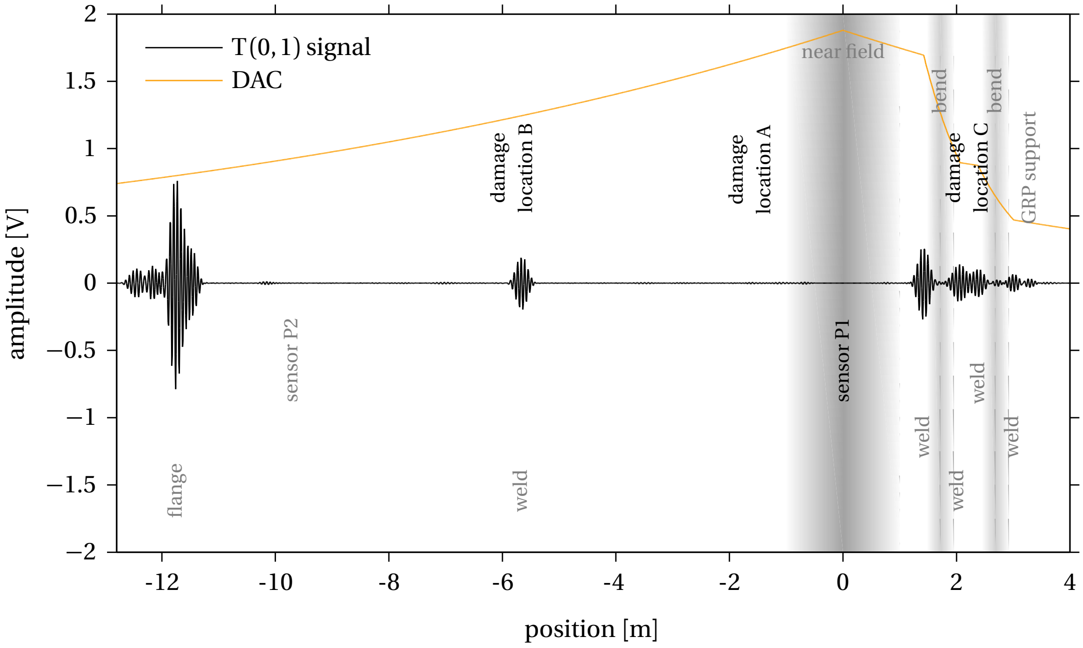

Figure 6.3: Torsional T(0, 1) signal recorded by the gPIMS® P1 sensor, with the DAC curve; the signal was gathered during baseline reading 1316, *i.e.* before any damage had been introduced; the transmitted signal is an eight-cycle 27kHz Hann-windowed toneburst.

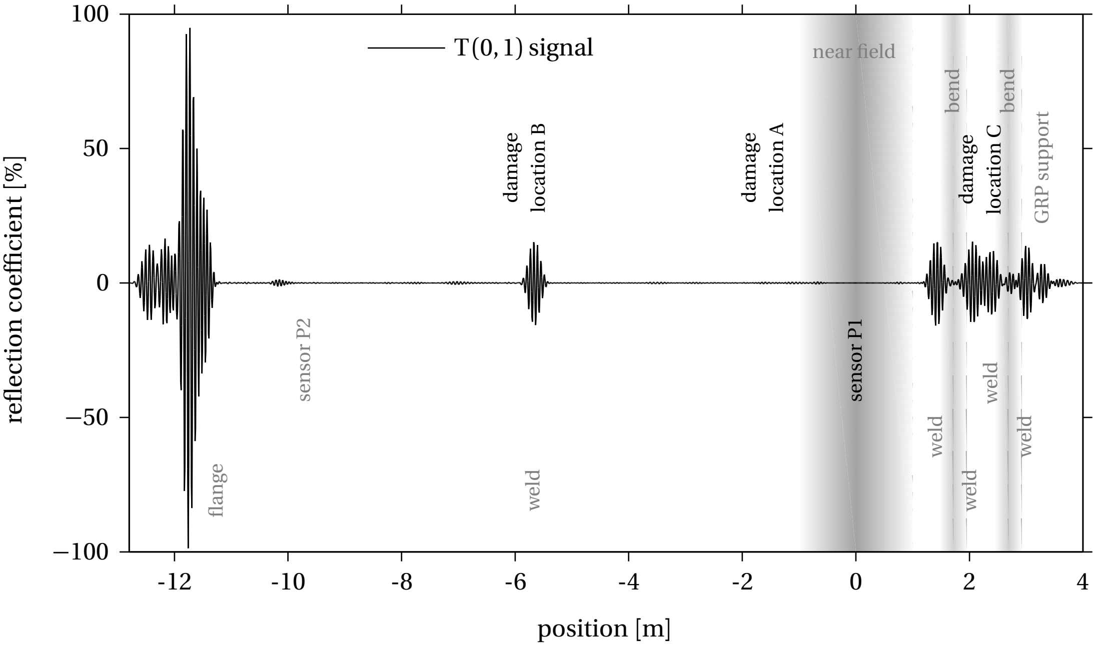

Figure 6.4: Torsional T(0, 1) Reflection Coefficient (RC) signal recorded by the gPIMS® P1 sensor; the signal was gathered during baseline reading 1316, *i.e.* before any damage had been introduced; the transmitted signal is an eight-cycle 27kHz Hann-windowed toneburst.

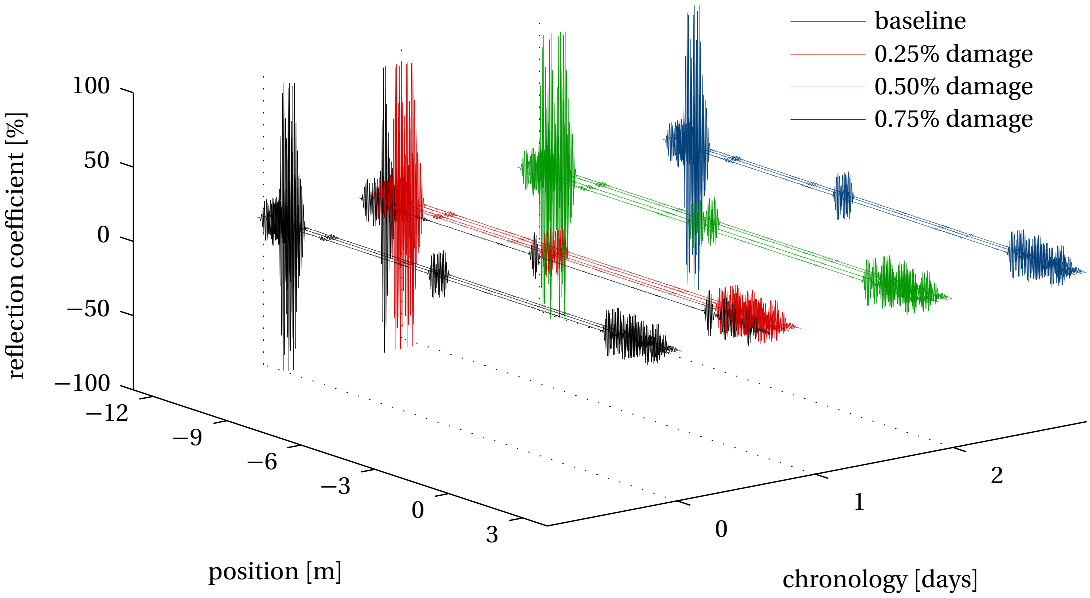

Figure 6.5: Torsional T(0,1) Reflection Coefficient (RC) signals for each reading recorded by the gPIMS® P1 sensor at 100°F (37.8°C); the transmitted signal is an eight-cycle 27kHz Hann-windowed toneburst.

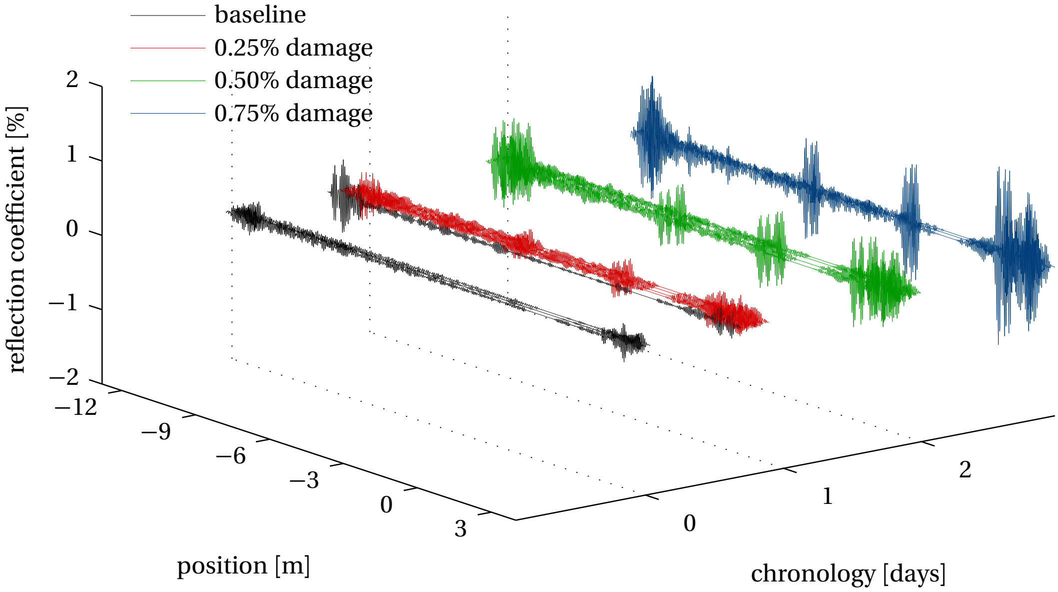

Figure 6.6: Torsional T(0,1) residual Reflection Coefficient (RC) signals for each reading recorded by the gPIMS® P1 sensor at 100°F (37.8°C); the transmitted signal is an eight-cycle 27kHz Hann-windowed toneburst.

Because the temperature of the pipe loop is computer controlled, and can in theory be precisely set at any value between 100°F (37.8°C) and 194°F (90°C), in principle one could think that to perform baseline subtraction between two readings collected while the pipe loop was at 100°F no baseline subtraction compensation would be necessary. Unfortunately, in practice baseline subtraction compensation is still necessary, as figure 6.7, which presents the residual RC signals for reading ID 1316 with and without baseline subtraction compensation, exemplifies. As can be observed in figure 6.7, when no compensation is applied relatively large echoes appear in the residual RC signal in correspondence of the flange and the welds, and therefore also in correspondence of locations B and C, as figure 6.8 shows. Such behaviour can be expected for many reasons but primarily because of small actual temperature differences between readings combined with sensor jitter, as discussed in section 4.4. Note how in absolute terms the weld echoes in the uncompensated residual RC signal are actually quite small since they have an amplitude of roughly 0.5%, which is equivalent to a thirtieth of the roughly 15% amplitude of the weld echoes in the original RC signal shown in figure 6.4. However, they have an amplitude that is roughly the same as that expected of the echoes from the introduced damage, and is therefore imperative to minimise them through baseline subtraction compensation in order to maximise damage detection chances.

For the purpose of illustrating how the concepts presented in sections 6.1 and 6.2 can be combined and exploited to detect damage growth in practical circumstances, it is of interest to detect and quantify the nominal 0.25%, 0.50% and 0.75% cross-sectional area loss damage in the pipe loop at locations A, B and C utilising just the $T(0,1)$ residual RC signals for all the readings listed in table 6.2.

Utilising the Metallic Materials Properties Development and Standardization (MMPDS) handbook [129], it can be shown that at the temperature of 100°F (37.8°C) the shear modulus of steel is equal to 83.80GPa. Assuming the density of steel is 7932kg/m^3 [129], it follows from equation 2.7 that the shear wave velocity, and therefore the $T(0,1)$ phase and group velocities, at the temperature of 100°F is equal to 3.25km/s. Therefore, in the frequency range of an eight-cycle 27kHz Hann-windowed toneburst the wavelength of the $T(0,1)$ is roughly 4.74" (120.4mm), and it follows that the 1" (25.4mm) diameter flat-bottomed holes at locations A, B and C can be assumed to behave as point reflectors because their axial length is equal to just less than a quarter of the wavelength of the incident $T(0,1)$ guided wave packet [59, 60].

Since damage at each location can be assumed to behave as a point reflector, the resulting $T(0,1)$ echoes can be assumed to be amplitude-scaled versions of the incident $T(0,1)$ guided wave packet [59, 60]. Utilising the concept introduced in section 6.2, detecting damage at

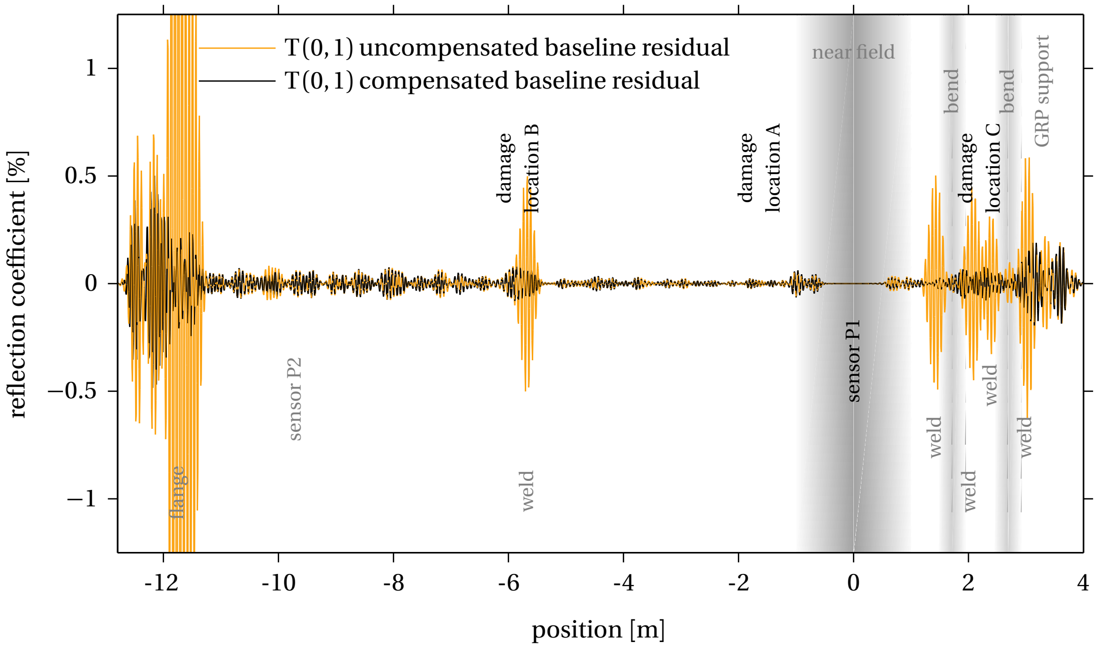

Figure 6.7: Torsional T(0,1) residual Reflection Coefficient (RC) signals from baseline reading ID 1316 with and without baseline subtraction compensation.

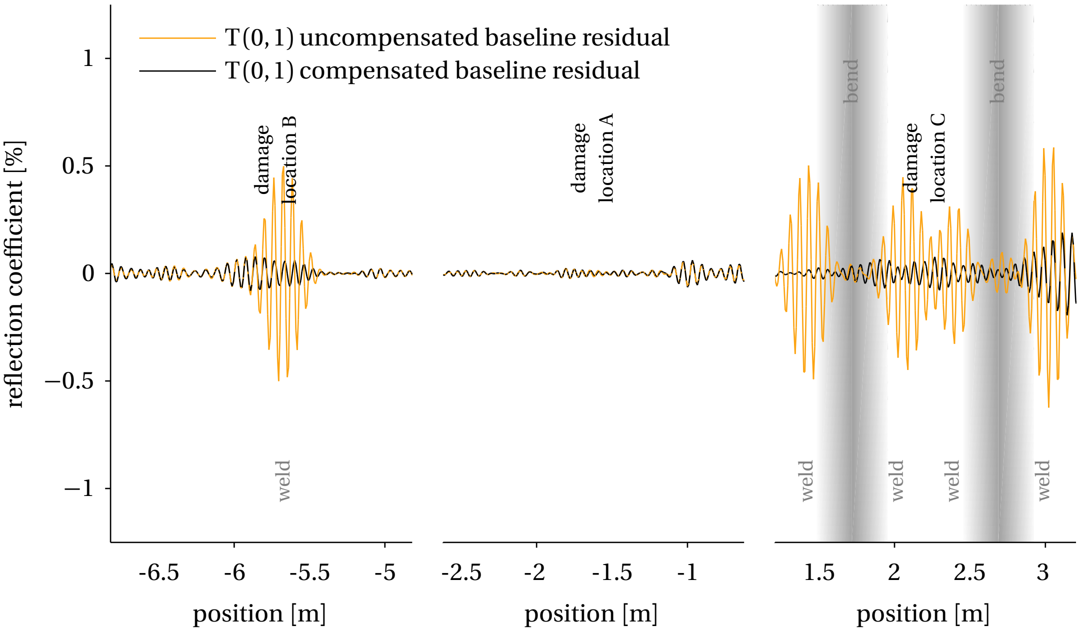

Figure 6.8: Detail at locations A, B and C of the torsional T(0,1) residual Reflection Coefficient (RC) signals from baseline reading ID 1316 with and without baseline subtraction compensation.

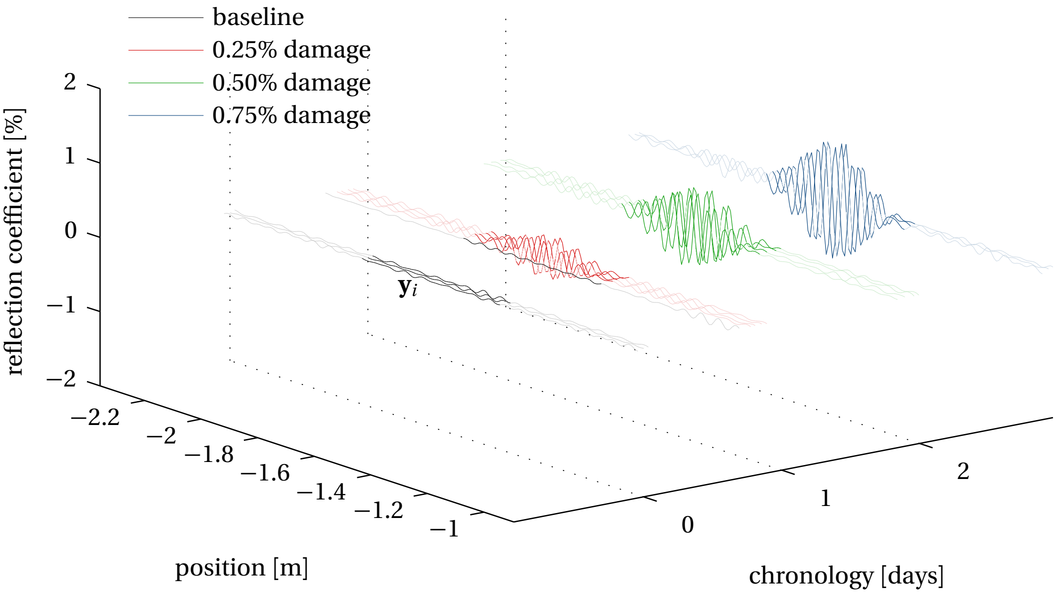

Figure 6.9: Section that spans from −1.866m to −1.384m of all the torsional $T(0,1)$ residual Reflection Coefficient (RC) signals for each reading recorded by the gPIMS® P1 sensor at 100°F (37.8°C); the transmitted signal is an eight-cycle 27kHz Hann-windowed toneburst.

locations A, B and C can be assumed to be equivalent to detecting a change between the baseline and the other residual signals at some position along the pipe loop that has the form of an eight-cycle 27kHz Hann-windowed toneburst.

Section 6.3.1 will illustrate a procedure to detect the appearance over time of a specific echo in the residual signals at a specific location along a pipe and to quantify its parameters such as its amplitude, while section 6.3.2 will exemplify how such procedure can be effectively utilised to detect and quantify the growth of damage at any position along a pipe.

6.3.1 Damage Detection Procedure

Consider for example the position along the pipe located -1.625m from the position of the gPIMS® P1 sensor. An eight-cycle 27kHz Hann-windowed toneburst lasts 8/27ms, and since the propagation velocity of T(0, 1) along the pipe loop at 100°F is 3.25km/s, it follows that the toneburst is 3.25/2×8/27≈0.4815m long. Consider then the section of all residual signals that spans from -1.866m to -1.384m, as shown in figure 6.9.

Because the sampling frequency of the Guided Ultrasonics Ltd. Wavemaker® G3 [54] integrated signal generator and receiver that drives the gPIMS® P1 sensor is 200kHz, it follows that the toneburst will be composed of ≈200×8/27=59 samples. Therefore, the 0.4815m section of residual RC signal centred at -1.625m can be thought of as a random column vector $\mathbf{y} \in \mathbb{R}^q$ of $q = 59$ entries fluctuating around a column vector $\boldsymbol{\mu} \in \mathbb{R}^q$ that represents the true underlying value of the residual RC signal when there is no damage growth.

As discussed in section 6.1, in the absence of damage growth the evolution over time of the residual RC signal $\mathbf{y}$ can be modelled as a linear process. Therefore, the column vector $\boldsymbol{\mu}$ can be modelled as a linear function

$$\boldsymbol{\mu} = f(\mathbf{X}) = \mathbf{X}\mathbf{w} \tag{6.53}$$

of a matrix $\mathbf{X} \in \mathbb{R}^{q\times p}$ composed of q known row vectors $\mathbf{x}_k$ of $p = 3$ independent inputs x_j and parameterised by the column vector $\mathbf{w} \in \mathbb{R}^p$, or explicitly

$$\begin{bmatrix} \mu_1 \\ \mu_2 \\ \vdots \\ \mu_q \end{bmatrix} = \boldsymbol{\mu} = \mathbf{X}\mathbf{w} = \begin{bmatrix} \mathbf{x}_1 \\ \mathbf{x}_2 \\ \vdots \\ \mathbf{x}_q \end{bmatrix} \begin{bmatrix} w_1 \\ w_2 \\ \vdots \\ w_p \end{bmatrix} = \begin{bmatrix} x_{1,1}w_1 + x_{1,2}w_2 + x_{1,3}w_3 \\ x_{2,1}w_1 + x_{2,2}w_2 + x_{2,3}w_3 \\ \vdots \\ x_{q,1}w_1 + x_{q,2}w_2 + x_{q,3}w_3 \end{bmatrix} \tag{6.54}$$

Specifically, the first entry $x_{k,1}$ of each row vector $\mathbf{x}_k$ is a constant, the second entry $x_{k,2}$ is the position along the pipe to which each signal sample corresponds, and the third entry $x_{k,3}$ is the time t at which reading k was gathered from the gPIMS® P1 sensor. Therefore, in the case under consideration

$$\mathbf{X} = \begin{bmatrix} 1 & -1.866\text{m} & t \\ \vdots & \vdots & \vdots \\ 1 & -1.384m & t \end{bmatrix} \tag{6.55}$$

The residual RC signal $\mathbf{y}$ can then be expressed as

$$\mathbf{y} = \boldsymbol{\mu} + \boldsymbol{\epsilon} = f(\mathbf{X}) + \boldsymbol{\epsilon} = \mathbf{X}\mathbf{w} + \boldsymbol{\epsilon} \tag{6.56}$$

where $\boldsymbol{\epsilon} \in \mathbb{R}^q$ is a zero-mean random column vector representing the uncompensated EOC effects which, as previously discussed, are assumed to have a non-degenerate normal probability density function

$$p(\boldsymbol{\epsilon} \mid \mathbf{0}, \boldsymbol{\Psi}) = (2\pi)^{-q/2} |\boldsymbol{\Psi}|^{-1/2} \exp\left(-\boldsymbol{\epsilon}^\top \boldsymbol{\Psi}^{-1} \boldsymbol{\epsilon}/2\right) \tag{6.57}$$

and symmetric positive-definite covariance matrix $\boldsymbol{\Psi} \in \mathbb{R}^{q\times q}$. Then by affinity the residual signal $\mathbf{y}$ is also a random column vector with a non-degenerate normal probability density function

$$p\left(\mathbf{y} \mid \mathbf{X}\mathbf{w}, \boldsymbol{\Psi}\right) = |2\pi\boldsymbol{\Psi}|^{-1/2} \exp\left(-\left(\mathbf{y} - \mathbf{X}\mathbf{w}\right)^\top \boldsymbol{\Psi}^{-1} \left(\mathbf{y} - \mathbf{X}\mathbf{w}\right)/2\right), \quad \mathbf{y} \sim \mathcal{N}(\mathbf{X}\mathbf{w}, \boldsymbol{\Psi}) \tag{6.58}$$

If both $\mathbf{w}$ and $\mathbf{\Psi}$ are unknown then, as discussed in section 6.1, for given baseline data the maximum-likelihood estimate $\hat{\mathbf{w}}$ of the parameter vector $\mathbf{w}$ is a random column vector with a t probability density function

$$p(\hat{\mathbf{w}}) = \frac{\Gamma_p\left((b+p)/2\right)}{\Gamma_p(b/2)(b\pi)^{p/2}|\mathbf{\Omega}|^{1/2}}\left(1+(\hat{\mathbf{w}}-\mathbf{w})^\top\mathbf{\Omega}^{-1}(\hat{\mathbf{w}}-\mathbf{w})/b\right)^{(-b-p)/2}, \quad \hat{\mathbf{w}}\sim\mathscr{T}_b(\mathbf{w},\mathbf{\Omega}) \tag{6.59}$$

with b degrees of freedom. Practical estimates $\hat{\mathbf{w}}$, $\hat{\mathbf{\Psi}}$ and $\hat{\mathbf{\Omega}}$ of respectively $\mathbf{w}$, $\mathbf{\Psi}$ and $\mathbf{\Omega}$ can be obtained by iterating

$$\hat{\mathbf{\Psi}}_n = \frac{1}{b}\sum_{i=1}^{b}\left(\mathbf{y}_i-\mathbf{X}_i\hat{\mathbf{w}}_{n-1}\right)\left(\mathbf{y}_i-\mathbf{X}_i\hat{\mathbf{w}}_{n-1}\right)^\top, \quad \mathbf{\Psi}_0=\mathbf{I} \tag{6.60}$$

with

$$\hat{\mathbf{w}}_{n-1} = \hat{\mathbf{\Omega}}_{n-1}\sum_{i=1}^{b}\mathbf{X}_i^\top\hat{\mathbf{\Psi}}_{n-1}^{-1}\mathbf{y}_i \tag{6.61}$$

and

$$\hat{\mathbf{\Omega}}_{n-1} = \left(\sum_{i=1}^{b}\mathbf{X}_i^\top\hat{\mathbf{\Psi}}_{n-1}^{-1}\mathbf{X}_i\right)^{-1} \tag{6.62}$$

utilising the $b=4$ baseline residual RC signals $\mathbf{y}_i$, namely those obtained from reading IDs 1310, 1312, 1314 and 1316, until a satisfactory convergence has been reached, as discussed in section 6.1.

Because the parameter vector $\mathbf{w}$ is what characterises the linear regression model f which represents the true underlying value of the residual RC signal $\mathbf{y}$, obtaining an estimate $\hat{\mathbf{w}}$ is equivalent to fitting the linear regression model f to the baseline data. The function

$$\hat{f}(\mathbf{X}) = \mathbf{X}\hat{\mathbf{w}}, \quad \hat{f}(\mathbf{X})\sim\mathscr{T}_b\left(\mathbf{X}\mathbf{w},\mathbf{X}\mathbf{\Omega}\mathbf{X}^\top\right) \tag{6.63}$$

parameterised by the estimate $\hat{\mathbf{w}}$ of the parameter vector $\mathbf{w}$ therefore represents an estimate of the linear regression model f fitted to the baseline data. Equivalently, the estimate $\hat{f}$ of the linear regression model f indicates what, according to the information encoded in the baseline data, should be the true underlying value of the residual RC signal from the gPIMS® P1 sensor in absence of damage growth in the 0.4815m section of residual RC signal centred at -1.625m. However, in the specific case under consideration one has by definition

$$\hat{\mathbf{w}}\sim\mathscr{T}_b(\mathbf{0},\mathbf{\Omega}) \tag{6.64}$$

and

$$\hat{f}(\mathbf{X}) = \mathbf{X}\hat{\mathbf{w}}, \quad \hat{f}(\mathbf{X})\sim\mathscr{T}_b\left(\mathbf{0},\mathbf{X}\mathbf{\Omega}\mathbf{X}^\top\right) \tag{6.65}$$

because, as previously discussed, in absence of damage growth the true response from pipeline features as well as from pre-existing damage should in principle remain constant during the period over which baseline signals are being collected, and any variation observed between the baseline residual RC signals must be caused by uncompensated EOC effects.

Once an estimate $\hat{f}$ of the linear regression model f has been obtained utilising the $b = 4$ baseline residual RC signals $\mathbf{y}_i$, in section 6.2 is has been discussed that the **optimal** way to detect damage growth or equivalently to detect a change between the baseline and the other residual RC signals that has the form of an eight-cycle 27kHz Hann-windowed toneburst is to utilise the Generalised Likelihood Ratio (GLR) algorithm outlined in section 6.2.2. Therefore, consider a new finite set $Y_n = \{\mathbf{y}_{\star 1}, \mathbf{y}_{\star 2}, \ldots, \mathbf{y}_{\star n}\}$ of samples $\mathbf{y}_{\star i}$ of the random column vector $\mathbf{y}_\star$ collected at times $t_1, t_2, \ldots, t_n$. The random column vector $\mathbf{y}_\star$ represents the 0.4815m section of residual RC signal centred at -1.625m that has been obtained from readings collected after the baseline readings and therefore after the estimate $\hat{f}$ of the linear regression model f has been created. Assume that before an unknown change time t_c the probability density function of $\mathbf{y}$ is given by $p\left(\mathbf{y}_\star \mid \mathbf{0}, \mathbf{\Delta}\right) = \mathcal{T}_b\left(\mathbf{0}, \mathbf{\Delta}\right)$, and that after t_c the probability density function of $\mathbf{y}$ is given by $p\left(\mathbf{y}_\star \mid \boldsymbol{\nu}, \mathbf{\Delta}_1\right) = \mathcal{T}_b\left(\boldsymbol{\nu}, \mathbf{\Delta}\right)$, where the vector $\boldsymbol{\nu}$ represent the response from the damage that has grown, and

$$\mathbf{\Delta} = \mathbf{\Psi} + \mathbf{\Theta} \tag{6.66}$$

as discussed in section 6.2. It is of interest to detect the onset of change in the probability density function of $\mathbf{y}_\star$ and to estimate t_c and $\boldsymbol{\nu}$. In other words, in the specific case under consideration it is of interest to detect damage the growth of which would produce a change that has the form of an eight-cycle 27kHz Hann-windowed toneburst between the baseline residual RC signals, expressed by the estimate $\hat{f}$ of the linear regression model f, and the other residual RC signals. It follows that the change vector $\boldsymbol{\nu} = \boldsymbol{\nu}\left(a, \phi\right)$ can be defined as an eight-cycle 27kHz Hann-windowed toneburst with amplitude a and phase ϕ.

Consider hypothesis $\mathbf{H}_0$ which states that the probability density function of $\mathbf{y}_\star$ is given by $p\left(\mathbf{y}_\star \mid \mathbf{0}, \mathbf{\Delta}\right) = \mathcal{T}_b\left(\mathbf{0}, \mathbf{\Delta}\right)$, and hypothesis $\mathbf{H}_1$ which states that the probability density function of $\mathbf{y}_\star$ is given by $p\left(\mathbf{y}_\star \mid \boldsymbol{\nu}\left(a, \phi\right), \mathbf{\Delta}\right) = \mathcal{T}_b\left(\boldsymbol{\nu}\left(a, \phi\right), \mathbf{\Delta}\right)$. The value of the log likelihood ratio

$$z_i\left(a, \phi\right) = \ln \frac{p\left(\mathbf{y}_{\star i} \mid \boldsymbol{\nu}\left(a, \phi\right), \mathbf{\Delta}\right)}{p\left(\mathbf{y}_{\star i} \mid \mathbf{0}, \mathbf{\Delta}\right)} \tag{6.67}$$

will be a function of the value of the sample $\mathbf{y}_{\star i}$ as well as of the amplitude a and phase ϕ of the eight-cycle 27kHz Hann-windowed toneburst. For a given sample $\mathbf{y}_{\star i}$, the value of $z_i\left(a, \phi\right)$ can therefore be maximised with respect to the amplitude a and phase ϕ of the eight-cycle 27kHz Hann-windowed toneburst that represents the echo from the damage that one seeks to detect. Similarly, the cumulative log likelihood ratio

$$Z_k^j(a,\phi) = \sum_{i=j}^{k} z_i(a,\phi) \tag{6.68}$$

can also be maximised with respect to the amplitude a and phase ϕ. For given values of amplitude a and phase ϕ the maximisation

$$\max_{1\le j\le k} Z_k^j(a,\phi) \tag{6.69}$$

will find, under the assumption that samples $\mathbf{y}_{\star 1},\ldots,\mathbf{y}_{\star j-1}$ have probability density function $p(\mathbf{y}_\star \mid \mathbf{0},\boldsymbol{\Delta}) = \mathcal{T}_b(\mathbf{0},\boldsymbol{\Delta})$, which samples $\mathbf{y}_{\star j},\ldots,\mathbf{y}_{\star k}$ are most likely to have probability density function $p(\mathbf{y}_\star \mid \boldsymbol{v}(a,\phi),\boldsymbol{\Delta}) = \mathcal{T}_b(\boldsymbol{v}(a,\phi),\boldsymbol{\Delta})$. It follows that the double maximisation

$$g_k = \max_{1\le j\le k} \sup_{a,\phi} Z_k^j(a,\phi) \tag{6.70}$$

will find the likeliest values of amplitude a and phase ϕ for which samples $\mathbf{y}_{\star j},\ldots,\mathbf{y}_{\star k}$ are most likely to have probability density function $p(\mathbf{y}_\star \mid \boldsymbol{v}(a,\phi),\boldsymbol{\Delta}) = \mathcal{T}_b(\boldsymbol{v}(a,\phi),\boldsymbol{\Delta})$, under the assumption that samples $\mathbf{y}_{\star 1},\ldots,\mathbf{y}_{\star j-1}$ have probability density function $p(\mathbf{y}_\star \mid \mathbf{0},\boldsymbol{\Delta}) = \mathcal{T}_b(\mathbf{0},\boldsymbol{\Delta})$. With prescribed probabilities $1-\beta$ of **detection** and α of **false-calling**, hypothesis $\mathbf{H}_1$ is accepted and change is detected at sample $\mathbf{y}_{\star d}$ and detection time t_d, where d is the smallest positive integer for which $g_d \ge \ln A$. As previously noted, $t_c \le t_d$ since at least one sample of the random variable $\mathbf{y}_\star$ must be collected at or after change time t_c for change to be detected. Once change has been detected the arguments of the double maximisation

$$e,a,\phi = \arg\max_{1\le e\le k} \sup_{a,\phi} Z_k^e(a,\phi) \ge \ln A \tag{6.71}$$

will give the the maximum likelihood estimates $\boldsymbol{v}(a,\phi)$ and t_e of respectively the echo from the damage and the change time t_c. Note that if $g_n < \ln A$ then hypothesis $\mathbf{H}_1$ is not accepted and change is not detected within the sample set Y_n, and further samples of y might be required if there is reason to believe change has actually occurred. As previously discussed, change detection is not equivalent to change occurrence since, subject to probabilities $1-\beta < 1$ of **detection** and $\alpha > 0$ of **false-calling**, change may occur but not be detected and may be detected but not have occurred. By maximising the expression

$$g_k = \max_{1\le j\le k} \sup_{a,\phi} Z_k^j(a,\phi) \tag{6.72}$$

it is therefore not only possible to detect whether there is change between the baseline and the other residual RC signals at a specific position along a pipe that has the form of an eight-cycle 27kHz Hann-windowed toneburst or indeed of any other given signal, such as the echo from a patch of corrosion, but it is also possible to estimate the parameters that define that signal, such as the amplitude a and phase ϕ in the case of an eight-cycle 27kHz Hann-windowed toneburst. Furthermore, because change is detected only when $g_k \geq \ln A$, and because by the definition of the Wald boundaries one has

$$A = \frac{1-\beta}{\alpha} \tag{6.73}$$

it follows in general that

$$\alpha = (1-\beta)\exp(-g_k) \tag{6.74}$$

or, in other words, that for a fixed probability $1-\beta$ of **detection** the probability α that any change between the baseline and the other residual RC signals at a specific position along a pipe is a false-call can be readily calculated.

The procedure described in this section can be easily repeated at all positions along a pipe, thereby enabling the detection of a specific echo in the residual signals at any location along a pipe, as will be exemplified in the next section.

6.3.2 Practical Damage Detection

Figure 6.10 presents the baseline residual RC signals obtained from reading IDs 1310, 1312, 1314 and 1316 together with the residual RC signals obtained from reading IDs 1319, 1321, 1323 and 1325 which were collected after the nominal 0.25% cross-sectional area loss damage had been introduced in the pipe loop, while figure 6.11 shows the details at locations A, B and C. As can be seen from figure 6.10, in both the baseline and the damage residuals there are large echoes in correspondence of the flange near -12m and of the GRP support near 3m. As discussed in chapter 4, it is common for the residual signal to have a large magnitude in correspondence of large, complex features as result of the imperfect subtraction of their echoes. In particular, complex features such as flanges and supports produce echoes in the signal recorded by permanently installed guided wave sensors that are very susceptible to tiny, and often difficult to measure, EOC variations, and that thereby further compromise the subtraction process.

Importantly, figure 6.11 reveals that near locations A, B and C there are differences between the baseline and the damage residuals as a result of the introduction of the 1” diameter flat-bottomed holes that produced a 0.25% cross-sectional area loss. Specifically, in the case of location A there is a very clear and stark difference between baseline residuals, whose magnitude is virtually null, and the damage residuals, which are perfectly superimposed and

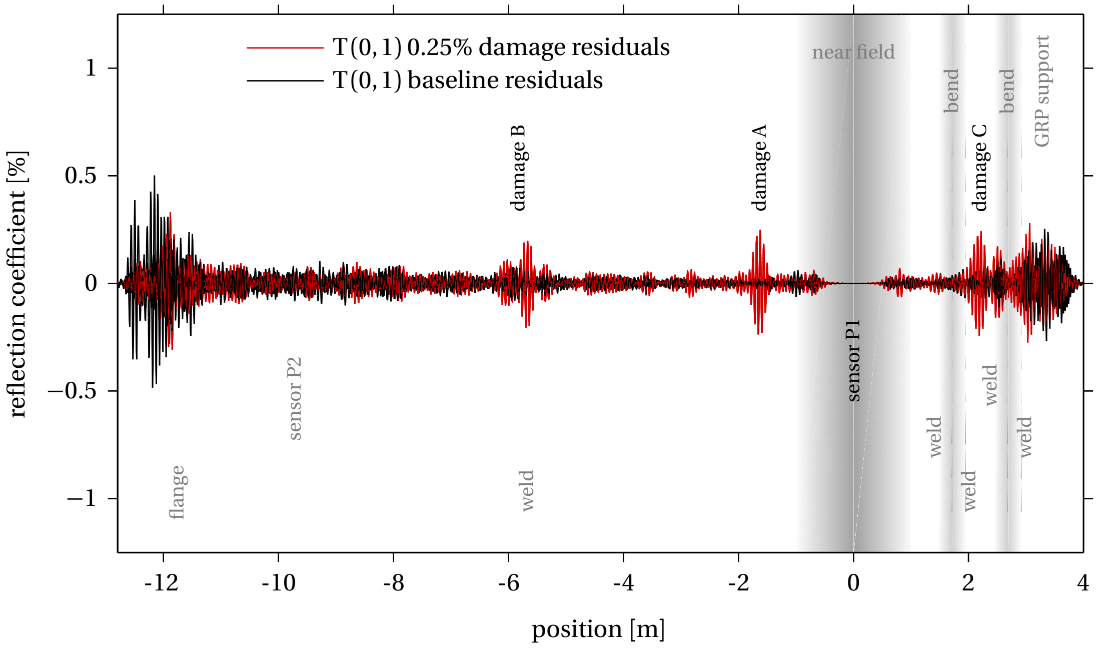

Figure 6.10: Torsional T(0, 1) residual Reflection Coefficient (RC) signals from baseline reading IDs 1310, 1312, 1314 and 1316, and from damage reading IDs 1319, 1321, 1323 and 1325 which were collected after the nominal 0.25% cross-sectional area loss damage had been introduced.

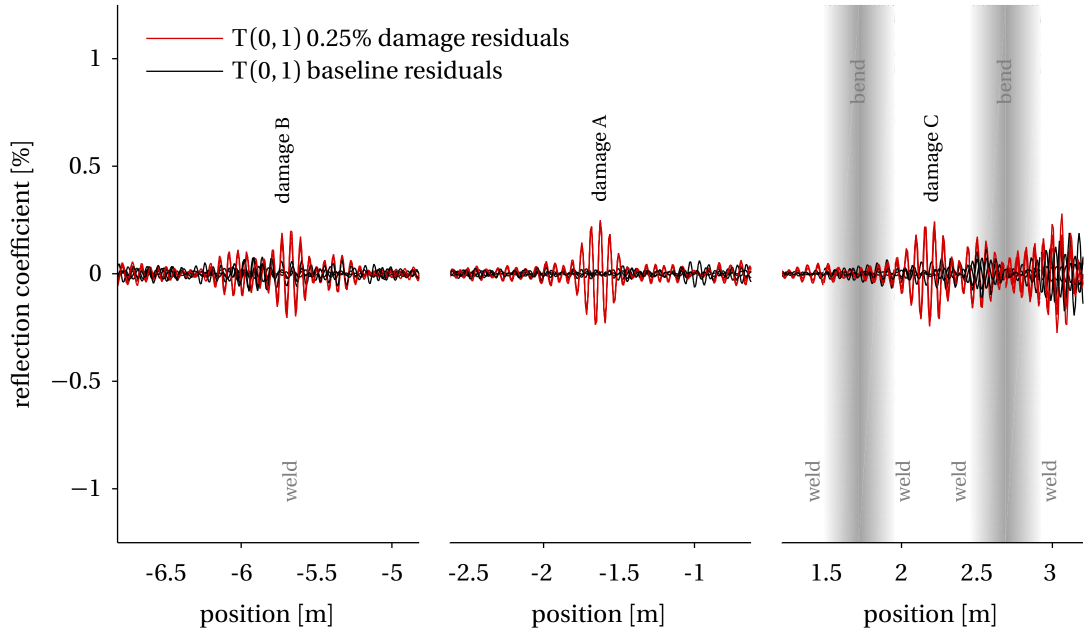

Figure 6.11: Detail at locations A, B and C of the torsional T(0, 1) residual Reflection Coefficient (RC) signals from baseline reading IDs 1310, 1312, 1314 and 1316, and from damage reading IDs 1319, 1321, 1323 and 1325 which were collected after the nominal 0.25% cross-sectional area loss damage had been introduced.

present a sole echo. As a result, even from a simple visual analysis and with no prior knowledge about the introduction of damage, it is straightforward to identify the damage echo at location A by comparing the echo-less baseline residuals with the other residuals. Conversely, at locations B and C not only do the baseline residuals present a number of echoes as a result of the imperfect subtraction of the echoes from the nearby welds, but also the damage residuals present many different echoes of similar magnitude which in practice originate from both the imperfect subtraction of the echoes from the nearby welds and from the interaction of the introduced damage with those same welds. As a result, without prior knowledge about the introduction of damage it becomes very difficult to establish whether there is any echo from damage growth and where it is located, especially since the magnitude of the baseline residuals is far from null and it is therefore non-trivial to determine whether an actual new echo has appeared or an existing echo has changed as a result of EOC effects.

The damage detection procedure introduced in section 6.3.1 will be utilised as the basis for a proposed automated approach to examine changes over time in the residuals and calculate how likely the residuals are to contain echoes from actual damage growth. The proposed approach is particularly valuable from an operator standpoint because it removes the bias a technician may have when assigned the task of examining changes over time in the residuals with the goal of detecting and monitoring damage growth, and because it clearly quantifies the likelihood that each call a technician makes is in actuality a false-call. Note however that this approach requires prior knowledge of the expected echo from actual damage growth, which, as previously discussed, in the present case has the form of an eight-cycle 27kHz Hann-windowed toneburst but might be different in general.

Following the damage detection procedure introduced in section 6.3.1, an estimate $\hat{f}$ of the linear regression model f that models the evolution over time of the residual RC signal in the absence of damage growth can be estimated by considering the 0.4815m section of residual RC signal centred in turn at each position along the pipe loop utilising from the set $\{\mathbf{y}_1, \mathbf{y}_2, \mathbf{y}_3, \mathbf{y}_4\}$ of the $b = 4$ baseline residual RC signals obtained from reading IDs 1310, 1312, 1314 and 1316. Once an estimate $\hat{f}$ of the linear regression model f has been obtained, consider the finite set $Y_\star = \{\mathbf{y}_{\star 1}, \mathbf{y}_{\star 2}, \mathbf{y}_{\star 3}, \mathbf{y}_{\star 4}\}$ of residual RC signals obtained from reading IDs 1319, 1321, 1323 and 1325. By maximising the GLR expression

$$g_k = \max_{1 \leq j \leq 4} \sup_{a,\phi} Z_4^j\left(a, \phi\right) \tag{6.75}$$

with

$$Z_4^j\left(a, \phi\right) = \sum_{i=j}^{4} z_i\left(a, \phi\right) \tag{6.76}$$

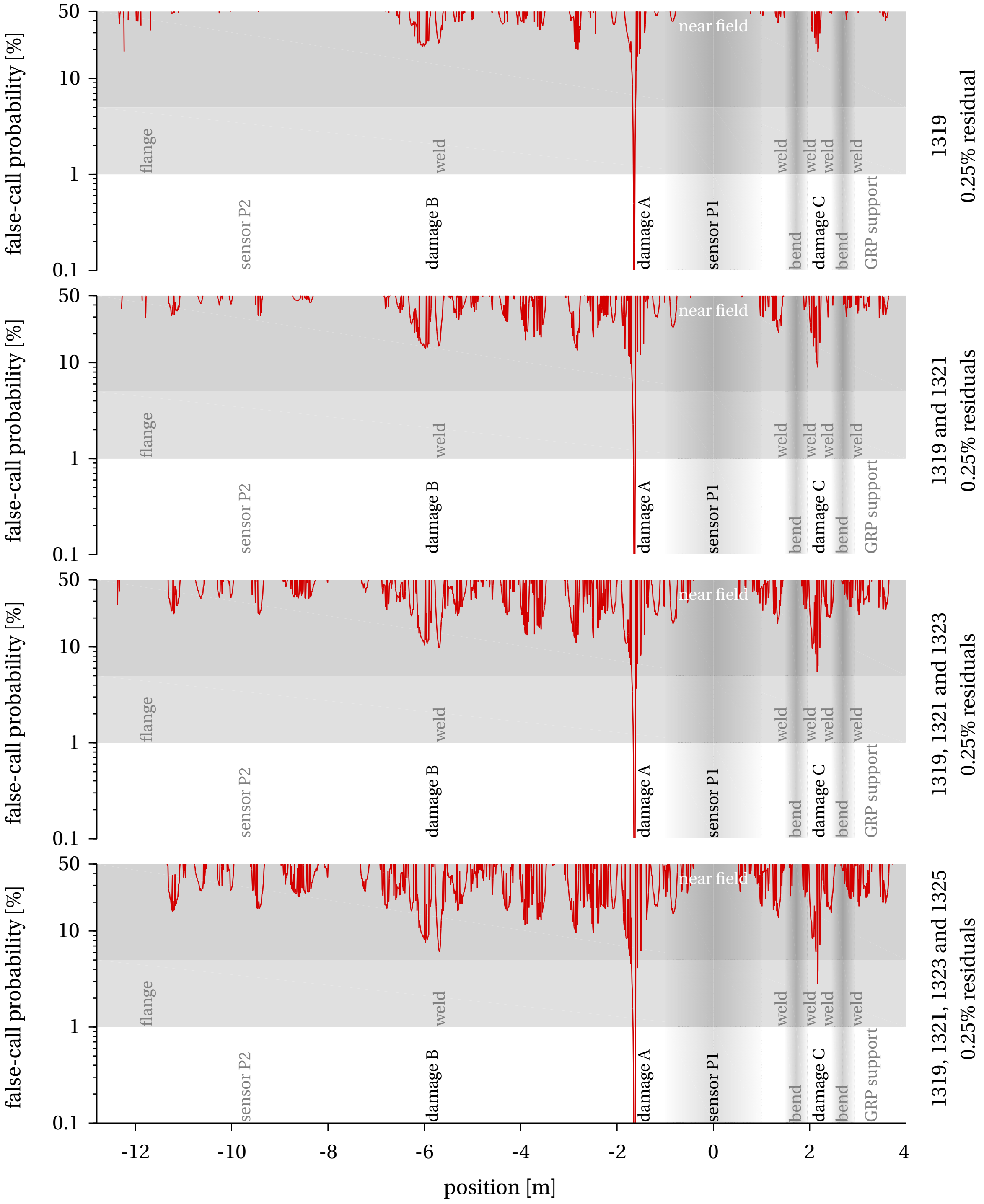

Figure 6.12: Results of the GLR maximisation with nominal 0.25% cross-sectional area loss damage in terms of the probability of false-call for a probability of damage detection equal to 99.9%; the different results were calculated with the finite set $Y_\star$ including, from top to bottom: reading ID 1319; reading IDs 1319 and 1321; reading IDs 1319, 1321 and 1323; and reading IDs 1319, 1321, 1323 and 1325.

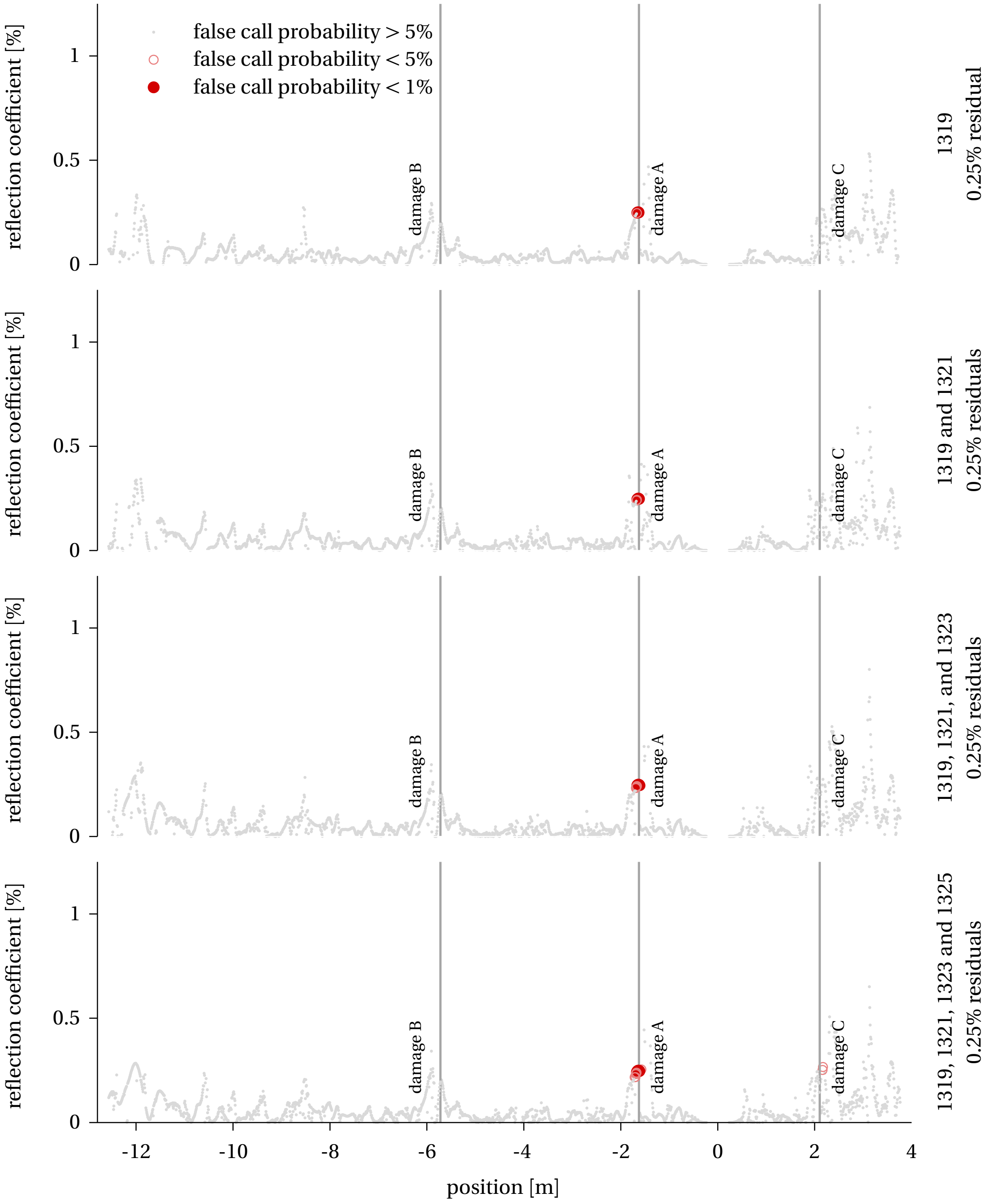

Figure 6.13: Results of the GLR maximisation with nominal 0.25% cross-sectional area loss damage in terms of the amplitude of the damage echo; the different results were calculated with the finite set $Y_\star$ including, from top to bottom: reading ID 1319; reading IDs 1319 and 1321; reading IDs 1319, 1321 and 1323; and reading IDs 1319, 1321, 1323 and 1325.

and

$$z_i\left(a,\phi\right)=\ln\frac{p\left(\mathbf{y}_{\star i}\,|\,\boldsymbol{v}\left(a,\phi\right),\boldsymbol{\Delta}\right)}{p\left(\mathbf{y}_{\star i}\,|\,\mathbf{0},\boldsymbol{\Delta}\right)} \tag{6.77}$$

in turn at each position along the pipe loop it is therefore possible to not only to detect whether there is change between the baseline and the other residual RC signals at any position along the pipe loop that has the form of an eight-cycle 27kHz Hann-windowed tonebeurst, *i.e.* of the expected echo from actual damage growth, but it is also possible to estimate the parameters that define that signal, such as its amplitude a and phase ϕ. Furthermore, because change is detected only when $g_k \geq \ln A$, and because by the definition of the Wald boundaries one has

$$A=\frac{1-\beta}{\alpha} \tag{6.78}$$

it follows in general that

$$\alpha=\left(1-\beta\right)\exp\left(-g_k\right) \tag{6.79}$$

or, in other words, that for a fixed probability $1-\beta$ of **detection**, the probability α that any change between the baseline and the other residual RC signals at any position along the pipe loop is a false-call can be readily calculated.

Figures 6.12 and 6.13 present the results of the GLR maximisation in terms of respectively the probability of false-call for a probability of damage detection equal to 99.9%, and the amplitude of the damage echo. In particular, the different results in each figure were calculated with the finite set $Y_\star$ including, from top to bottom: reading ID 1319; reading IDs 1319 and 1321; reading IDs 1319, 1321 and 1323; and reading IDs 1319, 1321, 1323 and 1325.

It can be seen in figure 6.12 that of all positions along the pipe loop, the only position where the probability of false-call falls to negligible levels is in the vicinity of location A regardless of the size of the finite set $Y_\star$. Simultaneously, figure 6.13 shows that where there is a low probability of false-call, *i.e.* in the vicinity of location A, the estimated amplitude of the damage echo is approximately 0.25%, which roughly corresponds to the nominal 0.25% cross-sectional area loss given that the damage axial length is equal to just less than a quarter of the wavelength of the incident $\mathrm{T}(0,1)$ guided wave packet [59, 60]. Importantly, as the size of the finite set $Y_\star$ increases the probability of false-call decreases significantly around locations B and C, although it does not fall to negligible levels. Such phenomenon can be expected because as the size of the finite set $Y_\star$ increases so does its information content. This is consistent with what can be observed in figure 6.11, where as previously discussed in the case of location A it is straightforward to identify the damage echo, while in the case of

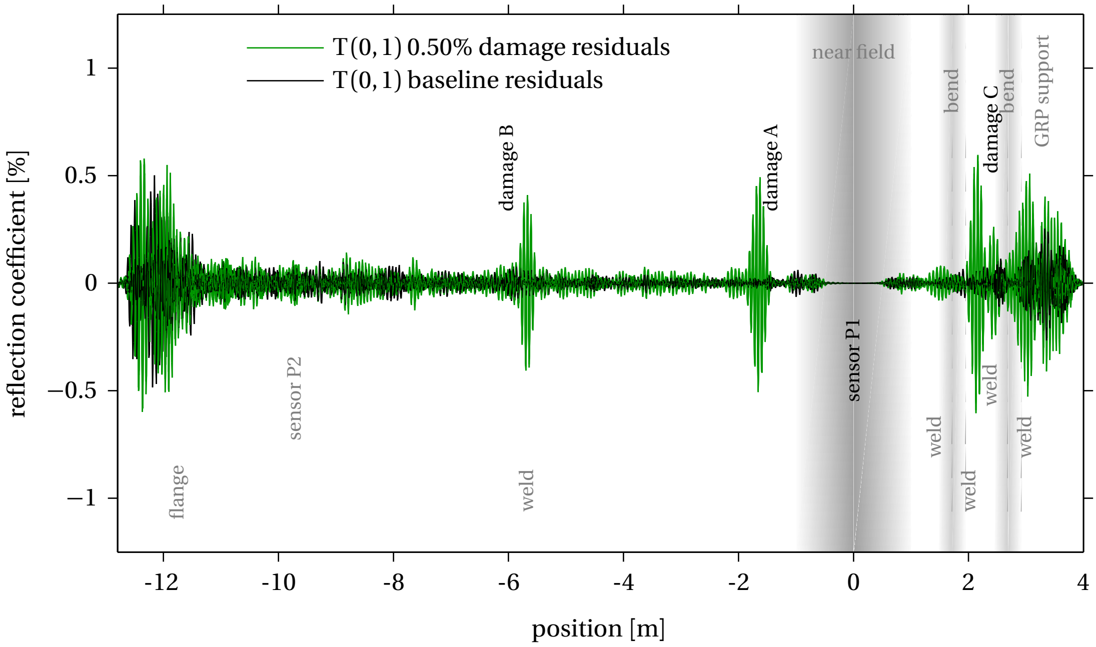

Figure 6.14: Torsional T(0, 1) residual Reflection Coefficient (RC) signals from baseline reading IDs 1310, 1312, 1314 and 1316, and from damage reading IDs 1337, 1339, 1341 and 1343 which were collected after the nominal 0.50% cross-sectional area loss damage had been introduced.

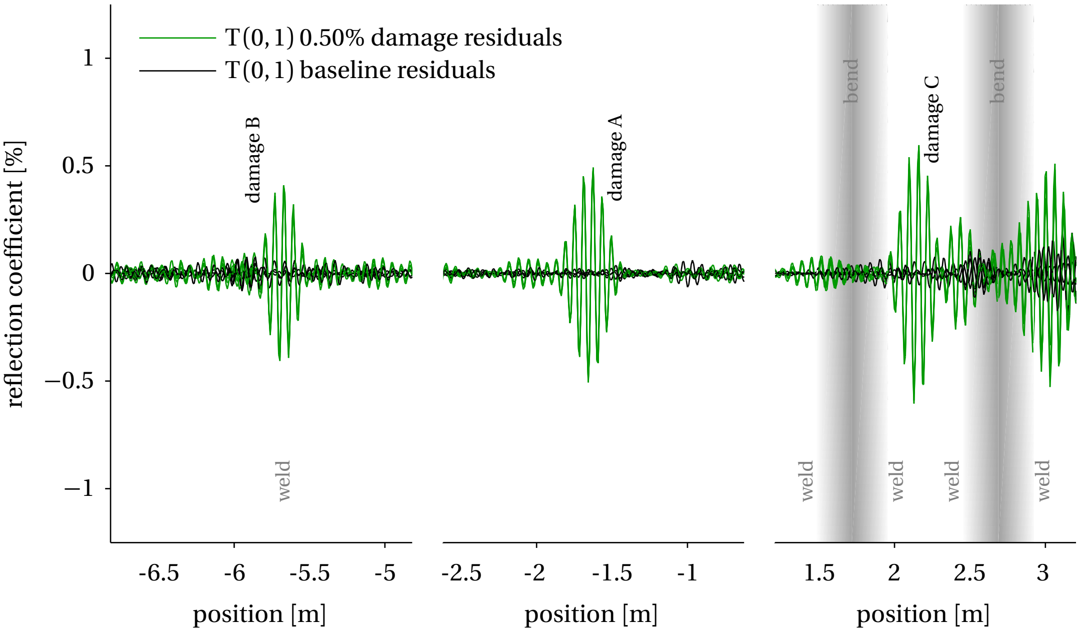

Figure 6.15: Detail at location A, B and C of the torsional T(0, 1) residual Reflection Coefficient (RC) signals from baseline reading IDs 1310, 1312, 1314 and 1316, and from damage reading IDs 1337, 1339, 1341 and 1343 which were collected after the nominal 0.50% cross-sectional area loss damage had been introduced.

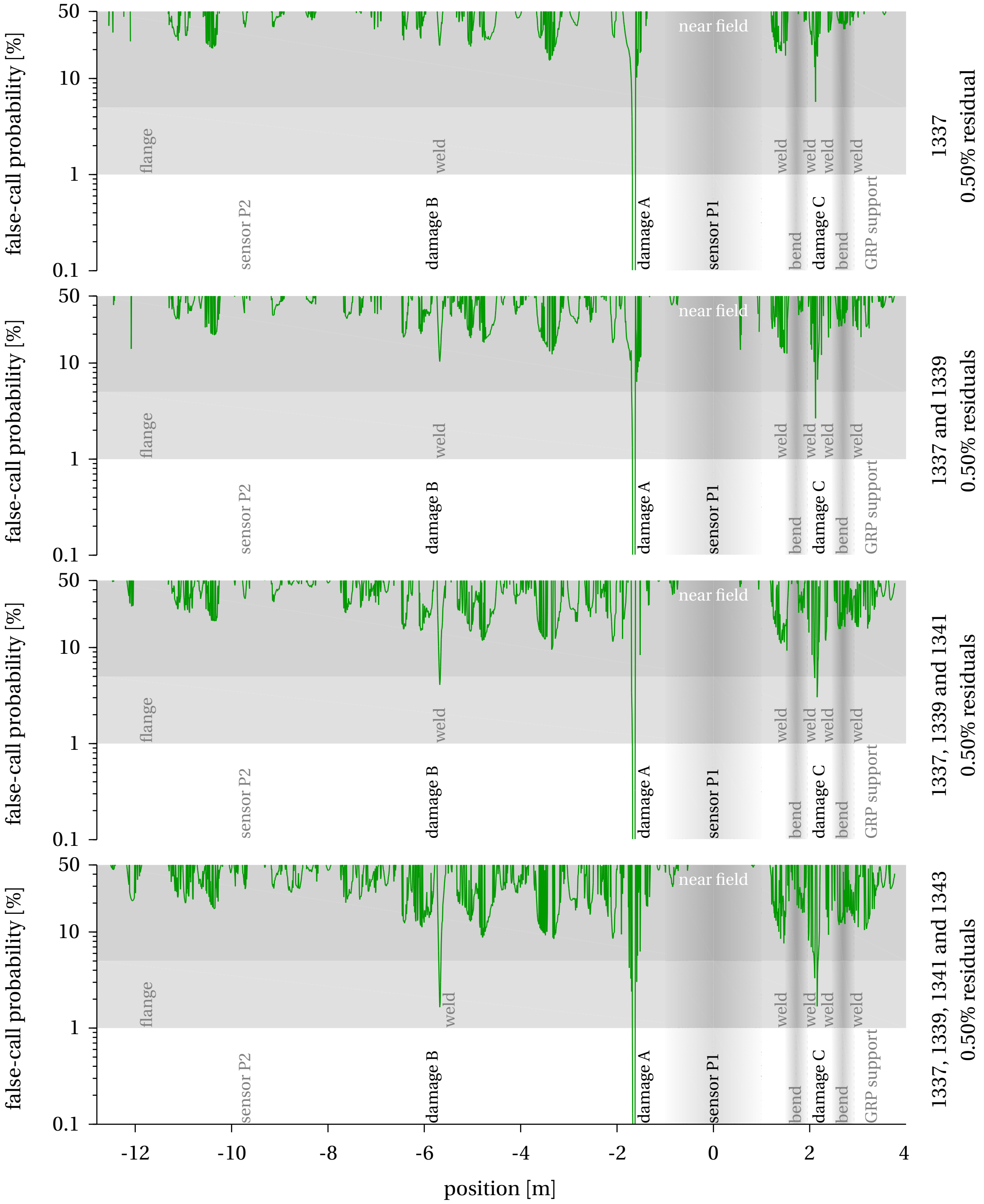

Figure 6.16: Results of the GLR maximisation with nominal 0.50% cross-sectional area loss damage in terms of the probability of false-call for a probability of damage detection equal to 99.9%; the different results were calculated with the finite set $Y_\star$ including, from top to bottom: reading ID 1337; reading IDs 1337 and 1339; reading IDs 1337, 1339 and 1341; and reading IDs 1337, 1339, 1341 and 1343.

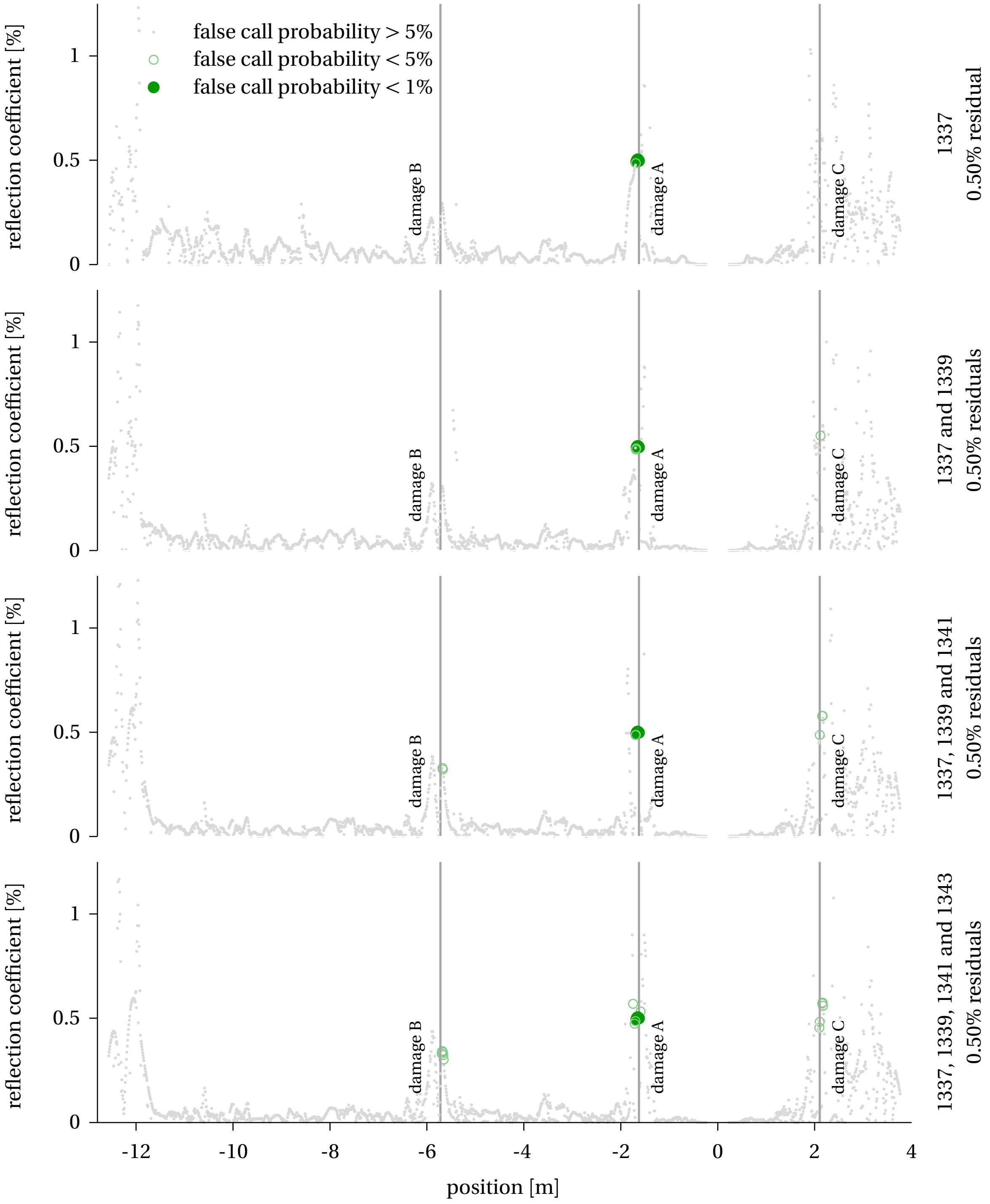

Figure 6.17: Results of the GLR maximisation with nominal 0.50% cross-sectional area loss damage in terms of the amplitude of the damage echo; the different results were calculated with the finite set $Y_\star$ including, from top to bottom: reading ID 1337; reading IDs 1337 and 1339; reading IDs 1337, 1339 and 1341; and reading IDs 1337, 1339, 1341 and 1343.

locations B and C it is non-trivial to determine whether an actual new echo has appeared or an existing echo has changed as a result of EOC effects. Importantly, none of the large echoes in correspondence of the flange and of the GRP support are identified by the proposed automated procedure as an indication of potential damage growth.

Figure 6.14 presents the baseline residual RC signals obtained from reading IDs 1310, 1312, 1314 and 1316 together with the residual RC signals obtained from reading IDs 1337, 1339, 1341 and 1343 which were collected after the nominal 0.50% cross-sectional area loss damage had been introduced in the pipe loop, while figure 6.15 shows the details at locations A, B and C. It can be seen from figure 6.14 that in both the baseline and the damage residuals there are large echoes in correspondence of the flange near -12m and of the GRP support near 3m as result of the imperfect subtraction of their echoes. Figure 6.15 highlights how near locations A, B and C there are differences between the baseline and the damage residuals as a result of the introduction of the 1” diameter flat-bottomed holes that produced a 0.50% cross-sectional area loss.

Similarly to the case of the nominal 0.25% cross-sectional area loss damage, in the case of location A there is a very clear and stark difference between baseline residuals, whose magnitude is virtually null, and the damage residuals, which are perfectly superimposed and present a sole echo. As a result, it is straightforward to identify the damage echo at location A by comparing the echo-less baseline residuals with the other residuals. However, at locations B and C once again the baseline residuals present a number of echoes as a result of the imperfect subtraction of the echoes from the nearby welds, and the damage residuals also present many different echoes of similar magnitude which originate from both the imperfect subtraction of the echoes from the nearby welds and from the interaction of the introduced damage with those same welds.

Figures 6.16 and 6.17 present the results of the GLR maximisation in terms of respectively the probability of false-call for a probability of damage detection equal to 99.9%, and the amplitude of the damage echo. In particular, the different results in each figure were calculated with the finite set $Y_\star$ including, from top to bottom: reading ID 1337; reading IDs 1337 and 1339; reading IDs 1337, 1339 and 1341; and reading IDs 1337, 1339, 1341 and 1343.

It can be seen in figure 6.16 that, similarly to the case of the nominal 0.25% cross-sectional area loss damage, of all positions along the pipe loop, the only position where the probability of false-call falls to negligible levels is in the vicinity of location A regardless of the size of the finite set $Y_\star$. Simultaneously, figure 6.17 shows that where there is a low probability of false-call, *i.e.* in the vicinity of location A, the estimated amplitude of the damage echo is approximately 0.50%, which corresponds roughly to a 0.50% cross-sectional area loss given that the damage axial length is equal to just less than a quarter of the wavelength of the incident T$(0,1)$ guided wave packet [59, 60]. Importantly, as the size of the finite set $Y_\star$ increases the probability of false-call decreases significantly around locations B and C, and although it does not fall to negligible levels it remains nevertheless significantly lower around locations B and C than at all other positions. This is consistent with what can be observed in figure 6.11, where as previously discussed in the case of location A it is straightforward to identify the damage echo, while in the case of locations B and C it is non-trivial to determine whether an actual new echo has appeared or an existing echo has changed as a result of EOC effects. Similarly to the case of the nominal 0.25% cross-sectional area loss damage, none of the large echoes in correspondence of the flange and of the GRP support are identified by the proposed automated procedure as an indication of potential damage growth.

Practical Damage Detection with Temperature Variations

Figures 6.18, 6.20, 6.22, 6.24, 6.26 and 6.28 each presents the baseline residual RC signals obtained from reading IDs 1310, 1312, 1314 and 1316 together with the residual RC signals obtained from readings which were collected after the nominal 0.75% cross-sectional area loss damage had been introduced in the pipe loop. In particular:

- figure 6.18 presents the residuals from reading IDs 1357, 1359 and 1362 which were collected with a temperature difference ΔT to the baseline readings of 0°F (0°C);
- figure 6.20 presents the residuals from reading IDs 1364, 1366 and 1368 which were collected with a temperature difference ΔT to the baseline readings of 10°F (5.56°C);
- figure 6.22 presents the residuals from reading IDs 1370, 1372 and 1374 which were collected with a temperature difference ΔT to the baseline readings of 20°F (11.11°C);
- figure 6.24 presents the residuals from reading IDs 1376, 1378 and 1380 which were collected with a temperature difference ΔT to the baseline readings of 30°F (16.67°C);
- figure 6.26 presents the residuals from reading IDs 1382, 1384 and 1386 which were collected with a temperature difference ΔT to the baseline readings of 40°F (22.22°C);
- figure 6.28 presents the residuals from reading IDs 1388, 1390 and 1392 which were collected with a temperature difference ΔT to the baseline readings of 50°F (27.78°C).

Figures 6.19, 6.21, 6.23, 6.25, 6.27 and 6.29 each shows a more detailed plot around the locations in respectively figures 6.18, 6.20, 6.22, 6.24, 6.26 and 6.28.

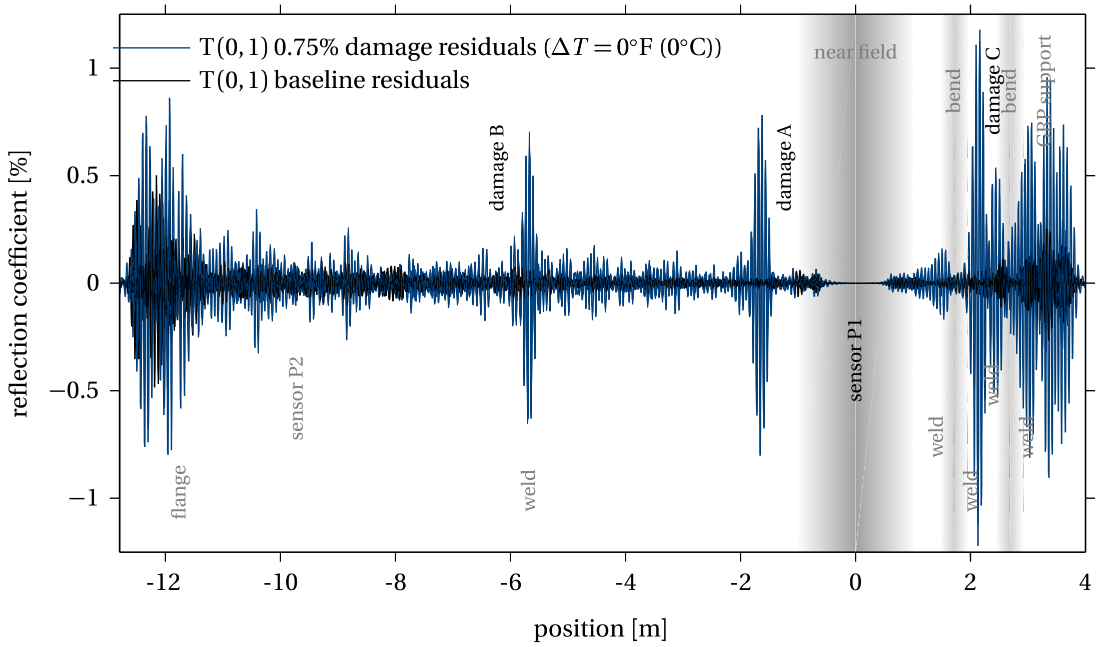

Figure 6.18: Torsional T(0, 1) residual RC signals from baseline reading IDs 1310, 1312, 1314 and 1316, and from damage reading IDs 1357, 1359 and 1362; the nominal cross-sectional area loss damage is 0.75% and the temperature difference ΔT to the baseline readings is 0°F (0°C).

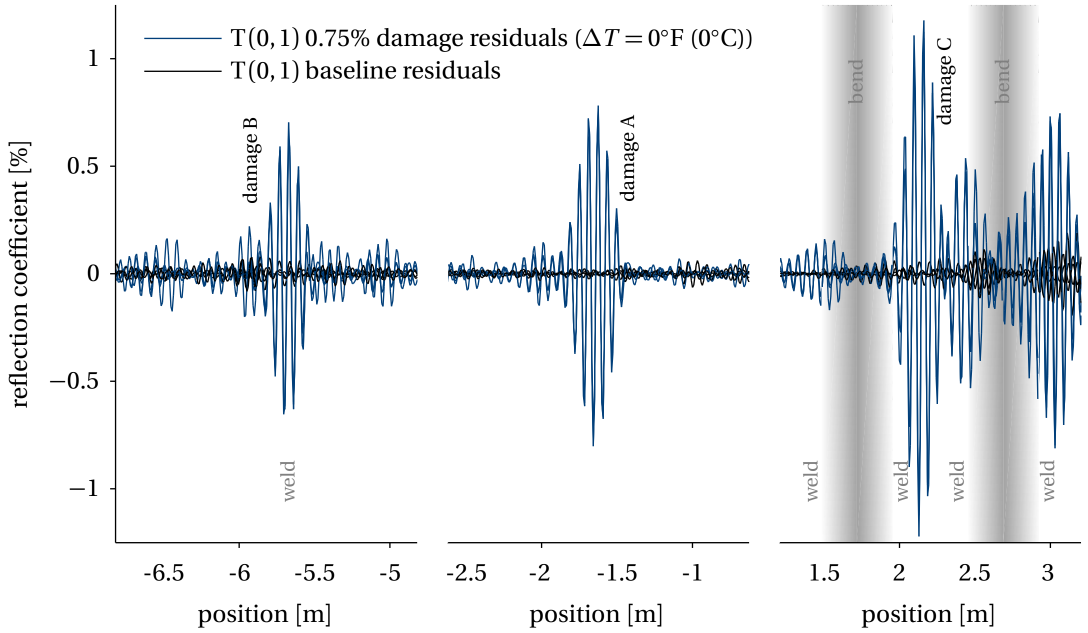

Figure 6.19: Detail at locations A, B and C of the torsional T(0, 1) residual RC signals from baseline reading IDs 1310, 1312, 1314 and 1316, and from damage reading IDs 1357, 1359 and 1362; the nominal cross-sectional area loss damage is 0.75% and the temperature difference ΔT to the baseline readings is 0°F (0°C).

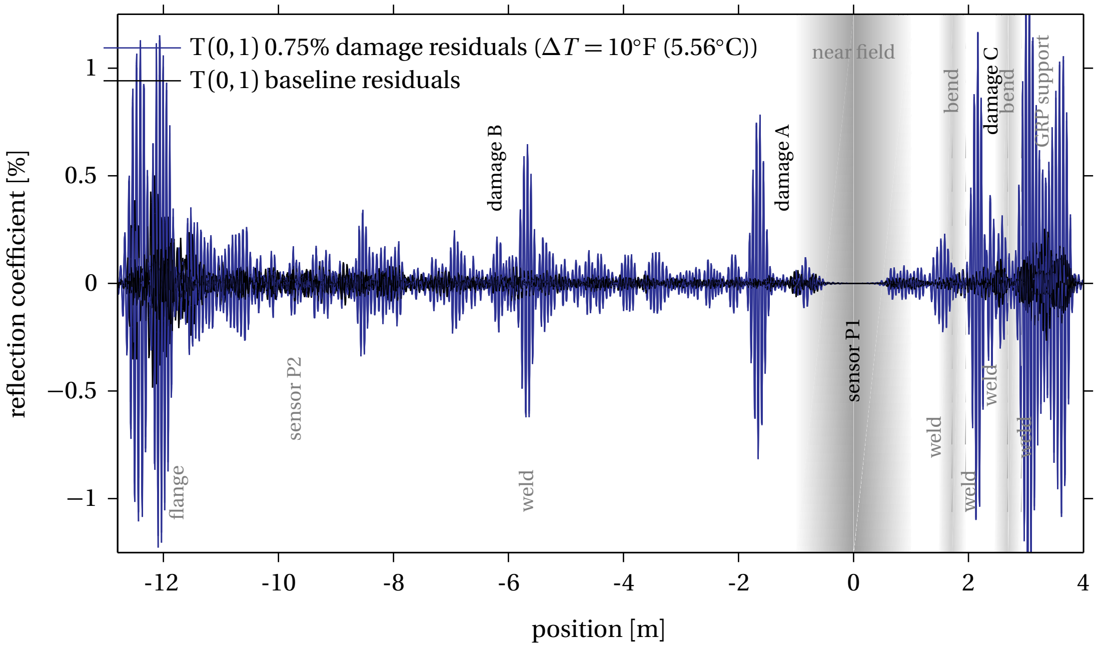

Figure 6.20: Torsional T(0, 1) residual RC signals from baseline reading IDs 1310, 1312, 1314 and 1316, and from damage reading IDs 1364, 1366 and 1368; the nominal cross-sectional area loss damage is 0.75% and the temperature difference ΔT to the baseline readings is 10°F (5.56°C).

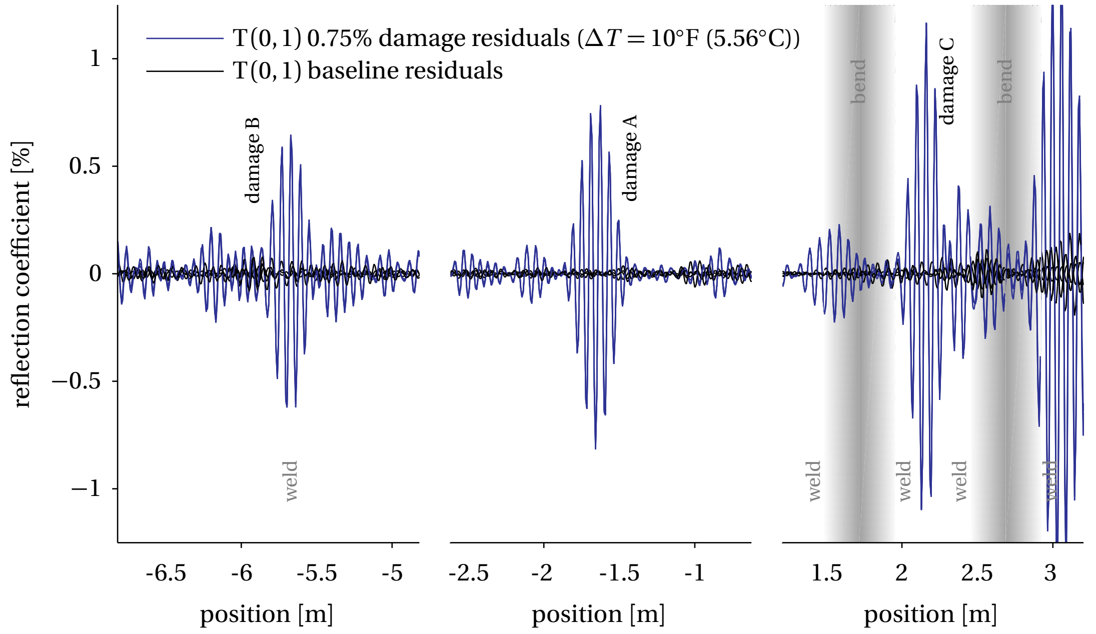

Figure 6.21: Detail at locations A, B and C of the torsional T(0, 1) residual RC signals from baseline reading IDs 1310, 1312, 1314 and 1316, and from damage reading IDs 1364, 1366 and 1368; the nominal cross-sectional area loss damage is 0.75% and the temperature difference ΔT to the baseline readings is 10°F (5.56°C).

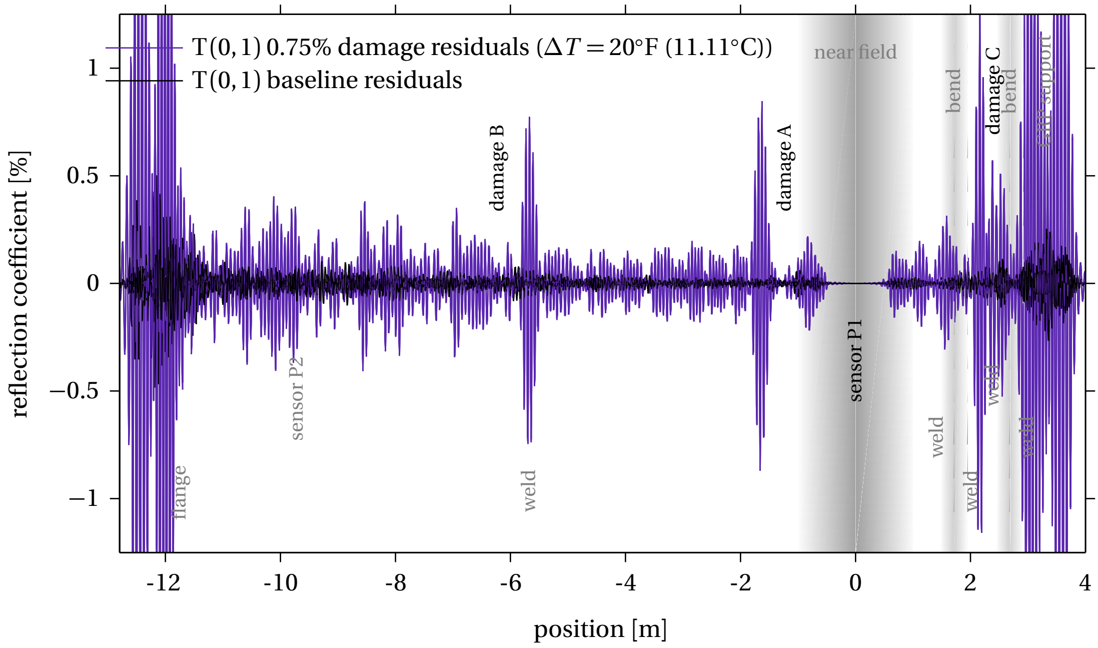

Figure 6.22: Torsional T(0, 1) residual RC signals from baseline reading IDs 1310, 1312, 1314 and 1316, and from damage reading IDs 1370, 1372 and 1374; the nominal cross-sectional area loss damage is 0.75% and the temperature difference ΔT to the baseline readings is 20°F (11.11°C).

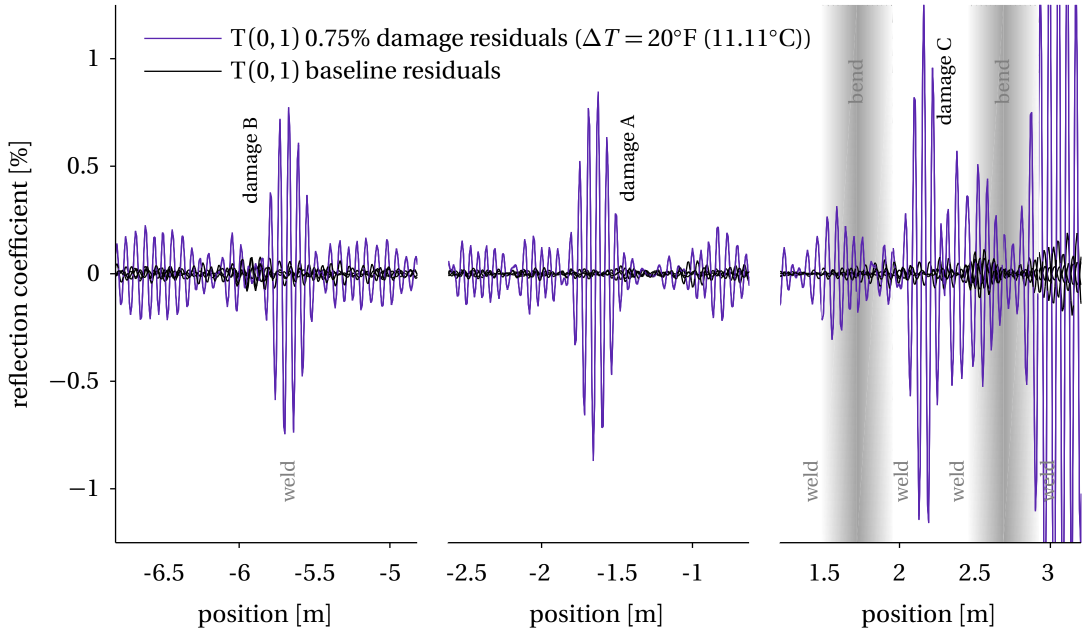

Figure 6.23: Detail at locations A, B and C of the torsional T(0, 1) residual RC signals from baseline reading IDs 1310, 1312, 1314 and 1316, and from damage reading IDs 1370, 1372 and 1374; the nominal cross-sectional area loss damage is 0.75% and the temperature difference ΔT to the baseline readings is 20°F (11.11°C).

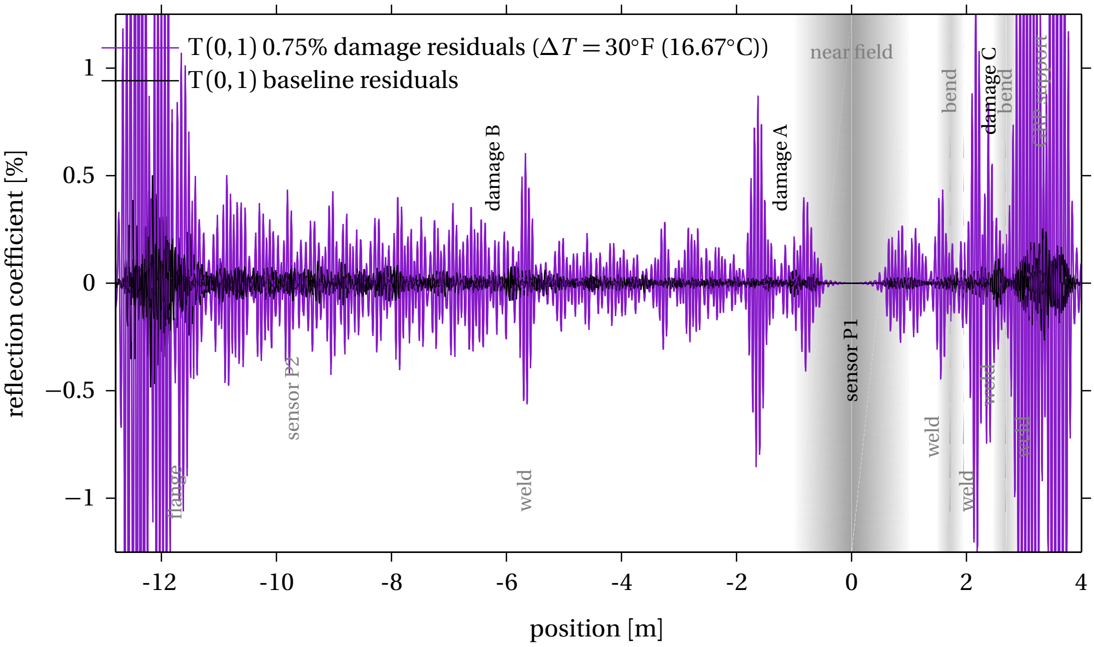

Figure 6.24: Torsional T(0, 1) residual RC signals from baseline reading IDs 1310, 1312, 1314 and 1316, and from damage reading IDs 1376, 1378 and 1380; the nominal cross-sectional area loss damage is 0.75% and the temperature difference ΔT to the baseline readings is 30°F (16.67°C).

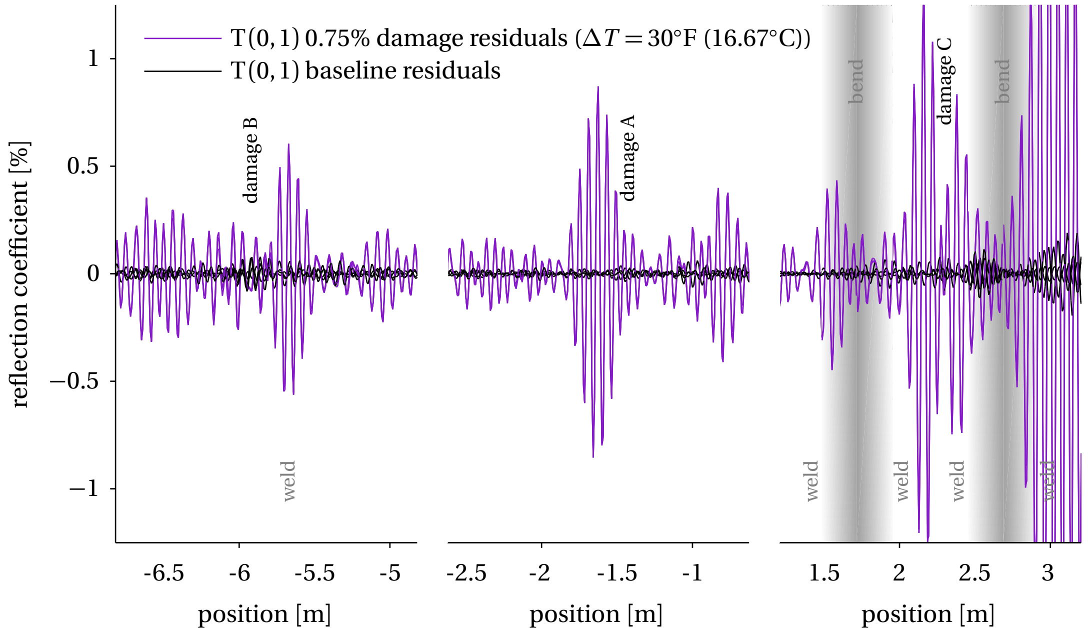

Figure 6.25: Detail at locations A, B and C of the torsional T(0, 1) residual RC signals from baseline reading IDs 1310, 1312, 1314 and 1316, and from damage reading IDs 1376, 1378 and 1380; the nominal cross-sectional area loss damage is 0.75% and the temperature difference ΔT to the baseline readings is 30°F (16.67°C).

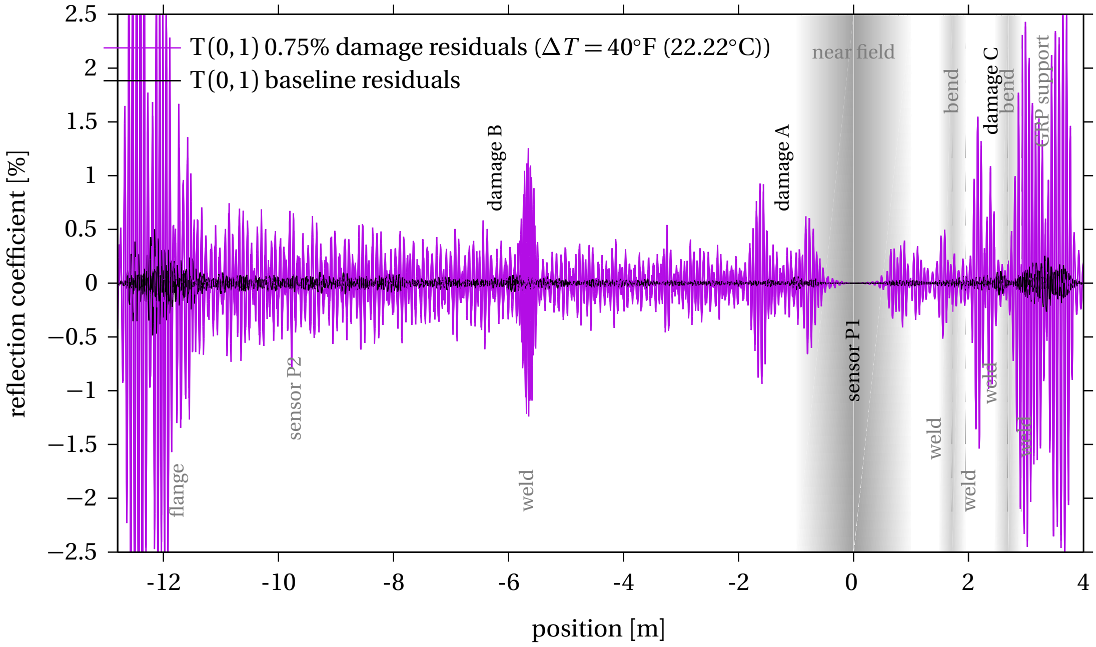

Figure 6.26: Torsional T(0,1) residual RC signals from baseline reading IDs 1310, 1312, 1314 and 1316, and from damage reading IDs 1382, 1384 and 1386; the nominal cross-sectional area loss damage is 0.75% and the temperature difference ΔT to the baseline readings is 40°F (22.22°C).

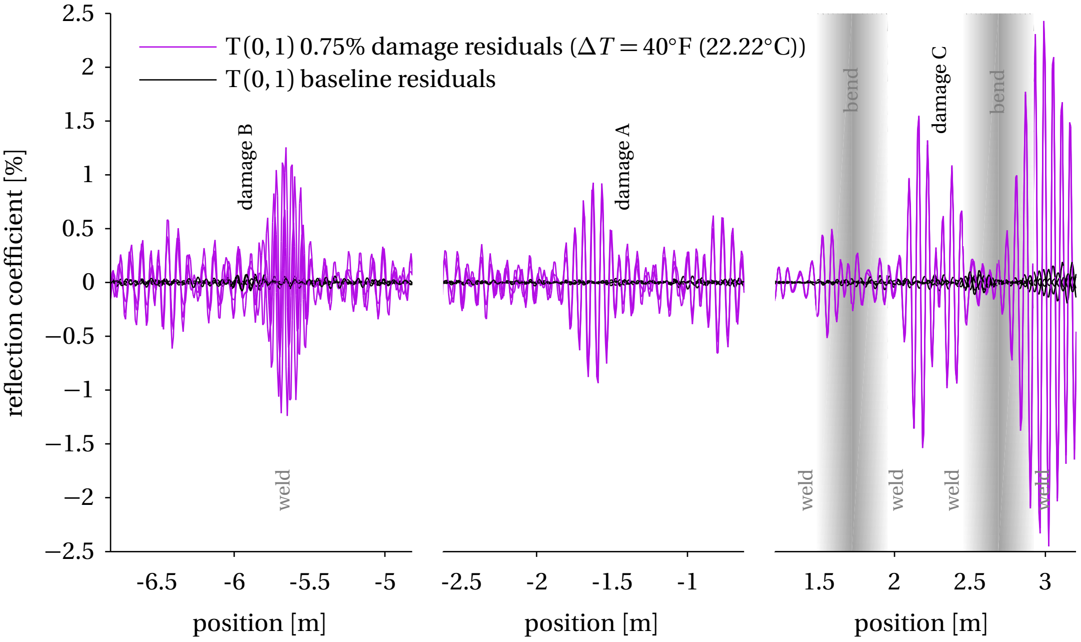

Figure 6.27: Detail at locations A, B and C of the torsional T(0,1) residual RC signals from baseline reading IDs 1310, 1312, 1314 and 1316, and from damage reading IDs 1382, 1384 and 1386; the nominal cross-sectional area loss damage is 0.75% and the temperature difference ΔT to the baseline readings is 40°F (22.22°C).

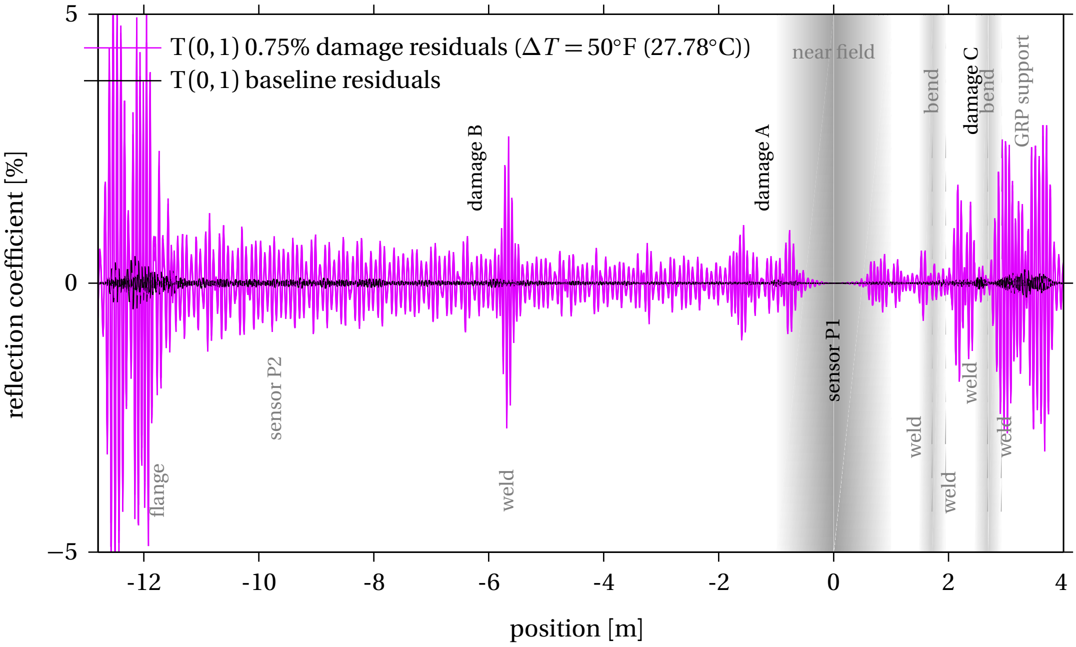

Figure 6.28: Torsional $T(0,1)$ residual RC signals from baseline reading IDs 1310, 1312, 1314 and 1316, and from damage reading IDs 1388, 1390 and 1392; the nominal cross-sectional area loss damage is 0.75% and the temperature difference ΔT to the baseline readings is 50°F (27.78°C).

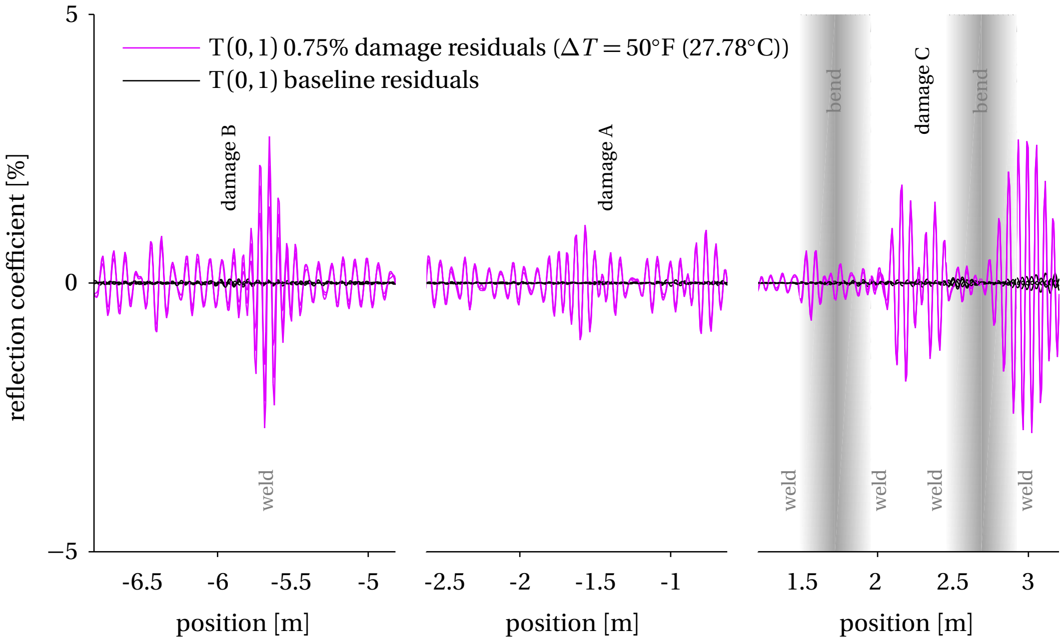

Figure 6.29: Detail at locations A, B and C of the torsional $T(0,1)$ residual RC signals from baseline reading IDs 1310, 1312, 1314 and 1316, and from damage reading IDs 1388, 1390 and 1392; the nominal cross-sectional area loss damage is 0.75% and the temperature difference ΔT to the baseline readings is 50°F (27.78°C).

Figures 6.18, 6.20, 6.22, 6.24, 6.26 and 6.28 show how in both the baseline and the damage residuals there are large echoes in correspondence of the flange near -12m and of the GRP support near 3m as result of the imperfect subtraction of their echoes. Importantly, as the temperature difference ΔT between baseline and damage readings increases, so does the amplitude of the echoes in correspondence not only of the flange and of the GRP support, but also in correspondence of the welds as a result of the increasingly imperfect subtraction of their echoes caused by the growing temperature difference ΔT. Notably, it can be easily observed how as the temperature difference ΔT increases so does the coherent noise in the damage residuals, *i.e.* the general signal amplitude away from features and damage. Such EOC effects are not only expected but also common in guided wave SHM applications, and are caused by temperature dependent variations in the coherent noise generated by the permanently installed guided wave sensor that are caused by many complex changes in the behaviour of the components of the permanently installed guided wave sensor itself and that become more significant as the temperature difference ΔT between baseline and damage readings increases, as discussed in chapter 4 and in section 4.3 in particular. Consequently, the subtraction of coherent noise becomes increasingly imperfect as the temperature difference ΔT increases.

Figures 6.19, 6.21, 6.23, 6.25, 6.27 and 6.29 highlights how near the locations A, B and C there are differences between the baseline and the damage residuals as a result of the introduction of the 1” diameter flat-bottomed holes that produced a 0.75% cross-sectional area loss.

When there is no temperature difference ΔT between baseline and damage readings, in the case of location A there is a very clear and stark difference between baseline residuals, whose magnitude is virtually null, and the damage residuals, which are perfectly superimposed and present a sole echo. As a result, it is straightforward to identify the damage echo at location A by comparing the echo-less baseline residuals with the other residuals. However, at locations B and C once again the baseline residuals present a number of echoes as a result of the imperfect subtraction of the echoes from the nearby welds, and the damage residuals also present many different echoes of similar magnitude which originate from both the imperfect subtraction of the echoes from the nearby welds and from the interaction of the introduced damage with those same welds.

As the temperature difference ΔT between baseline and damage readings increases a number of effects can be observed at locations A, B and C.

Firstly, it can be seen how the damage echo at location A becomes more and more swamped by coherent noise, to the point where, upon reaching a the temperature difference ΔT of

50°F it stops looking like an eight-cycle 27kHz Hann-windowed toneburst and becomes indistinguishable from the surrounding coherent noise, as shown in figures 6.28 and 6.29.

Secondly, it can be seen how the damage echo at location B begins to interact more and more with the echo of the nearby weld, whose amplitude in the damage residuals becomes larger and larger as the temperature difference ΔT increases and the subtraction becomes more and more imperfect. The occurrence of such interaction can be inferred by comparing the absolute amplitude of the damage echo at locations A and B as the temperature difference ΔT increases. Specifically, for $\Delta T = 0$°F the two echoes have roughly the same amplitude, as shown in figures 6.18 and 6.19. However, as ΔT increases to 10°F, 20°F and 30°F it can be seen in respectively figures 6.20 and 6.21, figures 6.22 and 6.23, and figures 6.24 and 6.25 that while the amplitude of the echo at location A remains constant, the amplitude of the echo at location B first decreases slightly, then increases only to decrease again as the damage echo moves slightly in and out of phase with the echo of the nearby weld as a result of the increasingly imperfect subtraction. Once ΔT reaches 40°F and 50°F the echo appears to lose coherence and consistency in phase and amplitude between the set of three readings and cannot be relied upon anymore, as shown in respectively figures 6.26 and 6.27, and figures 6.28 and 6.29.

There is no immediate way to explain the curious loss in phase coherence between the set of three readings that can be observed for the echo at location B once ΔT reaches 40°F, phase coherence that is then regained once ΔT reaches 50°F. Interestingly, by comparing figures 6.26 and 6.27 with figures 6.28 and 6.29 it is possible to see that the loss in phase coherence between the set of three readings is not restricted just to the echo at location B but appears to be present, although in a less severe form, along the entire signals. Given that this curious effect manifests itself in only one set of readings, and is not present neither the preceding ones nor the following ones, it is very likely that is it not systematic but rather caused by a small external source of electromagnetic or mechanical noise that corrupted one, two or even all three of the readings. This explanation appears even more likely to be true when considering that the pipe loop is mechanically and electrically connected to a much larger and complex multi-purpose test rig. It is also possible that the effect of the external noise source could have been magnified in the vicinity of location B by the interaction between the echo from the damage at location B and the echo from the nearby weld.

Finally, it can be seen how the damage echo at location C also begins to interact more and more with the echoes of the nearby welds, whose amplitudes in the damage residuals also becomes larger and larger as the temperature difference ΔT increases and the subtraction becomes more and more imperfect. As for location B, the occurrence of such interaction can be inferred by comparing the absolute amplitude of the damage echo at locations A and C as the temperature difference ΔT increases. Specifically, as ΔT increases to 10°F, 20°F and 30°F it can be seen in respectively figures 6.20 and 6.21, figures 6.22 and 6.23, and figures 6.24 and 6.25 that while the amplitude of the echo from damage A remains constant, the amplitude of the echo at location C first decreases slightly, then increases only to decrease again as the two echoes move slightly in and out of phase as a result of the increasingly imperfect subtraction. Once ΔT reaches 40°F and 50°F the echo arguably disappears altogether leaving in its place two echoes that appear to be shorter than the initial eight-cycle 27kHz Hann-windowed toneburst as a result of the interaction between the echo at location C and the echoes from the nearby welds, as shown in respectively figures 6.26 and 6.27, and figures 6.28 and 6.29.

Figures 6.30 through 6.41 present the results of the GLR maximisation in terms of the probability of false-call for a probability of damage detection equal to 99.9%, and in terms of the amplitude of the damage echo. In particular:

- figure 6.30 and 6.31 present the results when the temperature difference ΔT to the baseline readings is 0°F (0°C), *i.e.* for the residuals from reading IDs 1357, 1359 and 1362;
- figure 6.32 and 6.33 present the results when the temperature difference ΔT to the baseline readings is 10°F (5.56°C), *i.e.* for the residuals from reading IDs 1364, 1366 and 1368;
- figure 6.34 and 6.35 present the results when the temperature difference ΔT to the baseline readings is 20°F (11.11°C), *i.e.* for the residuals from reading IDs 1370, 1372 and 1374;
- figure 6.36 and 6.37 present the results when the temperature difference ΔT to the baseline readings is 30°F (16.67°C), *i.e.* for the residuals from reading IDs 1376, 1378 and 1380;
- figure 6.38 and 6.39 present the results when the temperature difference ΔT to the baseline readings is 40°F (22.22°C), *i.e.* for the residuals from reading IDs 1382, 1384 and 1386;
- figure 6.40 and 6.41 present the results when the temperature difference ΔT to the baseline readings is 50°F (27.78°C), *i.e.* for the residuals from reading IDs 1388, 1390 and 1392.

The different results in each figure were calculated with the finite set $Y_\star$ including, from top to bottom, an increasing number of readings, *e.g.* $Y_\star = \{\mathbf{y}_{\star 1}\}$, $Y_\star = \{\mathbf{y}_{\star 1}, \mathbf{y}_{\star 2}\}$, $Y_\star = \{\mathbf{y}_{\star 1}, \mathbf{y}_{\star 2}, \mathbf{y}_{\star 3}\}$.

When there is no temperature difference ΔT between baseline and damage readings, it can be seen in figure 6.30 that of all positions along the pipe loop, the only positions where the probability of false-call falls to negligible levels is in the vicinity of locations A and B. Importantly, as the size of the finite set $Y_\star$ increases the probability of false-call decreases to negligible levels also around location C. Simultaneously, figure 6.31 shows that where there is a low probability of false-call, *i.e.* in the vicinity of locations A, B and C, the estimated amplitude of the damage echo is respectively 0.75%, 0.6% and 1%, which corresponds roughly to the nominal 0.75% cross-sectional area loss given that the damage axial length is equal to just less than a quarter of the wavelength of the incident $\mathrm{T}(0,1)$ guided wave packet [59, 60]. This is consistent with what can be observed in figure 6.19, where as previously discussed in the case of location A it is straightforward to identify the damage echo, while in the case of locations B and C it is non-trivial to determine whether an actual new echo has appeared or an existing echo has changed as a result of EOC effects.

However, as the temperature difference ΔT between baseline and damage readings increases a number of effects can be observed especially at locations A, B and C. First of all, figures 6.30, 6.32, 6.34, 6.36, 6.38 and 6.40 show that in the vicinity of location A the probability of false-call remains negligible until $\Delta T = 30$°F. As ΔT increases to 40°F the probability of false-call decreases to negligible levels only as the size of the finite set $Y_\star$ increases, which intuitively means that more evidence in the form of more readings is required to drop the probability of false-call to negligible levels. When ΔT reaches 50°F the probability of false-call in the vicinity of location A remains relatively high irrespective of the size of the finite set $Y_\star$, indicating that the presence of damage A can no longer be confidently detected. Such results are consistent with what can be observed in figures 6.19, 6.21, 6.23, 6.25, 6.27 and 6.29, where, as previously discussed, it can be seen how as the temperature difference ΔT increases the damage echo at location A becomes more and more swamped by coherent noise, to the point where, upon reaching a the temperature difference ΔT of 50°F it stops looking like an eight-cycle 27kHz Hann-windowed toneburst and becomes indistinguishable from the surrounding coherent noise. Importantly, note how for as long as the probability of false-call remains at negligible levels, figures 6.31, 6.33, 6.35, 6.37 and 6.39 indicate that the amplitude of the echo from damage A remains consistently and reliably estimated at roughly 0.75%.

Secondly, figures 6.30, 6.32, 6.34, 6.36, 6.38 and 6.40 show that in the vicinity of location B the probability of false-call is negligible for $\Delta T = 0°$, increases to relatively high levels for $\Delta T =$

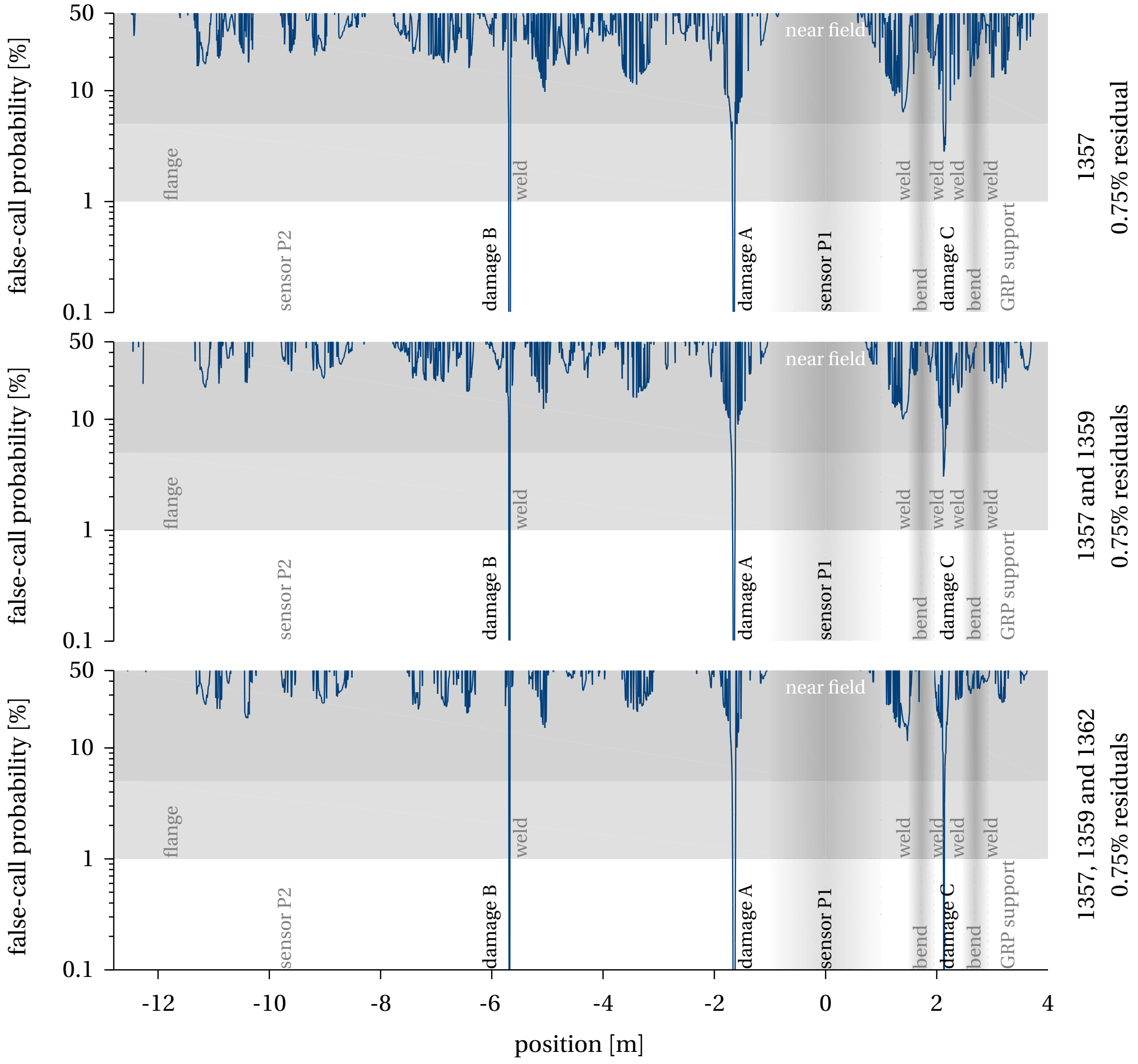

Figure 6.30: Results of the GLR maximisation with 0.75% cross-sectional area loss damage in terms of the probability of false-call for a probability of damage detection equal to 99.9%; the different results were calculated with the finite set $Y_{\star}$ including, from top to bottom: reading ID 1357; reading IDs 1357 and 1359; reading IDs 1357, 1359 and 1362; the temperature difference ΔT to the baseline readings is 0°F (0°C).

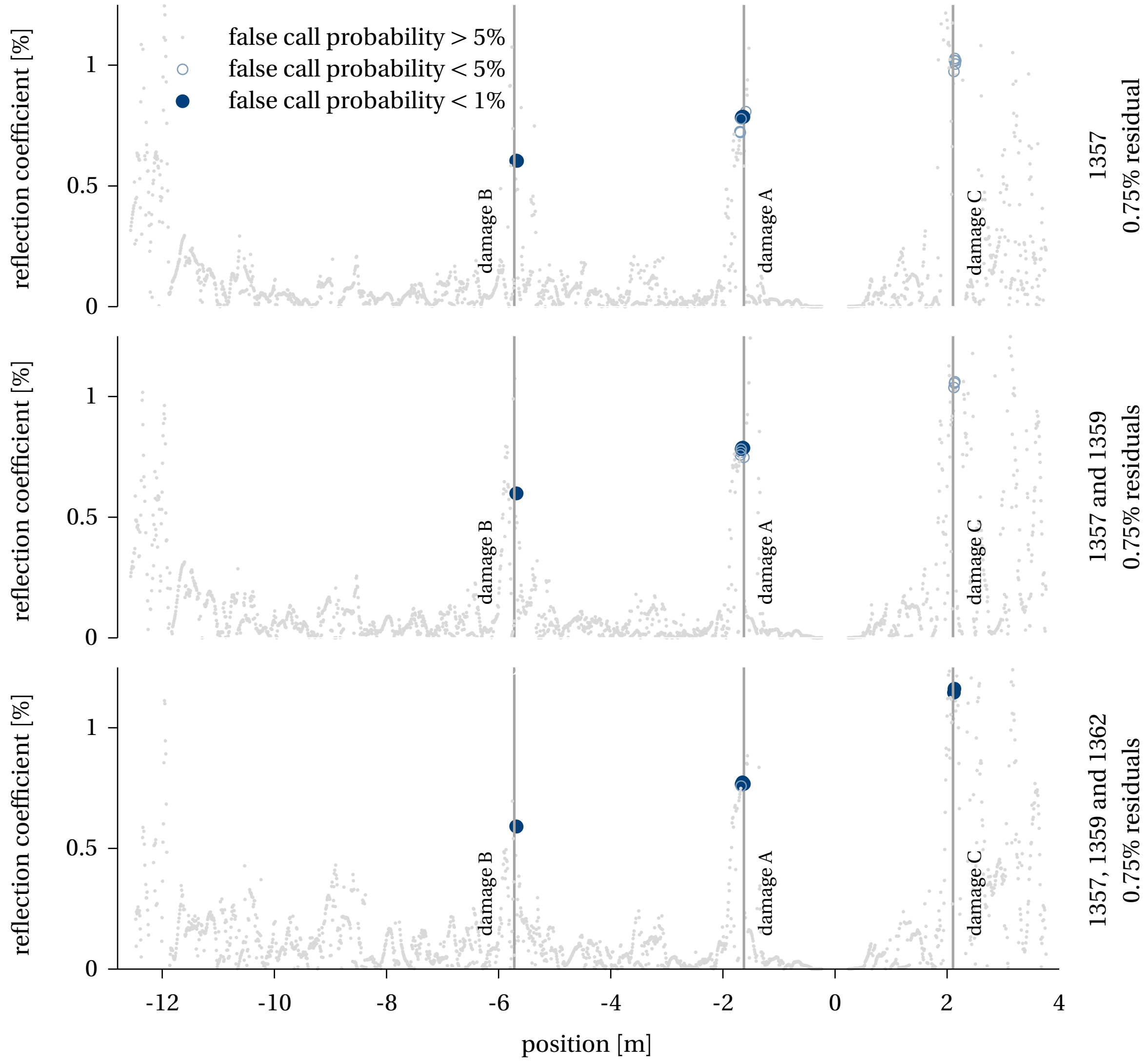

Figure 6.31: Results of the GLR maximisation with 0.75% cross-sectional area loss damage in terms of the amplitude of the damage echo; the different results were calculated with the finite set $Y_\star$ including, from top to bottom: reading ID 1357; reading IDs 1357 and 1359; reading IDs 1357, 1359 and 1362; the temperature difference ΔT to the baseline readings is 0°F (0°C).

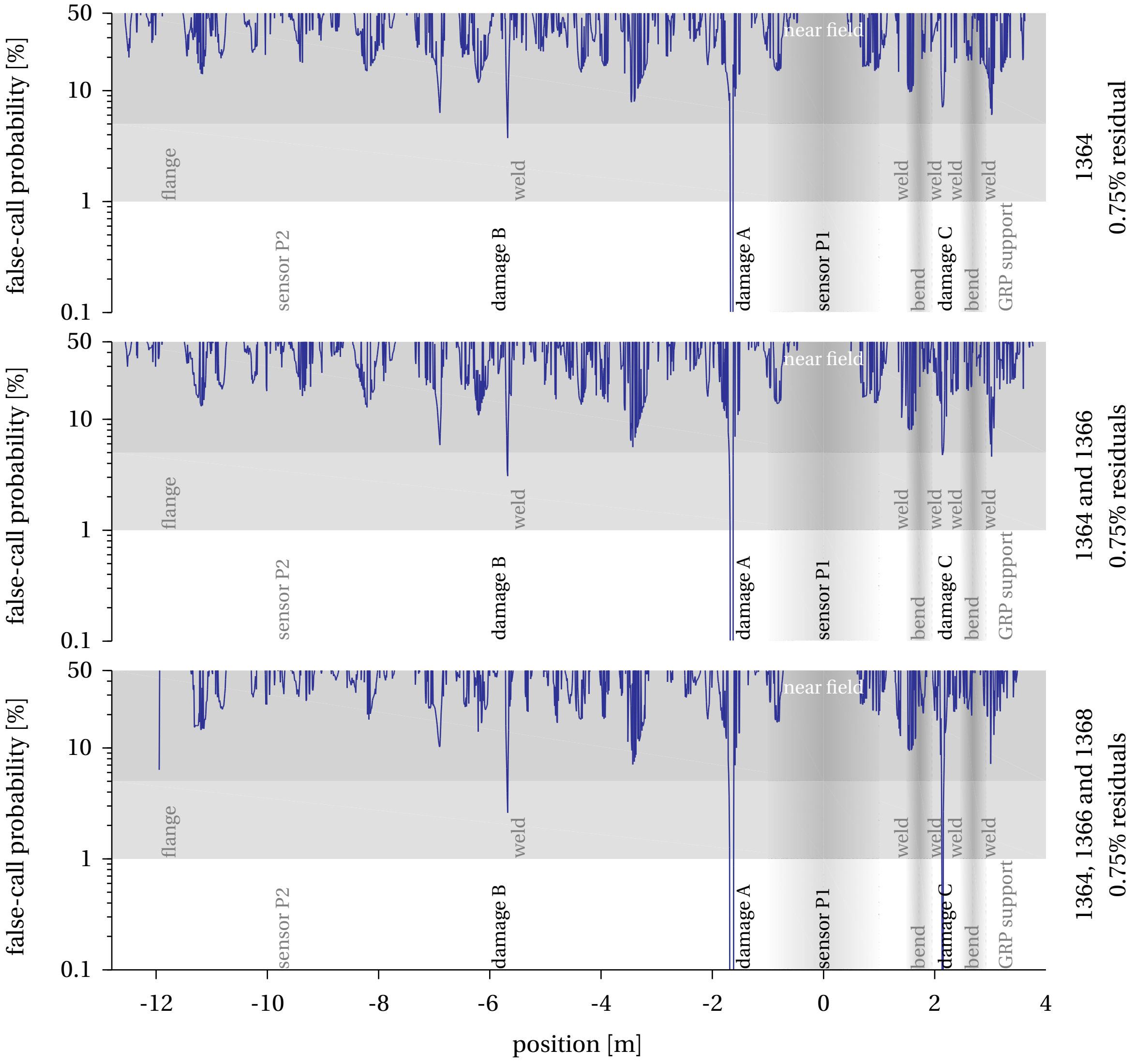

Figure 6.32: Results of the GLR maximisation with 0.75% cross-sectional area loss damage in terms of the probability of false-call for a probability of damage detection equal to 99.9%; the different results were calculated with the finite set $Y_\star$ including, from top to bottom: reading ID 1364; reading IDs 1364 and 1366; reading IDs 1364, 1366 and 1368; the temperature difference ΔT to the baseline readings is 10°F (5.56°C).

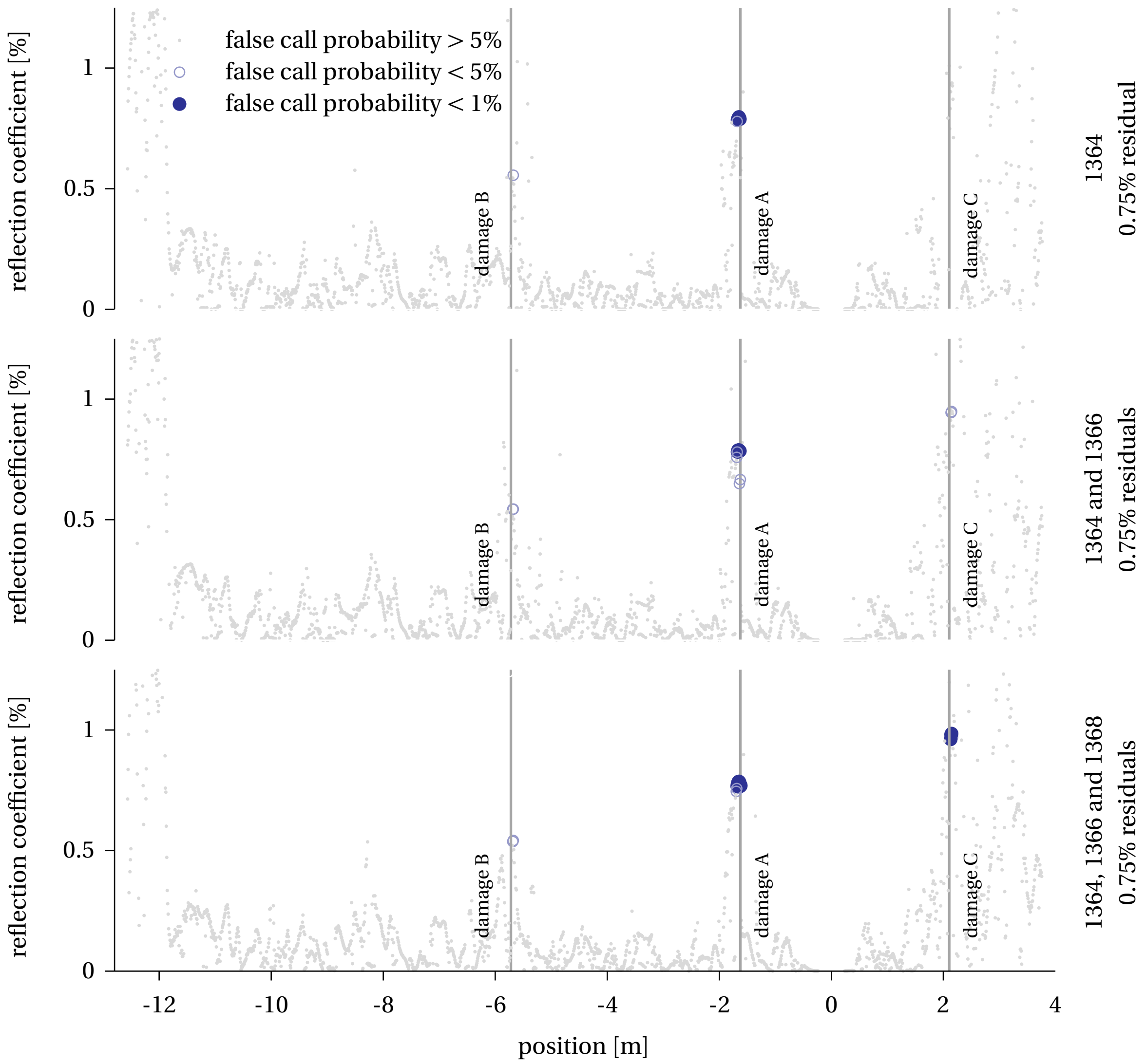

Figure 6.33: Results of the GLR maximisation with 0.75% cross-sectional area loss damage in terms of the amplitude of the damage echo; the different results were calculated with the finite set $Y_\star$ including, from top to bottom: reading ID 1364; reading IDs 1364 and 1366; reading IDs 1364, 1366 and 1368; the temperature difference ΔT to the baseline readings is 10°F (5.56°C).

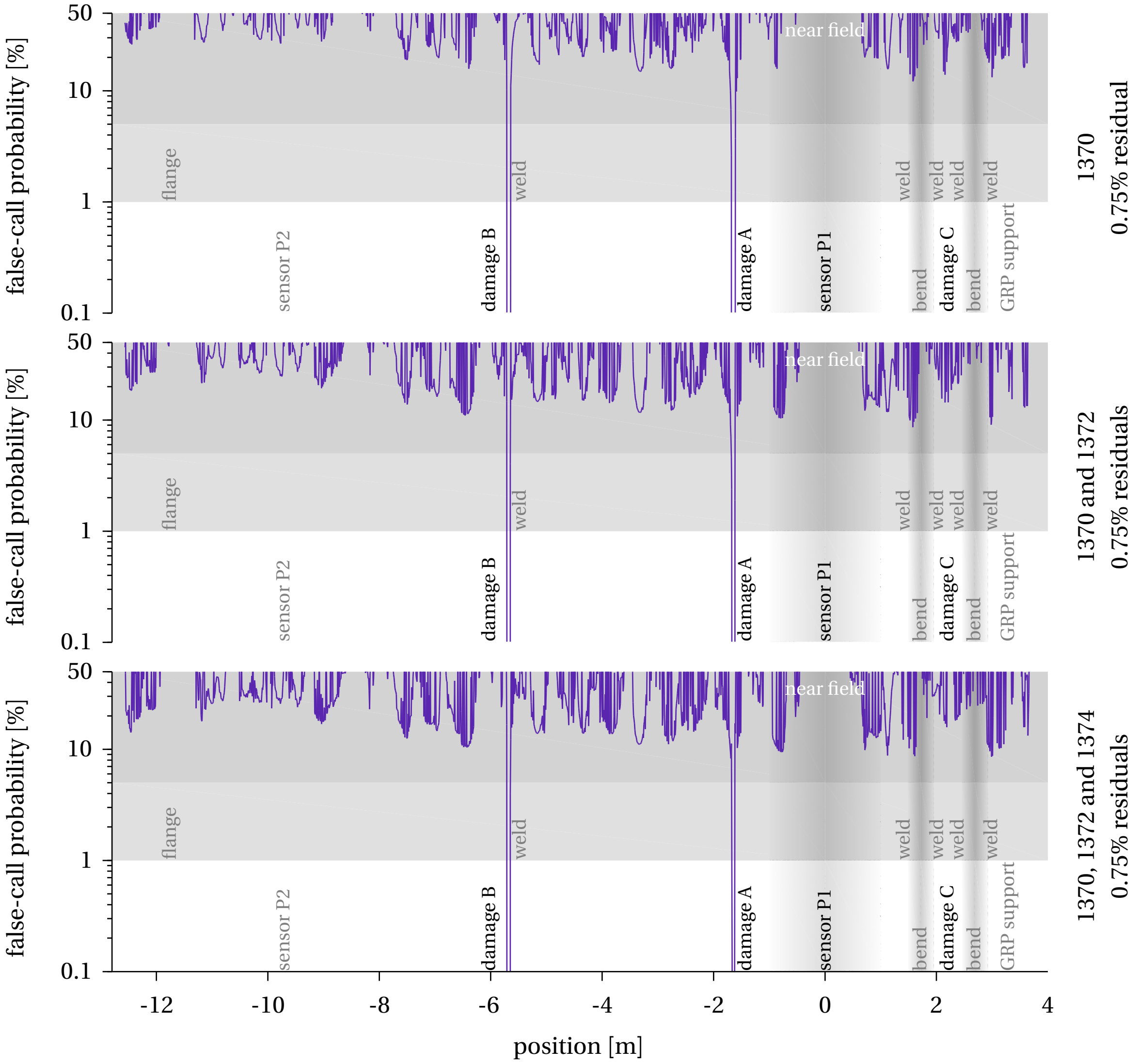

Figure 6.34: Results of the GLR maximisation with 0.75% cross-sectional area loss damage in terms of the probability of false-call for a probability of damage detection equal to 99.9%; the different results were calculated with the finite set $Y_\star$ including, from top to bottom: reading ID 1370; reading IDs 1370 and 1372; reading IDs 1370, 1372 and 1374; the temperature difference ΔT to the baseline readings is 20°F (11.11°C).

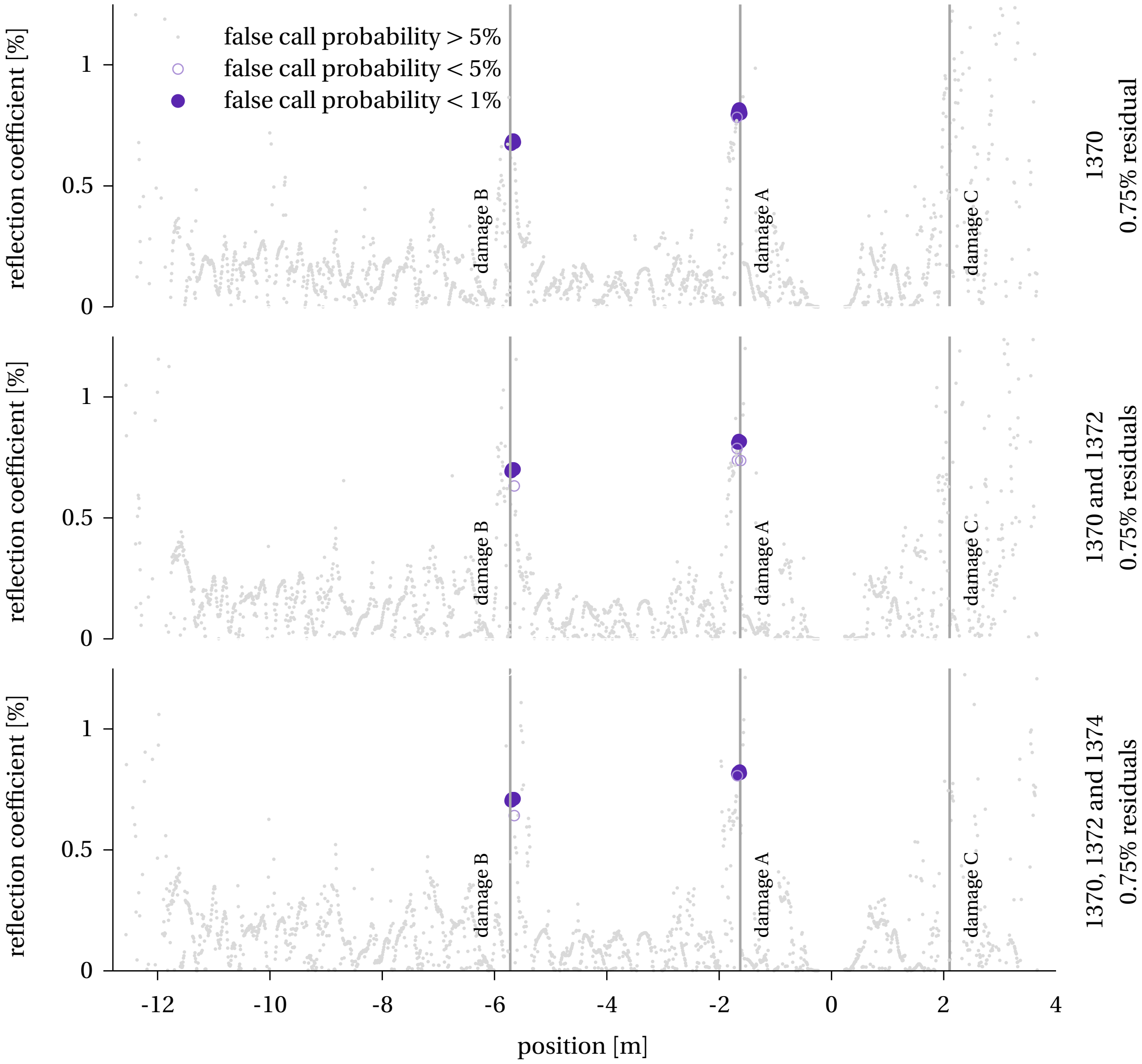

Figure 6.35: Results of the GLR maximisation with 0.75% cross-sectional area loss damage in terms of the amplitude of the damage echo; the different results were calculated with the finite set $Y_\star$ including, from top to bottom: reading ID 1370; reading IDs 1370 and 1372; reading IDs 1370, 1372 and 1374; the temperature difference ΔT to the baseline readings is 20°F (11.11°C).

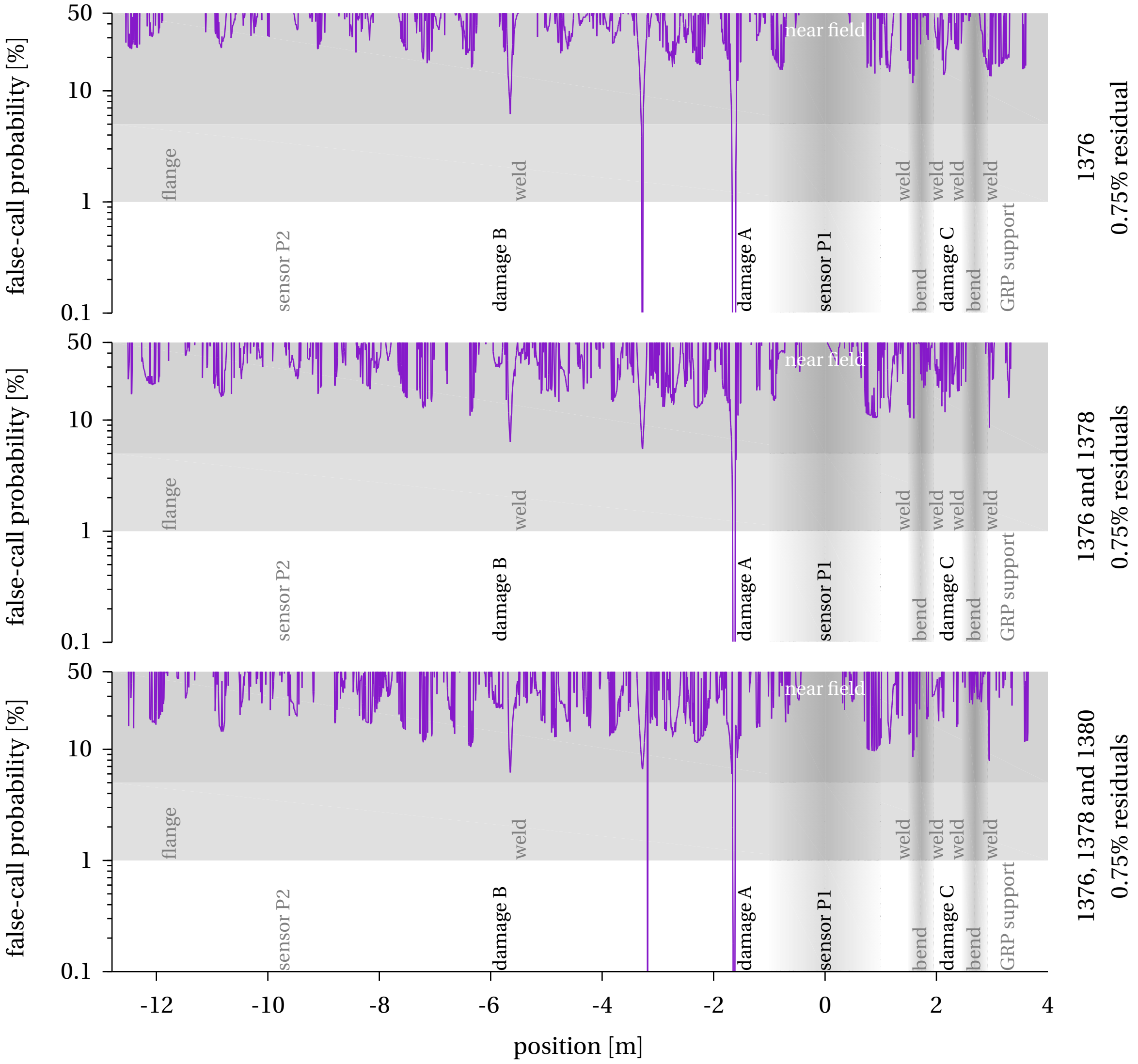

Figure 6.36: Results of the GLR maximisation with 0.75% cross-sectional area loss damage in terms of the probability of false-call for a probability of damage detection equal to 99.9%; the different results were calculated with the finite set $Y_\star$ including, from top to bottom: reading ID 1376; reading IDs 1376 and 1378; reading IDs 1376, 1378 and 1380; the temperature difference ΔT to the baseline readings is 30°F (16.67°C).

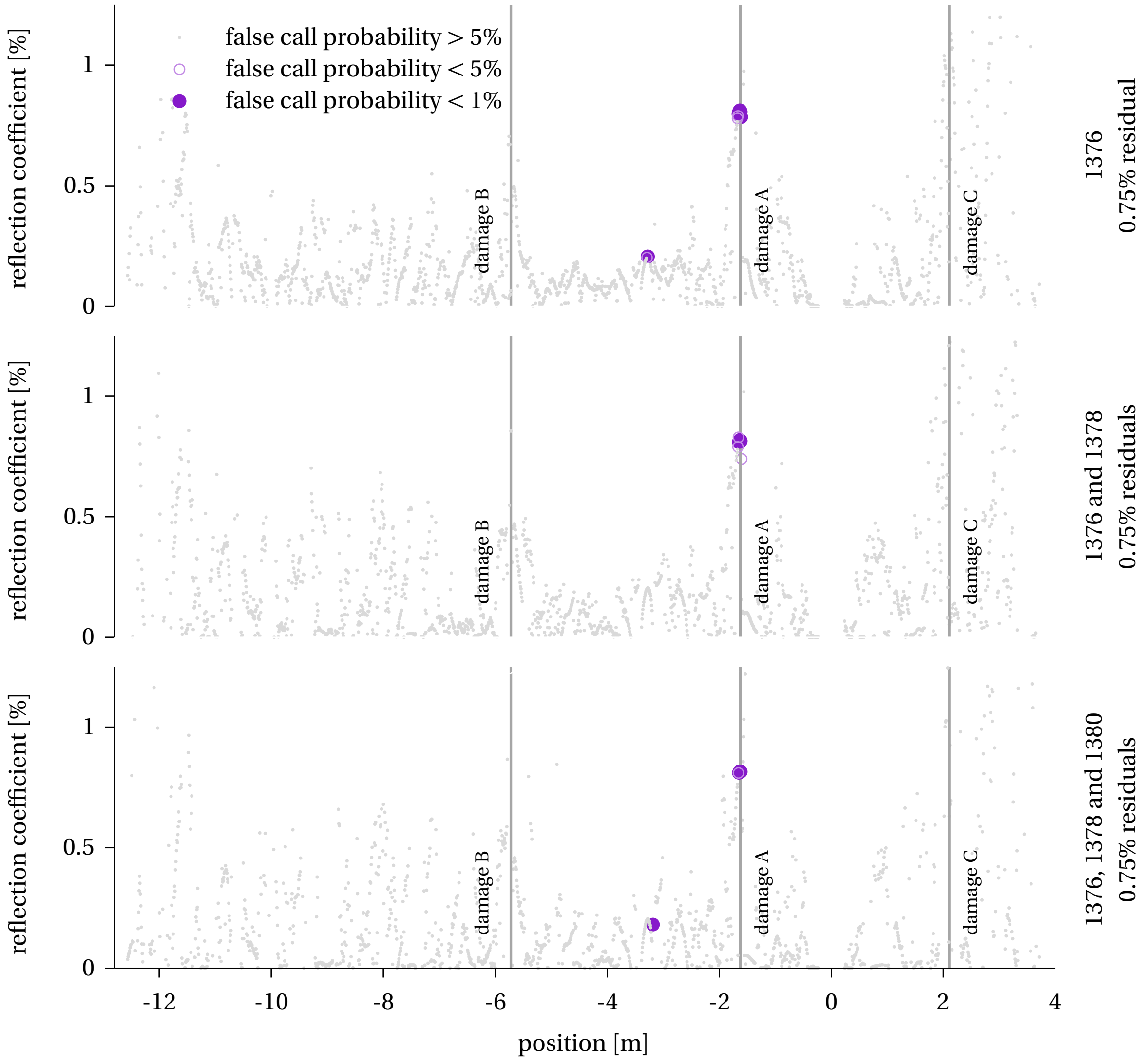

Figure 6.37: Results of the GLR maximisation with 0.75% cross-sectional area loss damage in terms of the amplitude of the damage echo; the different results were calculated with the finite set $Y_\star$ including, from top to bottom: reading ID 1376; reading IDs 1376 and 1378; reading IDs 1376, 1378 and 1380; the temperature difference ΔT to the baseline readings is 30°F (16.67°C).

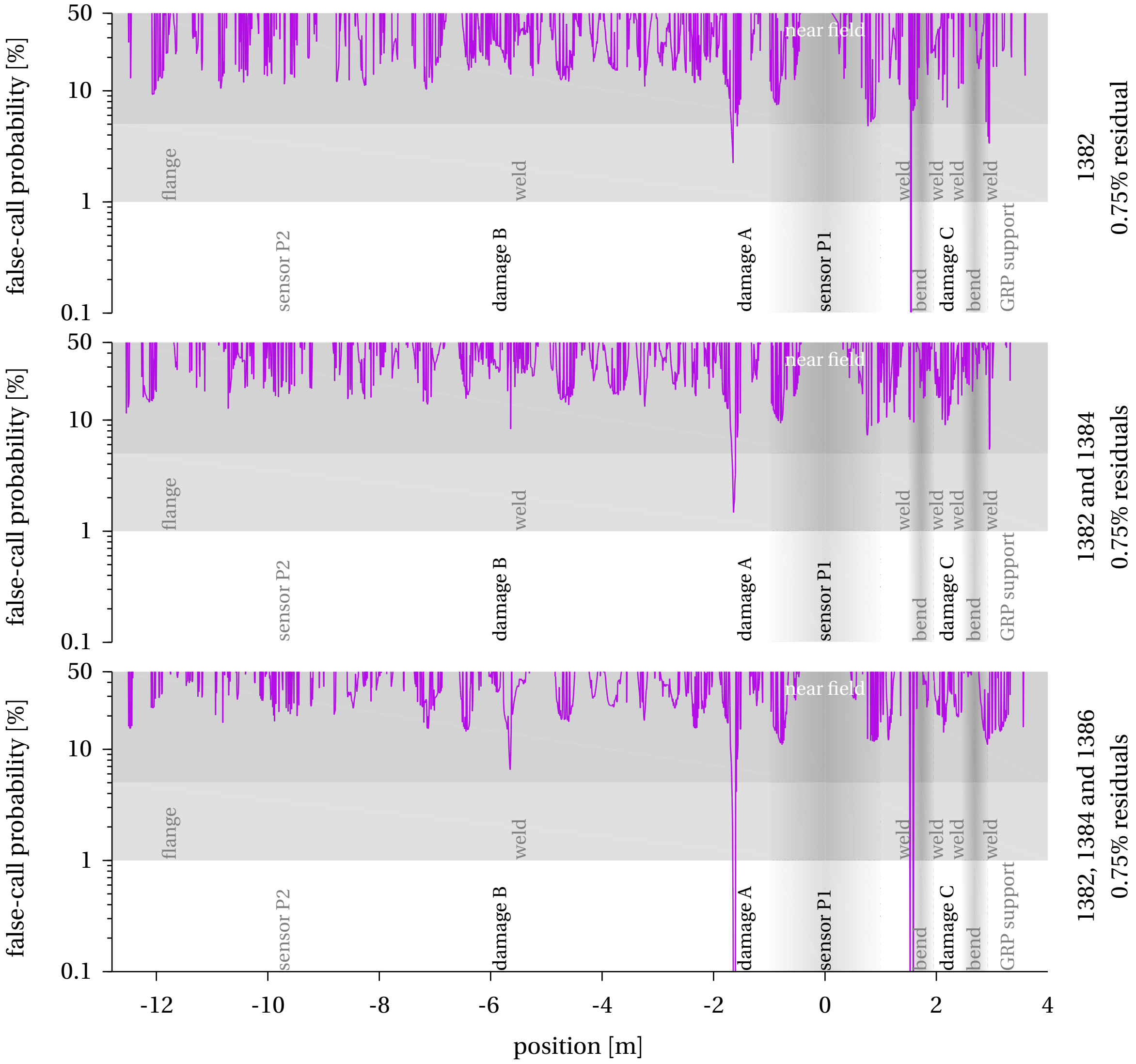

Figure 6.38: Results of the GLR maximisation with 0.75% cross-sectional area loss damage in terms of the probability of false-call for a probability of damage detection equal to 99.9%; the different results were calculated with the finite set $Y_\star$ including, from top to bottom: reading ID 1382; reading IDs 1382 and 1384; reading IDs 1382, 1384 and 1386; the temperature difference ΔT to the baseline readings is 40°F (22.22°C).

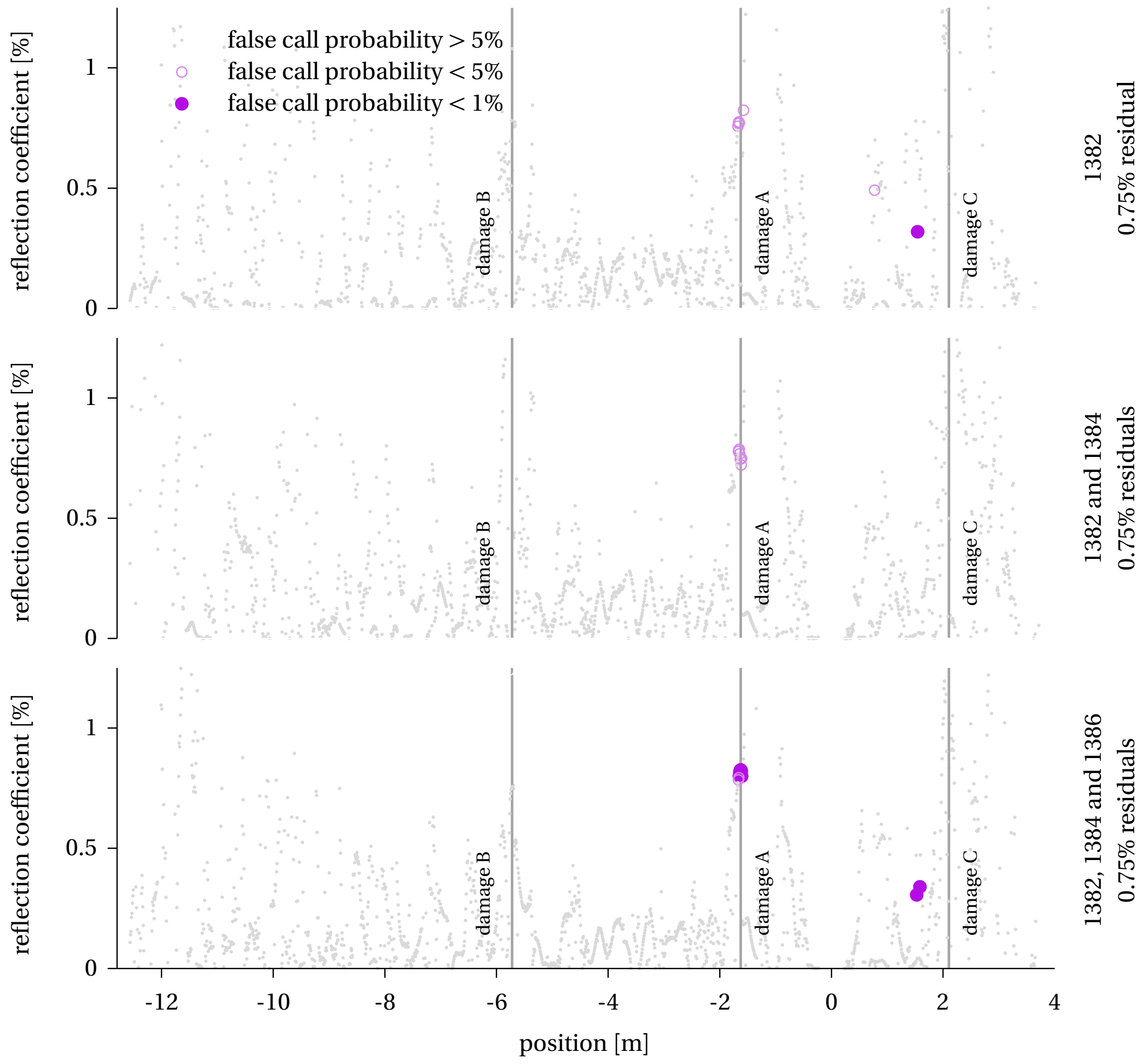

Figure 6.39: Results of the GLR maximisation with 0.75% cross-sectional area loss damage in terms of the amplitude of the damage echo; the different results were calculated with the finite set $Y_\star$ including, from top to bottom: reading ID 1382; reading IDs 1382 and 1384; reading IDs 1382, 1384 and 1386; the temperature difference ΔT to the baseline readings is 40°F (22.22°C).

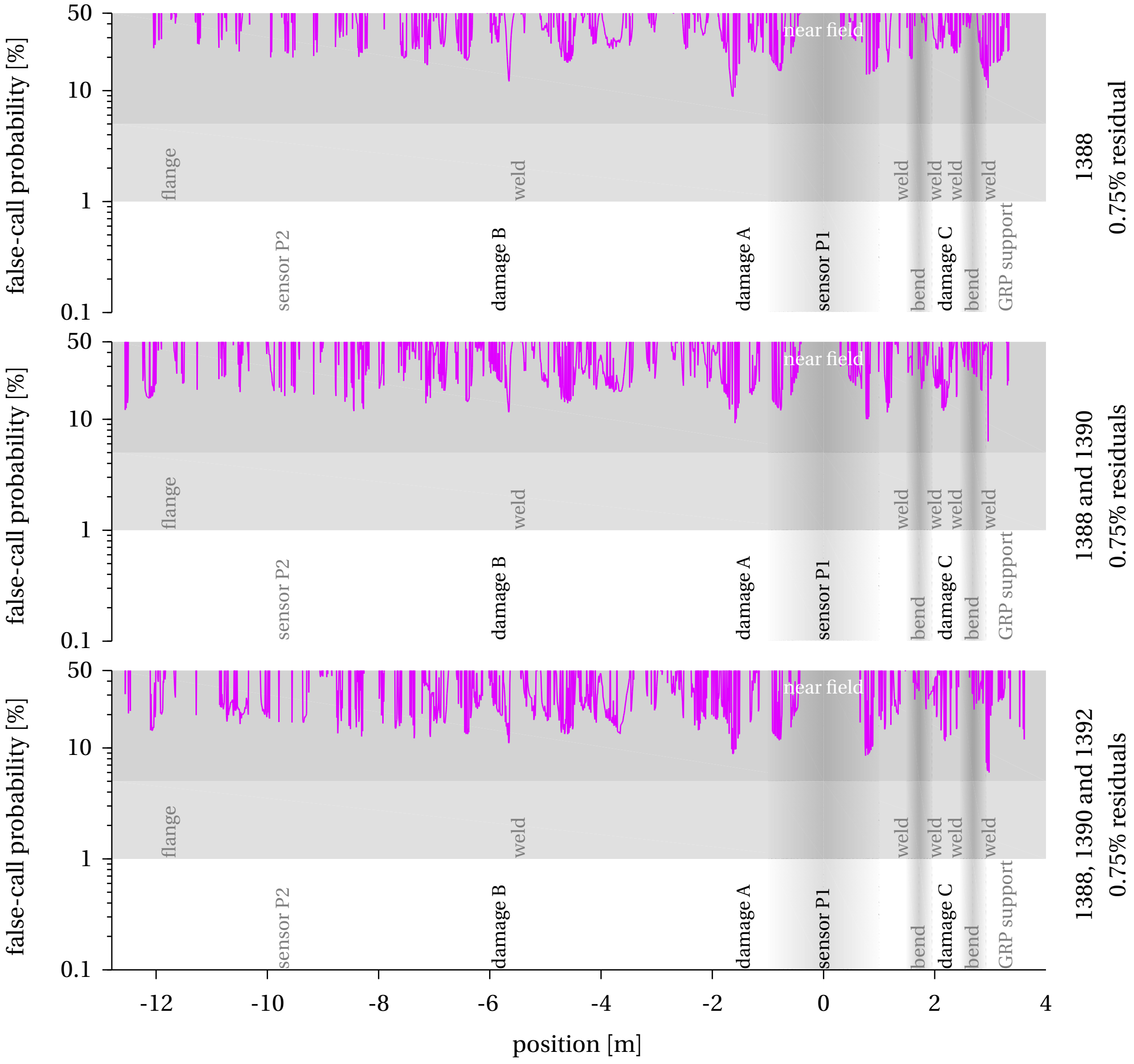

Figure 6.40: Results of the GLR maximisation with 0.75% cross-sectional area loss damage in terms of the probability of false-call for a probability of damage detection equal to 99.9%; the different results were calculated with the finite set $Y_\star$ including, from top to bottom: reading ID 1388; reading IDs 1388 and 1390; reading IDs 1388, 1390 and 1392; the temperature difference ΔT to the baseline readings is 50°F (27.78°C).

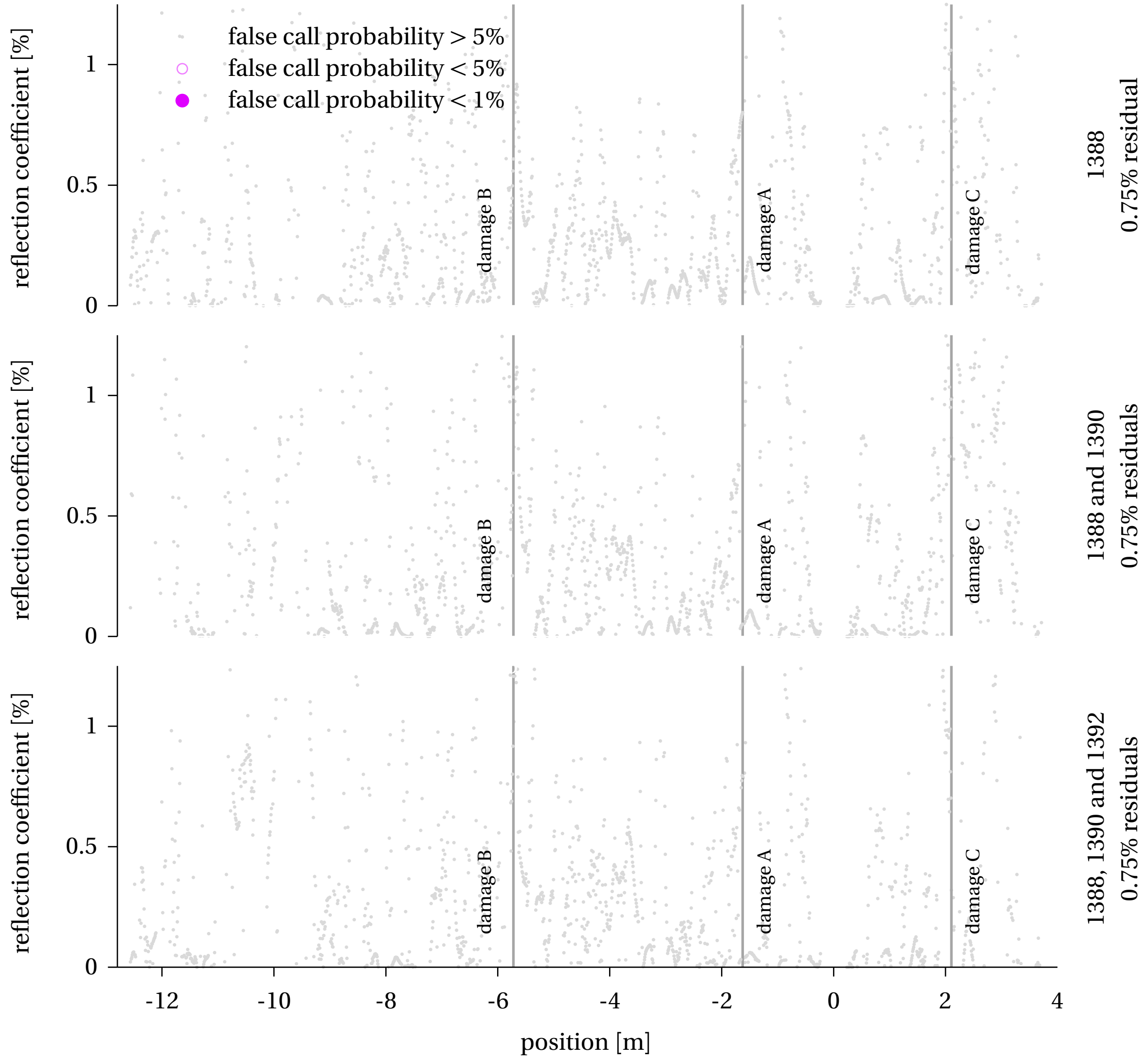

Figure 6.41: Results of the GLR maximisation with 0.75% cross-sectional area loss damage in terms of the amplitude of the damage echo; the different results were calculated with the finite set $Y_\star$ including, from top to bottom: reading ID 1388; reading IDs 1388 and 1390; reading IDs 1388, 1390 and 1392; the temperature difference ΔT to the baseline readings is 50°F (27.78°C).

10°, becomes negligible once more for $\Delta T = 20^\circ$ and successively increases back to relatively high levels when ΔT exceeds 30°F. Such results are consistent with the previously discussed behaviour of the echo at location B, whose amplitude fluctuates and whose shape becomes distorted as ΔT increases. Note how for as long as the probability of false-call remains at negligible levels, figures 6.31, 6.33, 6.35, 6.37 and 6.39 indicate that the amplitude of the echo from damage B remains consistently and reliably estimated at between 0.6% and 0.75%.

Finally, although in the vicinity of location C the probability of false-call falls to negligible levels for $\Delta T = 0^\circ$ and $\Delta T = 10^\circ$ as the size of the finite set $Y_\star$ increases, once ΔT exceeds 20°F the probability of false-call increases to relatively high levels, as shown in figures 6.30, 6.32, 6.34, 6.36, 6.38 and 6.40. As for the case of the echo at location B, such results are consistent with the previously discussed behaviour of the echo at location C which, as ΔT increases, begins to interact more and more with the echoes of the nearby welds until it arguably disappears altogether leaving behing two echoes that appear to be shorter than the initial eight-cycle 27kHz Hann-windowed toneburst. Figures 6.31 and 6.33 indicate that, for as long as the probability of false-call remains at negligible levels, the amplitude of the echo from damage C remains consistently and reliably estimated at roughly 1.0%.

Notably, none of the large echoes in correspondence of the flange and of the GRP support are identified by the proposed automated procedure as locations where damage might be growing, irrespective of the temperature difference ΔT between baseline and damage readings. Interestingly, however, figures 6.36 and 6.38 present evidence of what need to be regarded as actual false-calls of the proposed automated procedure in the vicinity of respectively -3.5m and 1.7m, *i.e.* of regions where the probability of false-call falls to negligible levels yet it is known no damage has been growing. A quick glance at respectively figures 6.37 and 6.39 reveals the estimated amplitude of the two false-calls to be respectively 0.15% and 0.3%.

The occurrence of the two false-calls, whose amplitude is similar to that of the coherent noise in the residual signals at their respective locations near -3.5m and 1.7m, as shown in figures 6.24 and 6.26, can be explained by considering that, out of simple chance, coherent noise together with uncompensated EOC effects might locally gain sufficient coherence and consistency in phase and amplitude across multiple readings to resemble the shape of an eight-cycle 27kHz Hann-windowed toneburst or of any other signal that could be sought for by the proposed automated procedure. Such chance effects are likely supported by the appearance of a small shadow ring near -3.5m, which is roughly twice the distance between the gPIMS® P1 sensor and the damage at location A, as well as by the appearance of a small mirror near 1.7m, which is a location specular to that of the damage at location A with respect to the gPIMS® P1 sensor, with both artefact possibly originating from expected deteriorations in the performance, and in particular in the direction control capabilities, of the gPIMS® P1 sensor at higher temperatures.

An immediate fix to address the issue of false-calls with an amplitude similar to that of the coherent noise would be to impose a minimum amplitude requirement to the signal that is being sought for by the proposed automated procedure.

More generally however, the occurrence of the two false-calls reveals one limitation of the proposed automated procedure, which analyses each position along a pipe separately rather than correlating evidence originating from multiple locations. A quick glance at either figure 6.24 or 6.26 quickly allows the two false calls to be dismissed by noticing how their estimated amplitude is roughly the same as that of coherent noise along the rest of the pipe loop.

6.4 Conclusions

This chapter first introduced the linear regression model, which has been identified as the preferred method to model the behaviour of the uncompensated EOC effects, in section 6.1 together with a discussion on the methodology and implications of estimating such a model from a set of b baseline residuals. Successively, in section 6.2 it has been shown how it is in general possible to determine whether a new sample, such as a new residual signal, is consistent or not with a given linear regression model, such as the one estimated from a set of b baseline residuals, thereby enabling the possibility of establishing whether variations in the residual signal from permanently installed guided wave sensors over time are due to uncompensated EOC effects or to damage growth. Finally, in section 6.3 it has been exemplified, utilising experimental data, how the concepts presented in sections 6.1 and 6.2 can be combined to detect damage growth in practical circumstances through a novel automated damage detection procedure. In particular, it has been shown how the proposed procedure is able to consistently ignore uncompensated EOC effects while being very effective at detecting and quantifying actual damage.

Chapter 7

Conclusion

The principal objective of this thesis has been to introduce a framework with which to utilise data gathered over time from permanently installed guided wave sensors in order to detect and monitor damage growth in pipelines. The proposed framework is intended to form the basis of a software complement to permanently installed guided wave sensors that would provide the petrochemical industry with a complete pipeline Structural Health Monitoring (SHM) solution that, through the early detection, diagnosis and monitoring of damage growth, can enable the formulation of reliable prognoses, reduce the risk of unexpected failures, and ultimately make possible the shift from time-based maintenance to the more cost-effective condition-based maintenance [1].

The main advantages of SHM and condition-based maintenance from a petrochemical industry standpoint are:

- **Operational.** No components will be taken out of service unless absolutely necessary, and since it becomes very unlikely for critical damage to grow undetected the overall safety and reliability of the pipeline network is increased. Furthermore, reliable prognoses imply that maintenance interventions can be appropriately planned in advance and synchronised to minimise pipeline down-time.

- **Economic.** Minimised pipeline down-time boosts production, revenue and profit. Furthermore, time-based integrity assessment and maintenance become superfluous, resulting in significant savings especially because it becomes no longer necessary to routinely service pipelines that may be buried, underwater, in deserts, or in other harsh environments, and that can prove extremely costly and problematic to access.

SHM and condition-based maintenance therefore promise to make pipeline networks safer and more reliable while at the same time more productive and less costly, and their practical enablement inherently constitutes the driving motivation behind this thesis.

In this chapter, section 7.1 presents a complete review of this thesis, while section 7.2 summarises its main contributions. Finally, section 7.3 highlights areas for potential future work.

7.1 Thesis Review

The aim of this thesis has been to introduce a practical automated pipeline damage detection procedure that utilises data gathered from permanently installed guided wave sensors over time to detect and monitor damage growth in pipelines. The framework provides the software complement to permanently installed guided wave sensors, thereby providing the petrochemical industry with a complete pipeline SHM solution.

This thesis can be conceptually divided in two major parts.

In the first part of this thesis a lot of emphasis was put on the study of the fundamental mechanics of ultrasonic guided wave propagation.

Firstly, **chapter 2** introduced the principles of guided wave propagation in free pipes, discussed how these principles can be utilised to inspect pipelines, and reviewed the state-of-the-art of guided wave pipeline inspection.

Successively, **chapter 3** thoroughly investigated how guided waves propagating along a free pipe interact with simple pipe supports, a subject of particular relevance to petrochemical pipeline SHM since effective detection and characterisation of damage at pipe support locations relies on the ability to distinguish between the echoes produced by the simple supports on which an undamaged pipe is lying and the echoes produced by damage. Very little work had previously been reported on this subject.

The second part of this thesis focused entirely on the practical challenges of implementing an effective pipeline SHM solution based on permanently installed guided wave sensors.

Chapter 4 at first introduced the concept of SHM, and then thoroughly reviews its advantages, challenges and recent advances particularly in light of its utilisation for petrochemical pipelines. Successively, it introduced permanently installed guided wave sensors, highlighting the differences and advantages compared to deployable guided wave sensors, and presented the concept of baseline subtraction, through which the sensitivity to damage growth of permanently installed guided wave sensors can be greatly enhanced. Then, it discussed the fundamental problem of damage detection, showing how it is effectively a problem of change detection. In particular, it explained the challenge that variations in the Environmental and Operational Conditions (EOC) of a pipeline represent to effective baseline subtraction, to effective damage detection, and ultimately to effective SHM, thereby motivating the need to utilise advanced techniques to synthetically compensate for EOC variations. Importantly, in this chapter the formal mathematical foundations for the analysis of the effects that pipeline operating temperature variations have on the signals recorded by permanently installed guided wave sensors were laid and successively utilised firstly to introduce two techniques to synthetically compensate for EOC variations in baseline subtraction, namely the Baseline Signal Stretch (BSS) technique and the novel Localised Baseline Signal Stretch (LBSS) technique, and secondly to thoroughly analyse the side-effects that baseline subtraction compensation techniques, and in particular BSS and LBSS, might have in practical situations. Finally, this chapter illustrated the challenge of dealing with the remaining uncompensated EOC effects that will invariably feature in the measurements from any SHM sensor, hence motivating the need for advanced damage detection, and consequently change detection, strategies.

Chapter 5 thoroughly discussed the general change detection problem, introduced the concept of sequential analysis and presented the mathematical principles behind the Cumulative Sum (CUSUM) algorithm for the solution of simple change detection problems and the Generalised Likelihood Ratio (GLR) algorithm for the solution of composite change detection problems. It also discussed how the CUSUM and GLR algorithms have been mathematically proven to be capable of optimally solving change detection problems so that the required number of samples, and therefore the delay between change time and detection time, is minimised, the probability of detecting a change is maximised and the probability of false-calling a change is minimised. Finally, it exemplified step and gradual change detection in the case of a normally distributed random variable utilising the GLR algorithm.

Finally, **chapter 6** discussed and demonstrated how the concepts of baseline subtraction and baseline subtraction compensation can be combined together with the GLR change detection algorithm to introduce a practical automated pipeline damage detection procedure. Specifically, utilising experimental data from a Guided Wave Permanently-Installed Monitoring System (gPIMS®) sensor, which is a permanently installed guided wave sensor produced and commercialised by Guided Ultrasonics Ltd. [20], installed on a purpose-built NPS 8 Schedule 40 pipe loop facility at BP's Naperville Campus, it illustrated how the procedure is able to consistently ignore the uncompensated EOC effects, which will invariably feature in the measurement from any permanently installed guided wave sensors, while being very effective at detecting and quantifying actual damage, thereby achieving the intended aim of this thesis.

7.2 Main Contributions

7.2.1 The Interaction of Guided Waves with Simple Supports in Pipes

The quantitative study of the interactions between guided waves propagating along a pipe and simple supports that has been conducted in chapter 3 revealed that, independently of pipe size, all modes that can propagate along a supported section of pipe, including torsional, present a non-zero cut-off frequency. Furthermore, it has been observed that because a supported section of pipe is not an axisymmetric waveguide, all flexural modes that can propagate along it behave differently depending on their orientation.

Importantly, in chapter 3 it has been shown both experimentally and through Finite Element Analysis (FEA) simulations that the $\mathrm{T}(0,1)$ mode reflection from a simple support quickly reduces to very low values once the frequency is increased past the torsional motion cut-off, independently of pipe size, support configuration and support loading. In particular, it was shown that variations in support loading have a very limited effect on the $\mathrm{T}(0,1)$ reflection coefficient, whereas variations in support geometry can have a very significant effect. From a SHM standpoint such finding implies that when a pipeline shifts on its supports following the thermal expansion of both the pipeline, as a result of changes in operating temperature, and the supporting structure, as a result of changes in the temperature of the environment, any significant changes in the echoes from the supports are much more likely to be due to a change in the geometry of the contact patch as a result of changes in support loading rather than to changes in support loading alone.

7.2.2 Baseline Subtraction Compensation

In chapter 4 the formal mathematical foundations for analysing the effects of operating temperature variations on the signals recorded by permanently installed guided wave sensors have been laid and have been utilised to introduce the novel Localised Baseline Signal

Stretch (LBSS) technique, which is an extension of the Baseline Signal Stretch (BSS) technique already discussed by other authors [115–117, 119] designed to compensate for uniform and non-uniform operating temperature variations along a pipeline.

Furthermore, a thorough analysis has been made of the side-effects that baseline subtraction compensation procedures, and in particular BSS and LBSS, might have in practical situations. It has been proven and extensively exemplified that baseline subtraction compensation may need to be utilised with care since it is only effective when the echoes from damage growth in the recorded signals are small compared to the echoes from features and pre-existing damage. In a practical SHM application such as a permanently installed guided wave sensor monitoring a petrochemical pipeline the use of baseline subtraction compensation is therefore always advisable because the typical petrochemical damage mechanisms operate relatively slowly, and consequently the echoes from damage growth will tend to remain quite small compared to the echoes from features and pre-existing damage. Furthermore, in chapter 6 it has been shown that when damage growth is very small the use of BSS compensation can be crucial to successfully detect it even when the Environmental and Operational Conditions (EOC) are precisely controlled.

7.2.3 Damage Detection in Pipelines

In chapter 6 a practical automated pipeline damage detection procedure has been introduced and demonstrated. The proposed procedure seeks to address the detection, location and, to a partial extent, diagnosis aspects of SHM when the system under consideration is a petrochemical pipeline being monitored by a permanently installed guided wave sensor.

The proposed procedure utilises two sets of permanently installed guided wave sensor readings, one of which is called the baseline set. The baseline set is composed of permanently installed guided wave sensor readings collected while the pipeline was in its baseline state, *i.e.* in a stable health condition. Note that in its baseline state the pipeline is operative and in a known, stable health condition, whether undamaged or partially damaged, that is being ascertained through means other than the permanently installed guided wave sensor. The proposed procedure consists essentially of a three-step process.

Firstly, baseline subtraction is performed utilising the baseline set to obtain a residual signal for each of the permanently installed guided wave sensor readings, including the ones in the baseline set. The baseline subtraction compensation procedure discussed in section 4.4 is utilised to minimise the impact of EOC effects. Specifically, baseline subtraction compensation minimises the impact of any EOC effect that presents a clear trend against EOC parameters that can be inferred, such as operating temperature, environmental temperature, and others. Any uncompensated EOC effect left in the residual signal after baseline subtraction compensation is regarded as measurement noise.

Successively, under the assumption that the true response from pipeline features as well as from pre-existing damage will generally remain constant in the future unless damage grows, a linear regression model whose mean remains constant over time and whose variance represents the variation between baseline residual signals caused by uncompensated EOC effects is utilised to reconstruct a statistical model that represents the true underlying value of the damage-sensitive property, *i.e.* the residual signal, while the monitored system, *i.e.* the pipeline, remains in its baseline state. All uncompensated EOC effects left in the baseline residual signals after baseline subtraction compensation are confined to the noise term of the statistical model.

Finally, utilising the linear regression model it becomes possible to predict the likely future magnitude of variations in the residual signals caused by uncompensated EOC effects, *i.e.* the measurement noise, and therefore to structure a composite change detection problem based on the GLR algorithm at each position along a pipeline which seeks to determine the likelihood that the variations observed in the residual signals outside the baseline set and the linear process model are due to damage growth. More specifically, the GLR algorithm enables the quantification of the likelihood that the variations observed in the residual signals are false-calls for a prescribed probability of damage detection.

Importantly, because by utilising baseline subtraction compensation, and therefore by making full use of all available information about the physics of EOC effects to minimise their impact, there is no need to learn the relationships between measurable EOC parameters and EOC effects, there is also no need to have a large number of baseline samples from which to learn such relationships. In other words, while previous approaches [109, 130, 131] utilised the information contained in the baseline samples to both learn the physical models that govern the relationships between measurable EOC parameters and EOC effects and to estimate the measurement noise, the proposed procedure requires baseline samples only to estimate the measurement noise, *i.e.* the uncompensated EOC effects. As a result, the minimum number of baselines samples required by the proposed procedure to operate effectively is much reduced.

7.3 Future Work

7.3.1 The Interaction of Guided Waves with Simple Supports in Pipes

Further investigations are required to better characterise the interactions between guided waves propagating along a pipe and other, more complex types of supports, such as clamps and saddle supports. In particular, the formation of corrosion deposits at the touch points between a pipe and its supports is likely to significantly alter the mechanical and geometrical properties of the contact interface and to lead to variations in the echo from contact supports. A better characterisation of the dependence of the echo from contact supports from the presence of corrosion deposits at the contact interface could prove crucial for the early detection of touchpoint corrosion.

7.3.2 Damage Detection in Pipelines

In light of the encouraging performance of the proposed automated damage detection procedure in the test case involving experimental data from a gPIMS® sensor installed on a purpose-built NPS 8 Schedule 40 pipe loop facility at BP's Naperville Campus, it is paramount to highlight its major limitations, which can be quite subtle and which constitute very relevant topics for potential future work which might lead to the development and implementation of a complete pipeline SHM solution.

First of all, one major aspect of the proposed procedure lies in its requirement for prior knowledge about the shape of the echo produced by the damage that one seeks to detect, or in other words about its frequency content. While this requirement can be seen as a limitation, as in general it cannot be expected that prior knowledge is available about the frequency content of the echo from damage whose presence, location and morphology are unknown, it is worth noting how it could actually represent an advantage. More specifically, by being very sensitive to the frequency content of echoes, the proposed procedure is able to consistently disregard both the significant coherent noise that often manifests itself in the damage residuals as the temperature difference ΔT between baseline and damage readings increases, as well as the large echoes that are present in the damage residuals in correspondence of large, complex features such as flanges and supports. In other words, by requiring prior knowledge about the frequency content of the echo from the damage that one seeks to detect, the proposed procedure is able to consistently ignore uncompensated EOC effects.

However, as soon as the echo from the damage changes its frequency content as a result of actual damage growth, and therefore of actual changes in the damage morphology, or as a result of its interaction with the echoes from nearby features or with coherent noise, as previously exemplified and discussed, the proposed procedure becomes unable to detect it unless it is instructed to seek an echo with a different frequency content.

From a purely practical standpoint, the advantages of this major aspect of the proposed procedure could be leveraged upon by a suitable pipeline health monitoring procedure in such a way as to effectively remove its disadvantages. For example, instead of seeking echoes with one specific frequency content, a dictionary could be devised that includes several frequency content variants, after which the proposed procedure could be instructed to seek any of the variants contained in the dictionary. In this way, the proposed procedure would be just as effective at ignoring EOC effects and yet it would be more sensitive to damage in general. In a typical pipeline health monitoring application the dictionary could be devised on the basis of the echoes of the typical damage morphologies that are expected to develop in the pipeline or that are already present. In particular, if the proposed procedure is instructed to look for an echo with a specific frequency content corresponding to that of an existing patch of damage, then the moment when the procedure does not detect the damage any longer could be regarded as indication that the damage has evolved and grown significantly.

The second, very subtle limitation of the proposed procedure is that, as discussed in section 6.1, it assumes that all the samples, *i.e.* the residual signals from the permanently installed guided wave sensor readings, are statistically independent. In practice this assumption may not always hold true, and it is often the case that the residual signals from any two permanently installed guided wave sensor readings, rather than being statistically independent, present a high degree of statistical correlation, *i.e.* present very similar uncompensated EOC effects. There are very significant implications that stem from this assumption.

As previously discussed, the proposed procedure attempts to reconstruct a statistical model that represents the true underlying value of the damage-sensitive property, *i.e.* the residual signal, while the monitored system, *i.e.* the pipeline, remains in its baseline state. All uncompensated EOC effects left after baseline subtraction compensation are confined to the noise term of the statistical model. Both the statistical model and in particular its noise term are estimated from the baseline samples, *i.e.* the baseline residuals. Clearly, the assumption is that the variability observed across the baseline samples is representative of the typical variability that would be observed in general between any two samples, *i.e.* two residuals, as a result of the uncompensated EOC effects, and that therefore the noise term estimated from the baseline samples is truly representative of the uncompensated EOC effects. However, in practice this may not be the case. For example, suppose all the baseline samples have been collected during daytime from a permanently installed guided wave sensor installed in a desert location, and another sample has been collected sometime later from the same permanently installed guided wave sensor yet during nighttime. It is therefore reasonable to expect that the uncompensated EOC effects, which as discussed in chapter 4 are mostly dependent on the environmental temperature and on the operating temperature of the pipeline, that corrupt the latest sample are quite different from those that corrupt the baseline set of samples. Consequently, the utilisation as part of the proposed procedure of a statistical model derived from the baseline set of samples is likely to lead to the classification of what are effectively previously unseen uncompensated EOC effects as damage.

More generally, uncompensated EOC effects tend to be dependent on a variety of relatively slowly evolving variables and phenomena. For example, the operating temperature of a pipeline in practice tends to remain fairly stable over time because the petrochemical production processes do not change very often, and it takes a relatively long time for polymer support gaskets to creep. It follows that any two samples, *i.e.* two residuals, are in practice very likely to present some degree of correlation, and that, in particular, two samples gathered one shortly after the other will likely present a high degree of correlation, while two samples gathered one much later after the other will likely present a low degree of correlation. Because highly correlated baseline samples will contain less information about the behaviour of the uncompensated EOC effects than weakly correlated ones, it ultimately follows that a method is needed to quantify and incorporate information about sample correlation into the statistical model and ultimately into the proposed procedure so that it can automatically account for any lack of or abundance of information when examining changes over time in the residuals to calculate how likely the residuals are to contain echoes from actual damage growth. It is likely that such a method will have to leverage not only on the data from permanently installed guided wave sensor readings, but also on other data such as environmental temperature, pipeline operating temperature, support loading, and many others.

Importantly, an area with great scope for significant future work is the characterisation of sensor performance. As previously discussed in chapter 6, it is an underlying assumption of the proposed procedure that uncompensated EOC effects are equivalent to normally distributed noise with a variance that remains nominally constant across all residual signals. As discussed in chapter 4.3 and in particular in section 4, any variation in the behaviour of a permanently installed guided wave sensor, possibly as a result of changes in the operating temperature of the pipeline, can result in very significant contributions to the magnitude of the uncompensated EOC effects along the entire monitored section of pipeline. Consequently, a reliable pipeline SHM solution must explicitly take into account the behaviour of permanently installed guided wave sensors in order to produce reliable health condition assessments.

More specifically, by developing a thorough and product-specific understanding of the behaviour and limitations of different permanently installed guided wave sensors, it would not only become possible to improve their sensitivity, stability and predictability, but it would also become possible to establish an envelope in terms of EOC parameters, such as operating temperature, and baseline subtraction compensation parameters, such as stretch factor or scale, inside which they can be expected to perform satisfactorily. By also tracking EOC and baseline subtraction compensation parameters over time, a future evolution of the proposed procedure could therefore automatically detect anomalous sensor working conditions and account for sensor performance when evaluating the likelihood that the variations observed between residual signals are due to damage growth, thereby improving the effectiveness of the pipeline SHM solution as a whole.

In conclusion, in this thesis it has been shown that the proposed automated damage detection procedure has performed encouragingly well in the discussed test case, and it expected that it would perform similarly well in specialised industrial scenarios where there is good knowledge of the typical echo produced by damage. Nevertheless, it presents some limitations which will have to be addressed in future work before it can be successfully implemented widely in industrial applications. Furthermore, the proposed procedure suffers from the additional limitation of not being baseline-less, which may limit its applicability in some scenarios.

Appendices

This page has been intentionally left blank.

Appendix A

Nominal Pipe Size

Table A.1 presents a summary of common Nominal Pipe Size (NPS) dimensions utilised throughout this thesis.

Table A.1: Summary of common Nominal Pipe Size (NPS) dimensions.

NPS	outside diameter [mm]	wall thickness [mm]		
		schedule 10	schedule 40	schedule 80
1	33.40	2.769	3.378	4.547
2	60.33	2.769	3.912	5.537
3	88.90	3.048	5.486	7.620
4	114.30	3.048	6.020	8.560
5	141.30	3.404	6.553	9.525
6	168.28	3.404	7.112	10.973
8	219.08	3.759	8.179	12.700
10	273.05	4.191	9.271	15.062

Appendix B

Sequential Analysis

This appendix chapter introduces sequential analysis, which is the fundamental mathematical theory behind the proposed statistical change detection framework, and therefore damage detection framework, presented in this thesis.

Sequential analysis was formally developed at Columbia University's Statistical Research Group by Abraham Wald during World War II as a tool for more efficient industrial production quality control. Sequential analysis responded to the need for the United States Department of War to ensure that products, particularly ammunitions, were reliable to its users. The quality testing of these products was not only expensive but also destructive, as bullets can only be tested by firing. There was therefore the need for a reliable method of quality testing that required a minimal sample size.

Sequential analysis revolves around the Sequential Probability Ratio Test (SPRT), which is a sequential test to discriminate between hypotheses on the underlying probability density function of a random variable. The main advantage of the SPRT is that, unlike the Neyman-Pearson lemma of which it is a sequential reformulation, it does not require a fixed number of samples. Instead, after testing one sample the SPRT provides a framework to decide whether to stop testing and accept one of the hypotheses, or to continue testing another sample. As a result, testing often concludes with significantly fewer samples than would otherwise be possible utilising classical hypothesis testing, and consequently with lower cost. Among all tests to discriminate between hypotheses on the underlying probability density function of a random variable the SPRT has been shown [134–136] to require the least amount of samples for given probabilities of **detection** and **false-calling**. In this sense, the SPRT is said to be **optimal**.

An approach similar to sequential analysis was independently developed by Alan Turing as part of the Banburismus technique utilised at Bletchley Park to test hypotheses about whether different messages coded by German Enigma machines should be connected and analysed together. This work however remained secret until the early eighties.

B.1 Neyman-Pearson Lemma

Consider a random variable y, and consider the hypothesis $\mathbf{H}_0$ that the probability density function of y is given by $p_0(y)$ and an alternative hypothesis $\mathbf{H}_1$ that the probability density function of y is given by $p_1(y)$. The likelihood ratio

$$s = \frac{p_1(y)}{p_0(y)} \tag{B.1}$$

will then be smaller than 1 if hypothesis $\mathbf{H}_0$ is true and larger than 1 if hypothesis $\mathbf{H}_1$ is true. Equivalently, the log likelihood ratio

$$z = \ln \frac{p_1(y)}{p_0(y)} \tag{B.2}$$

will be negative if hypothesis $\mathbf{H}_0$ is true and positive if hypothesis $\mathbf{H}_1$ is true. The Neyman-Pearson lemma [137] implies that for a given amount of information, *i.e.* samples of y and probability density functions $p_0(y)$ and $p_1(y)$, the log likelihood ratio is the most powerful test to discriminate between hypotheses $\mathbf{H}_0$ and $\mathbf{H}_1$.

B.2 Sequential Probability Ratio Test

If $Y_m = \{y_1, y_2, \ldots, y_m\}$ is a finite set of samples y_i of the random variable y it follows that for any positive integer value of m the probability of obtaining the sample set Y_m is given by

$$P_0(Y_m) = \prod_{i=1}^{m} p_0(y_i) \tag{B.3}$$

if hypothesis $\mathbf{H}_0$ is true and by

$$P_1(Y_m) = \prod_{i=1}^{m} p_1(y_i) \tag{B.4}$$

if hypothesis $\mathbf{H}_1$ is true. Given two positive constants A and B such that $B < A$, at each sampling stage m the SPRT consists in evaluating the cumulative likelihood ratio [138]

$$S_m = \frac{P_1(Y_m)}{P_0(Y_m)} = \prod_{i=1}^{m} \frac{p_1(y_i)}{p_0(y_i)} = \prod_{i=1}^{m} s_i \tag{B.5}$$

Hypothesis $\mathbf{H}_1$ is accepted if $S_m \geq A$, hypothesis $\mathbf{H}_0$ is accepted if $S_m \leq B$, and sampling is continued by taking sample y_{m+1} if $B < S_m < A$. Equivalently, after evaluating the cumulative log likelihood ratio

$$Z_m = \ln \frac{P_1(Y_m)}{P_0(Y_m)} = \sum_{i=1}^{m} \ln \frac{p_1(y_i)}{p_0(y_i)} = \sum_{i=1}^{m} z_i \tag{B.6}$$

it is chosen to accept hypothesis $\mathbf{H}_1$ if $Z_m \geq \ln A$, or to accept hypothesis $\mathbf{H}_0$ if $Z_m \leq \ln B$. If $\ln B < Z_m < \ln A$ then sample y_{m+1} is collected and Z_{m+1} is evaluated for the extended sample set $Y_{m+1} = \{Y_m, y_{m+1}\}$. The SPRT will eventually terminate if samples y_i are distributed independently and identically, but otherwise it might not terminate [138]. If it terminates, the SPRT is **optimal** in the sense that it minimises the amount of samples y_i required to accept either hypothesis $\mathbf{H}_0$ or $\mathbf{H}_1$ utilising the log likelihood ratio, which for a given amount of information, *i.e.* samples y_i and probability density functions $p_0(y)$ and $p_1(y)$, is the most powerful test to discriminate between hypotheses $\mathbf{H}_0$ and $\mathbf{H}_1$ [134–137, 139].

B.3 Test Boundaries

The value of A and B can be determined so that the SPRT will have a prescribed probability α of committing an error of the first kind, and a prescribed probability β of committing an error of the second kind. An error of the first kind consists in the rejection of hypothesis $\mathbf{H}_0$ when it is true, while an error of the second kind consists in the rejection of hypothesis $\mathbf{H}_1$ when it is true. In the context of change detection hypothesis $\mathbf{H}_0$ is representative of the no change condition. Therefore, the probability α of rejecting the hypothesis $\mathbf{H}_0$ when it is true corresponds to the probability of detecting a change when there is none, *i.e.* to the probability of **false-calling**. Conversely, the probability β of rejecting hypothesis $\mathbf{H}_1$ when it is true corresponds to the probability of not detecting a change when there is one, *i.e.* to the probability of **non-detection**. It follows that $1-\beta$ represents the probability of **detection**. In practice it is very laborious to determine the exact values of A and B for prescribed values of α and β. However, they can be efficiently approximated [138]. Consider a finite sample set Y_m, and assume that its subset Y_{m-1} is such that

$$B < S_{m-1} = \frac{P_1(Y_{m-1})}{P_0(Y_{m-1})} < A \tag{B.7}$$

Sample set Y_m is said to be of type 0 if

$$S_m = \frac{P_1(Y_m)}{P_0(Y_m)} \leq B \tag{B.8}$$

i.e. if it is the smallest sample set that leads to the acceptance of the hypothesis $\mathbf{H}_0$. Conversely, sample set Y_m is said to be of type 1 if

$$S_m = \frac{P_1(Y_m)}{P_0(Y_m)} \geq A \tag{B.9}$$

i.e. if it is the smallest sample set that leads to the acceptance of the hypothesis $\mathbf{H}_1$. For any sample set Y_m of type 1, it follows from equation B.9 that the probability $P_1(Y_m)$ of obtaining such a sample set if hypothesis $\mathbf{H}_1$ was true is at least A times as large as the probability $P_0(Y_m)$ of obtaining such a sample set if hypothesis $\mathbf{H}_0$ was true. Hence, for each and every sample set Y_m of type 1 the probability that the SPRT will end with the acceptance of hypothesis $\mathbf{H}_1$ is at least A times as large as the probability that the SPRT will end with the acceptance of hypothesis $\mathbf{H}_0$. Because the probability that hypothesis $\mathbf{H}_1$ is accepted when it is false is given by α, while the probability that hypothesis $\mathbf{H}_1$ is accepted when it is true is given by $1-\beta$, it follows that

$$P_1(Y_m) = 1-\beta \geq A\alpha = AP_0(Y_m) \tag{B.10}$$

and therefore an upper limit for A will be given by

$$A \leq \frac{1-\beta}{\alpha} \tag{B.11}$$

Similarly, for any sample set Y_m of type 0, it follows from equation B.8 that the probability $P_0(Y_m)$ of obtaining such a sample set if hypothesis $\mathbf{H}_0$ were true is at least $1/B$ times as large as the probability $P_1(Y_m)$ of obtaining such a sample set if hypothesis $\mathbf{H}_1$ were true. Hence, for each and every sample set Y_m of type 0 the probability that the SPRT will end with the acceptance of hypothesis $\mathbf{H}_0$ is at least $1/B$ times as large as the probability that the SPRT will end with the acceptance of hypothesis $\mathbf{H}_1$. Because the probability that hypothesis $\mathbf{H}_0$ is accepted when it is false is given by β, while the probability that hypothesis $\mathbf{H}_0$ is accepted when it is true is given by $1-\alpha$, it follows that

$$P_0(Y_m) = 1-\alpha \geq \beta/B = P_1(Y_m)/B \tag{B.12}$$

and therefore a lower limit for B will be given by

$$B \geq \frac{\beta}{1-\alpha} \tag{B.13}$$

Under the assumption that when the SPRT ends the excess of S_m over either boundary A or B is negligible, equations B.8 and B.9 become approximate equalities, resulting in the **Wald boundaries**

$$A = \frac{1-\beta}{\alpha} \quad \text{and} \quad B = \frac{\beta}{1-\alpha} \tag{B.14}$$

A SPRT with **Wald boundaries** will have a probability equal to or smaller than α of committing an error of the first kind, *i.e.* **false-calling**, and a probability equal to or smaller than β of committing an error of the second kind, *i.e.* **non-detection** [135, 138]. It follows that such SPRT will have a **detection** probability equal to or larger than $1-\beta$.

B.4 Average Sample Number

Let m denote the number of samples y_i of the random variable y required by the SPRT to terminate, *i.e.* the minimum cardinality of Y_m required to accept either hypothesis $\mathbf{H}_0$ or $\mathbf{H}_1$. Then m is clearly a random variable. It is of interest to calculate the expected value $\mathrm{E}[m]$ of m, known as the Average Sample Number (ASN).

B.4.1 General Density

Consider a random variable y, and consider the hypothesis $\mathbf{H}_0$ that the probability density function of y is given by $p_0(y)$ and an alternative hypothesis $\mathbf{H}_1$ that the probability density function of y is given by $p_1(y)$. For a fixed positive integer M the sum

$$Z_M = \sum_{i=1}^{M} \ln \frac{p_1(y_i)}{p_0(y_i)} = \sum_{i=1}^{M} z_i \tag{B.15}$$

can be split in two parts so that

$$Z_M = \sum_{i=1}^{m} z_i + \sum_{i=m+1}^{M} z_i = Z_m + Z_{m+1}^{M} \tag{B.16}$$

Taking the expected value on both sides of equation B.16 yields

$$\mathrm{E}[Z_M] = \sum_{i=1}^{M} \mathrm{E}[z_i] = M\,\mathrm{E}[z] = \mathrm{E}\left[Z_m + Z_{m+1}^{M}\right] \tag{B.17}$$

since $\mathrm{E}[z]$ is the expected value $\mathrm{E}[z_i]$ of each z_i. If $p_{M\geq m}$ is the probability that $M \geq m$, $p_{M<m} = 1 - p_{M\geq m}$ is the probability that $M < m$, and $\mathrm{E}_{M\geq m}$ and $\mathrm{E}_{M<m}$ are the expected value operators conditioned for respectively $M \geq m$ and $M < m$, then

$$\mathrm{E}\left[Z_m + Z_{m+1}^{M}\right] = p_{M\geq m}\,\mathrm{E}_{M\geq m}\left[Z_m + Z_{m+1}^{M}\right] + p_{M<m}\,\mathrm{E}_{M<m}[Z_M] \tag{B.18}$$

Because by definition Z_M will lie between $\ln B$ and $\ln A$ when $M < m$, and because $p_{M\geq m} \to 1$ and $p_{M<m} \to 0$ for $M \to \infty$, it follows from equations B.17 and B.18 that

$$\lim_{M\to\infty} M\,\mathrm{E}[z] - p_{M\geq m}\,\mathrm{E}_{M\geq m}\left[Z_m + Z_{m+1}^{M}\right] = 0 \tag{B.19}$$

Because $p_{M<m} M \rightarrow 0$ for $M \rightarrow \infty$ [150], and because

$$\mathrm{E}_{M \geq m}\left[Z_{m+1}^{M}\right] = \mathrm{E}_{M \geq m}\left[M - m\right] \mathrm{E}\left[z\right] = \left(M - \mathrm{E}_{M \geq m}\left[m\right]\right) \mathrm{E}\left[z\right] \tag{B.20}$$

it follows from equations B.19, B.20 that

$$\lim_{M \rightarrow \infty} p_{M \geq m} \mathrm{E}_{M \geq m}\left[m\right] \mathrm{E}\left[z\right] - p_{M \geq m} \mathrm{E}_{M \geq m}\left[Z_m\right] = 0 \tag{B.21}$$

Since $p_{M \geq m} \mathrm{E}_{M \geq m}\left[m\right] \rightarrow \mathrm{E}\left[m\right]$ and $p_{M \geq m} \mathrm{E}_{M \geq m}\left[Z_m\right] \rightarrow \mathrm{E}\left[Z_m\right]$ for $M \rightarrow \infty$, equation B.21 reduces to

$$\mathrm{E}\left[Z_m\right] = \mathrm{E}\left[m\right] \mathrm{E}\left[z\right] \tag{B.22}$$

Therefore, the expected value $\mathrm{E}\left[m\right]$ of m is given by

$$\mathrm{E}\left[m\right] = \frac{\mathrm{E}\left[Z_m\right]}{\mathrm{E}\left[z\right]} \tag{B.23}$$

or, if $\mathrm{E}\left[z\right] = 0$, by [138]

$$\mathrm{E}\left[m\right] = \frac{\mathrm{E}\left[Z_m^2\right]}{\mathrm{E}\left[z^2\right]} \tag{B.24}$$

If E_0 and E_1 are the conditioned expected value operators assuming that the SPRT will terminate with the acceptance of respectively hypothesis $\mathbf{H}_0$ and $\mathbf{H}_1$, then

$$\mathrm{E}\left[Z_m\right] = L \mathrm{E}_0\left[Z_m\right] + (1 - L) \mathrm{E}_1\left[Z_m\right] \tag{B.25}$$

where L, known as the Operating Characteristic (OC), represents the probability that the SPRT will terminate with the acceptance of hypothesis $\mathbf{H}_0$, *i.e.* the probability that $Z_m \leq \ln B$, and consequently $1 - L$ represents the probability that the SPRT will terminate with the acceptance of hypothesis $\mathbf{H}_1$, *i.e.* the probability that $Z_m \geq \ln A$. Under the assumption that when the SPRT terminates the excess of Z_m over either boundary $\ln A$ or $\ln B$ is negligible, it follows that $\mathrm{E}_0\left[Z_m\right] \approx \ln B$ and $\mathrm{E}_1\left[Z_m\right] \approx \ln A$. Therefore, because of equations B.23 and B.25, it can be concluded that

$$\mathrm{E}\left[m\right] \approx \frac{L \ln B + (1 - L) \ln A}{\mathrm{E}\left[z\right]} \tag{B.26}$$

If hypothesis $\mathbf{H}_0$ is true then $L = 1 - \alpha$, while if hypothesis $\mathbf{H}_1$ is true then $L = \beta$.

B.4.2 Parameterised Density

Consider a random variable y with a probability density function $p\left(y \mid \theta\right)$ parameterised by the parameter vector θ, and consider the hypothesis $\mathbf{H}_0$ that the parameter vector θ is equal to some value θ_0 and an alternative hypothesis $\mathbf{H}_1$ that the parameter vector θ is equal to some other value $\theta_1 \neq \theta_0$. Consequently, if hypothesis $\mathbf{H}_0$ is true then the probability density function of y is given by $p\left(y \mid \theta_0\right)$, and that if hypothesis $\mathbf{H}_1$ is true then the probability density function of y is given by $p\left(y \mid \theta_1\right)$. The derivation follows closely the one described in section B.4.1, except that in this particular case it becomes possible to calculate the ASN under the assumption that the true parameter vector θ may or may not be equal to either θ_0 or θ_1. Therefore, the expected value operators $\mathrm{E}[m]$, $\mathrm{E}[Z_m]$ and $\mathrm{E}[z]$ will all become conditioned by the true parameter value θ. From equation B.23 it follows that the expected value $\mathrm{E}[m \mid \theta]$ of m under the assumption that the true parameter value is θ is given by

$$\mathrm{E}[m \mid \theta] = \frac{\mathrm{E}[Z_m \mid \theta]}{\mathrm{E}[z \mid \theta]} \tag{B.27}$$

or, if $\mathrm{E}[z \mid \theta] = 0$, by [138]

$$\mathrm{E}[m \mid \theta] = \frac{\mathrm{E}\left[Z_m^2 \mid \theta\right]}{\mathrm{E}\left[z^2 \mid \theta\right]} \tag{B.28}$$

If E_0 and E_1 are the conditioned expected value operators assuming that the SPRT will terminate with the acceptance of respectively hypothesis $\mathbf{H}_0$ and $\mathbf{H}_1$, then

$$\mathrm{E}[Z_m \mid \theta] = L(\theta)\mathrm{E}_0[Z_m] + (1 - L(\theta))\mathrm{E}_1[Z_m] \tag{B.29}$$

where the Operating Characteristic (OC) function $L(\theta)$ represents the probability that the SPRT will terminate with the acceptance of hypothesis $\mathbf{H}_0$, *i.e.* with the acceptance that the parameter vector is equal to θ_0 when it is actually equal to θ. Consequently, the function $1 - L(\theta)$ represents the probability that the SPRT will terminate with the acceptance of hypothesis $\mathbf{H}_1$, *i.e.* with the acceptance that the parameter vector is equal to θ_1 when it is actually equal to θ. It follows from equations B.27 and B.29 that

$$\mathrm{E}[m \mid \theta] \approx \frac{L(\theta)\ln B + (1 - L(\theta))\ln A}{\mathrm{E}[z \mid \theta]} \tag{B.30}$$

since $\mathrm{E}_0[Z_m] \approx \ln B$ and $\mathrm{E}_1[Z_m] \approx \ln A$ under the assumption that when the SPRT terminates the excess of Z_m over either boundary $\ln A$ or $\ln B$ is negligible.

Operating Characteristic

Given a SPRT that tests between hypotheses $\mathbf{H}_0$ and $\mathbf{H}_1$, for any true parameter value θ the Operating Characteristic (OC) function $L(\theta)$ describes the probability that the SPRT will terminate with the acceptance of hypothesis $\mathbf{H}_0$, *i.e.* with the acceptance that the parameter vector is equal to θ_0 when it is actually equal to θ. By definition, $L(\theta_0) = 1 - \alpha$ and $L(\theta_1) = \beta$.

To derive the OC function $L(\theta)$ for any value of the parameter vector θ, define $\mathbb{D}'$ as the set of points d of the complex plane $\mathbb{I}$ for which $\phi(d) = \mathrm{E}\left[e^{zd}\right]$ exists and is finite, $\mathbb{D}''$ as the set of points d of the complex plane $\mathbb{I}$ for which $\left|\phi(d)\right| \geq 1$, and finally their intersection $\mathbb{D} = \mathbb{D}' \cap \mathbb{D}''$. For every point $d \in \mathbb{D}'$

$$\mathrm{E}\left[e^{Z_m d + (Z_M - Z_m) d}\right] = \mathrm{E}\left[e^{Z_M d}\right] = \mathrm{E}\left[e^{Mzd}\right] = \mathrm{E}\left[e^{zd}\right]^M = \phi(d)^M \tag{B.31}$$

where m denotes the number of samples y_i of the random variable y required by the SPRT to terminate. If $p_{M \geq m}$ is the probability that $M \geq m$, $p_{M<m} = 1 - p_{M \geq m}$ is the probability that $M < m$, and $\mathrm{E}_{M \geq m}$ and $\mathrm{E}_{M<m}$ are the expected value operators conditioned for respectively $M \geq m$ and $M < m$, it follows that

$$p_{M \geq m}\,\mathrm{E}_{M \geq m}\left[e^{Z_m d + (Z_M - Z_m) d}\right] + p_{M<m}\,\mathrm{E}_{M<m}\left[e^{Z_M d}\right] = \phi(d)^M \tag{B.32}$$

or, since $Z_M - Z_m$ is independent of Z_m for fixed $M \geq m$, that

$$p_{M \geq m}\,\mathrm{E}_{M \geq m}\left[e^{Z_m d}\phi(d)^{M-m}\right] + p_{M<m}\,\mathrm{E}_{M<m}\left[e^{Z_M d}\right] = \phi(d)^M \tag{B.33}$$

Because $p_{M \geq m} \to 1$ and $p_{M<m} \to 0$ for $M \to \infty$, and because $\left|\mathrm{E}_{M<m}\left[e^{Z_M d}\right]\right|$ can be shown [138] to be bounded function of M, for every point $d \in \mathbb{D} = \mathbb{D}' \cap \mathbb{D}''$ it follows that

$$\lim_{M \to \infty} p_{M<m}\,\mathrm{E}_{M<m}\left[e^{Z_M d}\right] = 0 \tag{B.34}$$

and that

$$\lim_{M \to \infty} p_{M \geq m}\,\mathrm{E}_{M \geq m}\left[e^{Z_m d}\phi(d)^{M-m}\right] = \mathrm{E}\left[e^{Z_m d}\phi(d)^{M-m}\right] \tag{B.35}$$

Combining equations B.33, B.34 and B.35 results in

$$\mathrm{E}\left[e^{Z_m d}\phi(d)^{-m}\right] = 1 \tag{B.36}$$

Under the assumptions that the expected values $\mathrm{E}[z]$ and $\mathrm{E}\left[e^{zh}\right]$ of the log likelihood ratio z exist for any value of the parameter vector θ and for any real value of h, and that there exists a positive real δ such that $P(e^z < 1 - \delta) > 0$ and $P(e^z > 1 + \delta) > 0$, then for $\mathrm{E}[z] \neq 0$ it can be shown [138] that there exists exactly one real function $h(\theta) \neq 0$ of θ such that $\mathrm{E}\left[e^{zh(\theta)}\right] = 1$. Substituting $h(\theta)$ for d in equation B.36 results in

$$\mathrm{E}\left[e^{Z_m h(\theta)}\phi(h(\theta))^{-m}\right] = \mathrm{E}\left[e^{Z_m h(\theta)}\right] = \mathrm{E}\left[e^{mzh(\theta)}\right] = \mathrm{E}\left[e^{zh(\theta)}\right]^m = 1 \tag{B.37}$$

because $\phi(h(\theta)) = \mathrm{E}\left[e^{zh(\theta)}\right] = 1$. If E_0 and E_1 are the conditioned expected value operators assuming that the SPRT will terminate with the acceptance of respectively hypothesis $\mathbf{H}_0$ and $\mathbf{H}_1$, then

$$L(\theta)\mathrm{E}_0\left[e^{Z_m h(\theta)}\right] + (1 - L(\theta))\mathrm{E}_1\left[e^{Z_m h(\theta)}\right] = 1 \tag{B.38}$$

Under the assumption that when the SPRT terminates the excess of Z_m over either boundary $\ln A$ or $\ln B$ is negligible, it follows that $\mathrm{E}_0\left[Z_m\right] \approx \ln B$ and $\mathrm{E}_1\left[Z_m\right] \approx \ln A$ and therefore, after solving equation B.38 for $L(\theta)$, it can be concluded that

$$L(\theta) \approx \frac{A^{h(\theta)} - 1}{A^{h(\theta)} - B^{h(\theta)}} \tag{B.39}$$

since $\mathrm{E}_0\left[e^{Z_m h(\theta)}\right] \approx B^{h(\theta)}$ and $\mathrm{E}_1\left[e^{Z_m h(\theta)}\right] \approx A^{h(\theta)}$.

B.4.3 Normal Density

Consider a random column vector $\mathbf{y} \in \mathbb{R}^k$ with a normal probability density function

$$p\left(\mathbf{y} \mid \theta\right) = p\left(\mathbf{y} \mid \boldsymbol{\mu}, \boldsymbol{\Sigma}\right) = (2\pi)^{-k/2} \left|\boldsymbol{\Sigma}\right|^{-1/2} e^{-(\mathbf{y}-\boldsymbol{\mu})^{\top} \boldsymbol{\Sigma}^{-1} (\mathbf{y}-\boldsymbol{\mu})/2} \tag{B.40}$$

parameterised by the parameter vector $\theta = \left(\boldsymbol{\mu}, \boldsymbol{\Sigma}\right)$ composed of the mean column vector $\boldsymbol{\mu} \in \mathbb{R}^k$ and the covariance matrix $\boldsymbol{\Sigma} \in \mathbb{R}^{k \times k}$, and consider the hypothesis $\mathbf{H}_0$ that the parameter vector is equal to some value $\theta_0 = \left(\boldsymbol{\mu}_0, \boldsymbol{\Sigma}_0\right)$ and an alternative hypothesis $\mathbf{H}_1$ that the parameter vector $\theta_1 = \left(\boldsymbol{\mu}_1, \boldsymbol{\Sigma}_1\right)$ is equal to some other value $\theta_1 \neq \theta_0$. Consequently, if hypothesis $\mathbf{H}_0$ is true then the probability density function of y is given by

$$p\left(\mathbf{y} \mid \theta_0\right) = p\left(\mathbf{y} \mid \boldsymbol{\mu}_0, \boldsymbol{\Sigma}_0\right) = (2\pi)^{-k/2} \left|\boldsymbol{\Sigma}_0\right|^{-1/2} e^{-(\mathbf{y}-\boldsymbol{\mu}_0)^{\top} \boldsymbol{\Sigma}_0^{-1} (\mathbf{y}-\boldsymbol{\mu}_0)/2} \tag{B.41}$$

and if hypothesis $\mathbf{H}_1$ is true then the probability density function of y is given by

$$p\left(\mathbf{y} \mid \theta_1\right) = p\left(\mathbf{y} \mid \boldsymbol{\mu}_1, \boldsymbol{\Sigma}_1\right) = (2\pi)^{-k/2} \left|\boldsymbol{\Sigma}_1\right|^{-1/2} e^{-(\mathbf{y}-\boldsymbol{\mu}_1)^{\top} \boldsymbol{\Sigma}_1^{-1} (\mathbf{y}-\boldsymbol{\mu}_1)/2} \tag{B.42}$$

The log likelihood ratio z is therefore given by

$$z = \frac{\left|\boldsymbol{\Sigma}_0\right|^{1/2}}{\left|\boldsymbol{\Sigma}_1\right|^{1/2}} + \frac{\left(\mathbf{y}-\boldsymbol{\mu}_0\right)^{\top} \boldsymbol{\Sigma}_0^{-1} \left(\mathbf{y}-\boldsymbol{\mu}_0\right) - \left(\mathbf{y}-\boldsymbol{\mu}_1\right)^{\top} \boldsymbol{\Sigma}_1^{-1} \left(\mathbf{y}-\boldsymbol{\mu}_1\right)}{2} \tag{B.43}$$

If it is of interest to test between hypothesis $\mathbf{H}_0$ that the parameter vector is equal to some value $\theta_0 = \left(\boldsymbol{\mu}_0, \boldsymbol{\Sigma}\right)$ and hypothesis $\mathbf{H}_1$ that the parameter vector $\theta_1 = \left(\boldsymbol{\mu}_1, \boldsymbol{\Sigma}\right)$ is equal to some other value $\theta_1 \neq \theta_0$, then the probability density function of equation B.40 is parameterised by the parameter vector $\theta = \boldsymbol{\mu}$, then the log likelihood ratio z of equation B.43 reduces to

$$z = \frac{\left(\mathbf{y}-\boldsymbol{\mu}_0\right)^{\top} \boldsymbol{\Sigma}^{-1} \left(\mathbf{y}-\boldsymbol{\mu}_0\right) - \left(\mathbf{y}-\boldsymbol{\mu}_1\right)^{\top} \boldsymbol{\Sigma}^{-1} \left(\mathbf{y}-\boldsymbol{\mu}_1\right)}{2} \tag{B.44}$$

and it follows that the expected value $\mathrm{E}\left[z \mid \boldsymbol{\mu}\right]$ of z is given by

$$\mathrm{E}\left[z \mid \boldsymbol{\mu}\right] = \frac{\left(\boldsymbol{\mu}-\boldsymbol{\mu}_0\right)^{\top} \boldsymbol{\Sigma}^{-1} \left(\boldsymbol{\mu}-\boldsymbol{\mu}_0\right) - \left(\boldsymbol{\mu}-\boldsymbol{\mu}_1\right)^{\top} \boldsymbol{\Sigma}^{-1} \left(\boldsymbol{\mu}-\boldsymbol{\mu}_1\right)}{2} \tag{B.45}$$

From equation B.30, it follows that the ASN is approximated by

$$\mathrm{E}\left[m \mid \boldsymbol{\mu}\right] \approx 2\,\frac{L\left(\boldsymbol{\mu}\right)\ln B + \left(1 - L\left(\boldsymbol{\mu}\right)\right)\ln A}{\left(\boldsymbol{\mu} - \boldsymbol{\mu}_0\right)^{\top} \boldsymbol{\Sigma}^{-1}\left(\boldsymbol{\mu} - \boldsymbol{\mu}_0\right) - \left(\boldsymbol{\mu} - \boldsymbol{\mu}_1\right)^{\top} \boldsymbol{\Sigma}^{-1}\left(\boldsymbol{\mu} - \boldsymbol{\mu}_1\right)} \tag{B.46}$$

Under the assumptions that the expected values $\mathrm{E}[z]$ and $\mathrm{E}\left[e^{zh(\mu)}\right]$ of the log likelihood ratio z exist for any value of the parameter vector $\boldsymbol{\mu}$ and for any real value of $h\left(\boldsymbol{\mu}\right)$, and that there exists a positive real δ such that $P(e^z < 1 - \delta) > 0$ and $P(e^z > 1 + \delta) > 0$, then for $\mathrm{E}[z] \neq 0$ it can be shown [138] that there exists exactly one real function $h\left(\boldsymbol{\mu}\right) \neq 0$ of $\boldsymbol{\mu}$ such that $\mathrm{E}\left[e^{zh(\mu)}\right] = 1$ and it can be easily verified that

$$h\left(\boldsymbol{\mu}\right) = \frac{\left(\boldsymbol{\mu}_1 + \boldsymbol{\mu}_0 - 2\boldsymbol{\mu}\right)^{\top}\left(\boldsymbol{\mu}_1 - \boldsymbol{\mu}_0\right)}{\left\|\boldsymbol{\mu}_1 - \boldsymbol{\mu}_0\right\|^2} \tag{B.47}$$

It follow that the approximate Operating Characteristic (OC) function

$$L\left(\boldsymbol{\mu}\right) \approx \frac{A^{h(\mu)} - 1}{A^{h(\mu)} - B^{h(\mu)}} \tag{B.48}$$

of equation B.39 can be calculated.

Appendix C

Linear Regression

This appendix introduces the linear regression model [147], which has been identified in chapter 6 as the preferred method to model the behaviour of the uncompensated Environmental and Operational Conditions (EOC) effects, together with a thorough discussion on the methodology and implications of estimating such model from a given set of samples.

Let $\mathbf{y} \in \mathbb{R}^q$ be a random column vector fluctuating around an underlying column vector $\boldsymbol{\mu} \in \mathbb{R}^q$. Assume $\boldsymbol{\mu}$ is a linear function f of a matrix $\mathbf{X} \in \mathbb{R}^{q \times p}$ composed of q known row vectors $\mathbf{x}_k$ composed of independent input entries x_j

$$\boldsymbol{\mu} = f(\mathbf{X}) = \mathbf{X}\mathbf{w} \tag{C.1}$$

parameterised by the column vector $\mathbf{w} \in \mathbb{R}^p$, or explicitly

$$\begin{bmatrix} \mu_1 \\ \mu_2 \\ \vdots \\ \mu_q \end{bmatrix} = \boldsymbol{\mu} = \mathbf{X}\mathbf{w} = \begin{bmatrix} \mathbf{x}_1 \\ \mathbf{x}_2 \\ \vdots \\ \mathbf{x}_q \end{bmatrix} \begin{bmatrix} w_1 \\ w_2 \\ \vdots \\ w_p \end{bmatrix} = \begin{bmatrix} x_{1,1} w_1 + x_{1,2} w_2 + \cdots + x_{1,p} w_p \\ x_{2,1} w_1 + x_{2,2} w_2 + \cdots + x_{2,p} w_p \\ \vdots \\ x_{q,1} w_1 + x_{q,2} w_2 + \cdots + x_{q,p} w_p \end{bmatrix} \tag{C.2}$$

The random column vector $\mathbf{y}$ can then be expressed as

$$\mathbf{y} = \boldsymbol{\mu} + \boldsymbol{\epsilon} = f(\mathbf{X}) + \boldsymbol{\epsilon} = \mathbf{X}\mathbf{w} + \boldsymbol{\epsilon} \tag{C.3}$$

where the fluctuation or noise $\boldsymbol{\epsilon} \in \mathbb{R}^q$ is a zero-mean random column vector with a non-degenerate normal probability density function

$$p(\boldsymbol{\epsilon} \mid \mathbf{0}, \boldsymbol{\Psi}) = |2\pi\boldsymbol{\Psi}|^{-1/2} \exp\left(-\boldsymbol{\epsilon}^\top \boldsymbol{\Psi}^{-1} \boldsymbol{\epsilon}/2\right), \quad \boldsymbol{\epsilon} \sim \mathcal{N}(\mathbf{0}, \boldsymbol{\Psi}) \tag{C.4}$$

and symmetric positive-definite covariance matrix $\mathbf{\Psi} \in \mathbb{R}^{q\times q}$. Then by affinity $\mathbf{y}$ is also a random column vector with a non-degenerate normal probability density function

$$p\left(\mathbf{y}\,|\,\mathbf{Xw},\mathbf{\Psi}\right) = |2\pi\mathbf{\Psi}|^{-1/2}\exp\left(-\left(\mathbf{y}-\mathbf{Xw}\right)^{\top}\mathbf{\Psi}^{-1}\left(\mathbf{y}-\mathbf{Xw}\right)/2\right), \quad \mathbf{y}\sim\mathcal{N}\left(\mathbf{Xw},\mathbf{\Psi}\right) \tag{C.5}$$

since it can be easily verified [147] that

$$f:\mathbf{z}\rightarrow\mathbf{c}+\mathbf{Bz}\Longleftrightarrow\mathcal{N}\left(\boldsymbol{\mu},\mathbf{\Psi}\right)\rightarrow\mathcal{N}\left(\mathbf{c}+\mathbf{B}\boldsymbol{\mu},\mathbf{B\Psi B}^{\top}\right) \tag{C.6}$$

for any affine transformation f and any normal probability density function

$$p\left(\mathbf{z}\,|\,\boldsymbol{\mu},\mathbf{\Psi}\right) = |2\pi\mathbf{\Psi}|^{-1/2}\exp\left(-\left(\mathbf{z}-\boldsymbol{\mu}\right)^{\top}\mathbf{\Psi}^{-1}\left(\mathbf{z}-\boldsymbol{\mu}\right)/2\right), \quad z\sim\mathcal{N}\left(\boldsymbol{\mu},\mathbf{\Psi}\right) \tag{C.7}$$

with $\mathbf{c}\in\mathbb{R}^{m}$ and $\mathbf{B}\in\mathbb{R}^{m\times q}$. Also, it can easily be verified that if $\mathbf{z}_1,\mathbf{z}_2\in\mathbb{R}^{q}$ are two random column vectors with non-degenerate normal probability density functions

$$\mathbf{z}_1\sim\mathcal{N}\left(\boldsymbol{\mu}_1,\mathbf{\Psi}_1\right), \quad \mathbf{z}_2\sim\mathcal{N}\left(\boldsymbol{\mu}_2,\mathbf{\Psi}_2\right), \quad \mathbf{z}_1+\mathbf{z}_2\sim\mathcal{N}\left(\boldsymbol{\mu}_1+\boldsymbol{\mu}_2,\mathbf{\Psi}_1+\mathbf{\Psi}_2\right) \tag{C.8}$$

Finally, since $\left(\mathbf{z}-\boldsymbol{\mu}\right)^{\top}\mathbf{\Psi}^{-1}\left(\mathbf{z}-\boldsymbol{\mu}\right)$ is a scalar quantity, then

$$\begin{aligned}\left(\mathbf{z}-\boldsymbol{\mu}\right)^{\top}\mathbf{\Psi}^{-1}\left(\mathbf{z}-\boldsymbol{\mu}\right) &= \operatorname{tr}\left(\left(\mathbf{z}-\boldsymbol{\mu}\right)^{\top}\mathbf{\Psi}^{-1}\left(\mathbf{z}-\boldsymbol{\mu}\right)\right)\\ &= \operatorname{tr}\left(\left(\mathbf{z}-\boldsymbol{\mu}\right)\left(\mathbf{z}-\boldsymbol{\mu}\right)^{\top}\mathbf{\Psi}^{-1}\right)\\ &= \operatorname{tr}\left(\mathbf{\Psi}^{-1}\left(\mathbf{z}-\boldsymbol{\mu}\right)\left(\mathbf{z}-\boldsymbol{\mu}\right)^{\top}\right)\end{aligned} \tag{C.9}$$

because of the cyclic properties of the trace operator.

C.1 Samples Joint Distribution

If $\mathring{\mathbf{Y}}\in\mathbb{R}^{r}$, with $r=qb$, is a column vector of b samples $\mathbf{y}_i$ of $\mathbf{y}$ each gathered for a known input matrix $\mathbf{X}_i$ then in general they will have a joint distribution

$$\mathring{\mathbf{Y}}=\mathring{\mathbf{X}}\mathbf{w}+\mathring{\mathbf{E}}, \quad \mathring{\mathbf{Y}}\sim\mathcal{N}\left(\mathring{\mathbf{X}}\mathbf{w},\mathbf{\Sigma}\right), \quad \mathring{\mathbf{E}}\sim\mathcal{N}\left(\mathbf{0},\mathbf{\Sigma}\right) \tag{C.10}$$

or, explicitly

$$\begin{bmatrix}\mathbf{y}_1\\ \mathbf{y}_2\\ \vdots\\ \mathbf{y}_b\end{bmatrix} = \begin{bmatrix}\mathbf{X}_1\\ \mathbf{X}_2\\ \vdots\\ \mathbf{X}_b\end{bmatrix}\begin{bmatrix}w_1\\ w_2\\ \vdots\\ w_p\end{bmatrix} + \begin{bmatrix}\boldsymbol{\epsilon}_1\\ \boldsymbol{\epsilon}_2\\ \vdots\\ \boldsymbol{\epsilon}_b\end{bmatrix} \tag{C.11}$$

where $\mathring{\mathbf{X}} \in \mathbb{R}^{r\times p}$ is a matrix of b input matrices $\mathbf{X}_i$ and $\boldsymbol{\Sigma} \in \mathbb{R}^{r\times r}$ is the symmetric positive-definite covariance matrix. Because each covariance matrix $\boldsymbol{\Psi}_i$ of sample $\mathbf{y}_i$ is symmetric positive-definite, then it has a unique positive-definite square root $\boldsymbol{\Psi}_i^{1/2}$. From the spectral theorem $\boldsymbol{\Psi}_i = \mathbf{Q}_i\boldsymbol{\Lambda}_i\mathbf{Q}_i^\top$, where $\mathbf{Q}_i \in \mathbb{R}^{q\times q}$ is an orthogonal matrix and $\boldsymbol{\Lambda}_i \in \mathbb{R}^{q\times q}$ is a diagonal matrix whose entries are the eigenvalues of $\boldsymbol{\Psi}_i$. It follows that $\boldsymbol{\Psi}_i^{1/2} = \mathbf{Q}_i\boldsymbol{\Lambda}_i^{1/2}\mathbf{Q}_i^\top$ and that $\boldsymbol{\Sigma}$ can be expressed as

$$\boldsymbol{\Sigma} = \begin{bmatrix} \boldsymbol{\Psi}_1 & \rho_{2,1}\boldsymbol{\Psi}_1^{1/2}\boldsymbol{\Psi}_2^{1/2} & \cdots & \rho_{b,1}\boldsymbol{\Psi}_1^{1/2}\boldsymbol{\Psi}_b^{1/2} \\ \rho_{2,1}\boldsymbol{\Psi}_1^{1/2}\boldsymbol{\Psi}_2^{1/2} & \boldsymbol{\Psi}_2 & \cdots & \rho_{b,2}\boldsymbol{\Psi}_2^{1/2}\boldsymbol{\Psi}_b^{1/2} \\ \vdots & \vdots & \ddots & \vdots \\ \rho_{b,1}\boldsymbol{\Psi}_1^{1/2}\boldsymbol{\Psi}_b^{1/2} & \rho_{b,2}\boldsymbol{\Psi}_2^{1/2}\boldsymbol{\Psi}_b^{1/2} & \cdots & \boldsymbol{\Psi}_b \end{bmatrix} \tag{C.12}$$

where $0 \leq \rho_{i,j,i\neq j} < 1$ is the correlation coefficient between samples $\mathbf{y}_i$ and $\mathbf{y}_j$. Because the covariance matrix $\boldsymbol{\Sigma}$ is symmetric positive-definite, by the Cholesky decomposition there exists a unique lower triangular matrix $\boldsymbol{\Gamma} \in \mathbb{R}^{r\times r}$ with strictly positive diagonal entries such that $\boldsymbol{\Sigma} = \boldsymbol{\Gamma}\boldsymbol{\Gamma}^\top$. By affinity it can be easily verified that

$$\mathring{\mathbf{E}}^{\mathcal{N}} = \boldsymbol{\Gamma}^{-1}\mathring{\mathbf{E}}, \quad \mathring{\mathbf{E}}^{\mathcal{N}} \sim \mathcal{N}(\mathbf{0}, \mathbf{I}) \tag{C.13}$$

and therefore that

$$\mathring{\mathbf{Y}}^{\mathcal{N}} = \boldsymbol{\Gamma}^{-1}\mathring{\mathbf{Y}} = \boldsymbol{\Gamma}^{-1}\left(\mathring{\mathbf{X}}\mathbf{w} + \mathring{\mathbf{E}}\right) = \mathring{\mathbf{X}}^{\mathcal{N}}\mathbf{w} + \mathring{\mathbf{E}}^{\mathcal{N}}, \quad \mathring{\mathbf{Y}}^{\mathcal{N}} \sim \mathcal{N}\left(\mathring{\mathbf{X}}^{\mathcal{N}}\mathbf{w}, \mathbf{I}\right) \tag{C.14}$$

i.e. the entries of $\mathring{\mathbf{E}}^{\mathcal{N}}$ have a standard normal distribution and the entries of $\mathring{\mathbf{Y}}^{\mathcal{N}}$ are independent and normally distributed with unit variance. If the samples $\mathbf{y}_i$ are independent then $\rho_{i,j,i\neq j} = 0 \; \forall \; 1 \leq i, j \leq m$ and $\boldsymbol{\Sigma}$ reduces to

$$\boldsymbol{\Sigma} = \begin{bmatrix} \boldsymbol{\Psi}_1 & \mathbf{0} & \cdots & \mathbf{0} \\ \mathbf{0} & \boldsymbol{\Psi}_2 & \cdots & \mathbf{0} \\ \vdots & \vdots & \ddots & \vdots \\ \mathbf{0} & \mathbf{0} & \cdots & \boldsymbol{\Psi}_b \end{bmatrix} = \begin{bmatrix} \boldsymbol{\Phi}_1\boldsymbol{\Phi}_1^\top & \mathbf{0} & \cdots & \mathbf{0} \\ \mathbf{0} & \boldsymbol{\Phi}_2\boldsymbol{\Phi}_2^\top & \cdots & \mathbf{0} \\ \vdots & \vdots & \ddots & \vdots \\ \mathbf{0} & \mathbf{0} & \cdots & \boldsymbol{\Phi}_b\boldsymbol{\Phi}_b^\top \end{bmatrix} = \boldsymbol{\Gamma}\boldsymbol{\Gamma}^\top \tag{C.15}$$

and it follows that

$$\mathbf{y}_i \sim \mathcal{N}(\mathbf{X}_i\mathbf{w}, \boldsymbol{\Psi}_i), \quad \boldsymbol{\epsilon}_i \sim \mathcal{N}(\mathbf{0}, \boldsymbol{\Psi}_i) \tag{C.16}$$

and ultimately that

$$\mathbf{y}_i^{\mathcal{N}} = \boldsymbol{\Phi}_i^{-1}\mathbf{y}_i \sim \mathcal{N}\left(\boldsymbol{\Phi}_i^{-1}\mathbf{X}_i\mathbf{w}, \mathbf{I}\right), \quad \boldsymbol{\epsilon}_i^{\mathcal{N}} = \boldsymbol{\Phi}_i^{-1}\boldsymbol{\epsilon}_i \sim \mathcal{N}(\mathbf{0}, \mathbf{I}) \tag{C.17}$$

where, since each covariance matrix $\boldsymbol{\Psi}_i$ of sample $\mathbf{y}_i$ is symmetric positive-definite, $\boldsymbol{\Phi}_i \in \mathbb{R}^{q\times q}$ is the unique lower triangular matrix with strictly positive diagonal entries given by the Cholesky decomposition such that $\boldsymbol{\Psi}_i = \boldsymbol{\Phi}_i\boldsymbol{\Phi}_i^\top$.

C.2 Parameter Estimation

Assume a column vector $\mathring{\mathbf{Y}}$ of b samples $\mathbf{y}_i$ of $\mathbf{y}$ has been gathered for a matrix $\mathring{\mathbf{X}}$ of b known input matrices $\mathbf{X}_i$. It is of interest to obtain the maximum-likelihood estimate $\hat{\mathbf{w}}$ of the vector $\mathbf{w}$ that parameterises the linear model f. The maximum of the log likelihood

$$\mathscr{L}(\mathbf{w}) = \ln p\left(\mathring{\mathbf{Y}} \,|\, \mathring{\mathbf{X}}\mathbf{w}, \boldsymbol{\Sigma}\right) = -\frac{1}{2}\ln|2\pi\boldsymbol{\Sigma}| - \frac{1}{2}\left(\mathring{\mathbf{Y}} - \mathring{\mathbf{X}}\mathbf{w}\right)^\top \boldsymbol{\Sigma}^{-1}\left(\mathring{\mathbf{Y}} - \mathring{\mathbf{X}}\mathbf{w}\right) \tag{C.18}$$

will lie at the point where its first derivative [148]

$$\frac{\partial \mathscr{L}(\mathbf{w})}{\partial \mathbf{w}} = -\mathring{\mathbf{X}}^\top\boldsymbol{\Sigma}^{-1}\mathring{\mathbf{Y}} + \mathring{\mathbf{X}}^\top\boldsymbol{\Sigma}^{-1}\mathring{\mathbf{X}}\mathbf{w} \tag{C.19}$$

nullifies, from which it can be seen at once that

$$\hat{\mathbf{w}} = \boldsymbol{\Omega}\mathring{\mathbf{X}}^\top\boldsymbol{\Sigma}^{-1}\mathring{\mathbf{Y}}, \quad \boldsymbol{\Omega}^{-1} = \mathring{\mathbf{X}}^\top\boldsymbol{\Sigma}^{-1}\mathring{\mathbf{X}}, \quad \hat{\mathbf{w}} \sim \mathscr{N}(\mathbf{w}, \boldsymbol{\Omega}) \tag{C.20}$$

is the maximum-likelihood estimate of $\mathbf{w}$ given $\mathring{\mathbf{Y}}$ and $\mathring{\mathbf{X}}$, and that, by equation C.6, $\hat{\mathbf{w}}$ is a normally distributed random column vector since it is an affine transformation of $\mathring{\mathbf{Y}}$. Because the parameter vector $\mathbf{w}$ is what characterises the linear regression model f, obtaining its estimate $\hat{\mathbf{w}}$ is equivalent to fitting the linear regression model f to the data $\mathring{\mathbf{Y}}$ and $\mathring{\mathbf{X}}$. The function

$$\hat{f}(\mathbf{X}) = \mathbf{X}\hat{\mathbf{w}}, \quad \hat{f}(\mathbf{X}) \sim \mathscr{N}\left(\mathbf{X}\mathbf{w}, \mathbf{X}\boldsymbol{\Omega}\mathbf{X}^\top\right) \tag{C.21}$$

parameterised by the estimate $\hat{\mathbf{w}}$ of the parameter vector $\mathbf{w}$ therefore represents an estimate of the linear regression model f fitted to the data $\mathring{\mathbf{Y}}$ and $\mathring{\mathbf{X}}$, and it is also a normally distributed random column vector since by equation C.6 it is an affine transformation of $\hat{\mathbf{w}}$.

C.3 Parameter and Covariance Estimation

Assume a column vector $\mathring{\mathbf{Y}}$ of b samples $\mathbf{y}_i$ of $\mathbf{y}$ has been gathered for a matrix $\mathring{\mathbf{X}}$ of b known input matrices $\mathbf{X}_i$. In general neither the vector $\mathbf{w}$ that parameterises the linear model f nor the covariance matrix $\boldsymbol{\Sigma}$ that parameterises the fluctuation or noise will be known in advance, and it is therefore of interest to obtain their joint estimates $\hat{\mathbf{w}}$ and $\hat{\boldsymbol{\Sigma}}$. Regardless of the distribution of the samples $\mathbf{y}_i$, each entry of the covariance matrix $\boldsymbol{\Sigma}$ is formally defined as [147]

$$\boldsymbol{\Psi}_i = \mathrm{E}\left[\left(\mathbf{y}_i - \mathrm{E}\left[\mathbf{y}_i\right]\right)\left(\mathbf{y}_i - \mathrm{E}\left[\mathbf{y}_i\right]\right)^\top\right] \tag{C.22}$$

$$\rho_{i,j}\boldsymbol{\Psi}_i^{1/2}\boldsymbol{\Psi}_j^{1/2} = \mathrm{E}\left[\left(\mathbf{y}_i - \mathrm{E}\left[\mathbf{y}_i\right]\right)\left(\mathbf{y}_j - \mathrm{E}\left[\mathbf{y}_j\right]\right)^\top\right] \tag{C.23}$$

Unless there is prior knowledge about the true distribution $p\left(\mathbf{y}_i \mid \mathbf{X}_i\mathbf{w}, \boldsymbol{\epsilon}_i\right)$ of each sample $\mathbf{y}_i$ it is not possible to evaluate the above expressions and estimate the covariance matrix $\boldsymbol{\Sigma}$ of the joint distribution of the b samples $\mathbf{y}_i$ of $\mathbf{y}$, since by definition given just one sample of a random column vector it is not possible to obtain a reliable estimate of its distribution. However, under the assumption that all b samples $\mathbf{y}_i$ of $\mathbf{y}$ are independent and identically distributed with a non-degenerate normal probability density function and covariance matrix $\boldsymbol{\Psi}$, then $\boldsymbol{\Psi}_i = \boldsymbol{\Psi}_j = \boldsymbol{\Psi}\ \forall\ 1 \leq i, j \leq b$, and the estimate of the covariance matrix

$$\boldsymbol{\Psi} = \mathrm{E}\left[\left(\mathbf{y}_i - \mathrm{E}\left[\mathbf{y}_i\right]\right)\left(\mathbf{y}_i - \mathrm{E}\left[\mathbf{y}_i\right]\right)^\top\right] = \mathrm{E}\left[\left(\mathbf{y} - \mathrm{E}\left[\mathbf{y}\right]\right)\left(\mathbf{y} - \mathrm{E}\left[\mathbf{y}\right]\right)^\top\right] \tag{C.24}$$

is by definition given by

$$\hat{\boldsymbol{\Psi}} = \frac{1}{b}\sum_{i=1}^{b}\left(\mathbf{y}_i - \mathrm{E}\left[\mathbf{y}\right]\right)\left(\mathbf{y}_i - \mathrm{E}\left[\mathbf{y}\right]\right)^\top, \quad \mathrm{E}\left[\mathbf{y}\right] = \frac{1}{b}\sum_{i=1}^{b}\mathbf{y}_i \tag{C.25}$$

regardless of the actual distribution of the samples so long as they are independent and identically distributed [147]. If the samples $\mathbf{y}_i$ are normally distributed it is easy to see that $\hat{\boldsymbol{\Psi}}$ is also the maximum-likelihood estimate of $\boldsymbol{\Psi}$. The log likelihood

$$\mathscr{L}\left(\mathbf{w}, \boldsymbol{\Psi}\right) = \ln p\left(\mathring{\mathbf{Y}} \mid \mathring{\mathbf{X}}\mathbf{w}, \boldsymbol{\Sigma}\right) = -\frac{b}{2}\ln\left|2\pi\boldsymbol{\Psi}\right| - \frac{1}{2}\sum_{i=1}^{b}\left(\mathbf{y}_i - \mathbf{X}_i\mathbf{w}\right)^\top\boldsymbol{\Psi}^{-1}\left(\mathbf{y}_i - \mathbf{X}_i\mathbf{w}\right) \tag{C.26}$$

will reach its maximum when its first derivatives [148]

$$\frac{\partial\mathscr{L}\left(\mathbf{w}, \boldsymbol{\Psi}\right)}{\partial\mathbf{w}} = -\sum_{i=1}^{b}\mathbf{X}_i^\top\boldsymbol{\Psi}^{-1}\mathbf{y}_i - \sum_{i=1}^{b}\mathbf{X}_i^\top\boldsymbol{\Psi}^{-1}\mathbf{X}_i\mathbf{w} \tag{C.27}$$

$$\frac{\partial\mathscr{L}\left(\mathbf{w}, \boldsymbol{\Psi}\right)}{\partial\boldsymbol{\Psi}} = -\frac{b}{2}\boldsymbol{\Psi}^{-1} + \frac{1}{2}\boldsymbol{\Psi}^{-1}\sum_{i=1}^{b}\left(\mathbf{y}_i - \mathbf{X}_i\mathbf{w}\right)\left(\mathbf{y}_i - \mathbf{X}_i\mathbf{w}\right)^\top\boldsymbol{\Psi}^{-1} \tag{C.28}$$

nullify. Given the data $\mathring{\mathbf{Y}}$ and $\mathring{\mathbf{X}}$, it follows at once that for known $\boldsymbol{\Psi}$, the maximum-likelihood estimate $\hat{\mathbf{w}}$ of the parameter vector $\mathbf{w}$ is

$$\hat{\mathbf{w}} = \boldsymbol{\Omega}\sum_{i=1}^{b}\mathbf{X}_i^\top\boldsymbol{\Psi}^{-1}\mathbf{y}_i, \quad \boldsymbol{\Omega}^{-1} = \sum_{i=1}^{b}\mathbf{X}_i^\top\boldsymbol{\Psi}^{-1}\mathbf{X}_i, \quad \hat{\mathbf{w}} \sim \mathscr{N}\left(\mathbf{w}, \boldsymbol{\Omega}\right) \tag{C.29}$$

as shown in section C.2, and that for known $\mathbf{w}$, the maximum-likelihood estimate $\hat{\boldsymbol{\Psi}}$ of the covariance matrix $\boldsymbol{\Psi}$ is

$$\hat{\boldsymbol{\Psi}} = \frac{1}{b}\sum_{i=1}^{b}\left(\mathbf{y}_i - \mathbf{X}_i\mathbf{w}\right)\left(\mathbf{y}_i - \mathbf{X}_i\mathbf{w}\right)^\top, \quad \hat{\boldsymbol{\Psi}} \sim \mathscr{W}_b\left(\boldsymbol{\Psi}/b\right) \tag{C.30}$$

which is equivalent to the formulation in equation C.25 since equation C.3 dictates that $\mathrm{E}\left[\mathbf{y}\right] = \mathbf{X}_i\mathbf{w}$. The estimate $\hat{\boldsymbol{\Psi}}$ is a random matrix with a Wishart probability density function with b degrees of freedom and mean $\mathbf{\Psi}$ because, by the definition of the Wishart distribution, the scatter matrix

$$\mathbf{S}=\sum_{i=1}^{b}\boldsymbol{\epsilon}_i\boldsymbol{\epsilon}_i^{\top}=\sum_{i=1}^{b}\left(\mathbf{y}_i-\mathbf{X}_i\mathbf{w}\right)\left(\mathbf{y}_i-\mathbf{X}_i\mathbf{w}\right)^{\top},\quad \mathbf{y}_i\sim\mathcal{N}\left(\mathbf{X}_i\mathbf{w},\mathbf{\Psi}\right),\quad \boldsymbol{\epsilon}_i\sim\mathcal{N}\left(\mathbf{0},\mathbf{\Psi}\right) \tag{C.31}$$

has a Wishart probability density function

$$p\left(\mathbf{S}\mid\mathbf{\Psi}\right)=\frac{|\mathbf{\Psi}|^{-b/2}}{2^{kb/2}\Gamma_k\left(b/2\right)}|\mathbf{S}|^{(b-q-1)/2}\exp\left(-\operatorname{tr}\left(\mathbf{\Psi}^{-1}\mathbf{S}\right)/2\right),\quad \mathbf{S}\sim\mathscr{W}_b\left(\mathbf{\Psi}\right) \tag{C.32}$$

with b degrees of freedom and mean $b\mathbf{\Psi}$ [147]. Equivalently, the inverse scatter matrix $\mathbf{S}^{-1}$ has an inverse Wishart probability density function

$$p\left(\mathbf{S}^{-1}\mid\mathbf{\Psi}^{-1}\right)=\frac{|\mathbf{\Psi}|^{b/2}}{2^{kb/2}\Gamma_k\left(b/2\right)}\left|\mathbf{S}^{-1}\right|^{(-b-q-1)/2}\exp\left(-\operatorname{tr}\left(\mathbf{\Psi}\mathbf{S}^{-1}\right)/2\right),\quad \mathbf{S}^{-1}\sim\mathscr{W}_b^{-1}\left(\mathbf{\Psi}^{-1}\right) \tag{C.33}$$

with

$$\Gamma_k\left(n\right)=\pi^{k(k-1)/4}\prod_{i=1}^{k}\Gamma\left(n+\left(1-i\right)/2\right) \tag{C.34}$$

It can be easily verified from the definitions of the Wishart and inverse-Wishart distributions that for any matrix $\mathbf{A}\in\Re^{k\times x}$

$$\mathbf{\Psi}\rightarrow\mathbf{A}^{\top}\mathbf{\Psi}\,\mathbf{A}\Longleftrightarrow\mathscr{W}_b\left(\mathbf{\Psi}/b\right)\rightarrow\mathscr{W}_b\left(\mathbf{A}^{\top}\mathbf{\Psi}\,\mathbf{A}/b\right) \tag{C.35}$$

It follows that

$$\hat{\mathbf{\Omega}}^{-1}=\sum_{i=1}^{b}\mathbf{X}_i^{\top}\hat{\mathbf{\Psi}}^{-1}\mathbf{X}_i\sim\mathscr{W}_b^{-1}\left(b\sum_{i=1}^{b}\mathbf{X}_i^{\top}\mathbf{\Psi}^{-1}\mathbf{X}_i\right)=\mathscr{W}_b^{-1}\left(b\mathbf{\Omega}^{-1}\right) \tag{C.36}$$

or equivalently

$$\hat{\mathbf{\Omega}}\sim\mathscr{W}_b\left(\mathbf{\Omega}/b\right) \tag{C.37}$$

If both $\mathbf{w}$ and $\mathbf{\Psi}$ are unknown then the joint distribution of their estimates $\hat{\mathbf{w}}$ and $\hat{\mathbf{\Psi}}$ will be given by the normal-Wishart distribution

$$\left(\hat{\mathbf{w}},\hat{\mathbf{\Psi}}\right)\sim\mathcal{N}\mathscr{W}_b\left(\mathbf{w},\mathbf{\Psi}\right)=\mathcal{N}\left(\mathbf{w},\mathbf{\Omega}\right)\mathscr{W}_b\left(\mathbf{\Psi}/b\right) \tag{C.38}$$

The conditional distribution $p\left(\hat{\mathbf{w}}\mid\mathbf{\Psi}\right)$ of $\hat{\mathbf{w}}$ given $\mathbf{\Psi}$, and therefore given $\mathbf{\Omega}$, is the normal distribution

$$p\left(\hat{\mathbf{w}}\mid\mathbf{\Psi}\right)=\mathcal{N}\left(\mathbf{w},\mathbf{\Omega}\right) \tag{C.39}$$

of equation C.29, while the marginal distribution of $p\left(\hat{\mathbf{\Psi}}\right)$ of $\hat{\mathbf{\Psi}}$ over all values of $\hat{\mathbf{w}}$ is the Wishart distribution of equation C.30 since

$$\begin{aligned} p\left(\hat{\mathbf{\Psi}}\right) &= \int p\left(\hat{\mathbf{w}} \,|\, \hat{\mathbf{\Psi}}\right) p\left(\hat{\mathbf{\Psi}}\right) \mathrm{d}\hat{\mathbf{w}} \\ &= p\left(\hat{\mathbf{\Psi}}\right) \int p\left(\hat{\mathbf{w}} \,|\, \hat{\mathbf{\Psi}}\right) \mathrm{d}\hat{\mathbf{w}} \\ &= p\left(\hat{\mathbf{\Psi}}\right) \\ &= \mathscr{W}_b\left(\mathbf{\Psi}/b\right) \end{aligned} \tag{C.40}$$

because the integral of a probability density function over all variable values is equal to unity regardless of the value of any of its parameters. Similarly, the joint distribution of the estimates $\hat{\mathbf{w}}$ and $\hat{\mathbf{\Omega}}$ of $\mathbf{w}$ and $\mathbf{\Omega}$ will be given by the normal-Wishart distribution

$$\left(\hat{\mathbf{w}}, \hat{\mathbf{\Omega}}\right) \sim \mathscr{N}\mathscr{W}_b\left(\mathbf{w}, \mathbf{\Omega}\right) = \mathscr{N}\left(\mathbf{w}, \mathbf{\Omega}\right) \mathscr{W}_b\left(\mathbf{\Omega}/b\right) \tag{C.41}$$

The conditional distribution $p\left(\hat{\mathbf{w}} \,|\, \mathbf{\Omega}\right)$ of $\hat{\mathbf{w}}$ given $\mathbf{\Omega}$ is the normal distribution

$$p\left(\hat{\mathbf{w}} \,|\, \mathbf{\Omega}\right) = \mathscr{N}\left(\mathbf{w}, \mathbf{\Omega}\right) \tag{C.42}$$

of equation C.29, while the marginal distribution of $p\left(\hat{\mathbf{\Omega}}\right)$ of $\hat{\mathbf{\Omega}}$ over all values of $\hat{\mathbf{w}}$ is the Wishart distribution of equation C.37 since

$$\begin{aligned} p\left(\hat{\mathbf{\Omega}}\right) &= \int p\left(\hat{\mathbf{w}} \,|\, \hat{\mathbf{\Omega}}\right) p\left(\hat{\mathbf{\Omega}}\right) \mathrm{d}\hat{\mathbf{w}} \\ &= p\left(\hat{\mathbf{\Omega}}\right) \int p\left(\hat{\mathbf{w}} \,|\, \hat{\mathbf{\Omega}}\right) \mathrm{d}\hat{\mathbf{w}} \\ &= p\left(\hat{\mathbf{\Omega}}\right) \\ &= \mathscr{W}_b\left(\mathbf{\Omega}/b\right) \end{aligned} \tag{C.43}$$

because the integral of a probability density function over all variable values is equal to unity regardless of the value of any of its parameters. Equation C.41 can be written as

$$\begin{aligned} p\left(\hat{\mathbf{w}} \,|\, \hat{\mathbf{\Omega}}\right) p\left(\hat{\mathbf{\Omega}}\right) = {} & (2\pi)^{-p/2} \left|\hat{\mathbf{\Omega}}\right|^{-1/2} \exp\left(-(\hat{\mathbf{w}} - \mathbf{w})^\top \hat{\mathbf{\Omega}}^{-1} (\hat{\mathbf{w}} - \mathbf{w})/2\right) \\ & \frac{\left|b\mathbf{\Omega}^{-1}\right|^{1/2}}{2^{pb/2}\Gamma_p(b/2)} \left|\hat{\mathbf{\Omega}}^{-1}\right|^{(-b-p-1)/2} \exp\left(-\operatorname{tr}\left(b\mathbf{\Omega}^{-1}\hat{\mathbf{\Omega}}\right)/2\right) \end{aligned} \tag{C.44}$$

or, after some manipulation

$$\begin{aligned} p\left(\hat{\mathbf{w}} \,|\, \hat{\mathbf{\Omega}}\right) p\left(\hat{\mathbf{\Omega}}\right) = {} & \frac{\left|b\mathbf{\Omega}^{-1}\right|^{1/2}}{2^{p(b+1)/2}\pi^{p/2}\Gamma_p(b/2)} \\ & \left|\hat{\mathbf{\Omega}}^{-1}\right|^{(-b-p)/2} \exp\left(-\operatorname{tr}\left(\left(b\mathbf{\Omega} + (\hat{\mathbf{w}} - \mathbf{w})(\hat{\mathbf{w}} - \mathbf{w})^\top\right) \hat{\mathbf{\Omega}}^{-1}\right)/2\right) \end{aligned} \tag{C.45}$$

Then, the marginal distribution of $p(\hat{\mathbf{w}})$ of $\hat{\mathbf{w}}$ over all values of $\hat{\boldsymbol{\Omega}}$ is given by [148]

$$\begin{aligned} p(\hat{\mathbf{w}}) &= \int p\left(\hat{\mathbf{w}} \mid \hat{\boldsymbol{\Omega}}\right) p\left(\hat{\boldsymbol{\Omega}}\right) \mathrm{d}\hat{\boldsymbol{\Omega}} \\ &\propto \int \left|\hat{\boldsymbol{\Omega}}^{-1}\right|^{(-b-p)/2} \exp\left(-\operatorname{tr}\left(\left(b\boldsymbol{\Omega} + (\hat{\mathbf{w}} - \mathbf{w})(\hat{\mathbf{w}} - \mathbf{w})^{\top}\right)\hat{\boldsymbol{\Omega}}^{-1}\right)/2\right) \mathrm{d}\hat{\boldsymbol{\Omega}} \\ &\propto \left|b\boldsymbol{\Omega} + (\hat{\mathbf{w}} - \mathbf{w})(\hat{\mathbf{w}} - \mathbf{w})^{\top}\right|^{(-b-p)/2} \\ &\propto \left(1 + (\hat{\mathbf{w}} - \mathbf{w})\boldsymbol{\Omega}^{-1}(\hat{\mathbf{w}} - \mathbf{w})^{\top}/b\right)^{(-b-p)/2} \end{aligned} \tag{C.46}$$

since the theory of determinants shows that for any square matrix $\mathbf{A} \in \Re^{k\times k}$ and column vector $\mathbf{v} \in \Re^{k}$

$$\left|\mathbf{A} + \mathbf{v}\mathbf{v}^{\top}\right| = |\mathbf{A}|\left(1 + \mathbf{v}\mathbf{A}^{-1}\mathbf{v}^{\top}\right) \tag{C.47}$$

from which it can be concluded that the estimate $\hat{\mathbf{w}}$ of the parameter vector $\mathbf{w}$ is a random column vector with a t probability density function with b degrees of freedom

$$p(\hat{\mathbf{w}}) = \frac{\Gamma_p\left((b+p)/2\right)}{\Gamma_p(b/2)(b\pi)^{p/2}|\boldsymbol{\Omega}|^{1/2}}\left(1 + (\hat{\mathbf{w}} - \mathbf{w})^{\top}\boldsymbol{\Omega}^{-1}(\hat{\mathbf{w}} - \mathbf{w})/b\right)^{(-b-p)/2}, \quad \hat{\mathbf{w}} \sim \mathscr{T}_b(\mathbf{w}, \boldsymbol{\Omega}) \tag{C.48}$$

Practical estimates $\hat{\mathbf{w}}$, $\hat{\boldsymbol{\Psi}}$ and $\hat{\boldsymbol{\Omega}}$ of respectively $\mathbf{w}$, $\boldsymbol{\Psi}$ and $\boldsymbol{\Omega}$ can be obtained by iterating

$$\hat{\boldsymbol{\Psi}}_n = \frac{1}{b}\sum_{i=1}^{b}\left(\mathbf{y}_i - \mathbf{X}_i\hat{\mathbf{w}}_{n-1}\right)\left(\mathbf{y}_i - \mathbf{X}_i\hat{\mathbf{w}}_{n-1}\right)^{\top}, \quad \boldsymbol{\Psi}_0 = \mathbf{I} \tag{C.49}$$

with

$$\hat{\mathbf{w}}_{n-1} = \hat{\boldsymbol{\Omega}}_{n-1}\sum_{i=1}^{b}\mathbf{X}_i^{\top}\hat{\boldsymbol{\Psi}}_{n-1}^{-1}\mathbf{y}_i \tag{C.50}$$

and

$$\hat{\boldsymbol{\Omega}}_{n-1} = \left(\sum_{i=1}^{b}\mathbf{X}_i^{\top}\hat{\boldsymbol{\Psi}}_{n-1}^{-1}\mathbf{X}_i\right)^{-1} \tag{C.51}$$

until a satisfactory convergence has been reached.

Because the parameter vector $\mathbf{w}$ is what characterises the linear regression model f, obtaining an estimate $\hat{\mathbf{w}}$ is equivalent to fitting the linear regression model f to the data $\mathring{\mathbf{Y}}$ and $\mathring{\mathbf{X}}$. The function

$$\hat{f}(\mathbf{X}) = \mathbf{X}\hat{\mathbf{w}}, \quad \hat{f}(\mathbf{X}) \sim \mathscr{N}\left(\mathbf{X}\mathbf{w}, \mathbf{X}\boldsymbol{\Omega}\mathbf{X}^{\top}\right) = \mathscr{N}\left(f(\mathbf{X}), \boldsymbol{\Theta}\right) \tag{C.52}$$

parameterised by the estimate $\hat{\mathbf{w}}$ of the parameter vector $\mathbf{w}$ therefore represents an estimate of the linear regression model f fitted to the data $\mathring{\mathbf{Y}}$ and $\mathring{\mathbf{X}}$, and for known $\boldsymbol{\Psi}$, and therefore known $\mathbf{\Omega}$ and $\mathbf{\Theta}$, it is also a normally distributed random column vector since it is an affine transformation of $\hat{\mathbf{w}}$, with symmetric covariance matrix

$$\mathbf{\Theta} = \mathbf{X\Omega X}^\top = \mathbf{X\Omega}^\top\mathbf{X}^\top = \left(\mathbf{X\Omega X}^\top\right)^\top = \mathbf{\Theta}^{-\top} \tag{C.53}$$

If $\hat{\mathbf{\Theta}}$ is an estimate of $\mathbf{\Theta}$, then from the properties of the Wishart distribution

$$\hat{\mathbf{\Theta}} = \mathbf{X}\hat{\mathbf{\Omega}}\mathbf{X}^\top \sim \mathscr{W}_b\left(\mathbf{X\Omega X}^\top/b\right) = \mathscr{W}_b\left(\mathbf{\Theta}/b\right) \tag{C.54}$$

The joint distribution of the estimates $\hat{f}$ and $\hat{\mathbf{\Theta}}$ of f and $\mathbf{\Theta}$ will be given by the normal-Wishart distribution

$$\left(\hat{f},\hat{\mathbf{\Theta}}\right) \sim \mathscr{N}\mathscr{W}_b\left(f,\mathbf{\Theta}\right) = \mathscr{N}\left(f,\mathbf{\Theta}\right)\mathscr{W}_b\left(\mathbf{\Theta}/b\right) \tag{C.55}$$

The conditional distribution $p\left(\hat{f}\,|\,\mathbf{\Theta}\right)$ of $\hat{f}$ given $\mathbf{\Theta}$ is the normal distribution

$$p\left(\hat{f}\,|\,\mathbf{\Theta}\right) = \mathscr{N}\left(f,\mathbf{\Theta}\right) \tag{C.56}$$

of equation C.52, while the marginal distribution of $p\left(\hat{\mathbf{\Theta}}\right)$ of $\hat{\mathbf{\Theta}}$ over all values of $\hat{f}$ is the Wishart distribution of equation C.54 since

$$\begin{aligned} p\left(\hat{\mathbf{\Theta}}\right) &= \int p\left(\hat{f}\,|\,\hat{\mathbf{\Theta}}\right) p\left(\hat{\mathbf{\Theta}}\right)\,\mathrm{d}\hat{f} \\ &= p\left(\hat{\mathbf{\Theta}}\right)\int p\left(\hat{f}\,|\,\hat{\mathbf{\Theta}}\right)\,\mathrm{d}\hat{f} \\ &= p\left(\hat{\mathbf{\Theta}}\right) \\ &= \mathscr{W}_b\left(\mathbf{\Theta}/b\right) \end{aligned} \tag{C.57}$$

because the integral of a probability density function over all variable values is equal to unity regardless of the value of any of its parameters. After some manipulation, equation C.55 can be written as

$$\begin{aligned} p\left(\hat{f}\,|\,\hat{\mathbf{\Theta}}\right) p\left(\hat{\mathbf{\Theta}}\right) = {} & \frac{\left|b\mathbf{\Theta}^{-1}\right|^{1/2}}{2^{q(b+1)/2}\pi^{q/2}\Gamma_q\left(b/2\right)} \\ & \left|\hat{\mathbf{\Theta}}^{-1}\right|^{(-b-q)/2} \exp\left(-\operatorname{tr}\left(\left(b\mathbf{\Theta} + \left(\hat{f}-f\right)\left(\hat{f}-f\right)^\top\right)\hat{\mathbf{\Theta}}^{-1}\right)/2\right) \end{aligned} \tag{C.58}$$

Then, the marginal distribution of $p\left(\hat{f}\right)$ of $\hat{f}$ over all values of $\hat{\mathbf{\Theta}}$ is given by [148]

$$\begin{aligned} p\left(\hat{f}\right) &= \int p\left(\hat{f}\,|\,\hat{\mathbf{\Theta}}\right) p\left(\hat{\mathbf{\Theta}}\right)\,\mathrm{d}\hat{\mathbf{\Theta}} \\ &\propto \int \left|\hat{\mathbf{\Theta}}^{-1}\right|^{(-b-q)/2} \exp\left(-\operatorname{tr}\left(\left(b\mathbf{\Theta} + \left(\hat{f}-f\right)\left(\hat{f}-f\right)^\top\right)\hat{\mathbf{\Theta}}^{-1}\right)/2\right)\,\mathrm{d}\hat{\mathbf{\Theta}} \\ &\propto \left|b\mathbf{\Theta} + \left(\hat{f}-f\right)\left(\hat{f}-f\right)^\top\right|^{(-b-q)/2} \\ &\propto \left(1 + \left(\hat{f}-f\right)\mathbf{\Theta}^{-1}\left(\hat{f}-f\right)^\top/b\right)^{(-b-q)/2} \end{aligned} \tag{C.59}$$

from which it can be concluded at once that the function

$$\hat{f}(\mathbf{X}) = \mathbf{X}\hat{\mathbf{w}}, \quad \hat{f}(\mathbf{X}) \sim \mathscr{T}_b\left(\mathbf{X}\mathbf{w}, \mathbf{X}\boldsymbol{\Omega}\mathbf{X}^\top\right) = \mathscr{T}_b\left(f(\mathbf{X}), \boldsymbol{\Theta}\right) \tag{C.60}$$

parameterised by the estimate $\hat{\mathbf{w}}$ of the parameter vector $\mathbf{w}$ that represents an estimate of the linear regression model f fitted to the data $\mathring{\mathbf{Y}}$ and $\mathring{\mathbf{X}}$ is also a random column vector with a t probability density function with b degrees of freedom.

References

[1] C. R. Farrar and K. Worden, "An introduction to structural health monitoring," *Phil. Trans. R. Soc. A*, vol. 365, p. 303, 2007.

[2] K. Worden, C. R. Farrar, G. Manson, and G. Park, "The fundamental axioms of structural health monitoring," *Proc. R. Soc. A*, vol. 463, p. 1639, 2007.

[3] F. I. Khan and M. M. Haddara, "Risk-based maintenance (rbm): a quantitative approach for maintenance/inspection scheduling and planning," *J. Loss Prevent. Proc.*, vol. 16, p. 561, 2003.

[4] D. N. Alleyne, M. J. S. Lowe, and P. Cawley, "The reflection of guided waves from circumferential notches in pipes," *J. Appl. Mech.*, vol. 65, p. 635, 1998.

[5] H. Bai, A. Shah, N. Popplewell, and S. Datta, "Scattering of guided waves by circumferential cracks in steel pipes," *J. Appl. Mech.*, vol. 68, p. 619, 2001.

[6] P. Cawley, M. J. S. Lowe, F. Simonetti, C. Chevalier, and A. G. Roosenbrand, "The variation of the reflection coefficient of extensional guided waves in pipes from defects as a function of defect depth, axial extent, circumferential extent and frequency," in *Proc. IME C J. Mech. Eng. Sci.*, vol. 216, p. 1131, 2002.

[7] Y. M. Cheong, D. H. Lee, and H. K. Jung, "Ultrasonic guided wave parameters for detection of axial cracks in feeder pipes of phwr nuclear power plants," *Ultrasonics*, vol. 42, p. 883, 2004.

[8] A. Demma, P. Cawley, M. J. S. Lowe, and B. Pavlakovic, "The effect of bends on the propagation of guided waves in pipes," *Trans. Am. Soc. Mech. Eng.*, vol. 127, p. 328, 2005.

[9] A. Demma, P. Cawley, M. J. S. Lowe, and A. G. Roosenbrand, "The reflection of the fundamental torsional mode from cracks and notches in pipes," *J. Acoust. Soc. Am.*, vol. 114, p. 611, 2003.

[10] J. J. Ditri, “Utilization of guided elastic waves for the characterization of circumferential cracks in hollow cylinders,” *J. Acoust. Soc. Am.*, vol. 96, p. 3769, 1994.

[11] H. E. Engan, “Torsional wave scattering from a diameter step in a rod,” *J. Acoust. Soc. Am.*, vol. 104, p. 2015, 1998.

[12] Z. Liu, C. He, B. Wu, X. Wang, and S. Yang, “Circumferential and longitudinal defect detection using t(0,1) mode excited by thickness shear mode piezoelectric elements,” *Ultrasonics*, vol. 44, p. 1135, 2006.

[13] M. J. S. Lowe, D. N. Alleyne, and P. Cawley, “The mode conversion of a guided wave by a part-circumferential notch in a pipe,” *J. Appl. Mech.*, vol. 65, p. 649, 1998.

[14] W. Luo, X. G. Zhao, and J. Rose, “A guided wave plate experiment for a pipe,” *J. Press. Vess. Technol.*, vol. 127, p. 345, 2005.

[15] J. Rose, “A baseline and vision of ultrasonic guided wave inspection potential,” *J. Press. Vess. Technol.*, vol. 124, p. 273, 2002.

[16] M. G. Silk and K. F. Bainton, “The propagation in metal tubing of ultrasonic wave modes equivalent to lamb waves,” *Ultrasonics*, vol. 17, p. 11, 1979.

[17] X. G. Zhao and J. Rose, “Boundary element modeling for defect characterization potential in a wave guide,” *Int. J. Solids. Struct.*, vol. 40, p. 2645, 2003.

[18] W. Zhu, “An fem simulation for guided elastic wave generation and reflection in hollow cylinders with corrosion defects,” *J. Press. Vess. Technol.*, vol. 124, p. 108, 2002.

[19] W. Zhuang, A. Shah, and S. Datta, “Axisymmetric guided wave scattering by cracks in welded steel pipes,” *J. Press. Vess. Technol.*, vol. 119, p. 401, 1997.

[20] Guided Ultrasonics Ltd., “gPIMS® Sensors,” 2013. url: `http://www.guided-ultrasonics.com/public2013/?page_id=922`.

[21] W. Mohr and P. H. Höller, “On inspection of thin-walled tubes for transverse and longitudinal flaws by guided ultrasonic waves,” *IEEE Trans. Sonics Ultrason.*, vol. 23, p. 369, 1976.

[22] R. B. Thompson, G. A. Alers, and M. A. Tennison, “Application of direct electromagnetic lamb wave generation to gas pipeline inspection,” in *Ultrasonics Symposium*, p. 91, 1972.

[23] P. Cawley, “Practical long-range guided wave inspection - managing complexity,” in *Review of Progress in QNDE*, vol. 22, p. 22, 2003.

[24] D. N. Alleyne and P. Cawley, “The excitation of lamb waves in pipes using dry-coupled piezoelectric transducers,” *J. Nondestr. Eval.*, vol. 15, p. 11, 1996.

[25] P. D. Wilcox, “A rapid signal processing technique to remove the effect of dispersion from guided wave signals,” *IEEE Trans. Ultrason., Ferroelect., Freq. Contr.*, vol. 50, p. 419, 2003.

[26] H. F. Pollard, *Sound Waves in Solids.* Pion, 1977.

[27] D. C. Gazis, “Three-dimensional investigation of the propagation of waves in hollow circular cylinders,” *J. Acoust. Soc. Am.*, vol. 31, p. 568, 1959.

[28] P. M. Morse and H. Feshbach, *Methods of Theoretical Physics.* McGraw-Hill, 1953.

[29] A. H. Fitch, “Observation of elastic-pulse propagation in axially symmetric and non-axially symmetric longitudinal modes of hollow cylinders,” *J. Acoust. Soc. Am.*, vol. 35, p. 706, 1963.

[30] B. N. Pavlakovic, *Leaky Guided Ultrasonic Waves in NDT.* PhD thesis, Mechanical Engineering Department, Imperial College London, 1998.

[31] B. Pavlakovic, M. J. S. Lowe, D. N. Alleyne, and P. Cawley, “Disperse: a general purpose program for creating dispersion curves,” in *Review of Progress in QNDE*, vol. 16, p. 185, 1997.

[32] A. Chakraborty and S. Gopalakrishnan, “A spectrally formulated finite element for wave propagation analysis in layered composite media,” *Int. J. Solids. Struct.*, vol. 41, p. 5155, 2004.

[33] S. Datta, A. Shah, R. Bratton, and T. Chakraborty, “Wave propagation in laminated composite plates,” *J. Acoust. Soc. Am.*, vol. 83, p. 2020, 1988.

[34] S. Finnveden, “Spectral finite element analysis of the vibration of straight fluid-filled pipes with flanges,” *J. Sound Vibrat.*, vol. 199, p. 125, 1997.

[35] J. M. Galan and R. Abascal, “Lamb mode conversion at edges. a hybrid boundary element-finite-element solution,” *J. Acoust. Soc. Am.*, vol. 117, p. 1777, 2005.

[36] L. Gavric, “Computation of propagative waves in free rail using a finite element technique,” *J. Sound Vibrat.*, vol. 185, p. 531, 1995.

[37] T. Hayashi, W. J. Song, and J. Rose, “Guided wave dispersion curves for a bar with an arbitrary cross-section, a rod and rail example,” *Ultrasonics*, vol. 41, p. 175, 2003.

[38] T. Hayashi, C. Tamayama, and M. Murase, “Wave structure analysis of guided waves in a bar with an arbitrary cross section,” *Ultrasonics*, vol. 44, p. 17, 2006.

[39] P. E. Lagasse, “Higher-order finite-element topographic guides supporting elastic surface waves,” *J. Acoust. Soc. Am.*, vol. 53, p. 1116, 1973.

[40] B. R. Mace, D. Duhamel, M. J. Brennan, and L. Hinke, “Finite element prediction of wave motion in structural waveguides,” *J. Acoust. Soc. Am.*, vol. 117, p. 2835, 2005.

[41] D. R. Mahapatra and S. Gopalakrishnan, “A spectral finite element model for analysis of axial-flexural-shear coupled wave propagation in laminated composite beams,” *Compos. Struct.*, vol. 59, p. 67, 2003.

[42] T. Mazuch, “Wave dispersion modelling anisotropic shells and rods by the finite element method,” *J. Sound Vib.*, vol. 198, p. 429, 1996.

[43] J. M. Mencik and M. N. Ichchou, “Multi-mode propagation and diffusion in structures through finite elements,” *Eur. J. Mech. A*, vol. 24, p. 877, 2005.

[44] U. Orrenius and S. Finnveden, “Calculation of wave propagation in rib stiffened plate structures,” *J. Sound Vib.*, vol. 198, p. 203, 1996.

[45] P. J. Shorter, “Wave propagation and damping in linear viscoelastic laminates,” *J. Acoust. Soc. Am.*, vol. 115, p. 1917, 2004.

[46] Z. Xi, G. Liu, K. Lam, and H. Shang, “Dispersion and characteristic surfaces of waves in laminated composite circular cylindrical shells,” *J. Acoust. Soc. Am.*, vol. 108, p. 2179, 2000.

[47] W. X. Zhong and F. W. Williams, “On the direct solution of wave propagation for repetitive structures,” *J. Sound Vibrat.*, vol. 181, p. 485, 1995.

[48] COMSOL® Inc., “COMSOL® Multiphysics®,” 2013. url: `http://www.comsol.com`.

[49] The MathWorks®, Inc., “MATLAB®,” 2013. url: `http://www.mathworks.com`.

[50] P. D. Wilcox, M. J. S. Lowe, and P. Cawley, “Mode and transducer selection for long range lamb wave inspection,” *Key Eng. Mat.*, vol. 167-168, p. 152, 1999.

[51] R. Carandente, J. Ma, and P. Cawley, “The scattering of the fundamental torsional mode from axi-symmetric defects with varying depth profile in pipes,” *J. Acoust. Soc. Am.*, vol. 127, p. 3440, 2010.

[52] R. Carandente and P. Cawley, “The effect of complex defect profiles on the reflection of the fundamental torsional mode in pipes,” *NDT&E International*, vol. 46, p. 41, 2012.

[53] R. Carandente, A. Lovstad, and P. Cawley, “The influence of sharp edges in corrosion profiles on the reflection of guided waves,” *NDT&E International*, vol. 52, p. 57, 2012.

[54] Guided Ultrasonics Ltd., “Wavemaker® Pipe Screening System,” 2013. url: `http://www.guided-ultrasonics.com/public2013/?page_id=772`.

[55] M. Ratassepp, S. Fletcher, and M. J. S. Lowe, “Scattering of the fundamental torsional mode at an axial crack in a pipe,” *J. Acoust. Soc. Am.*, vol. 127, p. 730, 2010.

[56] J. Davies and P. Cawley, “The application of synthetic focusing for imaging crack-like defects in pipelines using guided waves,” *IEEE Trans. Ultrason., Ferroelect., Freq. Contr.*, vol. 56, p. 759, 2009.

[57] L. Moreau, A. Velichko, and P. D. Wilcox, “Accurate finite element modeling of guided wave scattering from irregular defects,” *NDT&E International*, vol. 45, p. 46, 2012.

[58] A. Velichko and P. D. Wilcox, “A generalized approach for efficient finite element modeling of elastodynamic scattering in two and three dimensions,” *J. Acoust. Soc. Am.*, vol. 128, p. 1004, 2010.

[59] A. Lovstad and P. Cawley, “The reflection of the fundamental torsional guided wave from multiple circular holes in pipes,” *NDT&E International*, vol. 44, p. 553, 2011.

[60] A. Lovstad and P. Cawley, “The reflection of the fundamental torsional mode from pit clusters in pipes,” *NDT&E International*, vol. 46, p. 83, 2012.

[61] R. Kirby, Z. Zlatev, and P. Mudge, “On the scattering of torsional elastic waves from axisymmetric defects in coated pipes,” *J. Sound Vibrat.*, vol. 331, p. 3989, 2012.

[62] W. Luo and J. Rose, “Phased array focusing with guided waves in a viscoelastic coated hollow cylinder,” *J. Acoust. Soc. Am.*, vol. 121, p. 1945, 2007.

[63] J. Li and J. Rose, “Natural beam focusing of non-axisymmetric guided waves in large-diameter pipes,” *Ultrasonics*, vol. 44, p. 35, 2006.

[64] J. Li and J. Rose, “Excitation and propagation of non-axisymmetric guided waves in a hollow cylinder,” *J. Acoust. Soc. Am.*, vol. 109, p. 457, 2001.

[65] J. W. Cheng, S. K. Yang, and B. H. Li, “Guided wave attenuation in clamp support mounted pipes,” *Mater. Eval.*, vol. 65, p. 317, 2007.

[66] S. K. Yang, P. H. Lee, and J. W. Cheng, “Effect of welded pipe support brackets on torsional guided wave propagation,” *Mater. Eval.*, vol. 67, p. 935, 2009.

[67] K. L. Johnson, *Contact Mechanics.* Cambridge University Press, 1985.

[68] B. Bhushan, *Modern Tribology Handbook.* CRC Press, 2001.

[69] L. C. Hale, *Principles and Techniques for Designing Precision Machines.* PhD thesis, Mechanical Engineering Department, Massachusetts Institute of Technology, 1999.

[70] H. Sherif and S. S. Kossa, “Relationship between normal and tangential contact stiffness of nominally flat surfaces,” *Wear*, vol. 151, p. 49, 1991.

[71] J. G. Harris, “Rayleigh wave propagation in curved waveguides,” *Wave Motion*, vol. 36, p. 425, 2002.

[72] W. Hassan and P. B. Nagy, “On the low-frequency oscillation of a fluid layer between two elastic plates,” *J. Acoust. Soc. Am.*, vol. 102, p. 3343, 1997.

[73] B. Hosten and M. Castaings, “Surface impedance matrices to model the propagation in multilayered media,” *Ultrasonics*, vol. 41, p. 501, 2003.

[74] M. J. S. Lowe, “Matrix techniques for modelling ultrasonic waves in multilayered media,” *IEEE Trans. Ultrason., Ferroelect., Freq. Contr.*, vol. 42, p. 525, 1995.

[75] A. L. Shuvalov, O. Poncelet, and M. Deschamps, “General formalism for plane guided waves in transversely inhomogeneous anisotropic plates,” *Wave Motion*, vol. 40, p. 413, 2004.

[76] V. Damljanovic and R. L. Weaver, “Propagating and evanescent elastic waves in cylindrical waveguides of arbitrary cross section,” *J. Acoust. Soc. Am.*, vol. 115, p. 1572, 2004.

[77] T. Bartoli, A. Marzania, F. Lanza di Scalea, and E. Viola, “Modeling wave propagation in damped waveguides of arbitrary cross-section,” *J. Sound Vibrat.*, vol. 295, p. 685, 2006.

[78] M. V. Predoi, M. Castaings, B. Hosten, and C. Bacon, “Wave propagation along transversely periodic structures,” *J. Acoust. Soc. Am.*, vol. 121, p. 1935, 2007.

[79] K. Jezzine and A. Lhemery, “Diffraction effects on ultrasonic guided waves radiated or received by transducers mounted on the section of the guide,” in *Review of Progress in QNDE*, vol. 25, p. 134, 2006.

[80] M. Castaings and M. J. S. Lowe, “Finite element model for waves guided along solid systems of arbitrary section coupled to infinite solid media,” *J. Acoust. Soc. Am.*, vol. 123, p. 696, 2008.

[81] X. Shi and A. A. Polycarpou, “Measurement and modelling of normal contact stiffness and contact damping at the meso scale,” *J. Vib. Acoust.*, vol. 127, p. 52, 2005.

[82] D. J. Ewins, *Modal Testing.* Research Studies Press Ltd., 2000.

[83] X. Bao, P. Raju, and H. Uberall, “Circumferential waves on an immersed, fluid-filled elastic cylindrical shell,” *J. Acoust. Soc. Am.*, vol. 105, p. 2704, 1999.

[84] X. Bao, H. Franklin, P. Raju, and H. Uberall, “The splitting of dispersion curves for plates fluid-loaded on both sides,” *J. Acoust. Soc. Am.*, vol. 102, p. 1246, 1997.

[85] G. Maze, F. Leon, J. Ripoche, and H. Uberall, “Repulsion phenomena in the phase velocity dispersion curves of circumferential waves on elastic cylindrical shells,” *J. Acoust. Soc. Am.*, vol. 105, p. 1695, 1999.

[86] J. Sessarego, J. Sageloli, C. Gazanhes, and H. Uberall, “Two scholte-stoneley waves on doubly fluid-loaded plates and shells,” *J. Acoust. Soc. Am.*, vol. 101, p. 135, 1997.

[87] F. Simonetti and P. Cawley, “On the nature of shear horizontal wave propagation in elastic plates coated with viscoelastic materials,” *Proc. R. Soc. A*, vol. 460, p. 2197, 2004.

[88] H. Uberall, B. Hosten, M. Deschamps, and A. Gerard, “Repulsion of phase velocity dispersion curves and the nature of plate vibrations,” *J. Acoust. Soc. Am.*, vol. 96, p. 908, 1994.

[89] Dassault Systèmes SA, “ABAQUS Unified FEA,” 2013. url: `http://www.3ds.com/products-services/simulia/portfolio/abaqus/overview/`.

[90] D. N. Alleyne and P. Cawley, “The interaction of lamb waves with defects,” *IEEE Trans. Ultrason., Ferroelect., Freq. Contr.*, vol. 39, p. 381, 1992.

[91] M. Castaings, C. Bacon, B. Hosten, and M. V. Predoi, “Finite element predictions for the dynamic response of thermo-viscoelastic material structures,” *J. Acoust. Soc. Am.*, vol. 115, p. 1125, 2004.

[92] M. Castaings and C. Bacon, “Finite element modeling of torsional wave modes along pipes with absorbing materials,” *J. Acoust. Soc. Am.*, vol. 119, p. 3741, 2006.

[93] M. Drozdz, L. Moreau, M. Castaings, M. J. S. Lowe, and P. Cawley, “Efficient numerical modelling of absorbing regions for boundaries of guided waves problems,” in *Review of Progress in QNDE*, vol. 25, p. 126, 2006.

[94] M. Drozdz, E. Skelton, R. V. Craster, and M. J. S. Lowe, “Modeling bulk and guided wave propagation in unbounded elastic media using absorbing layers,” in *Review of Progress in QNDE*, vol. 26, p. 87, 2007.

[95] B. Masserey and P. Fromme, “On the reflection of coupled rayleigh-like waves at surface defects in plates,” *J. Acoust. Soc. Am.*, vol. 123, p. 88, 2008.

[96] E. N. Codaro, R. Z. Nakazato, A. L. Horovistiz, L. M. F. Ribeiro, R. B. Ribeiro, and L. R. O. Hein, “An image processing method for morphology characterization and pitting corrosion evaluation,” *Mater. Sci. Eng.*, vol. A334, p. 298, 2002.

[97] M. B. Kermani and A. Morshed, “Carbon dioxide corrosion in oil and gas production âĂŤ a compendium,” *Corrosion*, vol. 59, p. 659, 2003.

[98] B. Kermani, J. Martin, and K. Esaklul, “Materials design strategy: Effects of h_2s/co_2 corrosion on materials selection,” in *NACE Int.*, p. 06121, 2006.

[99] J. Kvarekval, “Morphology of localised corrosion attacks in sour environments,” in *NACE Int.*, p. 07659, 2007.

[100] R. Nyborg, “Initiation and growth of mesa corrosion attack during co_2 corrosion of carbon steel,” in *NACE Int.*, p. 48, 1998.

[101] S. Papavinasam, A. Doiron, and R. Winston-Revie, “A model to predict internal pitting corrosion of oil and gas pipelines,” in *NACE Int.*, p. 0758, 2007.

[102] A. J. Croxford, P. D. Wilcox, B. W. Drinkwater, and G. Konstantinidis, “Strategies for guided-wave structural health monitoring,” *Proc. R. Soc. A*, vol. 463, p. 2961, 2007.

[103] J. E. Michaels and T. E. Michaels, “Detection of structural damage from the local temporal coherence of diffuse ultrasonic signals,” *IEEE Trans. Ultrason., Ferroelect., Freq. Contr.*, vol. 52, p. 1769, 2005.

[104] M. I. Friswell and J. E. Mottershead, *Finite element model updating in structural dynamics.* Kluwer Academic Publishers, 1995.

[105] C. P. Fritzen and K. Bohle, "Global damage identification of the steelquake structure using modal data," *Mech. Syst. Signal Process.*, vol. 17, p. 111, 2003.

[106] E. Goerl and M. Link, "Damage identification using changes of eigenfrequencies and modeshapes," *Mech. Syst. Signal Process.*, vol. 7, p. 110, 2003.

[107] J. E. Mottershead and M. I. Friswell, "Model updating in structural dynamics: A survey," *J. Sound Vib.*, vol. 167, p. 347, 1993.

[108] K. Worden and G. Manson, "The application of machine learning to structural health monitoring," *Phil. Trans. R. Soc. A*, vol. 365, p. 515, 2007.

[109] K. Worden, H. Sohn, and C. R. Farrar, "Novelty detection in a changing environment: Regression and interpolation approaches," *J. Sound Vibrat.*, vol. 258, p. 741, 2002.

[110] N. Stubbs, J. T. Kim, and C. R. Farrar, "Field verification of a nondestructive damage localisation and severity estimation algorithm," in *Proc. IMAC XIII*, 1995.

[111] H. Sohn, H. Park, K. H. Law, and C. R. Farrar, "Instantaneous online monitoring of unmanned aerial vehicles without baseline signals," in *Proc. IMAC XXIII*, 2005.

[112] D. Donskoy, A. Zagrai, A. Chudnovsky, E. Golovin, and V. Agarwala, "Nonlinear vibroacoustic modulation technique for life prediction of aging aircraft components," in *Proc. Third Eur. Workshop on SHM*, p. 251, 2006.

[113] M. Ryles, I. McDonald, F. H. Ngau, and W. J. Staszewski, "Ultrasonic wave modulations for damage detection in metallic structures," in *Proc. Third Eur. Workshop on SHM*, p. 275, 2006.

[114] N. Stubbs and J. T. Kim, "Damage localization without baseline modal parameters," *AIAA J.*, vol. 34, p. 1644, 1996.

[115] A. J. Croxford, J. Moll, P. D. Wilcox, and J. E. Michaels, "Efficient temperature compensation strategies for guided wave structural health monitoring," *Ultrasonics*, vol. 50, p. 517, 2010.

[116] T. Clarke, P. Cawley, P. D. Wilcox, and A. J. Croxford, "Evaluation of the damage detection capability of a sparse-array guided-wave shm system applied to a complex structure under varying thermal conditions," *IEEE Trans. Ultrason., Ferroelect., Freq. Contr.*, vol. 56, p. 2666, 2009.

[117] T. Clarke, F. Simonetti, and P. Cawley, "Guided wave health monitoring of complex structures by sparse array systems: Influence of temperature changes on performance," *J. Sound Vibrat.*, vol. 329, p. 2306, 2010.

[118] T. Clarke, F. Simonetti, S. Rohklin, and P. Cawley, "Development of a low-frequency high purity a0 mode transducer for shm applications," *IEEE Trans. Ultrason., Ferroelect., Freq. Contr.*, vol. 56, p. 1457, 2009.

[119] A. J. Croxford, P. D. Wilcox, G. Konstantinidis, and B. W. Drinkwater, "Strategies for overcoming the effect of temperature on guided wave structural health monitoring," in *Proc. SPIE*, vol. 6532, p. 65321T, 2007.

[120] G. Konstantinidis, B. W. Drinkwater, and P. D. Wilcox, "The temperature stability of guided wave structural health monitoring systems," *Smart Mater. Struct.*, vol. 15, p. 967, 2006.

[121] F. Lanza di Scalea and S. Salamone, "Temperature effects in ultrasonic lamb wave structural health monitoring," *J. Acoust. Soc. Am.*, vol. 124, p. 161, 2008.

[122] Y. Lu and J. E. Michaels, "Feature extraction and sensor fusion for ultrasonic structural health monitoring under changing environmental conditions," *IEEE Sensors J.*, vol. 9, p. 1462, 2009.

[123] Y. Lu and J. E. Michaels, "A methodology for structural health monitoring with diffuse ultrasonic waves in the presence of temperature variations," *Ultrasonics*, vol. 43, p. 717, 2005.

[124] H. Sohn, "Effects of environmental and operational variability on structural health monitoring," *Phil. Trans. R. Soc. A*, vol. 365, p. 539, 2007.

[125] R. L. Weaver and O. I. Lobkis, "Temperature dependence of diffuse field phase," *Ultrasonics*, vol. 38, p. 491, 2000.

[126] S. Boyd and L. Vandenberghe, *Convex Optimization.* Cambridge University Press, 2004.

[127] D. E. Goldberg, *Genetic Algorithms in Search, Optimization, and Machine Learning.* Addison-Wesley Professional, 1989.

[128] J. Nocedal and S. Wright, *Numerical Optimization.* Springer, 2006.

[129] Federal Aviation Administration, *Metallic Materials Properties Development and Standardization (MMPDS) Handbook.* Battelle Memorial Institute, 2012.

[130] E. J. Cross, K. Worden, and Q. Chen, "Cointegration: A novel approach for the removal of environmental trends in structural health monitoring data," *Proc. R. Soc. A*, vol. 467, p. 2712, 2011.

[131] E. J. Cross, G. Manson, K. Worden, and S. G. Pierce, "Features for damage detection with insensitivity to environmental and operational variations," *Proc. R. Soc. A*, vol. 468, p. 4098, 2012.

[132] M. Basseville and I. V. Nikiforov, *Detection of Abrupt Changes: Theory and Application.* Prentice-Hall, Inc., 1993.

[133] F. Gustafsson, *Adaptive Filtering and Change Detection.* John Wiley & Sons, Inc., 2000.

[134] D. L. Burkholder and R. A. Wijsman, "Optimum properties and admissibility of sequential tests," *Ann. Math. Stat.*, vol. 34, p. 1, 1963.

[135] B. Eisenberg, B. K. Ghosh, and G. Simons, "Properties of generalized sequential probability ratio tests," *Ann. Stat.*, vol. 4, p. 237, 1976.

[136] A. Wald and J. Wolfowitz, "Optimum character of the sequential probability ratio test," *Ann. Math. Stat.*, vol. 19, p. 326, 1948.

[137] J. Neyman and E. S. Pearson, "On the problem of the most efficient tests of statistical hypotheses," *Phil. Trans. R. Soc. A*, vol. 231, p. 289, 1933.

[138] A. Wald, *Sequential Analysis.* John Wiley & Sons, Inc., 1947.

[139] B. K. Ghosh and P. K. Sen, *Handbook of Sequential Analysis.* Marcel Dekker, Inc., 1991.

[140] E. S. Page, "Continuous inspection schemes," *Biometrika*, vol. 41, p. 100, 1954.

[141] G. Lorden, "Procedures for reacting to a change in distribution," *Ann. Math. Stat.*, vol. 42, p. 1897, 1971.

[142] G. V. Moustakides, "Optimal stopping times for detecting changes in distributions," *Ann. Stat.*, vol. 14, p. 1379, 1986.

[143] Y. Ritov, "Decision theoretic optimality of the cusum procedure," *Ann. Math. Stat.*, vol. 18, p. 1464, 1990.

[144] A. N. Shiryaev, “The problem of the most rapid detection of a disturbance in a stationary process,” *Soviet Math. Dokl.*, vol. 2, p. 795, 1961.

[145] E. Flynn, M. D. Todd, A. J. Croxford, B. W. Drinkwater, and P. D. Wilcox, “Enhanced detection through low-order stochastic modeling for guided-wave structural health monitoring,” *Struct. Health Monit.*, vol. 11, p. 149, 2012.

[146] E. Flynn, M. D. Todd, P. D. Wilcox, B. W. Drinkwater, and A. J. Croxford, “Maximum likelihood estimation of damage location in guided wave structural health monitoring,” *Proc. R. Soc. A*, vol. 467, p. 2575, 2011.

[147] G. A. F. Seber and A. J. Lee, *Linear Regression Analysis.* John Wiley & Sons, Inc., 2003.

[148] P. S. Dwyer, “Some applications of matrix derivatives in multivariate analysis,” *J. Am. Stat. Assoc.*, vol. 62, p. 607, 1967.

[149] Stopaq B. V., “Stopaq® CZH Paste,” 2013. url: `http://www.stopaq.com/en/products/oil_and_gas_products/corrosion_prevention/paste_czh/`.

[150] C. Stein, “A note on cumulative sums,” *Ann. Math. Stat.*, vol. 17, p. 198, 1946.

List of Publications

[P1] A. Galvagni and P. Cawley, “The reflection of guided waves from simple supports in pipes,” *J. Acoust. Soc. Am.*, vol. 129, p. 1869, 2011.

[P2] A. Galvagni and P. Cawley, “The reflection of guided waves from simple supports in pipes,” in *Review of Progress in QNDE*, vol. 30, p. 105, 2011.

[P2] A. Galvagni and P. Cawley, “A permanently installed guided wave system for pipe monitoring,” in *Proc. SPIE*, vol. 8348, p. 83480B, 2012.

[P4] A. Galvagni and P. Cawley, “Guided wave permanently installed pipeline monitoring system,” in *Review of Progress in QNDE*, vol. 31, p. 1591, 2012.

[P5] M. J. S. Lowe, P. Cawley, and A. Galvagni, “Monitoring of corrosion in pipelines using guided waves and permanently installed transducers,” *J. Acoust. Soc. Am.*, vol. 132, p. 1932, 2012.

[P6] P. Cawley, F. Cegla, and A. Galvagni, “Guided waves for NDT and permanently-installed monitoring,” *Insight*, vol. 54, p. 594, 2012.

[P7] A. Galvagni and P. Cawley, “Permanently installed guided wave pipeline monitoring,” in *Review of Progress in QNDE*, vol. 32, p. 159, 2013.